Stimuli-responsive polymer coatings based on (poly-L-Lysine)-g-poly(N-isopropylacrylamide) to control specific cell adhesion

Fabrice Dalier

▶ To cite this version:

Fabrice Dalier. Stimuli-responsive polymer coatings based on (poly-L-Lysine)-g-poly(N-isopropylacrylamide) to control specific cell adhesion. Polymers. Université Paris sciences et lettres, 2016. English. NNT : 2016PSLEE019 . tel-01474357

HAL Id: tel-01474357

https://theses.hal.science/tel-01474357v1

Submitted on 22 Feb 2017

THÈSE DE DOCTORAT
de l'Université de recherche
Paris Sciences et Lettres –
PSL Research University

préparée à
l'Ecole normale supérieure
Département de Chimie
Pôle de Chimie-Biophysique

Stimuli-responsive polymer coatings based on (poly-L-lysine)-g-poly(N-isopropylacrylamide) to control specific cell adhesion

Revêtements polymères stimulables à base de (poly-L-lysine)-g-poly(N-isopropylacrylamide) pour contrôler l'adhésion cellulaire spécifique

par Fabrice Dalier

dirigée par Emmanuelle MARIE

Ecole doctorale n°388
Spécialité : Chimie
Soutenue le 08.09.2016

Composition du Jury :

M. Yong CHEN
Ecole Normale Supérieure
Président du jury

Mme. Karine ANSELME
Université Haute-Alsace
Rapporteur

M. Patrice WOISEL
Université Lille 1
Rapporteur

Mme. Emmanuelle MARIE
Ecole Normale Supérieure
Directeur de thèse

M. Andre LASCHEWSKY
Université Potsdam
Membre du jury

M. Christophe TRIBET
Ecole Normale Supérieure
Membre invité

M. Matthieu PIEL
Institut Curie
Membre invité

Résumé

Des revêtements polymères basés sur la physisorption de copolymères en peigne, dérivés du (Poly-L-Lysine)-g-poly(N-Isopropylacrylamide) noté PLL-g-PNIPAM, ont été développés afin de contrôler réversiblement l'adhésion cellulaire. La préparation de ces revêtements repose sur l'adsorption spontanée de la poly(lysine) sur la plupart des substrats anioniques usuels en biologie, aisément mis en œuvre par le non-spécialiste : une simple immersion du substrat dans une solution de PLL-g-PNIPAM donne une mono-couche résistante au rinçage et dense en chaines poly(N-Isopropylacrylamide) thermosensibles. L'adsorption de copolymères en peigne dérivés de la PLL et portant des chaînes latérales de natures variées permet d'ajuster à souhait les propriétés du revêtement. Notre attention s'est portée particulièrement sur l'étude de couches thermosensibles poly(N-Isopropylacrylamide-co-ligand), où le ligand est soit un groupe biotine, soit un peptide d'adhésion.

Une voie de synthèse générique de dérivés PLL-g-PNIPAM est décrite. Elle se fonde sur la polymérisation RAFT du N-acryloxysuccinimide et la post-modification des unités de répétition puis des extrémités de chaînes. Des mesures de la température de transition soluble/insoluble en solution et des caractérisations par AFM et QCM-d de l'extension des chaînes en surface ont permis de démontrer que la transition au sein des revêtements s'opère à une température proche de celle en solution. La stabilité en termes de composition et d'épaisseur des revêtements suite à des cycles de transitions thermiques a été vérifiée. Une étude de l'adsorption de particules décorées par des protéines comme l'avidine a permis de montrer la capacité des couches adsorbée à exposer/masquer la biotine, et à réguler la formation de liaisons spécifiques par simple changement de température. Pour s'assurer de la possibilité d'ajustement du contraste d'accessibilité de ligands, cette étude a été complétée par des mesures sur des couches mixtes contenant des mélanges de chaînes fonctionnelles ou non fonctionnalisées. Enfin, en utilisant un peptide d'adhésion (RGD) comme ligand, il a été montré que l'interaction avec la surface de cellules HeLA peut être réversiblement contrôlée via une variation de température de quelques degrés, moyennant d'optimiser la densité en peptides et la présence de chaînes répulsives en surface.

Un control local par stimulation lumineuse a été envisagé. Des poly(N-Isopropylacrylamide) contenant des azobenzenes furent synthétisés mais ne montrent qu'une faible réponse lumineuse.

Mots Clés

Revêtement thermo-stimulable, (Poly-L-Lysine)-g-poly(N-Isopropylacrylamide), adsorption, culture cellulaire, adhésion spécifique

Abstract

Polymer coatings based on the physorption of comb-like polymers, (Poly-L-Lysine)-g-poly(N-Isopropylacrylamide) derivatives (PLL-g-PNIPAM), have been developed to reversibly modulate specific cell adhesion on demand. This technique of coating relies on the spontaneous adsorption of PLL on typical anionic substrates used in biology: a simple bath application of substrates in solution of PLL-g-PNIPAM affords a stable polymer adlayer with dense and thermoresponsive poly(N-Isopropylacrylamide) brushes. Adsorption of comb-like polymers with different strands enables to easily modulate properties of the coatings. We focused on thermoresponsive poly(N-Isopropylacrylamide-co-ligand) brushes where ligand is Biotin or a peptide of adhesion.

A versatile synthesis of PLL-g-PNIPAM is presented. This synthesis is based on RAFT polymerization of N-acryloxysuccinimide and post-modifications of both the backbone and the polymer ends. Detection of the transition soluble/insoluble in solution and AFM/QCM-d studies of PNIPAM adlayers demonstrate that the critical temperature in adlayers are close to the one in solution. Stability in terms of composition and thickness has been checked after temperature cycles. The study of the adsorption of Avidin-coated particles suggests that these adlayers can expose/mask Biotin, and so regulate specific interaction by simple change in temperature. To optimize the thermal contrast of ligand accessibility, this study includes measurements on mixed adlayers with functionalized/unfunctionalized brushes. Finally, specific adhesion of HeLa cells can be thermally modulated on adlayers presenting repellent brushes and with controlled densities of adhesive peptides (RGD).

A local control has been considered on such coatings by using light stimulus. In this context, azobenzene-containing Poly(N-Isopropylacrylamide) were synthesized but they shown only a weak light-response.

Keywords

Thermo-responsive coating, (Poly-L-Lysine)-g-poly(N-Isopropylacrylamide), adsorption, cell culture, specific adhesion

Numero national de thèse :
....

Contents

Abbreviations & acronyms

- PLL : poly-L-lysine
- PNIPAM : poly(N-isopropylacrylamide)
- PEG : poly(ethylene glycol)
- OEG : oligo(ethylene glycol)
- RGD : sequence arginine-glycine-aspartic acid
- PS : poly(styrene)
- NHS : N-hydroxysuccinimide
- NAS : N-acryloxysuccinimide
- PNAS : poly(N-acryloxysuccinimide)
- CTA : chain transfer agent
- AIBN : azobis(isobutyronitrile)
- RAFT : reversible addition-fragmentation chain transfer
- DMSO : dimethylsulfoxide
- DMF : N,N-dimethylformamide
- NMR : nuclear magnetic resonance spectroscopy
- SEC : size exclusion chromatography
- AFM : atomic force microscopy
- QCM-d : quartz crystal microbalance with dissipation
- LCST : lower critical solution temperature
- DMEM : Dulbecco's modified eagle medium
- PBS : phosphate saline buffer
- azo : azobenzene

Chapter 1 - Introduction

It has been established for a while that growth and proliferation of mammalian cells generally proceed better on soft matrices or solid substrates with promoted cell-adhesive properties. In vivo and in vitro cell adhesion, usually in cooperation with other signals, regulates cell responses such as polarization/migration/division/differentiation. Manipulation of cells in artificial environments mimicking the interactions network of natural matrices represents a fundamental issue in cell biology. Not surprisingly, works in tissue engineering invest a lot of efforts in the development of artificial materials allowing spatio-temporal control of cell/matrix interactions. These materials are designed to help the reconstitution of functional tissues, with increasing complexity (e.g. co-cultures of several cell types, multilayered cell sheets, organoids, up to the "grail" of a whole organ) (Ratner et al., 2013).

Pioneer strategies in the design of such materials have typically relied on macromolecular networks endowed with controlled specific interactions with cells, via the presence of peptides or various biomolecules attached or dispersed in/on the matrix. These "passive" scaffolds enable to set several important parameters impacting cell adhesion (biochemical composition, mechanical properties, roughness, porosity, *etc*). New strategies in the design of biomaterials seek to modulate these parameters *in situ*, in response to a non-invasive stimulus. These approaches are now promising routes toward the dynamic control of cells.

Among the vast literature on biomaterials and control of cell culture, we selected and summarized in this chapter a limited subset of results that describe controlled adhesion, and in particular integrin binding which is of primary importance for our work on stimuli-triggered adhesion. Our point of view is focused on highlighting the molecular features that have been identified as key control parameters. Minimal references on the huge variety of biochemical mechanisms involving integrins are included here (Akhmanova et al., 2015; Streuli, 2009), except for some clarifications when needed. It is also far beyond the scope of this introduction to review developments of artificial substrates and control of the complexity of cell responses. Hence, simultaneous interplay of multiple factors and crosstalk between membrane receptors, growth factors, nutrients, guidance cues, ... aren't mentioned. From the point of view of chemists working at the boundary with cell biology, we seek to illustrate recent advances in the molecular design of dynamic biocompatible materials controlling specific adhesion. A brief review about the adhesive-related ECM key parameters introduces the chapter and is primarily focused on responses mediated by integrins. Then, we introduce strategies similar to the one investigated in this thesis, aiming to modulate the exposition of adhesive peptides on the top of cell-repellent layers.

Contents

1 Integrin binding to extracellular matrix, a model for adhesion on biomaterials

The cell microenvironment is a complex and dynamic assembly of secreted molecules. This highly hydrated network holds three major components: fibrous elements (collagens, elastin), space filling molecules (glycosaminoglycans covalently linked to proteins in the form of proteoglycans), and adhesive glycoproteins (fibronectin, laminin, vibronectin) (Figure 1). Cell-ECM interactions aren't fully understood up to date due to their complexity. Nevertheless, studies of cell growth in artificial environments have revealed that both physical and chemical characteristic features of ECM (stiffness, topography, roughness, concentrations and concentration gradients of several molecular cues) can impact the cell behavior (Akhmanova et al., 2015; Ratner et al., 2013). Indeed, cells sense these ECM properties via different membrane receptors, and integrate the information received on the outer membrane via cooperative activations and clustering of these receptors that trigger cascades of downstream biochemical reactions.

As regards adhesion-involved receptors, integrins and glycans are major ECM adhesion receptors which cooperate in signaling events (Geiger et al., 2009). These cell sensors can integrate both external and internal signals spatio-temporally due to their direct connections with external adhesion sites and possible crosstalk with other membrane or cytosolic proteins, involved in signaling pathways (e.g. growth factor receptor signaling pathways) (Kim et al., 2011).

In the following, we focus only on the external conditions that have been shown to facilitate the binding of integrins and its first consequences, that is the formation of a local adhesion patch on cell membrane. The diameter of integrin receptors is between 8 and 12 nm (Xiong et al., 2002). They are composed of two heterodimeric subunits: one α and one β unit. 24 integrin dimers can be formed by the combination of eighteen α and eight β different subunits in mammals.

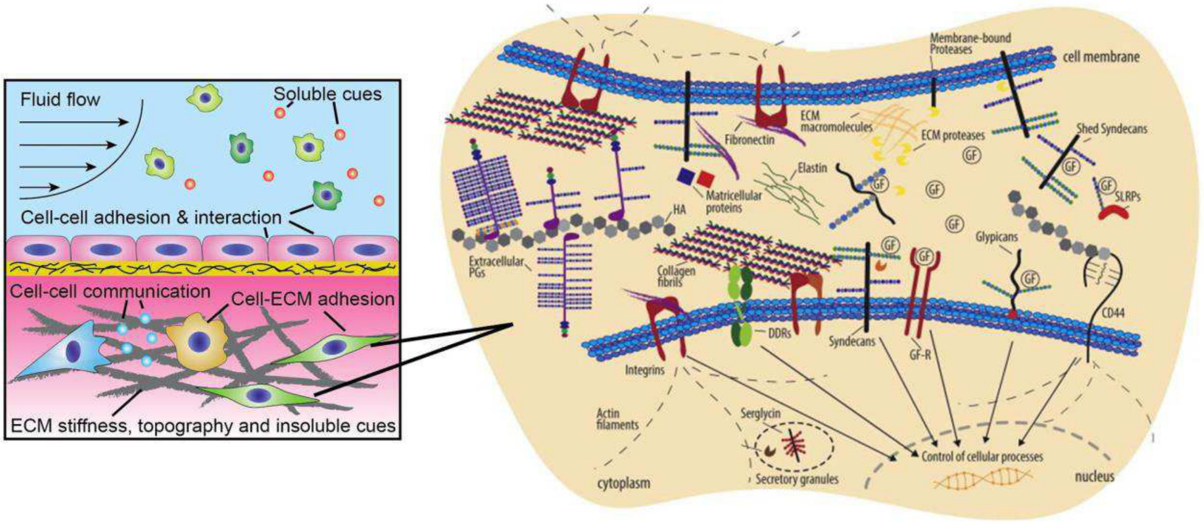

Figure 1 - Schematic overview of cells into their natural environment (left) and a zoom on the interstitial matrice (right) (HA: hyaluronan, PG: proteoglycan, GF: growth factor) (Kim et al., 2011).

Integrins bind to short amino acid sequences of various ECM proteins (collagens, fibronectin, laminin) which mediates cell adhesion. Most integrins bind to the sequence Arg-Gly-Asp (RGD), which was first discovered in fibronectin and later found in many other ECM proteins including laminin, tenascin, vitronectin and thrombospondin. On similar basis, other peptide sequences have been recognized to promote adhesion of specific cell lines displaying specific integrins (e.g. YIGSR or IKVAV for neurite extension, KQAGDV for smooth muscle cells, *etc*) (Ventre et al., 2012). A convenient method to make biomaterials cell adhesive thus consists in functionalizing them with relevant ECM proteins or fragment of those proteins. Hence, fibronectin and collagens are typically adsorbed on surfaces of usual substrates (polystyrene, glass, PDMS, polyacrylamide gels, ...) prior to cell deposition and cultures. Moreover, commercially reactive RGD peptides are now available, and can be used to functionalize a broad range of synthetic surfaces or hydrogels by covalent modifications (Delaittre et al., 2012). These peptides have several advantages over proteins in terms of reproducibility and selectivity. Reactive RGD peptides of different affinities were design by changing residues closed to the adhesive motif: pentacyclic RGD peptides show greater stability and selectivity over linear peptides (Dechantsreiter et al., 1999).

Once integrins have interacted with a cognate peptide sequence, named "epitope" in the following, they may form clusters leading to complex multimolecular assemblies called "focal adhesions" (FAs) (Figure 2). These FAs consist of transmembrane integrin receptors that are linked to the actin cytoskeleton via cytoplasmic anchor proteins such as vinculin, paxillin, and focal adhesion kinase. Consequently, integrins serve as transmembrane mechanical links from those extracellular contacts to the cytoskeleton: they can trigger a large variety of signal transduction events (proliferation, survival/apoptosis, shape, polarity, motility, gene expression, and differentiation) (Berrier and Yamada, 2007; Streuli, 2009)(Hynes, 2002).

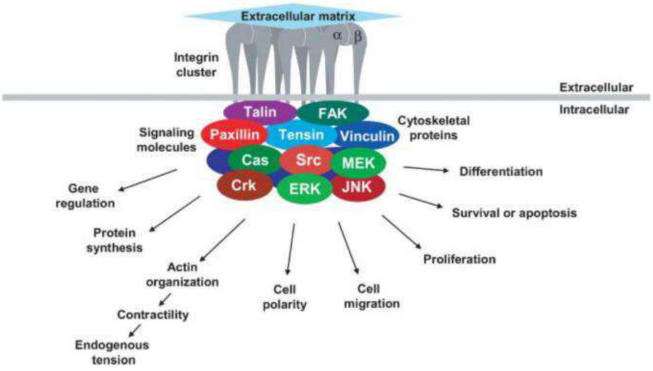

Figure 2 - General model of cell-matrix adhesions and their downstream regulation. Cell-extracellular matrix adhesions containing clusters of integrins recruit cytoplasmic proteins, which in cooperation with other cell surface receptors control diverse cellular processes, functions, and phenotypes (Berrier and Yamada, 2007).

1.1 Integrins as sensor of substrate's biochemical composition and surface patterns

FAs play the role of transducers of physico-chemical properties of the ECM. In particular, the formation of FAs depends on the surface density of epitopes and on their distribution (patterns) at nanoscale up to micrometer scale. Various techniques of surface functionalization with or without patterning have allowed precise spacing at the molecular level of adhesion proteins and peptides (colloidal patterning (Malmström et al., 2010), photolithography + grafting from chemistry (Cheng et al., 2013), nanoimprint + self-assembled monolayers (Gallant et al., 2005)). A representative and comprehensive investigation in this field has been conducted by Spatz *et al.* who used block copolymer/gold nanoparticle nanolithography (Figure 3). Results established that the density of adhesive sites, or of corresponding peptide/proteins must be increased above a threshold to induce cell adhesion (Arnold et al., 2004; Hudalla and Murphy, 2009; Lagunas et al., 2012). Furthermore, this threshold density depends on several additional factors (chemical composition of coatings, adhesive cues, cell line, ...). For example, Spatz *et al.* worked on glass substrates bearing a quasi-hexagonally ordered array of gold nanoparticles (Arnold et al., 2004; Huang et al., 2009) (Figure 3A). Glass was passivated by PLL-g-PEG while cyclic(RGDfK)-thiol was used to functionalize the array of nanoparticles. These authors report a drastic decrease in cell adhesion upon increasing the interparticle distance above 73 nm (Figure 3B). Moreover, as an integrin receptor has a large radius than the one of nano-adhesive particles, only one integrin can bind to each nanoparticle: this enabled authors to study the integrin clustering phenomenon. They showed that the window of inter-receptor distances ranging between 58 and 73 nm is a universal length scale for integrin clustering and activation, since these properties are shared by a variety of cultured cells. Based on comparison between micro-patterned and homogeneous substrates, they argued that the development of stable focal adhesions, their number, and their size as well as the cellular adhesion strength are influenced by the local (length scale ≤ one micrometer) rather than the average ligand density (Deeg et al., 2011). Similarly, FA properties and compositions vary above and below a threshold area of patterned RGD-presenting surfaces (Gallant 2005).

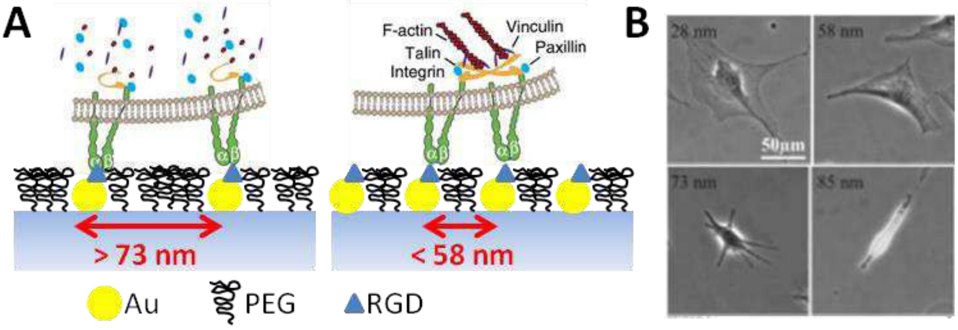

Figure 3 - (A) Scheme of biofunctionalized nanopattern to control integrin clustering in cell membranes: Au dots are functionalized by thiol-coupled c(RGDfK) and areas between cell-adhesive Au dots were passivated by PEG. No integrin clustering below 73 nm (i.e. no focal adhesion). (B) Pictures of MC3T3-osteoblasts on substrates of different distances between nanoparticles (28 nm, 58 nm, 73 nm and 85 nm) (Arnold et al., 2004).

Cells sense gradients of adherent molecules, and migrate towards higher concentrations of adhesive cues. Spatz's team investigated the cell sensitivity to nanoscale variation in adhesion density on their Au-nanoarrays (Arnold et al., 2008). Examination of cell behavior on such surfaces indicated that the weakest gradient to which cells responded was 15 nm.mm^{-1}. Using the estimate of a typical cell length of 60 µm, this implies that cells respond to an inter-particle distance difference of 1 nm between its front and rear parts. Finally, the distance between the surface and the epitope may also matter. The presence of a molecular tether and its flexibility has been reported to modify the time of adhesion. As the length of the tether increases, the time required for cell spreading increases. The penetration depth of integrin-containing filopodia into gel-like surface layers has also been discussed, and epitopes below the surface by significantly more than ~ 10 nm are generally considered as inaccessible (Halperin and Kröger, 2012).

1.2 Integrins as sensor of substrate's mechanical properties

The majority of cells within multi-cellular organisms experiences forces that are highly regulated in space and time. Mechanical forces contribute to control cellular fate, including changes in gene expression, proliferation, and differentiation (Vogel and Sheetz, 2006). Cells sense external stiffness or forces through FAs, by intracytosolic association of the cytoskeleton to the membrane adhesion spots, which exerts a pulling force on FAs that triggers or not kinase activation (mechano-transduction signaling pathway) (Ingber, 2003). Cell responses to either local application of a force, or to substrate rigidity have been investigated on various model conditions that are briefly illustrated below.

1.2.1 Effect of mechanical strain on cells

Sniadecki *et al.* (Sniadecki et al., 2007) designed an original device to apply forces onto living cells. External forces were applied to cells thanks to micro-fabricated magnetic posts (pillars) containing cobalt nanowires interspersed among an array of nonmagnetic PDMS elastomeric posts (Figure 4). In a magnetic field, nanowire-containing posts are bended, which transduce a force to cells bound on their top. Deflection (δ) of nonmagnetic posts are measured to characterize the response to traction forces of the cells. Using this system, local FA growth was observed only at magnetically actuated posts and not at nonmagnetic posts. They also recorded a loss in traction forces upon local force application that was non-uniformly distributed across the cells. These data suggest that cells actively adjust their internal tension to mechanical forces arising from their microenvironment.

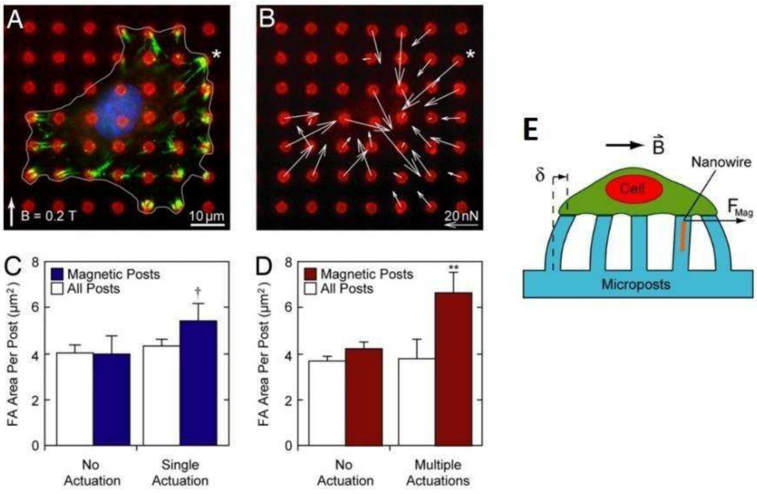

Figure 4 - Microfabricated fibronectin-coated PDMS arrays of magnetic and nonmagnetic posts for applying external forces and measuring traction force responses. (E) External force F_{Mag} is applied to the adherent cell through magnetic posts that bend under the influence of a magnetic field. Nonmagnetic posts report local traction forces through post deflections δ. (A) Representative immunofluorescent micrograph of FAs (green), microposts (red), and nucleus (blue) after force actuation. The cell is outlined, and the location of the magnetic post is marked by the asterisk (*). (B) Vector plot of traction forces at each post are shown with white arrows. (C, D) Plot of average FA area for all posts underneath cells (white bars) and average FA area at magnetic posts (blue bars) when cells are subjected to no actuation and single or multiple actuation.

1.2.2 Effect of rigidity on cells

Stiffness of the different parts of the body ranges from ~ 0 Pa (blood) to > 10^9 Pa (bone). In soft tissues/organs, stiffness varies from 100 Pa to MPa as a consequence of complex reticulation of networks of collagen and elastin fibers.

Engler *et al.* first showed that adhesion strength of myotubes increased monotonically with substrate stiffness and eventually reached the strongest adhesion on rigid substrates such as glass (Engler et al., 2004). Then, Engler *et al.* reported the influence of substrate rigidity in stem cell differentiation (Engler et al., 2006) (Figure 5). Mesenchymal stem cells seeded on soft matrices, whose rigidity is similar to that of brain, formed branched shapes. When they were seeded on rigid surfaces, closer to bone matrix rigidity, polygonal shapes were observed. These results suggest that rigid matrices are osteogenic while soft ones are neurogenic.

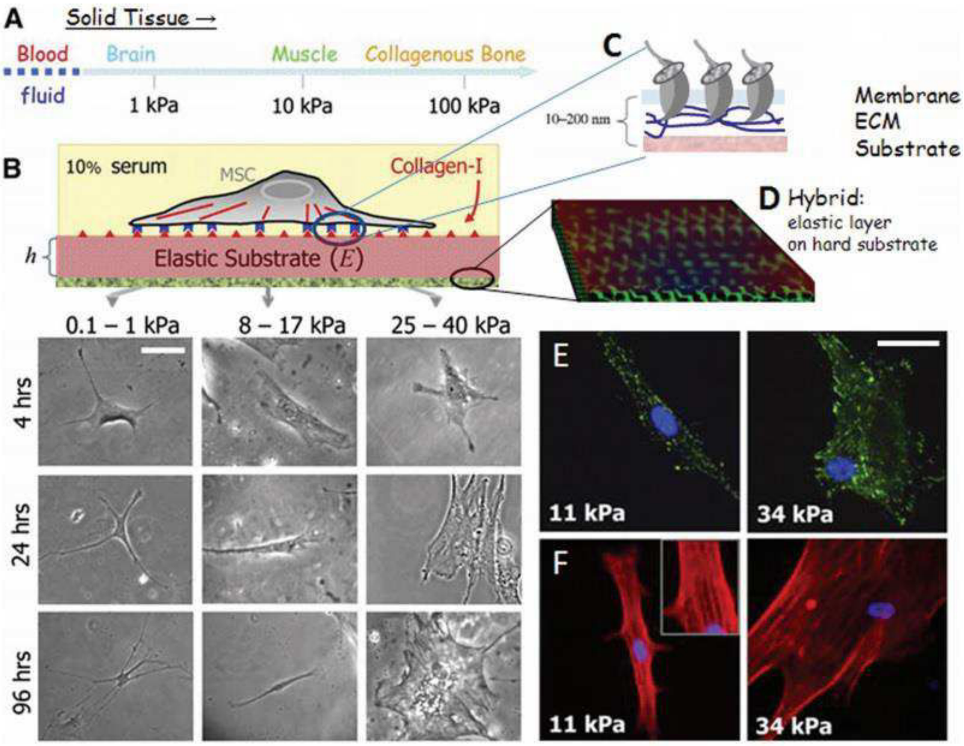

Figure 5 - Tissue elasticity and differentiation of naive mesenchymal stem cells (MSCs). (A) Solid tissues exhibit a range of stiffness, as quantified by the elastic modulus, E. (B) In vitro polyacrylamide gel system allows for control of E through crosslinking, control of cell adhesion by covalent attachment of collagen-I, and control of thickness. MSCs of a standard expression phenotype are initially small and round but develop increasingly branched, spindle, or polygonal shapes when grown on matrices of increasing elasticity. (E) Paxillin-labeled cells showing diffuse ''contacts'' on softer gels (11 kPa) and long and thin adhesions on the stiffer gels (34 kPa). (F) F-actin labelling showing similar trend, from diffused on soft gels to progressively organized on stiffer substrates. Scale bar is 20 µm (Engler et al., 2006).

By seeding motile 3T3 fibroblasts on collagen-coated polyacrylamide substrates with a rigidity gradient, Lo *et al.* showed that cells can sense stiffness gradient and consistently migrates in the direction of increasing stiffness (Lo et al., 2000). This kind of migration is called "durotaxis". Although its traction mechanism is still unclear, it appears that FAs are considered as local rigidity sensors, allowing discernment of differences in the extracellular matrix rigidity with a high spatial resolution(Plotnikov and Waterman, 2013).

1.3 Integrins as sensor of substrate's geometrical properties

1.3.1 Physical confinement

Into their natural niche, cells adopt a shape by anchoring their cytoskeleton on the surrounding 3D environment. Up to now, the use of 2D scaffolds with micro-patterns represent a convenient way to study effects of cell shape, although the third dimensionality is entirely missing. For example, Peng *et al.* (Peng et al., 2011) investigated the differentiation of mesenchymal stem cells (MSCs) from rats on adhesive patterns of the same adhesive area but differing by their shapes (Figure 6A). The osteogenic and adipogenic differentiations exhibited different trends depending on the cell shape. In this case, they found that extents of both adipogenic and osteogenic differentiations were linearly related to cell perimeter, which reflects the non-roundness or local anisotropy of cells. On Figure 6B, we can see that the mean alkaline phosphatase (ALP) activity per cell, a marker of osteogenic differentiation, increases with the average cell perimeter. The opposite trend is noticed for adipogenic differentiation.

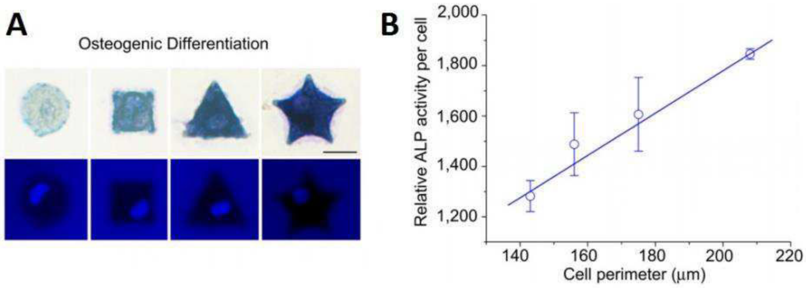

Figure 6 - Differentiation of single stem cells on different micro-adhesive patterns. (A) Optical micrographs of MSCs; Upper panel shows bright-field images; lower one shows the corresponding fluorescent micrographs with cellular nuclei labeled by DAPI. Scale bars: 25 µm. (B) Extent of differentiation (ALP expression stained by Fast Blue shown in A, upper panel) as a function of measured perimeter of single cells on globally isotropic micropatterns (Peng et al., 2011).

A few studies take into account the three dimensionality of ECM, reveling different cell behavior from flat surfaces. Liu *et al.*(Liu et al., 2015a) studied migration of different kind of cells with or without confinement. On low adhesive substrates, cells don't migrate without confinement whereas they acquired a fast migration mechanism ("amoeboid migration") under confinement by imposing a cell thickness of 3 µm.

1.3.2 Topography

Micrometer and/or nanometer scale topographies affect different aspects of cell behavior as illustrated here by considering roughness and porosity (Anselme and Bigerelle, 2011, 2014; Bigerelle et al., 2011; Zinger et al., 2004).

- **nano/micro roughness**

Roughness is recognized to influence cell behavior. Moreover, different regimes of cell response to roughness were identified, depending on the amplitude of reliefs. The minimal height threshold at which substrate nanogroove dimensions may influence filopodial guidance and subsequent whole-cell alignment is around 35 nm (Loesberg et al., 2007). Zinger *et al.* studied osteoblastic cell adhesion and proliferation on titanium surfaces of different roughness(Zinger et al., 2004). They seeded human bone-derived cells (MG63 cells) on almost only flat surfaces differing at the nanoscale roughness, smooth surfaces with micrometer features (disks of 10, 30 and 100 µm), and surfaces combining the two roughness scales (Figure 7). The cells responded to nanoscale roughness by a higher cell thickness and a delayed apparition of the focal contacts. On surfaces with micrometric hemispherical cavities, the MG63 cells preferably adhered and proliferated inside cavities of 30 or 100 µm in diameter, whereas they did not recognize the 10 µm diameter cavities. On surfaces combining micrometer-size cavities and nanometric roughness, cell proliferation exhibited a marked synergistic effect of microscale and nanoscale topographies.

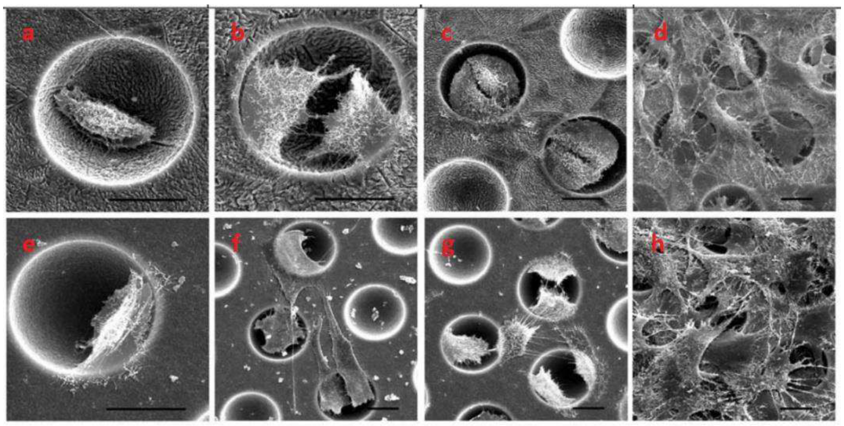

Figure 7 - SEM pictures of MG63 cells cultured on surfaces composed of cavities (30 µm in diameter) with two different nanoscale roughness. (a-d) correspond to pictures taken respectively after 4 h, 24 h, 3 days or 7 days for one nanoscale roughness while (e-h) correspond to one other nanoscale roughness. Scale bar: 15 µm (Zinger et al., 2004).

- **Porosity**

Porosity is the equivalent of surface roughness in 3D and is known for decades to be critical for cell proliferation in scaffolds. Many reviews and reports have been published on benefits of controlled porosity, pointing in particular sizes of ~ 100 micrometers for tissue reconstitution and preservation of cell viability (Akhmanova et al., 2015; Di Cio and Gautrot, 2016; Ventre et al., 2012). Part of the effect may be due to facilitation of the circulation of nutrient and gases. Micrometer curvatures are now clearly identified as an important signal that cells can interpret. Similarly to cultures on flat surfaces, thinner topographies matter in 3D scaffolds. For instance, TiO_2 nanotubes with different diameters were studied to direct cell vitality (Figure 8) (Park et al., 2007). Self-assembled layers of vertically oriented TiO_2 nanotubes with defined diameters between 15 and 100 nm can regulate adhesion, spreading, growth, and differentiation of mesenchymal stem cells. The nanotubes with a spacing < 30 nm and a diameter ~ 15 nm provided an effective length scale for accelerated integrin clustering/focal contact formation and strongly enhanced cellular activities compared to smooth TiO_2 surfaces. Cell adhesion and spreading were severely impaired on nanotube layers with a tube diameter > 50 nm, resulting in dramatically reduced cellular activity and a high extent of programmed cell death. Thus, on a TiO_2 nanotube surface, a lateral spacing geometry with openings of 30 - 50 nm represents a critical borderline for cell fate.

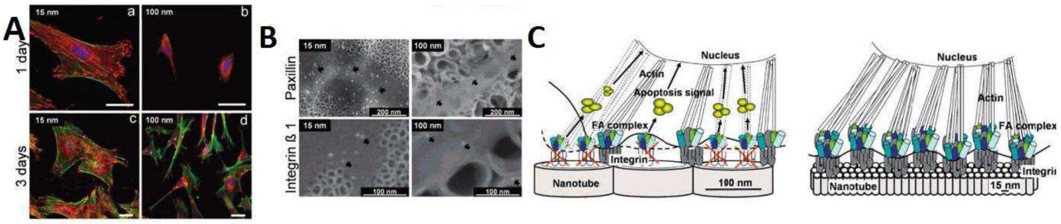

Figure 8 - Focal contact formation, differentiation, and apoptosis of mesenchymal stem cells on 15 and 100 nm nanotubes. (A) Nanoscale spacing directs cell fate: hypothetical model showing the lateral spacing of focal contacts on nanotubes of different diameters. A spacing of 15 nm seems optimal for integrin assembly into focal contacts, thus inducing assembly of actin filaments and signaling to the nucleus. Nanotubes larger than 70 nm diameter do not support focal contact formation and cell signaling, thus leading to apoptosis. (B) Analysis of focal contacts by SEM using immunogold staining with paxillin, and β1-integrin. (C) Schematic representation of the influence of porosity on cell fate(Park et al., 2007).

1.4 Conclusion on the relevant surface parameters

With the goal to better understand the early events of cell adhesion and downstream consequences on cell behaviors, exploration of the detailed temporal and spatial pattern of FA proteins is nowadays very active. In this context, a generic approach consists in perturbing experimentally specific association or interaction of cells with a polymer layer. This approach is based on molecular tools as well as engineered materials enabling to adjust the cell environment. Dynamic modulation of this environment is emerging. Namely, versatile and accurate tools are desirable to study the role of the presentation of epitopes on biomaterial surfaces, and to investigate the effect of:

1- Surface density and distribution of epitopes at nanometer resolution. Indeed, the formation of stable cell adhesions involves grouping of integrins, which depends on epitope organization (density, random/regular distributions) and mobility (attachment to deformable or fluid surfaces),

2- Nanoreliefs: as it guides cell spreading/migration, and/or commitment in specific lineage. Indeed, cell perceives grooves of > 30 nm depth, a size of the order of the radius of long polymer chains,

3- Micrometer-large reliefs and patterns: both geometry and deepness affect spreading, division, …

4- Rigidity: requiring deposition of epitopes on various substrates whose rigidity ranges from soft elastomers to solid-like materials,

5- Synergetic effects: the simultaneous presentation of several signals are likely key triggers (Ventre et al., 2012).

Direct comparisons between different epitope attachment/presentation systems are challenging. Indeed, changing the surface chemistry introduces alterations in concentration, spacing, substrate rigidity, or affinity of integrins for the epitopes. A close mimic of the plasticity and constant remodeling of ECM is provided by surfaces able to trigger *in situ* variations of surface properties in contact of living cells. Dynamic switchable systems are thus desirable for fundamental purposes for direct comparison of the effect of external parameters. This objective can be reached by the design of surface-bound functional layers combining excellent anti-biofouling properties and dynamic presentation of specific epitopes. Promising candidates are reviewed in the next paragraph.

2 Stimuli-responsive biomaterials to modulate *in situ* the effects of adhesive cues

A few reviews report on specific cases of bioswitchable interfaces, including optically controlled hiding/presentation of epitopes, and thermally responsive layers used for triggered cell detachment/harvesting (Cole et al., 2009; Nakanishi, 2014; Uhlig et al., 2014). Representative and robust approaches developed up to now are detailed in this section. Special attention is accorded on the ones providing good control on specific adhesion and detachment. We introduce the topic with additional indications about the need for absence of non-specific binding, that may not be easy to achieve with some technologies.

2.1 Antibiofouling background

The study of cell responses to specific immobilized biomolecules at solid–liquid interfaces needs an antibiofouling background. Indeed, once immersed into biological media, biomolecules (proteins, ...) spontaneously adsorb on non-passivated surfaces, causing non-specific cell adhesion or responses.

Chemically, nonadhesive molecules can be grouped as carbohydrates (agarose(Nelson et al., 2003), mannitol (Luk et al., 2000)), synthetic polymers (poly-(ethylene glycol), polyacrylamide), or proteins (albumin (Nelson et al., 2003)). Physically, nonadhesive regions are either monolayers, swollen hydrogels, lipid bilayers, or polyelectrolyte multilayers. They all appear to resist adhesion of cells by preventing nonspecific protein adsorption. The functional lifespan of these nonadhesive materials varies widely in the literature (24 h to 60 days).

Supported phospholipid bilayers constitute an effective class of cell/protein repellent adlayers(Andersson et al., 2003). To explain the passivation of such adlayers, a cooperativity between the following factors has been mentioned: polarizability, electrical neutrality (when using zwitterionic lipids), strongly bound/hydration water, and fluidity. Surface-immobilized lipid bilayers suffer from one major drawback they cannot be dried and must therefore always be stored in aqueous solution.

Polyelectrolyte multilayers (deposited by the layer-by-layer technique) have been reported as cell resistant materials under specific pH conditions(Berg et al., 2004). Weak polyelectrolytes offer the advantage of being able to change the film's molecular architecture by simply adjusting the assembly pH. Using this approach, it was found that highly swellable films prohibit cell adhesion while tight ionically stitched films support cell attachment. They are now widely studied as substrates for tissues engineering (Boudou et al., 2010; Kerdjoudj et al., 2011; Lee et al., 2011; Monge et al., 2013, 2015).

Poly-(ethylene glycol) (PEG) with the monomeric repeat unit [-CH_2-CH_2-O-] is the most widely used system to passivate surfaces. Many different strategies have been successfully designed to immobilize PEG on substrates relying on "grafting to" methods.

- Chemisorption : On solid surfaces such as glass or silicon, PEG can be grafted covalently thanks to the silane coupling reaction (Blümmel et al., 2007). Silanes are nowadays less popular because of their hygroscopic behavior, their tendency to polymerize and form island-like domains leading to heterogeneities. Another widely used method relies on PEG-modified alkanethiolates to form self-assembled monolayers (SAMs) on metal surfaces (mainly on gold). Due to their tendency to oxidation under ambient conditions, Bearinger *et al.* reported an alternative method for gold passivation based on PEG-PPS-PEG triblock copolymers with poly(propylene sulfide) (PPS) as the central anchoring block (Bearinger et al., 2003).
- Physisorption: Poloxamers or Pluronics® have been extensively used to modify hydrophobic surfaces. These polymers are triblock co-polymers PEG-PPO-PEG with a hydrophilic part (PEG) and a hydrophobic part (PPO polypropylene glycol) which are able to spontaneously assemble on hydrophobic surfaces via hydrophobic-hydrophobic interactions. The adsorbed layer of copolymer is thought to form a comblike structure at the surface, with hydrophobic PPO bound to the surface, while hydrophilic PEG extremities are exposed to the surrounded solution. These polymers must be used for short-term experiments because they are prone to detach from the surface(Nelson et al., 2003). Poly(L-Lysine)-g-Poly(ethyleneglycol) is

similarly used to passivate anionic surfaces (glass, metal oxides, tissue culture polystyrene), affording a stable adlayer (Huang et al., 2001; Kenausis et al., 2000). The better layer stability stems from electrostatic interactions between the polycationic PLL backbone and the anionic surface under appropriate pH and ionic strengths.

Among the numerous model proposed to explain the antibiofouling properties of PEG coatings, steric stabilization and excluded-volume effects are the most commonly cited (Israels et al., 1995; Jeon et al., 1991). Hence, Sofia *et al.*(Sofia et al., 1998) shown that non-overlapping linear PEG brushes was not efficient to significantly prevent protein adsorption. By increasing the density to obtain overlapping PEG brushes, PEGylated surfaces become protein-repellent. The degree of overlap can be evaluated by the expression $\frac{L}{2R_g}$, where L and R_g are respectively the distance between two PEG chains and the radius of gyration of the PEG side chains. Considering this expression, degrees of overlap inferior to unity imply that the neighboring PEG chains overlap and that the surface is densely packed. Conversely, values superior to unity correspond to non-overlapping PEG chains. According to the results of Sofia *et al.*, this degree of overlap appeared to be independent of PEG molecular weight and protein size. Of course, short PEG chains need a grafting density higher than long PEG chains to guarantee a dense surface with efficient PEG packing. Kenausis *et al.* gather data from different surface-immobilized PEG systems (Figure 9), including PLL-g-PEG on metal oxides, SAMs of PEG-alkanethiolates on gold and PEG covalently linked to silanized silica. On Figure 9, we can see that surfaces with a low $\frac{L}{2R_g}$ decrease considerably the quantity of adsorbed proteins, thus confirming that systems with the lowest degree of overlap are the most protein-repulsive. Moreover, this behavior seems to be independent from the surface-immobilized PEG system. In the case of PLL-g-PEG, optimizations based on the polymer architecture (Huang et al., 2001) shown that PLL-g[3.5]-PEG(2000) was strongly effective to passivate anionic surfaces.

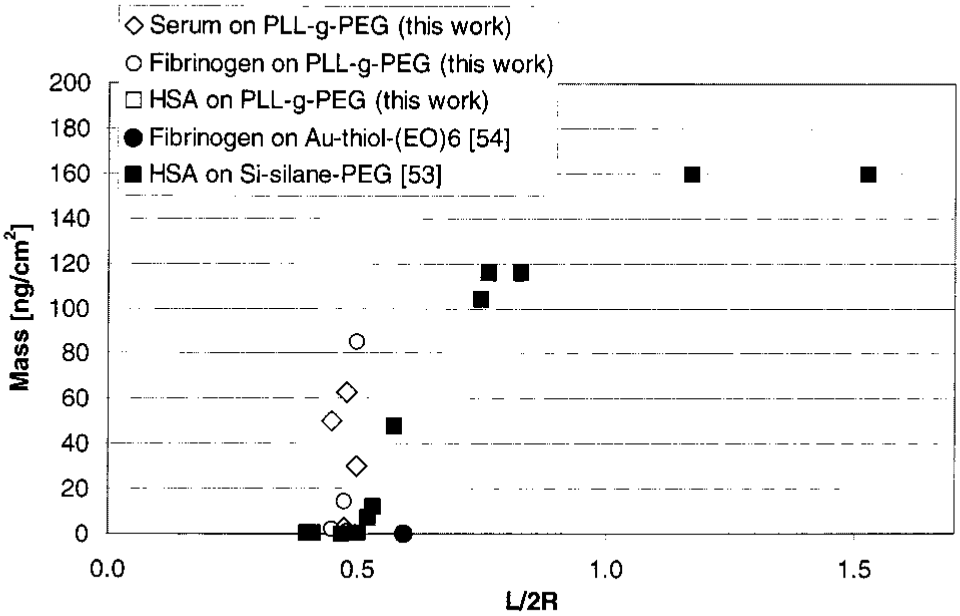

Figure 9 - dependence of serum adsorption over different surface-immobilized PEG systems with the degree of overlap (Kenausis et al., 2000).

For physically stable PEGylated surfaces (i.e. surfaces obtained from chemisorption or passivated with PLL-g-PEG), the functional lifetime is generally less than ten days and strongly depends on cell line (Nelson et al., 2003). Indeed, PEG chains are prone to degradation in water via oxidation mechanism (Pidhatika et al., 2012). Moreover, specific cell lines (3T3-L1 pre-adipocytes) express enzymes able to catalyze this oxidation (3T3-L1 pre-adipocytes), and consequently accelerate the decrease in repellency of the PEG layer. Further information on PLL-g-PEG is given on the last part of this chapter (see section 3.1).

The choice of the passivation chemistry is dictated by different factors:

- the type of substrate (glass, silicium, metal oxides, gold, ...)
- the complexity of the chemistry involved in the layer formation
- the functional lifetime
- the compatibility with patterning techniques.

2.2 Chemical stimulus

Basically, chemical-sensitive materials respond to changes in pH, ionic strength, introduction of co-solvents or solutes. Every chemical stimulus isn't however, by far, compatible with manipulation of living cells. Variation of pH, ionic strength and co-solvent can't be used in general because mammalian cells need a specific culture medium. Introduction of non-toxic solutes that can spontaneously adsorb, or bind by bio-orthogonal chemistry to the surface is the only biocompatible chemical trigger. These solutes can covalently react or non-covalently interact with surfaces. When they are used as a trigger (*in situ* introduction and not pre-stamping), the whole surface is exposed to solutes. A local control is thus achieved only on pre-patterned surfaces. Representative examples are listed below with a focus on systems allowing to control sequentially adhesion/detachment of cells, and revealing a high degree of control of specific cell-substrate interactions.

2.2.1 Covalent surface modifications

Here, the idea consists in adding to the culture medium a reactant able to modulate a ligand accessibility on the surface. The reaction must be rapid, quantitative and biocompatible (i.e. involving non-toxic reagents, and no side reaction with biological components such as proteins). These requirements limit drastically the choice of reactions.

Azide-containing surfaces fulfill these conditions. Indeed, azides can undergo a series of chemoselective reactions such as the Curtius rearrangement, Staudinger ligations, and Huisgen 1,3-dipolar cycloadditions. Azide-based cycloaddition reactions have recently received significant attention and the strain-promoted azide-alkyne cycloaddition is a copper-free non-toxic reaction. It employs a strained cyclooctyne to react with an azide in a spontaneous, catalyst-free cycloaddition. Van Dongen *et al.* used this reaction to introduce an adhesive peptide onto an cell-repulsive azide-functionalized surface (van Dongen et al., 2012; van Dongen et al., 2013). Via this reaction, the stimulus isn't reversible.

Another solution consists in using enzymes to modify artificial surfaces as it is the case in ECM remodeling. Todd *et al.* (Todd et al., 2009) reported the use of elastase, a protease associated with tissue remodeling, switching the surface from bioinert to adhesive (Figure 10). They worked on a poly(ethyleneglycol) monolayer coupled to glass substrate. On the top of the layer, a RGD cue is protected by a cleavable steric group (Fmoc-alanine-alanine-RGD-PEG). Before hydrolysis of the specific alanine-alanine sequence, RGD isn't accessible while after cleavage cells can recognize and interact with RGD via their integrins. This stimulus isn't reversible.

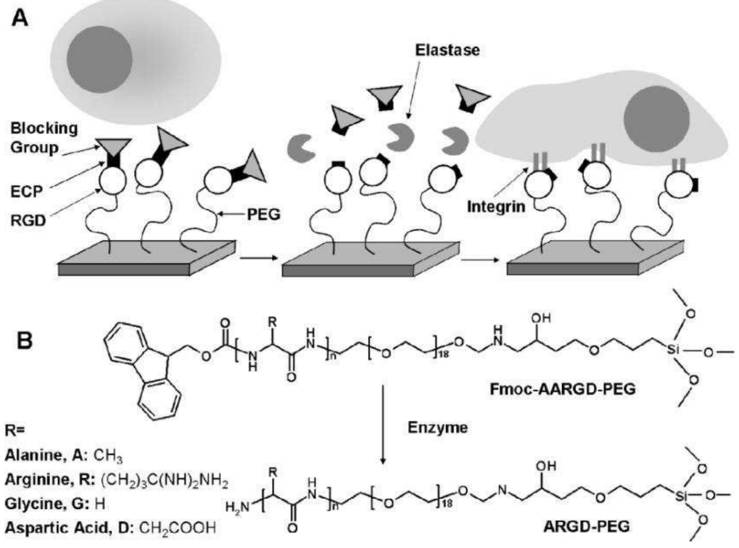

Figure 10 - (A) Schematic representation of the enzyme responsive system. (B) Structural representation of the system. Each surface bound group consists of the Fmoc blocking group, "n" amino acids whose identity depends on the nature of the side groups (R), and a PEG linker attached to glass via an epoxy silane. (Todd et al., 2009)

2.2.2 Non-covalent surface modifications

Non-covalent methods, based on reversible interactions between a bioinert surface and adhesive factors, represent a promising approach to realize dynamic cell adhesion. Current attempts rely on host-guest supermolecular chemistry, electrostatic interactions, complexation, and hydrogen bonding.

Boekhoven *et al.* reported a method based on host-guest supermolecular chemistry (Boekhoven et al., 2013). They worked on an alginate matrix covalently functionalized with β-cyclodextrin (host), which is cell repellent. Addition of guest molecules containing a RGD peptide to culture medium induced focal adhesion formation and spreading of 3T3 fibroblasts due to the host-guest interaction. The spreading was reversed by adding competitive guest molecules of higher affinity for β-cyclodextrin and bearing the mutated non-bioactive sequence RGE.

The major drawback of this method is related to the weak non-covalent link between the surface and adhesive cues which can be broken by adherent cells. Indeed, cells exert important forces via integrin on the adhesive cues (Jurchenko et al., 2014), leading to the dissociation of streptavidin-biotin tethered ligands in focal adhesions. Pan *et al.* (Pan et al., 2014) suggest that multivalency non-covalent interactions between an adhesive cue and surface could make it possible to maintain the stability of the assembly. To a layer of poly(hydroxyethyl methacrylate)-graft-(phenylboronic acid) (PHEMA-graft-PBA) polymer brushes, they exposed a solution of RGD-poly(3-gluconamidopropyl methacrylamide) (RGD-PGAPMA), forming a stable polymeric complex via PBA/cis-diol interactions (Figure 11). Stable focal adhesions give a proof of the stability of the polymeric assembly. The introduction of high concentrations in fructose makes it possible to destroy this polymeric assembly. This system shows a reversible switching between adhesive/repulsive state simply by changing the fructose concentration of the culture medium. Cell detachment has been studied after 3 h of incubation in DMEM (i.e. allowing cell spreading) by adding fructose (final concentration: 60 mM). As clearly shown in Figure 11c, gradual transition of the cell morphology from a spread-out shape to a round shape was observed. About 64% of the cells were released in fructose-containing DMEM after 30 min of incubation. No longer incubations in this medium were reported to investigate a quantitative cell release.

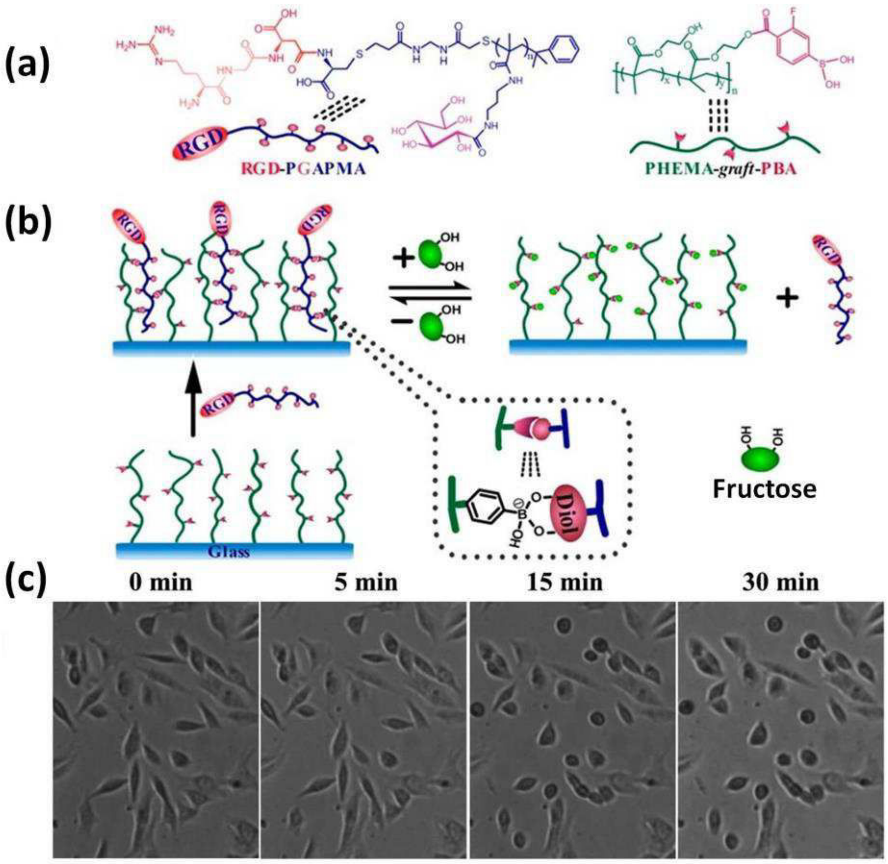

Figure 11 - (a) Chemical structures of RGD-PGAPMA and PHEMA-graft-PBA; (b) Schematic illustration of dynamic introduction of RGD-PGAPMA on PHEMA-graft-PBA modified matrix via reversible multivalent PBA/cis-Diol complexes; (c) MG63 cell release from RGD-PGAPMA10 coupled GlassPBA400 at different times by incubation with 60 mM fructose (Pan et al., 2014).

Dynamic properties of these surfaces come from the addition of molecules showing a higher affinity with the guest to remove/fix RGD on surfaces. Complex showing an affinity sensitive to other stimuli could be used in the same context. An *et al.* developed a supramolecular system for the electrochemically controlled release of cells based on cucurbit[8]uril, a macrocyclic host molecule capable of binding two aromatic guest molecules simultaneously (An et al., 2012).

2.3 Electrical stimulus

Electrical stimulation is biocompatible and implies the use of conductive substrates. By combining patterning and/or microelectrodes (An et al., 2012; Kaji et al., 2004; Zhao et al., 2006), a local stimulation is possible.

2.3.1 Potential-induced conformational change

Electrical stimuli can induce a reversible and rapid conformational change of low-density end-charged SAMs (Lahann et al., 2003). Indeed, molecules adopt an extended conformation by application of the same potential than the end-charged tether. Conversely, the charged extremity is attracted by an opposite charged substrate.

This phenomenon has been used by Ng *et al.* to dynamically control RGD accessibility and so cell adhesion (Ng et al., 2012). They worked on SAMs composed of two organic molecules. The first component is a repellent hexa(ethyleneglycol) with a sulfonate (anionic) extremity or an ammonium (cationic) extremity (Figure 12A). The second component is an alkane bearing an adhesive GRGDS peptide at its end. They showed that cell adhesion is more pronounced when the charged-extremity is attracted by the surface (i.e. RGD is more accessible). This material was used to electrically trigger cell migration into a newly adhesive region from a confluent region (Figure 12B, C). However, it must be noticed that it's impossible to detach cells by switching these surfaces from cell-adhesive to cell-repellent.

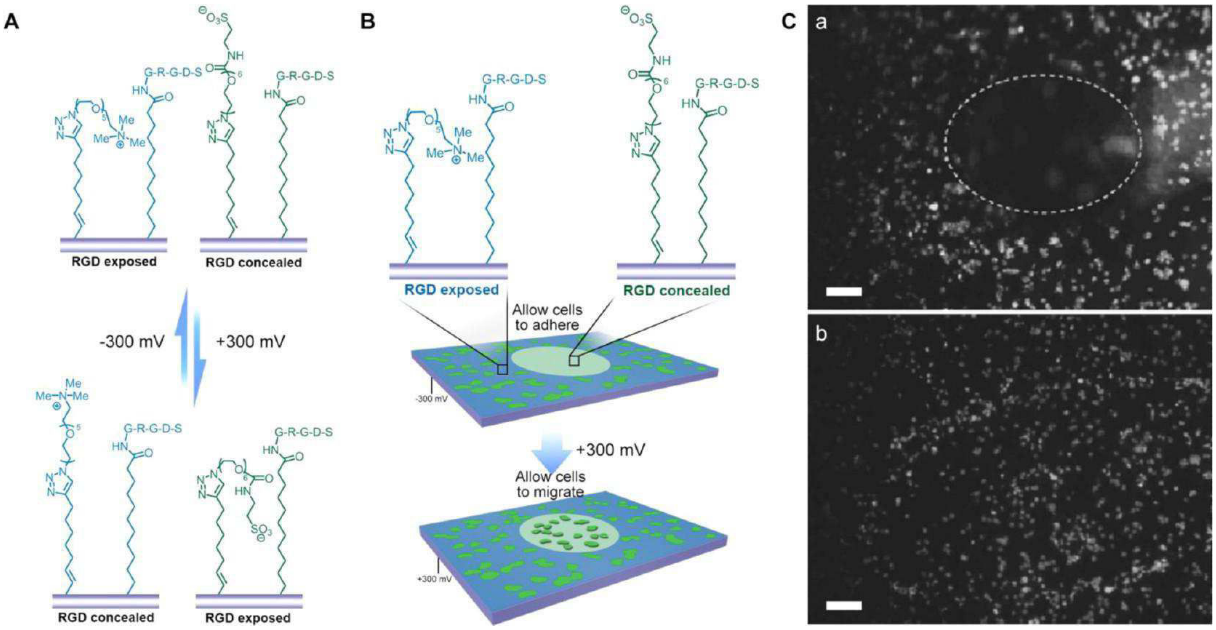

Figure 12 - (A) Schematic representation of the dynamic RGD display under electrical stimulus. (B) Schematic of how the patterned surface that contains a central region of negatively charged sulfonate-terminal species that surround the RGD ligands and the exterior region of positively charged ammonium-terminal species surrounding the RGD ligands responds to an externally applied potential. HL60 cells were expected to be confined to the exterior region when a negative potential was applied. Cells were expected to migrate toward the central region upon application of +300 mV. (C) Fluorescent images of adhered HL60 (Cell tracker staining) showed that the cells adhered to the outer region (outside the dashed line) when−300 mV was applied to the surface. The cells then migrated into the circular region upon switching the potential to +300 mV. Scale bar = 100 µm.(Ng et al., 2012)

2.3.2 Benzoquinone/hydroquinone chemistry

The hydroquinone/benzoquinone (HQ/BQ) redox couple has been embedded into SAMs to control surface functionalities in response to an applied potential. Mrksich's group was the first to use this system to control interactions between surfaces and cells on demand. Their strategy consists in coupling the redox HQ/BQ reaction to HQ or BQ specific reactions, introducing/releasing adhesive cues. For example, they succeeded in releasing immobilized RGD ligands (i.e. cells) from the surface via benzoquinone reduction (Figure 13) (Yeo et al., 2001). Indeed, the electrically formed HQ made an intramolecular cyclization, thus giving a lactone with release of the RGD. Other reactions such as Diels-Alder reaction have been coupled to HQ/BQ. By combining reactions specific to both HQ and BQ, they reported a surface able to switch from adhesive to repellent, and then to adhesive again (Yeo et al., 2003).

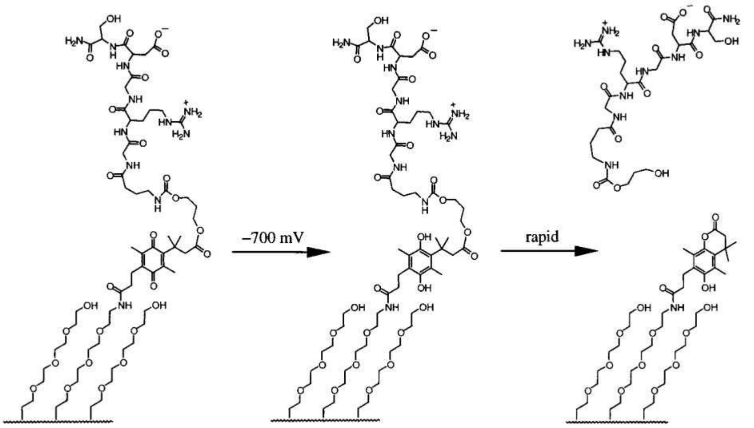

Figure 13 - Release of RGD ligand by BQ reduction coupled with HQ lactonisation. This substrate was placed into cell-culture media and a suspension of 3T3 Swiss fibroblast cells was added. The cells were evenly distributed on the surface and adopted a spread morphology over the entire substrate. After cells were cultured at 37°C for 30 minutes, an electrical potential of - 700 mV (versus an Ag pseudo-reference) was applied to the gold substrate for 4 minutes. Immediately after the electrochemical treatment, more than 70 % of the cells reverted to a rounded morphology and rested unattached on the substrate. (Yeo et al., 2001)

Lamb *et al.* succeeded in electrically modulating the affinity of the RGD-integrin interaction on a HQ/BQ SAM (Lamb and Yousaf, 2011) (Figure 14). At the extremity of the alkanethiolate, there is a cyclic RGD-peptide containing a BQ-oxime. Cells can't easily bind the RGD sequence under the cyclic conformation which presents a "blocking" group on the top of surfaces. An electrical reduction broke the oxime bond and the surface became cell-adhesive thanks to a better RGD accessibility. This change in surface properties is irreversible due to the formation of an alcohol-terminated peptide and loss of the oxyamine function.

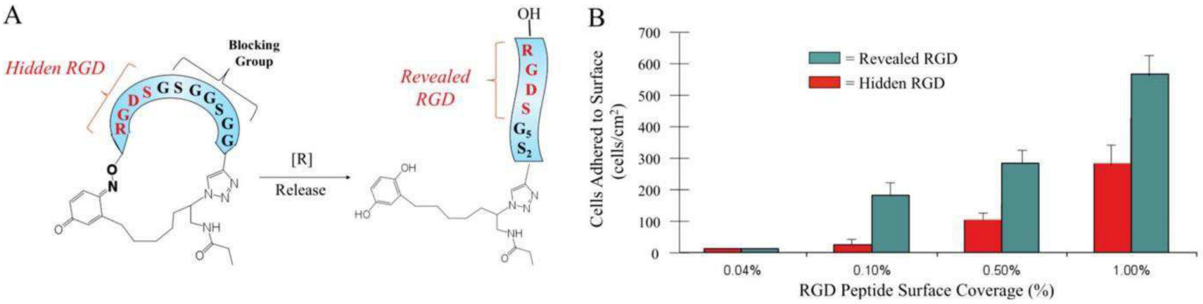

Figure 14 - Dynamic hide-and-reveal ligand strategy for controlling substrate adhesiveness. (A) A cyclized RGDS peptide containing a blocking sequence does not permit cell adhesion (left). Reductive cleavage of the oxime bond reveals the adhesive RGDS peptide for cell adhesion (right). (B) Cell adhesion profiles on surfaces presenting hidden and revealed peptides (Lamb and Yousaf, 2011).

2.3.3 Release of alkanethiolates from SAMs

Reduction or oxidation of the sulfur-gold bonds on SAMs can be broken by changing the electrical potential. Based on this idea, many methods have been designed to develop dynamic SAMs through the release of alkanethiolates.

Inaba *et al.* (Inaba et al., 2009) reported the noninvasively harvesting of adherent cells, cell sheets, and spheroids from a SAM of RGD-ended alkanethiol. The application of a negative electrical potential caused the reductive desorption of the SAM, resulting in the detachment of cells. This approach makes it possible to detach more than 90% of adherent cells within 5 min (Figure 15A).

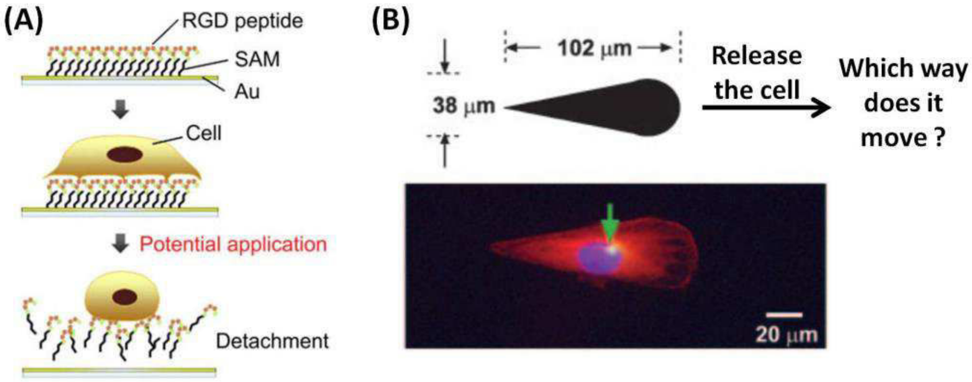

Figure 15 - (A) Detachment of cells due to the electrochemical desorption of a SAM. (B) On the top: pattern used for the cell confinement. On the bottom: The Golgi and the centrosome are located closer to the half of a cell with the blunt end. Confocal picture where actin and the nucleus are represented in red and blue respectively. The green arrows indicate the location of centrosomes in 3T3 cells (Jiang et al., 2005).

By using the release of alkanethiolates from patterned SAMs, Jiang *et al.* have shown that the direction of polarization directs cell migration (Jiang et al., 2005) (Figure 15B). Patterns of alkanethiolates were obtained on gold by stamping. $HS(CH_2)_{17}CH_3$ was first deposited, forming asymmetric micropatterns. The background was passivated by olygo(ethylneglycol)-thiol ($HS(CH_2)_{12}(OCH_2CH_2)_3OH$). After fibronectin absorption, cells were confined on micropatterns and hence adopt a polarization. By triggering electrochemical desorption of the SAM, cells move toward their blunt ends while they could move on the whole surface.

Conducting polymers such as polypyrrole represents an emerging technology platform. For instance, swelling of such conducting polymers are used as actuators to detach cells on demand (Persson et al., 2015; et al., 2011)but haven't still been used to control activity of adhesive cues.

2.4 Optical stimulus

The advantage of light is to easily achieve local stimulation over other stimuli. However, the wavelength of irradiation must be preferably chosen closed to infra-red than to UV in order to avoid problems of cell toxicity.

Optical control of cell cultures has been recently achieved in hydrogels that can be photo-reticulated under UV light prior to cell seeding (because of UV toxicity). Formation of tight networks of polymer chains, or local increase of the rigidity hamper the development of cells (Lutolf, 2012; Marklein and Burdick, 2009). Recent development of this principle propose the use of biocompatible mild photocleavable enzymes (Mosiewicz et al., 2013), or thiol-based chemistry to modify (irreversibly) hydrogel stiffness with spatiotemporal control (Mosiewicz et al., 2014). The main goal was however to pattern cell adhesion sites in 3D while reversibility is generally not considered. In comparison, diverse surfaces allowed to trigger optically at least partial cell detachment.

2.4.1 Azobenzene chemistry

Azobenzene is a chromophore which can undergo a reversible photo-isomerization under blue/UV illumination (Figure 16). The isomerization between the *cis* and the *trans* isomers has been used for different biological applications including photo-control of cell adhesion.

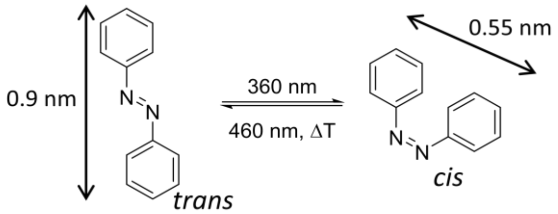

Figure 16 - azobenzene photo-isomerization.

Azobenzene could be used to photo-control the RGD-integrin affinity and consequently cell adhesion. For instance, a RGD-containing heptapeptide was cyclized with the (4-aminomethyl)phenylazobenzoic acid (AMPB) photoswitch by Schutt *et al.* (Schütt et al., 2003). The isomeric state of the azobenzene unit (AMPB) is coupled with the peptide conformation, thus modulating its binding with integrins: the peptide flanked with *trans* isomer showed a higher affinity than the *cis* one. Nevertheless, the RGD-integrin affinity doesn't show a sufficient gap between blue and UV light to control cell adhesion with this approach (Milbradt et al., 2005; Schütt et al., 2003).

Auernheimer *et al.* (Auernheimer et al., 2005) considered differently the azobenzene isomerization to photo-control cell adhesion. On the top of PMMA disks, they covalently grafted RGD peptides via an azobenzene linker. After incubation of MC3T3 E1 mouse osteoblasts, no specific adhesion was noticed on *cis* azobenzene (UV illumination) while cells specifically interact with RGD on *trans* azobenzene (Blue illumination). This phenomenon can be explained by the degree of exposure of the RGD sequence, thus encouraging Liu *et al.* (Liu et al., 2009) to work on SAMs with a similar way of RGD-exhibition (Figure 17A). Liu *et al.* confirm that RGD is more accessible on *trans* azobenzene than on its *cis* isomer (Figure 17B). Moreover, they couldn't detach cells by switching the wavelength. However, a soluble GRGDS peptide (1 mg.mL^{-1}) was successfully used to detach quantitatively the cells from the surface (this process needs about 30 min), because the soluble peptide competed with immobilized RGD for the cell surface integrin receptors. Irradiating these cleaned surface with UV light for 10 H converted the *cis* configuration of azobenzene into the *trans* form, and the GRGDS ligand was masked in PEG to give a cell-repellent surface. A treatment of the inert surface with visible light for 1 H allowed the SAMs to support cell adhesion again as a result of the conformational switch of azobenzene from *cis* to *trans* isomer. This surface, therefore, allows completely reversible control of cell adhesion.

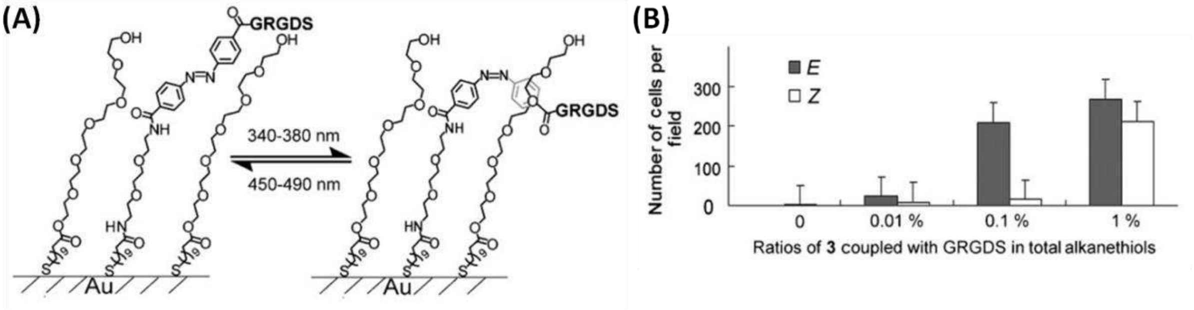

Figure 17 - (A) The azobenzene moiety can be converted photochemically between the *cis* and *trans* configurations to either present or mask the RGD ligand. (B) Number of NIH 3T3 fibroblasts adhered on the corresponding surface (Liu et al., 2009).

2.4.2 O-nitrobenzyl cage chemistry

Under UV irradiation, o-nitrobenzyl undergoes an irreversible cleavage of the bond at the benzylic position. Hence, different o-nitrobenzyl groups have been used to develop photo-triggering substrates that reveal various functional groups such as carboxilic acids, peptides.

Maeda's team designed a method for photo-activation of localized regions from repellent to adhesive. They worked on 2-nitrobenzyl-presenting substrates coated with non-adhesive macromolecules (BSA or pluoronic F108) (Figure 18 A and B) (Nakanishi et al., 2004, 2007). Before UV irradiation, non-adhesive macromolecules layer prevents from cell adhesion. On the UV-irradiated regions (irradiation: 365 nm, 10s, 300W), fibronectin adsorbed on hydrophilic carboxilates, making the surface cell adhesive. After cell attachment on the photo-activated regions, cell migration was induced by repeated photo-activation and adsorption of fibronectins in a region alongside cells (Figure 18C). They studied the extension rates of two cell protrusions of fibroblast-like NIH3T3 cells. Lamellipodia and filopodia were analyzed by activating a wide path (25 µm) and a narrow path (5 µm) respectively.

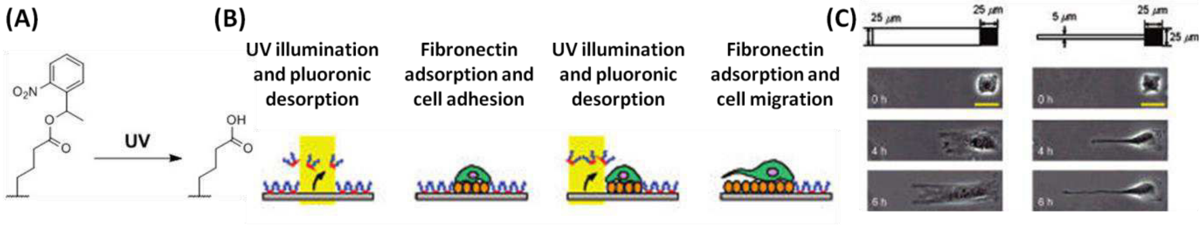

Figure 18 - (A) The photochemical reaction on the substrate surface by UV illumination at 365 nm. (B) Schematic illustrations of the placement of single cells followed by the induction of cell migration on the substrate. (C) Selective induction of two characteristic protrusions in NIH3T3 cells (left: lamellipodia, right: filopodia). In upper figures, primary (black square) and secondary (white rectangle) illuminated regions are illustrated. Times after induction of cell migration are shown in the phase-contrast images (0, 4 and 6H from the top to the bottom). Yellow scale bars represent 25 µm (Nakanishi et al., 2007).

In these studies, Maeda's team triggered non-specific cell adhesion on light-induced fibronectin adlayers. To study specific cell adhesion, Campo's group embedded o-nitrobenzyl-caged RGD peptides on surfaces (Petersen et al., 2008). They showed that fibroblasts 3T3 made specific adhesion on irradiated samples (10 minutes, 351 nm, 1 mW.cm^{-2}, cleaving yield: 64 %) while no adhesion was noticed on non-irradiated samples. Although there is a sixfold affinity difference between caged and uncaged RGD, some cells don't succeed in attaching on irradiated surfaces (Wirkner et al., 2011).

This technique to uncage peptides has been used by Griffin *et al.* (Griffin et al., 2014) in a 3D hydrogel of hyaluronic acid (Figure 19). UV irradiation activated the covalently "caged K peptide". Indeed, FXIIIa enzyme made an amide bond between the K peptide and a Q peptide bearing a biological signal. They succeeded in immobilizing bioactive growth factors, and peptides of different molecular weights. Classic photo-mask patterning technique enables the formation of 2D patterns while 3D micropatterns have been drawn by two-photon deprotection. They induced the formation of cluster of mouse mesenchymal stem cells by patterning 100 µm circles with Q-RGD (Figure 19C-D). This hydrogel could be used to address locally and irreversibly a biological signal into a 3D microenvironment to pre-embedded cells.

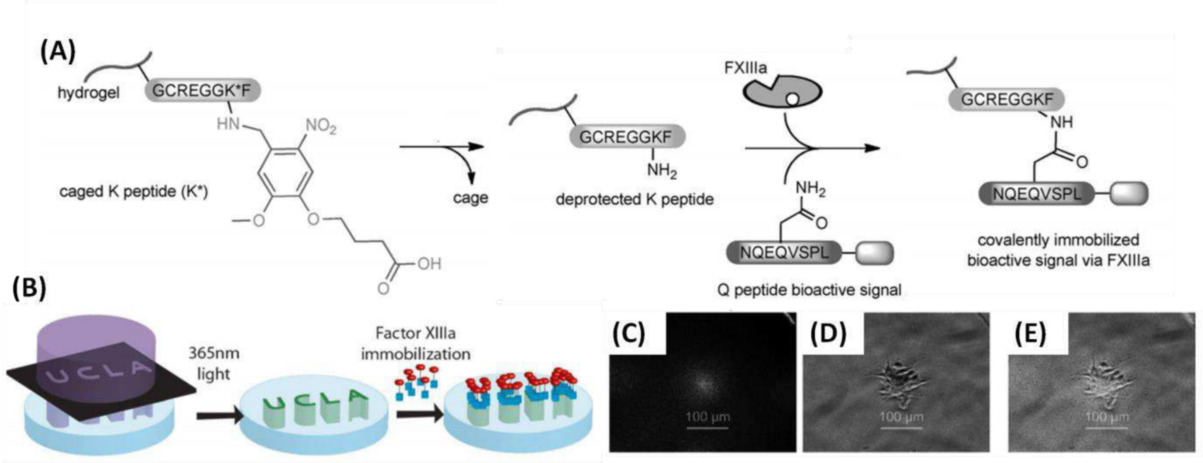

Figure 19 - (A) A caged peptide substrate for FXIIIa (K* peptide) preventing FXIIIa activity unless the substrate has been deprotected by exposure to light at 365 nm. This allows for site-specific deprotection of the K* peptide. Following deprotection, the bioactive signal can be immobilized by adding both the Q peptide bioactive signal and FXIIIa to the hydrogel. (Photodeprotection: 365 nm light, 10 mW.cm^{-2}, 10 minutes). (B) Technique for patterning the hydrogel and successive immobilization with Q peptides. (C) 100 µm circle of FITC-labelled RGD. (D) Cells cluster to the location of the pattern. (E) Overlay of the pattern and cell cluster (Griffin et al., 2014).

It is worth noticing that the photohydrolysis of o-nitrobenzylester (or similar derivatives such as carbamate, and ureas) required long exposures to UV (wavelengths < 360 nm and powers > mW/cm^2), which is toxic to many cells. The future of such approaches is therefore dependent on the design of new photocages which can be cleaved with high efficiency in the visible range or by 2-photons excitation in the infra-red range.

2.5 Thermal stimulus

Thermo-responsive polymer films are used to control the exposition of adhesive cues under variation of temperature by a few °C. Synthetic polymers are actually used although systems based on polypeptides, such as elastin are emerging. Poly(N-isopropylacrylamide) (PNIPAM) is the most studied thermo-responsive polymer with a characteristic lower critical solution temperature (LCST) of ~ 32 °C in water, a value close to the body temperature making it attractive for biological applications. Upon heating above a threshold temperature, PNIPAM undergoes a solubility transition (at lower critical solution temperature, LCST). At the molecular level, isolated chains undergo conformational transition from coil to globule. At low temperatures, PNIPAM chains are hydrated while they collapse and become hydrophobic above the LCST. Most techniques using thermo-responsive polymers to control exposition of RGD relies on this conformational change (i.e. swelling/collapse transition at the surface of substrates).

2.5.1 PNIPAM films

Okano's group initiated works on PNIPAM coatings as a thermo-responsive platform for cell adhesion. According to their first reports, electron-beam irradiation method was used to polymerize PNIPAM hydrogels directly on tissue culture polystyrene substrates (“grafting from” technique) (Akiyama et al., 2004; Yamada et al., 1990). On thin coatings (PNIPAM layer: 1.4 µg/cm², 15.5 nm), cells can adhere, spread and proliferate above the LCST (cultures were generally conducted at 37 °C). According to Okano, tis non-specific adhesion comes from the adsorption of proteins such as fibronectin on the hydrophobic PNIPAM. A decrease in temperature (generally down to 20 °C) below the LCST caused the detachment of cells. By increasing the hydrogel thickness (PNIPAM layer: 2.9 µg/cm², 29.3 nm), protein adsorption and consequently cell adhesion are prevented irrespective of temperature. In order to induce biospecific interactions between cells and the surface, thicker "nonfouling" PNIPAM hydrogels have been modified with RGD peptides (Ebara et al., 2004). Technically, it consists in polymerizing a mixture of NIPAM and 2-carboxisopropylcarylamide by e-beam irradiation and subsequent RGD grafting via the carboxilic acid. Above the LCST, binding of the RGD peptides to integrins mediate cell adhesion. Below the LCST, the PNIPAM film swells and masks the RGD ligands, thus leading to detachment of cells. On Figure 20A, the specificity of cell adhesion on RGD-containing hydrogels can be appreciated. By reducing temperature, hydrogels with high RGD quantity release 75% of initially adhered cells (Figure 20B). For hydrogels with RGD densities inferior to 0.5 nmol.cm^{-2}, every cell detaches in 60-100 minutes. Pan *et al.* reported a PNIPAM hydrogel designed to release pre-embedded RGD peptides in order to accelerate cell detachment (Pan et al., 2013). RGD peptides were added during the hydrogel polymerization: this technique gives a PNIPAM-based molecularly imprinted polymers containing thermo-responsive RGD recognition sites. At 37 °C, RGD showed a high affinity for these recognition sites and facilitate cell adhesion. At 20 °C, RGD are release from the hydrogel due to a low affinity to the recognition sites. This hydrogel makes it possible to detach every adherent cell in less than 30 minutes.

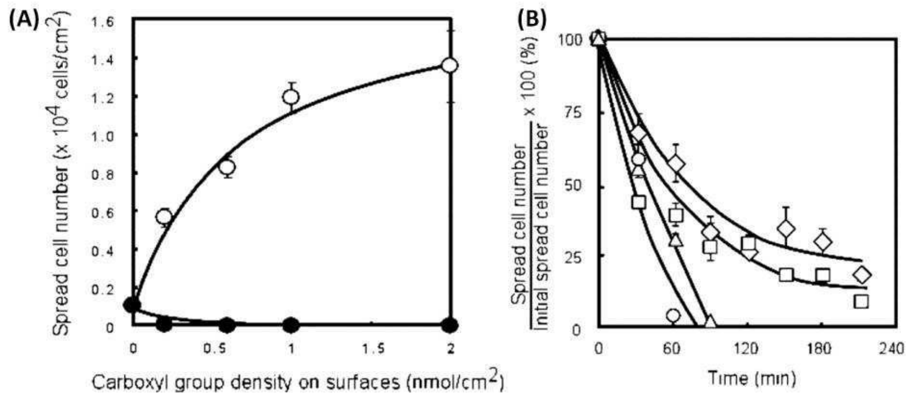

Figure 20 - (A) Human umbilical vein endothelial cells (HUVECs) spreading on RGDS and RGES-immobilized temperature-responsive culture surfaces after a 6-h culture without serum at 37°C. These peptides were covalently grafted on P(NIPAM-co-CIPAM)-grafted surfaces. The feed concentration of peptides was 2 mM. Symbols: RGDS (open circle) and RGES (closed circle). (B) HUVEC detachment from RGDS-immobilized temperature-responsive culture surfaces by lowering the temperature. Cells on RGDS hydrogel were subjected to low-temperature treatment at 20 °C after a 24 H culture at 37 °C without serum. CIPAAm compositions were 0.15 (open circle), 0.5 (triangle), 1 (square), and 2 nmol.cm^{-2} (diamond) (Ebara et al., 2004).

PNIPAM brushes (Xue et al., 2012) and PNIPAM microgel films (Schmidt et al., 2010) are other material classes used to control non-specific cell adhesion. Similarly to PNIPAM hydrogels, cells stick on dehydrated PNIPAM films (37 °C) while they can't adhere on hydrated PNIPAM films (20 °C). For instance, these PNIPAM substrates haven't been reported to modulate the activity of specific adhesive cues. Protein adsorption on PNIPAM brushes represents a complex phenomenon which is still unclear and implies intensive studies (Tang et al., 2014). Importance of PNIPAM brush density and nature of the end-group on protein adsorption may be an origin of variability in results as suggested by Leckband *et al* (Choi et al., 2013). The need for a high degree of control of surface chemistry is clearly a drawback for a general use of such layers all the more in the absence of commercial production of patterned PNIPAM.

Although thermo-responsive films are primarily used to control RGD accessibility and so cell adhesion, they can be used to induce mechanotransduction via application of forces on integrins. Liu *et al.* reported nanoscale optomechanical actuators based on gold nanorods coated with a PNIPAM hydrogel (Liu et al., 2015b) (Figure 21A). The nanorods play as photothermal transducers, converting NIR light into localized heat that drives polymer collapse. By imposing an alternative field on the surface, the alternative collapse/swelling of the PNIPAM film delivers piconewton forces to integrin via the PNIPAM end (i.e. the RGD peptide). They succeeded in controlling integrin-based focal adhesion formation, cell protrusion and migration (Figure 21B).

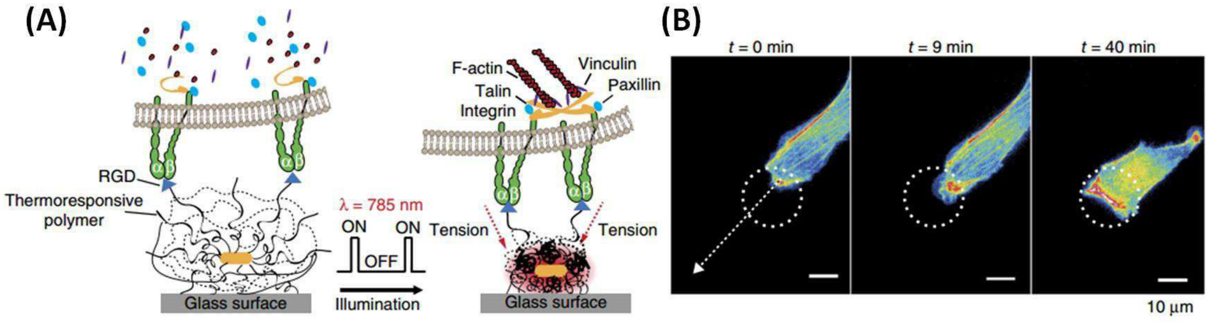

Figure 21 - (A) Schematic and proposed mechanism of optomechanical actuator nanoparticles. (B) Time-lapse images of NIH/3T3 cell migration in response to OMA stimulation. The white dashed circles represent the region of NIR illumination (785 nm, 10 Hz, 11.3 µW.µm^{-2}). (Liu et al., 2015b)

2.5.2 Other thermo-responsive films

Novel smart substrates combining thermo-responsiveness and bio-repellence on a broad temperature range are emerging. In fact, this kind of coatings could make it possible to thermally modulate specific interactions without non-specific phenomenon.

Zareire *et al.* worked directly on SAMs of the classic repellent OEG. While the phase separation temperature of PEG is typically above 100 °C (LCST behavior), short OEG tethered chains (n = 12, M = 500 g.mol^{-1}) showed a transition at 37 °C on gold. The potential of OEG$_{12}$ SAMs to modulate the accessibility of a ligand while keeping its protein-resistance has been demonstrated on a model study. Indeed, temperature-dependent streptavidin immobilization onto a mixed SAM of OEG$_{12}$ and a biotinylated disulfide was investigated. SPR and AFM studies showed that these thermo-responsive OEG SAMs can be utilized to control the affinity binding of streptavidin to the biotintethered surface in a temperature-dependent manner while still offering the nonspecific protein-resistance to the surface (Zareie et al., 2008).

ATRP-initiated copolymer brushed based on 2-(2-methoxyethoxy)ethyl methacrylate (MEO$_2$MA) have been used to reversibly mask/unmask biological ligands upon temperature stimuli (film thickness ∼100 nm) (Desseaux and Klok, 2014; Laloyaux et al., 2010). Indeed, the LCST value of these brushes can be adjusted around 37 °C by incorporating the appropriate comonomer during the polymerization. In these two studies, the layer transition occurs for a broad temperature range (at least 15 °C) while maintaining their antibiofouling properties. By modifying their thermo-responsive brushes with RGD peptides, Desseaux *et al.* showed integrin-mediated adhesion of 3T3 fibroblasts at 37 °C and their quantitative detachment takes 15 minutes by cooling to 23 °C (Figure 22) (Desseaux and Klok, 2014). The RGD peptide is more accessible on the hydrophobic surface than on the swollen surface as previously reported for PNIPAM hydrogels. Any complementary information is given on the mechanism of detachment. Interestingly, Laloyaux *et al.* reported the opposite behavior concerning the thermal exposition of both Biotin-MAG-Cys and MAG-Cys ligands (MAG-Cys = Metionine-Alanine-Glycine-Cysteine) : the ligand is more accessible on the extended brushes than on the hydrophobic brushes (Laloyaux et al., 2010). The hydrophobicity of the Biotin-MAG compared to the RGD could explain that it was hidden at high T in the hydrophobic, collapsed polymer chains.

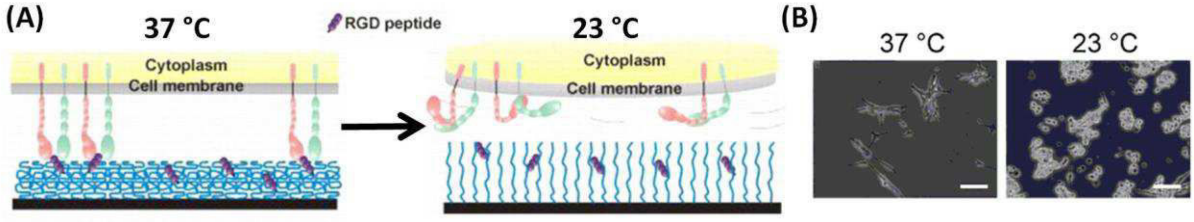

Figure 22 - (A) Schematic illustration of the RGD exposition on thermo-responsive brushes. (B) Optical micrographs of 3T3 fibroblasts on RGD-modified MEO$_2$MA brushes at 37°C and after 15 min at 23°C (scale bar = 1 mm) (Desseaux and Klok, 2014).

3 Coating based on PLL-g-P(NIPAM-co-RGD)

3.1 Previous results on PLL-g-PEG coatings

3.1.1 PLL-g-PEG coatings

Textor's team has introduced PLL-g-PEG as a simple tool to passivate anionic surfaces (Kenausis et al., 2000). In situ optical lightmode spectroscopy (OWLS) and ex situ X-ray photoelectron spectroscopy were used to demonstrate that PLL-g-PEG adsorbs spontaneously from aqueous solution onto anionic surfaces (metal oxides, glass, ...), forming a saturated layer. The polycationic PLL backbone acts as an anchor (lying flat via its ammoniums) to the anionic substrate, thereby exposing PEG side chains to the surrounding solution (Figure 23A). In solution, PLL backbone tends to adopt a linear conformation due to both electrostatic repulsions between the cationic ammonium and steric hindrance coming from the PEG side chains. Once adsorbed, the conformation of the PLL backbone must be similar to the one in solution. In the following, the results shown correspond to PLL backbone of 20 000 g.mol^{-1}.

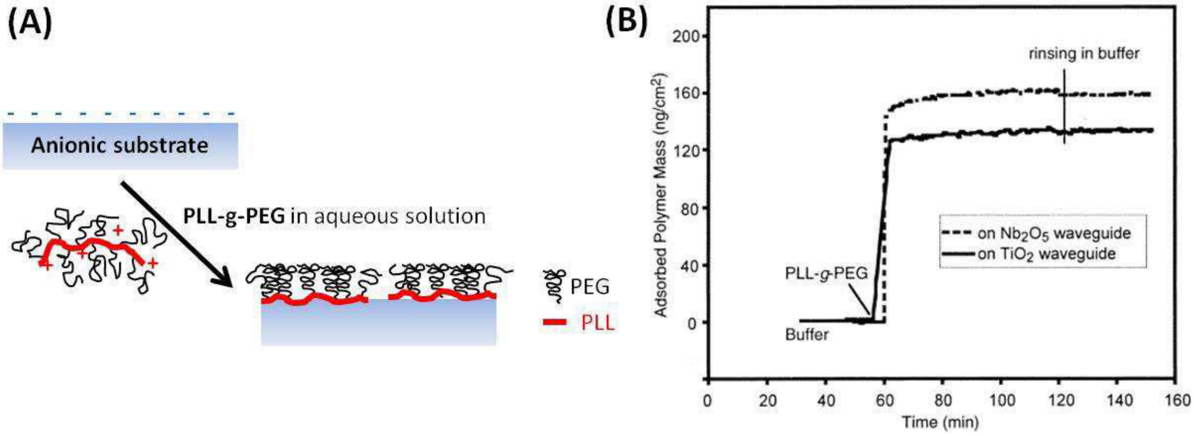

Figure 23 - (A) Schematic representation of the PLL-g-PEG adsorption on an anionic substrate. (B) OWLS monitoring the adsorption on two metal oxides (Nb$_2$O$_5$ and TiO$_2$) (Huang et al., 2001)

Adsorption kinetics of PLL-g[3.5]-PEG(2) was monitored by OWLS (Huang et al., 2001). On Figure 23B, we can see the adsorption results on two different metal oxides (Nb$_2$O$_5$ and TiO$_2$). Independently of the metal oxide nature, 95 % of the total PLL-g-PEG coverage achieved within the first 5 minutes of incubation. After 20 minutes, the adsorbed mass reached a plateau. The amount of PLL-g-PEG adsorbed on the surface is found to be different, 1.23 ± 0.04 mg.m^{-2} for TiO_2 and 1.48 ± 0.10 mg.m^{-2} for Nb_2O_5, which reflects the difference of charge density between the two metal oxides. These adsorbed masses are in agreement with Santore's results obtained by optical reflectometry on silica (Table 1). The quantity of adsorbed polymers is limited by the packing of the PEG side chains at the surface. Based on the saturation coverage of 1.1 mg.m^{-2} obtained by reflectometry, Santore deduced some characteristics of the PEG coating (Table 1). With a grafting ratio of 3.5 and a PEG molecular weight of 2000 g.mol^{-1}, this saturation coverage corresponds to 206 nm^{-2} per adsorbed PLL-g-PEG molecule and 3.6 nm^{-2} per interfacial PEG chain, or a 1.9 nm between two consecutive PEG chains. In good solvent, the calculated radius of a 2000 molecular weight PEG chain is 2.4. On PLL-g-PEG coatings, PEG can be considered in a brush regime because the distance between two PEG on the surface is smaller than the characteristic size of the PEG chain alone in solution.

Adlayer	PLL	PLL-[37%]PEG(2K)	PLL-[45%]PEG(5K)	PLL-[22%]PEG(5K)
Adsorbed mass (mg.m^{-2})	0.4	1.1	0.9	1.3
Adsorbed PEG (mg.m^{-2})	0	0.94	0.85	1.16
Adsorbed PLL (mg.m^{-2})	0.4	0.16	0.05	0.14
Area/copolymer (nm²)	83	206	680	247
Area/PEG tether (nm²)		3.6	9.6	7.2
Tether spacing (nm)		1.9	3.1	2.7
Number of blobs		4.7	5.1	6.4
Brush height (nm)		9	15.5	17.2
Zeta potentiel (mV)	+ 5	- 15		

Table 1 - Characteristics of saturated PLL and PLL-g-PEG layers on silica (data obtained from optical reflectometry (Gon and Santore, 2011; Gon et al., 2010))

Due to the high charge of PLL at physiological pH, the physisorption is strong and allows for stable adlayers. Kenausis et al. reported stability of the layer under flow conditions at 37 °C and pH 7.4 (buffers: HEPES and PBS), giving an evidence of the irreversibility of the adsorption. pH and ionic strength are important factors for the adlayer stability because the immobilization relies on electrostatic interactions.

By optimizing the PLL-g-PEG architecture (PEG molecular weight, grafting ratio on PLL), Huang *et al.* (Huang et al., 2001)demonstrated that PLL-g[3.5]-PEG(2000) was the best antibiofouling structure. It enables to considerably decrease the amount of fibrinogen adsortion lower than 2 ng.cm^{-2}. Moreover, PLL-g-PEG keeps its repellent properties up to some days (Lussi et al., 2006).

3.1.2 Chemical-responsive Azido-(PLL-g-PEG) coatings

A chemical-responsive Azido-(PLL-g-PEG) (APP) has been developed at the lab (Dongen et al., 2012). Due to the similar structure between the PLL-g-PEG and the APP (Figure 24A), APP combines the advantages of PLL-g-PEG (straightforward surface preparation, antibiofouling, photolitography patterning) with the on-demand orthogonal reactivity of azides. The strained cyclo-octyne bicyclo[6.1.0]-nonyne (BCN) reacts specifically with azides via a spontaneous and catalyst-free azide-alkyne cycloaddition in aqueous media. Hence, this biocompatible reaction has been used to immobilize molecules of choice when it is paired with compounds containing BCN.

In order to demonstrate the potential of APP as a stimuli-responsive biomaterials, studies of cell dynamics have been achieved on APP coatings by triggering with the addition of BCN-RGD in the culture medium(van Dongen et al., 2013). For example, a repellent PLL-g-PEG surface was micro-patterned with APP and fibronectin to trigger a cell shape change (Figure 24B-D). After seeding, single cells are confined on fibronectin spots, adopting a round shape. Once BCN-RGD added on the culture medium, cells stretched out on APP stripes and became linear. This experiment demonstrates that cells require 6.2 ±0.3 h to polarize and enter themselves into migration along one direction. Similarly, other applications have been investigated (the induction of both single and collective cell migration to model wound healing, cocultures of two cell types).

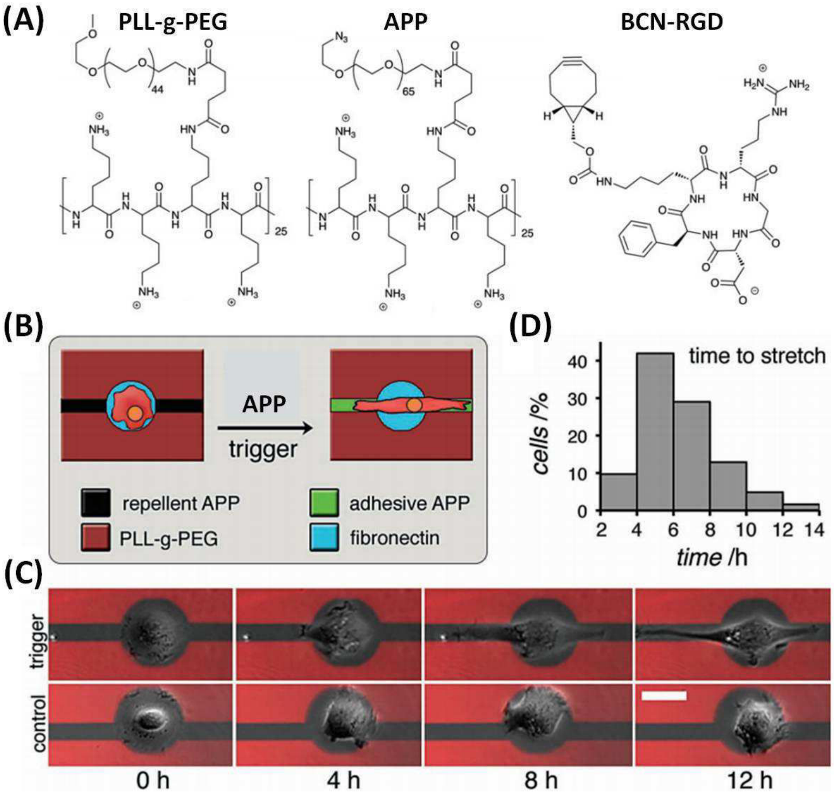

Figure 24 - (A) Chemical structures of PLL-g-PEG, APP and BCN-RGD. (B) Cartoon representation of the strategy to control of cell shape change. (C) The stretching of RPE1 cells in time after addition of BCN-RGD (20 µM). The double pattern is visible due to a fluorescent label on PLL-g-PEG (Alexa594). No BCN-RGD was added for control experiments. Scale bar: 25 µm. (D) Quantization of the average time needed for cells to leave the primary pattern (n = 62).

The control of the N_3 surface density (i.e. density of clickable proteins, peptides, …) has been achieved by diluting APP with standard PLL-g-PEG. This approach has the advantage to easily modulate surface properties without any additional synthesis, only by mixing the appropriate PLL derivatives.

PLL derivatives are useful tools due to adsorption properties of PLL. Indeed, the coating is versatile and compatible with many substrates (glass, quartz, metal oxides, PDMS or cell culture treated polystyrene). Because the coating consists in simple bath applications of activated surfaces in solutions for a few minutes, any chemistry at the bench is required. Furthermore, PLL coatings allow patterning via photolithography and the adjustment of surface properties on mixed layers. As a conclusion, PLL derivatives represent promising tools for non-specialists working on surfaces.

3.2 PLL-g-P(NIPAM-co-RGD) coatings as promising thermo/light-responsive surfaces to modulate cell adhesion

With this thesis, we want to extend this strategy based on PLL-g-PEG in order to develop thermo-responsive or photo-responsive coatings showing a reversible control of cell adhesion. A first strategy relies on adsorbing mixture of PLL-g-PEG and PLL-g-P(NIPAM-co-RGD) to combine the antibiofouling PEG properties with the thermo-responsive properties of PNIPAM brushes on the same adlayer (Figure 25). While the PEG background should suppress non-specific phenomenon, RGD peptides are specific anchorage points to induce integrin-mediated cell adhesion. At temperatures below/above the LCST, extended/collapsed conformations of PNIPAM chains will be explored to modulate a ligand accessibility.

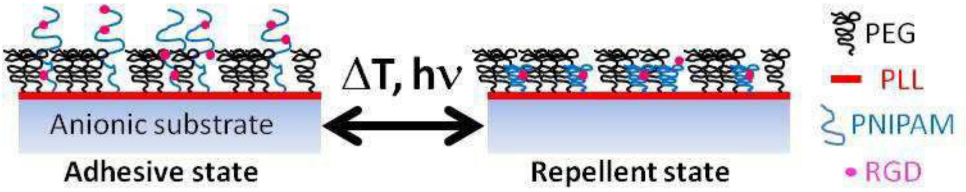

Figure 25 - Schematic illustration of the expected stimuli-responsive behavior of mixed PLL-g-PEG and PLL-g-P(NIPAM-co-RGD) coatings.

A second objective consists in exploring the properties of light-responsive PLL-g-P(modified NIPAM) that had to be designed to preserve biocompatibility and a robust response to light in cell-culture media. To this end, we considered:

- azobenzene-containing PNIPAM brushes. Indeed, in solution, the reversible precipitation/redissolution of azobenzene-containing PNIPAM polymers have been reported by triggering with blue/UV irradiation.
- arrays of thermoplasmonic nanoparticles, as a local heating platform. Indeed, the excitation of thermoplasmonic nanoparticles by laser is converted into heating. The idea for this project consists in coating a thermoplasmonic substrate and to locally trigger PNIPAM transition by laser excitation.

Bibliography

Akhmanova, M., Osidak, E., Domogatsky, S., Rodin, S., Domogatskaya, A., Akhmanova, M., Osidak, E., Domogatsky, S., Rodin, S., and Domogatskaya, A. (2015). Physical, Spatial, and Molecular Aspects of Extracellular Matrix of In Vivo Niches and Artificial Scaffolds Relevant to Stem Cells Research. Stem Cells Int. *2015, 2015*, e167025.

Akiyama, Y., Kikuchi, A., Yamato, M., and Okano, T. (2004). Ultrathin Poly(N-isopropylacrylamide) Grafted Layer on Polystyrene Surfaces for Cell Adhesion/Detachment Control. Langmuir *20*, 5506–5511.

An, Q., Brinkmann, J., Huskens, J., Krabbenborg, S., de Boer, J., and Jonkheijm, P. (2012). A Supramolecular System for the Electrochemically Controlled Release of Cells. Angew. Chem. Int. Ed. *51*, 12233–12237.

Andersson, A.-S., Glasmästar, K., Sutherland, D., Lidberg, U., and Kasemo, B. (2003). Cell adhesion on supported lipid bilayers. J. Biomed. Mater. Res. A *64A*, 622–629.

Anselme, K., and Bigerelle, M. (2011). Role of materials surface topography on mammalian cell response. Int. Mater. Rev. *56*, 243–266.

Anselme, K., and Bigerelle, M. (2014). On the relation between surface roughness of metallic substrates and adhesion of human primary bone cells. Scanning *36*, 11–20.

Arnold, M., Cavalcanti-Adam, E.A., Glass, R., Blümmel, J., Eck, W., Kantlehner, M., Kessler, H., and Spatz, J.P. (2004). Activation of Integrin Function by Nanopatterned Adhesive Interfaces. ChemPhysChem *5*, 383–388.

Arnold, M., Hirschfeld-Warneken, V.C., Lohmüller, T., Heil, P., Blümmel, J., Cavalcanti-Adam, E.A., López-García, M., Walther, P., Kessler, H., Geiger, B., et al. (2008). Induction of Cell Polarization and Migration by a Gradient of Nanoscale Variations in Adhesive Ligand Spacing. Nano Lett. *8*, 2063–2069.

Auernheimer, J., Dahmen, C., Hersel, U., Bausch, A., and Kessler, H. (2005). Photoswitched Cell Adhesion on Surfaces with RGD Peptides. J. Am. Chem. Soc. *127*, 16107–16110.

Bearinger, J.P., Terrettaz, S., Michel, R., Tirelli, N., Vogel, H., Textor, M., and Hubbell, J.A. (2003). Chemisorbed poly(propylene sulphide)-based copolymers resist biomolecular interactions. Nat. Mater. *2*, 259–264.

Berg, M.C., Yang, S.Y., Hammond, P.T., and Rubner, M.F. (2004). Controlling Mammalian Cell Interactions on Patterned Polyelectrolyte Multilayer Surfaces. Langmuir *20*, 1362–1368.

Berrier, A.L., and Yamada, K.M. (2007). Cell–matrix adhesion. J. Cell. Physiol. *213*, 565–573.

Bigerelle, M., Giljean, S., and Anselme, K. (2011). Existence of a typical threshold in the response of human mesenchymal stem cells to a peak and valley topography. Acta Biomater. *7*, 3302–3311.

Blümmel, J., Perschmann, N., Aydin, D., Drinjakovic, J., Surrey, T., Lopez-Garcia, M., Kessler, H., and Spatz, J.P. (2007). Protein repellent properties of covalently attached PEG coatings on nanostructured SiO2-based interfaces. Biomaterials *28*, 4739–4747.

Boekhoven, J., Rubert Pérez, C.M., Sur, S., Worthy, A., and Stupp, S.I. (2013). Dynamic Display of Bioactivity through Host–Guest Chemistry. Angew. Chem. Int. Ed. *52*, 12077–12080.

Boudou, T., Crouzier, T., Ren, K., Blin, G., and Picart, C. (2010). Multiple Functionalities of Polyelectrolyte Multilayer Films: New Biomedical Applications. Adv. Mater. *22*, 441–467.

Cheng, Z.A., Zouani, O.F., Glinel, K., Jonas, A.M., and Durrieu, M.-C. (2013). Bioactive Chemical Nanopatterns Impact Human Mesenchymal Stem Cell Fate. Nano Lett. *13*, 3923–3929.

Cole, M.A., Voelcker, N.H., Thissen, H., and Griesser, H.J. (2009). Stimuli-responsive interfaces and systems for the control of protein–surface and cell–surface interactions. Biomaterials *30*, 1827–1850.

Dechantsreiter, M.A., Planker, E., Mathä, B., Lohof, E., Hölzemann, G., Jonczyk, A., Goodman, S.L., and Kessler, H. (1999). N-Methylated Cyclic RGD Peptides as Highly Active and Selective αVβ3 Integrin Antagonists. J. Med. Chem. *42*, 3033–3040.

Deeg, J.A., Louban, I., Aydin, D., Selhuber-Unkel, C., Kessler, H., and Spatz, J.P. (2011). Impact of Local versus Global Ligand Density on Cellular Adhesion. Nano Lett. *11*, 1469–1476.

Delaittre, G., Greiner, A.M., Pauloehrl, T., Bastmeyer, M., and Barner-Kowollik, C. (2012). Chemical approaches to synthetic polymer surface biofunctionalization for targeted cell adhesion using small binding motifs. Soft Matter *8*, 7323–7347.

Desseaux, S., and Klok, H.-A. (2014). Temperature-Controlled Masking/Unmasking of Cell-Adhesive Cues with Poly(ethylene glycol) Methacrylate Based Brushes. Biomacromolecules *15*, 3859–3865.

Di Cio, S., and Gautrot, J.E. (2016). Cell sensing of physical properties at the nanoscale: Mechanisms and control of cell adhesion and phenotype. Acta Biomater. *30*, 26–48.

van Dongen, S.F.M., Janvore, J., Berkel, S.S. van, Marie, E., Piel, M., and Tribet, C. (2012). Reactive protein-repellent surfaces for the straightforward attachment of small molecules up to whole cells. Chem. Sci. *3*, 3000–3006.

van Dongen, S.F.M., Maiuri, P., Marie, E., Tribet, C., and Piel, M. (2013). Triggering Cell Adhesion, Migration or Shape Change with a Dynamic Surface Coating. Adv. Mater. *25*, 1687–1691.

Ebara, M., Yamato, M., Aoyagi, T., Kikuchi, A., Sakai, K., and Okano, T. (2004). Temperature-Responsive Cell Culture Surfaces Enable “On−Off” Affinity Control between Cell Integrins and RGDS Ligands. Biomacromolecules *5*, 505–510.

Engler, A.J., Griffin, M.A., Sen, S., Bönnemann, C.G., Sweeney, H.L., and Discher, D.E. (2004). Myotubes differentiate optimally on substrates with tissue-like stiffness pathological implications for soft or stiff microenvironments. J. Cell Biol. *166*, 877–887.

Engler, A.J., Sen, S., Sweeney, H.L., and Discher, D.E. (2006). Matrix Elasticity Directs Stem Cell Lineage Specification. Cell *126*, 677–689.

Gallant, N.D., Michael, K.E., and García, A.J. (2005). Cell Adhesion Strengthening: Contributions of Adhesive Area, Integrin Binding, and Focal Adhesion Assembly. Mol. Biol. Cell *16*, 4329–4340.

Geiger, B., Spatz, J.P., and Bershadsky, A.D. (2009). Environmental sensing through focal adhesions. Nat. Rev. Mol. Cell Biol. *10*, 21–33.

Gon, S., and Santore, M.M. (2011). Sensitivity of Protein Adsorption to Architectural Variations in a Protein-Resistant Polymer Brush Containing Engineered Nanoscale Adhesive Sites. Langmuir *27*, 15083–15091.

Gon, S., Bendersky, M., Ross, J.L., and Santore, M.M. (2010). Manipulating Protein Adsorption using a Patchy Protein-Resistant Brush. Langmuir *26*, 12147–12154.

Griffin, D.R., Borrajo, J., Soon, A., Acosta-Vélez, G.F., Oshita, V., Darling, N., Mack, J., Barker, T., Iruela-Arispe, M.L., and Segura, T. (2014). Hybrid Photopatterned Enzymatic Reaction (HyPER) for in Situ Cell Manipulation. ChemBioChem *15*, 233–242.

Halperin, A., and Kröger, M. (2012). Thermoresponsive Cell Culture Substrates Based on PNIPAM Brushes Functionalized with Adhesion Peptides: Theoretical Considerations of Mechanism and Design. Langmuir *28*, 16623–16637.

Huang, J., Gräter, S.V., Corbellini, F., Rinck, S., Bock, E., Kemkemer, R., Kessler, H., Ding, J., and Spatz, J.P. (2009). Impact of Order and Disorder in RGD Nanopatterns on Cell Adhesion. Nano Lett. *9*, 1111–1116.

Huang, N.-P., Michel, R., Voros, J., Textor, M., Hofer, R., Rossi, A., Elbert, D.L., Hubbell, J.A., and Spencer, N.D. (2001). Poly(l-lysine)-g-poly(ethylene glycol) Layers on Metal Oxide Surfaces: Surface-Analytical Characterization and Resistance to Serum and Fibrinogen Adsorption. Langmuir *17*, 489–498.

Hudalla, G.A., and Murphy, W.L. (2009). Using “Click” Chemistry to Prepare SAM Substrates to Study Stem Cell Adhesion. Langmuir *25*, 5737–5746.

Hynes, R.O. (2002). Integrins: Bidirectional, Allosteric Signaling Machines. Cell *110*, 673–687.

Inaba, R., Khademhosseini, A., Suzuki, H., and Fukuda, J. (2009). Electrochemical desorption of self-assembled monolayers for engineering cellular tissues. Biomaterials *30*, 3573–3579.

Ingber, D.E. (2003). Tensegrity II. How structural networks influence cellular information processing networks. J. Cell Sci. *116*, 1397–1408.

Israels, R., Leermakers, F.A.M., and Fleer, G.J. (1995). Adsorption of Charged Block Copolymers: Effect on Colloidal Stability. Macromolecules *28*, 1626–1634.

Jeon, S.I., Lee, J.H., Andrade, J.D., and De Gennes, P.G. (1991). Protein—surface interactions in the presence of polyethylene oxide. J. Colloid Interface Sci. *142*, 149–158.

Jiang, X., Bruzewicz, D.A., Wong, A.P., Piel, M., and Whitesides, G.M. (2005). Directing cell migration with asymmetric micropatterns. Proc. Natl. Acad. Sci. U. S. A. *102*, 975–978.

Jurchenko, C., Chang, Y., Narui, Y., Zhang, Y., and Salaita, K.S. (2014). Integrin-Generated Forces Lead to Streptavidin-Biotin Unbinding in Cellular Adhesions. Biophys. J. *106*, 1436–1446.

Kaji, H., Kanada, M., Oyamatsu, D., Matsue, T., and Nishizawa, M. (2004). Microelectrochemical Approach to Induce Local Cell Adhesion and Growth on Substrates. Langmuir *20*, 16–19.

Kenausis, G.L., Vörös, J., Elbert, D.L., Huang, N., Hofer, R., Ruiz-Taylor, L., Textor, M., Hubbell, J.A., and Spencer, N.D. (2000). Poly(l-lysine)-g-Poly(ethylene glycol) Layers on Metal Oxide Surfaces: Attachment Mechanism and Effects of Polymer Architecture on Resistance to Protein Adsorption†. J. Phys. Chem. B *104*, 3298–3309.

Kerdjoudj, H., Boulmedais, F., Berthelemy, N., Mjahed, H., Louis, H., Schaaf, P., Voegel, J.C., and Menu, P. (2011). Cellularized alginate sheets for blood vessel reconstruction. Soft Matter *7*, 3621–3626.

Kim, S.-H., Turnbull, J., and Guimond, S. (2011). Extracellular matrix and cell signalling: the dynamic cooperation of integrin, proteoglycan and growth factor receptor. J. Endocrinol. *209*, 139–151.

Lagunas, A., Comelles, J., Martínez, E., Prats-Alfonso, E., Acosta, G.A., Albericio, F., and Samitier, J. (2012). Cell adhesion and focal contact formation on linear RGD molecular gradients: study of non-linear concentration dependence effects. Nanomedicine Nanotechnol. Biol. Med. *8*, 432–439.

Lahann, J., Mitragotri, S., Tran, T.-N., Kaido, H., Sundaram, J., Choi, I.S., Hoffer, S., Somorjai, G.A., and Langer, R. (2003). A Reversibly Switching Surface. Science *299*, 371–374.

Laloyaux, X., Fautré, E., Blin, T., Purohit, V., Leprince, J., Jouenne, T., Jonas, A.M., and Glinel, K. (2010). Temperature-Responsive Polymer Brushes Switching from Bactericidal to Cell-Repellent. Adv. Mater. *22*, 5024–5028.

Lamb, B.M., and Yousaf, M.N. (2011). Redox-Switchable Surface for Controlling Peptide Structure. J. Am. Chem. Soc. *133*, 8870–8873.

Lee, H., Jang, Y., Seo, J., Nam, J.-M., and Char, K. (2011). Nanoparticle-Functionalized Polymer Platform for Controlling Metastatic Cancer Cell Adhesion, Shape, and Motility. ACS Nano *5*, 5444–5456.

Liu, D., Xie, Y., Shao, H., and Jiang, X. (2009). Using Azobenzene-Embedded Self-Assembled Monolayers To Photochemically Control Cell Adhesion Reversibly. Angew. Chem. Int. Ed. *48*, 4406–4408.

Liu, Y.-J., Le Berre, M., Lautenschlaeger, F., Maiuri, P., Callan-Jones, A., Heuzé, M., Takaki, T., Voituriez, R., and Piel, M. (2015a). Confinement and Low Adhesion Induce Fast Amoeboid Migration of Slow Mesenchymal Cells. Cell *160*, 659–672.

Liu, Z., Liu, Y., Chang, Y., Seyf, H.R., Henry, A., Mattheyses, A.L., Yehl, K., Zhang, Y., Huang, Z., and Salaita, K. (2015b). Nanoscale optomechanical actuators for controlling mechanotransduction in living cells. Nat. Methods *advance online publication*.

Lo, C.-M., Wang, H.-B., Dembo, M., and Wang, Y. (2000). Cell Movement Is Guided by the Rigidity of the Substrate. Biophys. J. *79*, 144–152.

Loesberg, W.A., te Riet, J., van Delft, F.C.M.J.M., Schön, P., Figdor, C.G., Speller, S., van Loon, J.J.W.A., Walboomers, X.F., and Jansen, J.A. (2007). The threshold at which substrate nanogroove dimensions may influence fibroblast alignment and adhesion. Biomaterials *28*, 3944–3951.

Luk, Y.-Y., Kato, M., and Mrksich, M. (2000). Self-Assembled Monolayers of Alkanethiolates Presenting Mannitol Groups Are Inert to Protein Adsorption and Cell Attachment. Langmuir *16*, 9604–9608.

Lussi, J.W., Falconnet, D., Hubbell, J.A., Textor, M., and Csucs, G. (2006). Pattern stability under cell culture conditions—A comparative study of patterning methods based on PLL-g-PEG background passivation. Biomaterials *27*, 2534–2541.

Lutolf, M.P. (2012). Materials science: Cell environments programmed with light. Nature *482*, 477–478.

Malmström, J., Christensen, B., Jakobsen, H.P., Lovmand, J., Foldbjerg, R., Sørensen, E.S., and Sutherland, D.S. (2010). Large Area Protein Patterning Reveals Nanoscale Control of Focal Adhesion Development. Nano Lett. *10*, 686–694.

Marklein, R.A., and Burdick, J.A. (2009). Spatially controlled hydrogel mechanics to modulate stem cell interactions. Soft Matter *6*, 136–143.

Milbradt, A.G., Löweneck, M., Krupka, S.S., Reif, M., Sinner, E.-K., Moroder, L., and Renner, C. (2005). Photomodulation of conformational states. IV. Integrin-binding RGD-peptides with (4-aminomethyl)phenylazobenzoic acid as backbone constituent. Biopolymers *77*, 304–313.

Monge, C., Saha, N., Boudou, T., Pózos-Vásquez, C., Dulong, V., Glinel, K., and Picart, C. (2013). Rigidity-Patterned Polyelectrolyte Films to Control Myoblast Cell Adhesion and Spatial Organization. Adv. Funct. Mater. *23*, 3432–3442.

Monge, C., Almodóvar, J., Boudou, T., and Picart, C. (2015). Spatio-temporal control of LbL films for biomedical applications: from 2D to 3D. Adv. Healthc. Mater. *4*, 811–830.

Mosiewicz, K.A., Kolb, L., van der Vlies, A.J., Martino, M.M., Lienemann, P.S., Hubbell, J.A., Ehrbar, M., and Lutolf, M.P. (2013). In situ cell manipulation through enzymatic hydrogel photopatterning. Nat. Mater. *12*, 1072–1078.

Mosiewicz, K.A., Kolb, L., Vlies, A.J. van der, and Lutolf, M.P. (2014). Microscale patterning of hydrogel stiffness through light-triggered uncaging of thiols. Biomater. Sci. *2*, 1640–1651.

Nakanishi, J. (2014). Switchable Substrates for Analyzing and Engineering Cellular Functions. Chem. – Asian J. *9*, 406–417.

Nakanishi, J., Kikuchi, Y., Takarada, T., Nakayama, H., Yamaguchi, K., and Maeda, M. (2004). Photoactivation of a Substrate for Cell Adhesion under Standard Fluorescence Microscopes. J. Am. Chem. Soc. *126*, 16314–16315.

Nakanishi, J., Kikuchi, Y., Inoue, S., Yamaguchi, K., Takarada, T., and Maeda, M. (2007). Spatiotemporal Control of Migration of Single Cells on a Photoactivatable Cell Microarray. J. Am. Chem. Soc. *129*, 6694–6695.

Nelson, C.M., Raghavan, S., Tan, J.L., and Chen, C.S. (2003). Degradation of Micropatterned Surfaces by Cell-Dependent and -Independent Processes. Langmuir *19*, 1493–1499.

Ng, C.C.A., Magenau, A., Ngalim, S.H., Ciampi, S., Chockalingham, M., Harper, J.B., Gaus, K., and Gooding, J.J. (2012). Using an Electrical Potential to Reversibly Switch Surfaces between Two States for Dynamically Controlling Cell Adhesion. Angew. Chem. Int. Ed. *51*, 7706–7710.

Pan, G., Guo, Q., Ma, Y., Yang, H., and Li, B. (2013). Thermo-Responsive Hydrogel Layers Imprinted with RGDS Peptide: A System for Harvesting Cell Sheets. Angew. Chem. Int. Ed. *52*, 6907–6911.

Pan, G., Guo, B., Ma, Y., Cui, W., He, F., Li, B., Yang, H., and Shea, K.J. (2014). Dynamic Introduction of Cell Adhesive Factor via Reversible Multicovalent Phenylboronic Acid/cis-Diol Polymeric Complexes. J. Am. Chem. Soc. *136*, 6203–6206.

Park, J., Bauer, S., von der Mark, K., and Schmuki, P. (2007). Nanosize and Vitality: TiO2 Nanotube Diameter Directs Cell Fate. Nano Lett. *7*, 1686–1691.

Peng, R., Yao, X., and Ding, J. (2011). Effect of cell anisotropy on differentiation of stem cells on micropatterned surfaces through the controlled single cell adhesion. Biomaterials *32*, 8048–8057.

Persson, K.M., Lönnqvist, S., Tybrandt, K., Gabrielsson, R., Nilsson, D., Kratz, G., and Berggren, M. (2015). Matrix Addressing of an Electronic Surface Switch Based on a Conjugated Polyelectrolyte for Cell Sorting. Adv. Funct. Mater. *25*, 7056–7063.

Petersen, S., Alonso, J.M., Specht, A., Duodu, P., Goeldner, M., and del Campo, A. (2008). Phototriggering of Cell Adhesion by Caged Cyclic RGD Peptides. Angew. Chem. Int. Ed. *47*, 3192–3195.

Pidhatika, B., Rodenstein, M., Chen, Y., Rakhmatullina, E., Muehlebach, A., Acikgoez, C., Textor, M., and Konradi, R. (2012). Comparative Stability Studies of Poly(2-methyl-2-oxazoline) and Poly(ethylene glycol) Brush Coatings. Biointerphases *7*, 1.

Plotnikov, S.V., and Waterman, C.M. (2013). Guiding cell migration by tugging. Curr. Opin. Cell Biol. *25*, 619–626.

Ratner Biomaterials Science, 3rd Edition | Buddy Ratner, Allan Hoffman, Frederick Schoen, Jack Lemons | ISBN 9780123746269.

Schmidt, S., Zeiser, M., Hellweg, T., Duschl, C., Fery, A., and Möhwald, H. (2010). Adhesion and Mechanical Properties of PNIPAM Microgel Films and Their Potential Use as Switchable Cell Culture Substrates. Adv. Funct. Mater. *20*, 3235–3243.

Schütt, M., Krupka, S.S., Milbradt, A.G., Deindl, S., Sinner, E.-K., Oesterhelt, D., Renner, C., and Moroder, L. (2003). Photocontrol of Cell Adhesion Processes: Model Studies with Cyclic Azobenzene-RGD Peptides. Chem. Biol. *10*, 487–490.

Sniadecki, N.J., Anguelouch, A., Yang, M.T., Lamb, C.M., Liu, Z., Kirschner, S.B., Liu, Y., Reich, D.H., and Chen, C.S. (2007). Magnetic microposts as an approach to apply forces to living cells. Proc. Natl. Acad. Sci. *104*, 14553–14558.

Sofia, S.J., Premnath, V., and Merrill, E.W. (1998). Poly(ethylene oxide) Grafted to Silicon Surfaces: Grafting Density and Protein Adsorption. Macromolecules *31*, 5059–5070.

Streuli, C.H. (2009). Integrins and cell-fate determination. J. Cell Sci. *122*, 171–177.

Tang, Z., Akiyama, Y., and Okano, T. (2014). Recent development of temperature-responsive cell culture surface using poly(N-isopropylacrylamide). J. Polym. Sci. Part B Polym. Phys. *52*, 917–926.

Todd, S.J., Scurr, D.J., Gough, J.E., Alexander, M.R., and Ulijn, R.V. (2009). Enzyme-Activated RGD Ligands on Functionalized Poly(ethylene glycol) Monolayers: Surface Analysis and Cellular Response. Langmuir *25*, 7533–7539.

Uhlig, K., Boerner, H.G., Wischerhoff, E., Lutz, J.-F., Jaeger, M.S., Laschewsky, A., and Duschl, C. (2014). On the Interaction of Adherent Cells with Thermoresponsive Polymer Coatings. Polymers *6*, 1164–1177.

Ventre, M., Causa, F., and Netti, P.A. (2012). Determinants of cell–material crosstalk at the interface: towards engineering of cell instructive materials. J. R. Soc. Interface *9*, 2017–2032.

Vogel, V., and Sheetz, M. (2006). Local force and geometry sensing regulate cell functions. Nat. Rev. Mol. Cell Biol. *7*, 265–275.

Wirkner, M., Weis, S., San Miguel, V., Álvarez, M., Gropeanu, R.A., Salierno, M., Sartoris, A., Unger, R.E., Kirkpatrick, C.J., and del Campo, A. (2011). Photoactivatable Caged Cyclic RGD Peptide for Triggering Integrin Binding and Cell Adhesion to Surfaces. ChemBioChem *12*, 2623–2629.

Xiong, J.-P., Stehle, T., Zhang, R., Joachimiak, A., Frech, M., Goodman, S.L., and Arnaout, M.A. (2002). Crystal Structure of the Extracellular Segment of Integrin αVβ3 in Complex with an Arg-Gly-Asp Ligand. Science *296*, 151–155.

Yamada, N., Okano, T., Sakai, H., Karikusa, F., Sawasaki, Y., and Sakurai, Y. (1990). Thermo-responsive polymeric surfaces; control of attachment and detachment of cultured cells. Makromol. Chem. Rapid Commun. *11*, 571–576.

Yeo, W.-S., Hodneland, C.D., and Mrksich, M. (2001). Electroactive Monolayer Substrates that Selectively Release Adherent Cells. ChemBioChem *2*, 590–593.

Yeo, W.-S., Yousaf, M.N., and Mrksich, M. (2003). Dynamic Interfaces between Cells and Surfaces: Electroactive Substrates that Sequentially Release and Attach Cells. J. Am. Chem. Soc. *125*, 14994–14995.

Zareie, H.M., Boyer, C., Bulmus, V., Nateghi, E., and Davis, T.P. (2008). Temperature-Responsive Self-Assembled Monolayers of Oligo(ethylene glycol): Control of Biomolecular Recognition. ACS Nano *2*, 757–765.

Zhao, C., Witte, I., and Wittstock, G. (2006). Switching On Cell Adhesion with Microelectrodes. Angew. Chem. Int. Ed. *45*, 5469–5471.

Zinger, O., Anselme, K., Denzer, A., Habersetzer, P., Wieland, M., Jeanfils, J., Hardouin, P., and Landolt, D. (2004). Time-dependent morphology and adhesion of osteoblastic cells on titanium model surfaces featuring scale-resolved topography. Biomaterials *25*, 2695–2711.

Kristin, Persson, K.M., Karlsson, R., Svennersten, K., Loffler, S., Jager, E.W.H., Löffler, S., Richter Dahlfors, A., Konradsson, P., and Berggren, M. (2011). Electronic Control of Cell Detachment Using a Self-Doped Conducting Polymer. Adv. Mater. *23*, 4403.

Chapter 2 - Synthetic route to PLL-g-PNIPAM derivatives

Contents

Introduction

During this project, a family of PLL-g-PNIPAM derivatives was obtained and their generic structures are represented on Figure 26A. The following nomenclature was adopted to distinguish between the different PLL-g-PNIPAM compounds. PLL-g-[τ_1]A-[τ_2]α-C$_i$,ω-N-Butanamido-P(NIPAM-co-B)(M$_n$) corresponds to a PLL backbone bearing two different grafts randomly distributed: grafts "A" and "α-C$_i$,ω-N-Butanamido-P(NIPAM-co-B)" with grafting ratios τ_1 and τ_2 respectively. Considering macromolecular grafts "α-C$_i$,ω-N-Butanamido-P(NIPAM-co-B)(M$_n$)", M$_n$ relates to its molecular weight (kg.mol^{-1}) and C$_i$ represents the free extremity. During the synthesis, grafts “A” were introduced before grafts "α-C$_i$,ω-N-Butanamido-P(NIPAM-co-B)(M$_n$)" on PLL-g-[τ_1]A-[τ_2]α-C$_i$,ω-N-Butanamido-P(NIPAM-co-B)(M$_n$) as the smallest grafts. When C$_i$ = COOH, the name of the corresponding PLL derivatives is simplified to PLL-g-[τ_1]A-[τ_2]P(NIPAM-co-B)(M$_n$) (instead of PLL-g-[τ_1]A-[τ_2]α-COOH,ω-N-Butanamido-P(NIPAM-co-B)(M$_n$)). In solution, PLL-g-PNIPAM are comb-like copolymers with the PLL backbone tending to adopt a linear conformation (Figure 26A) (Feuz et al., 2008). After adsorption on an anionic surface, cationic ammoniums of the PLL lie to the surface while the PNIPAM grafts are exposed to the surrounding medium (Figure 26B). Hence, adlayer properties come from the PLL-g-PNIPAM architecture.

A versatile synthesis was adopted to obtain the family of PLL-g-[τ_1]A-[τ_2]α-C$_i$,ω-N-Butanamido-P(NIPAM-co-B)(M$_n$) compounds starting from a commercial PLL hydrobromide of 20 kg.mol^{-1}. Adsorption of these polymers enable us to easily modify properties of PNIPAM coatings. This is a convenient approach in comparison with classical "grafting from" techniques which imply a complex surface chemistry. For example, the ability to reversibly expose/mask a ligand represents one major challenge for our PLL-g-PNIPAM adlayers. To tackle this challenge, different parameters of PLL-g-PNIPAM architecture could be considered: the position of the ligand in PLL-g-PNIPAM coatings, the length of the PNIPAM grafts, ... In particular, during this thesis, the position of the ligand has been considered by designing PLL-g-PNIPAM architectures with ligands at the extremity of PNIPAM grafts, or along PNIPAM grafts, or directly on the PLL backbone (Figure 27). Hence, the study of the ligand position relies on the synthesis of PLL-g-PNIPAM compounds represented on Figure 27.

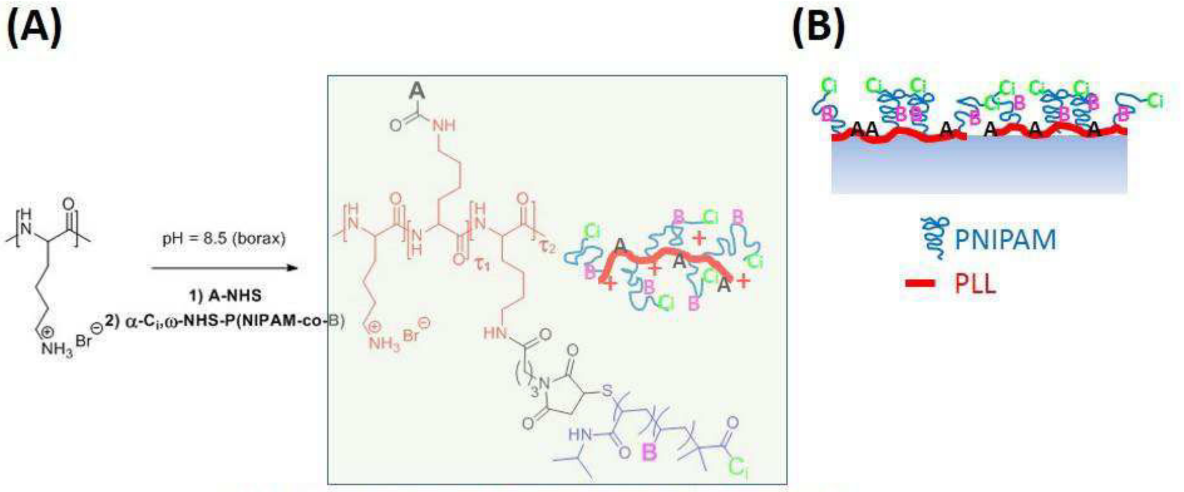

PLL-g-[τ_1]A-[τ_2]α-C$_i$,ω-N-Butanamido-P(NIPAM-co-B)(M$_n$)

Figure 26 - (A) Scheme of the grafting on PLL, affording our target molecules PLL-g-[τ_1]A-[τ_2]α-C$_i$,ω-N-Butanamido-P(NIPAM-co-B)(M$_n$). Schematic representation in solution. (B) Expected conformation of target molecules on anionic surfaces.

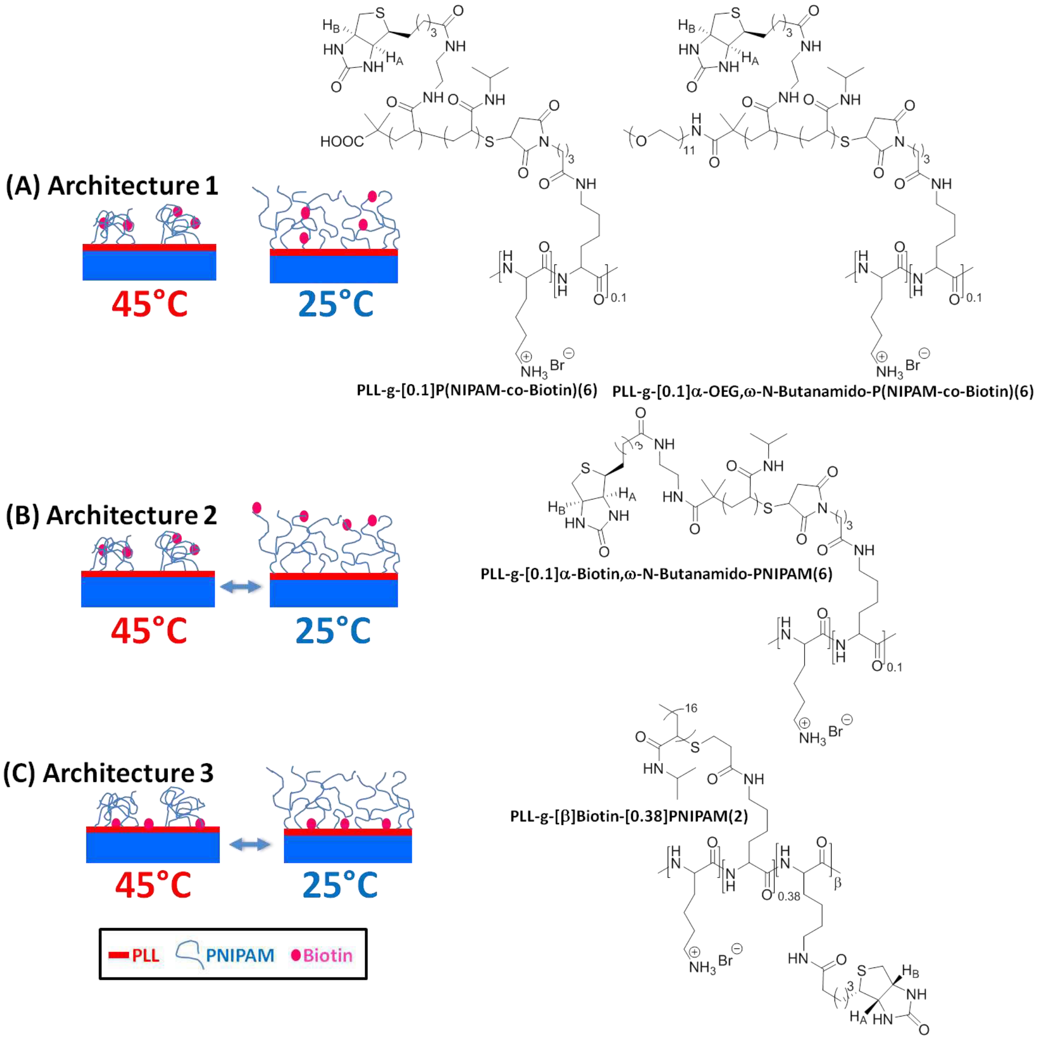

Figure 27 - Representation of expected ligand accessibility on three different PLL-g-PNIPAM architectures (with the corresponding chemical structure of PLL-g-PNIPAM compounds). (A) Architecture 1: Biotin is located along PNIPAM chains - PLL-g-[0.1]P(NIPAM-co-Biotin)(6) or PLL-g-[0.1]α-OEG,ω-N-Butanamido-P(NIPAM-co-Biotin)(6), (B) Architecture 2: Biotin is located at the free extremity - PLL-g-[0.1]α-Biotin,ω-N-Butanamido-PNIPAM(6), (C) Architecture 3: Biotin is on the substrate - PLL-g-[β]Biotin-[0.38]PNIPAM(2).

1 PLL functionalization

To functionalize the PLL, we have used the grafting technique introduced by the pioneering works of Textor on PLL-g-PEG (Kenausis et al., 2000). It consists in coupling *N*-hydroxysuccinimide (NHS) ester compounds with primary amines of the PLL (Figure 26A). This reaction affords good grafting yields in sodium borate buffer (pH ~ 8.5) where amines are partially uncharged and consequently nucleophilic. Synthesis protocols of the different PLL compounds are summarized on Appendix 1. PLL compounds were dialyzed against water and lyophilized before polymer characterizations and utilizations.

Different commercial NHS compounds were grafted on PLL:

- PEG-NHS of 2 kg.mol^{-1} was used to afford the repellent PLL-g-[0.4]PEG(2). Because this is the only PEGylated PLL compounds considered during this project, we simplify its name to PLL-g-PEG.

- Alexa-NHS was used to fluorescently label PLL derivatives.
- PNIPAM-NHS of 2 kg.mol^{-1} was used to afford PLL-g-[0.27]PNIPAM(2) (Figure 28).

Because the grafting ratio of the PLL side chains plays an important role on adlayer properties (density of brushes, ligand density, ...), a particular attention was taken to assure a good grafting ratio. ^{1}H-NMR analyses was used to evaluate this grafting ratio. Indeed, the methylene group (CH_2) covalently linked to the Lysine primary amine undergoes a shift from 2.85 ppm to 3.05 ppm during the amide bond formation. The grafting ratio τ can be simply calculated from the corresponding integrals I(-$(CH_2)_2$-C**H**$_2$-NH_2) and I(-$(CH_2)_2$-C**H**$_2$-NH_2-CO): $\tau = \frac{\mathrm{I}(-(\mathrm{CH_2})_2-\mathbf{CH_2}-\mathrm{NH}-\mathrm{CO}-)}{\mathrm{I}(-(\mathrm{CH_2})_2-\mathbf{CH_2}-\mathrm{NH_2})}$ as illustrated on Figure 28 with PLL-g-[0.27]PNIPAM(2).

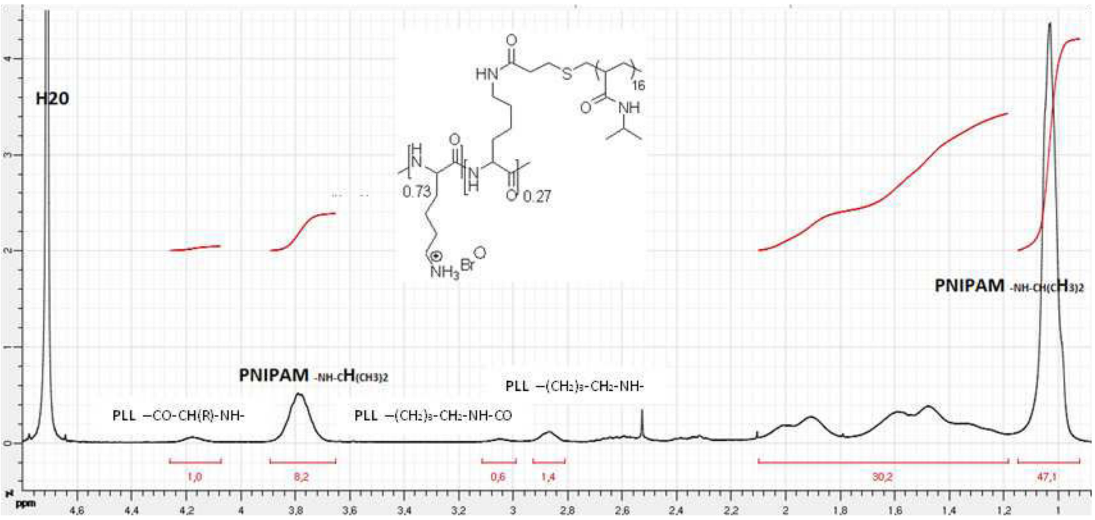

Figure 28 - ^{1}H-NMR spectrum (D_2O) of PLL-g-[0.27]PNIPAM(2), synthesized from commercial PNIPAM-NHS.

2 Synthesis of α-C$_i$,ω-NHS-P(NIPAM-co-B) grafts

A versatile synthesis has been designed to obtain α-C$_i$,ω-NHS-P(NIPAM-co-B)(M_n) random copolymers bearing two defined polymer ends (C$_i$ and NHS) and different comonomers B with a defined molecular weight, and a low dispersity. Our approach can be divided in three parts (Figure 29).

First, a reactive parent chain (C$_i$-PNAS, poly-N-acryloxysuccinimide) was synthesized by reversible addition-fragmentation chain-transfer (RAFT) polymerization. This method of controlled radical polymerization affords low-disperse polymers with a good control over molecular weight and chain end functionalities.

Then, the conversion of C$_i$-PNAS in PNIPAM random copolymers was achieved via successive amine additions. C$_i$-PNAS was first exposed to B-NH_2 before the addition of an excess of isopropylamine Ipr-NH_2. Beyond the modification of the polymer backbone in polyacrylamide, the Ipr-NH_2 excess reacts on the trithiocarbonate function too, thus giving polymers with a thiol end α-C$_i$,ω-SH-P(NIPAM-co-B). Formation of disulfide bond was prevented by working under reductive conditions ($Ar_{(g)}$, tributylphosphine).

Finally, the macro-thiol was coupled with maleimides (M-COOH or M-NHS) in order to convert the thiol end into COOH or NHS ends. Copolymers with a COOH end, α-C$_i$,ω-COOH-P(NIPAM-co-B), were used for physico-chemical analyses in solution while NHS-ended copolymers were coupled to the PLL.

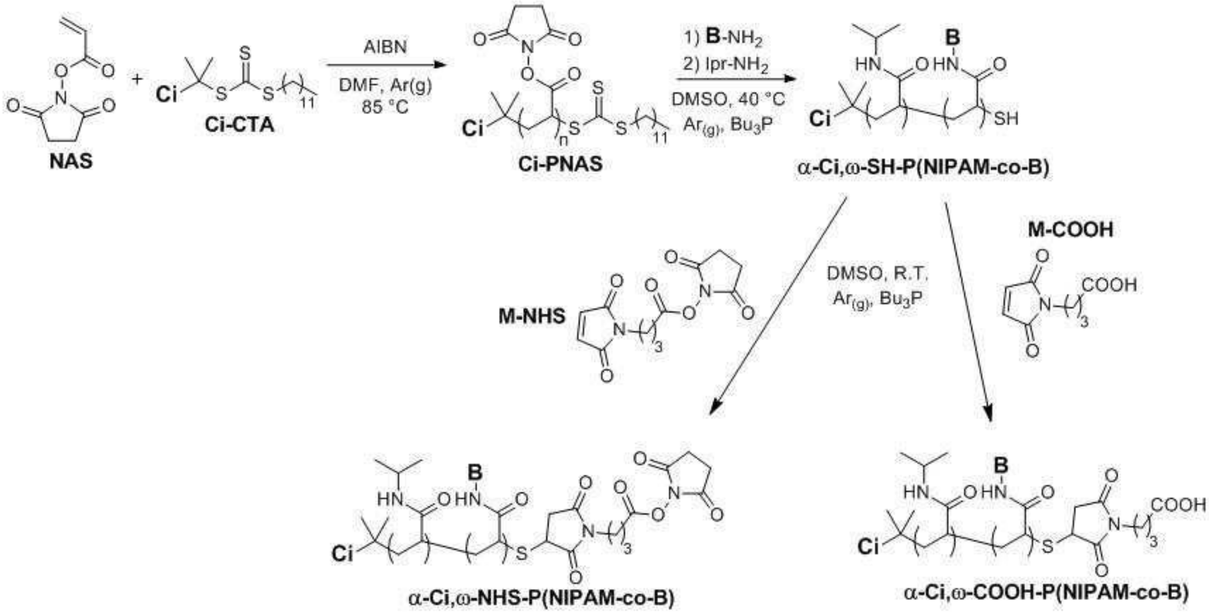

Figure 29 - Scheme of the synthetic route to α-C$_i$,ω-COOH-P(NIPAM-co-B) and α-C$_i$,ω-NHS-P(NIPAM-co-B) random copolymers.

2.1 RAFT agents (C$_i$-CTAs)

The choice of the appropriate Chain Transfer Agent (CTA) for RAFT polymerization has to be made considering many factors: the chemical nature of the monomer, reaction conditions (solubility), requisite end-group functionality for the intended application.

Trithiocarbonate function is known to guarantee an optimal control in RAFT polymerization of acrylate monomers (Keddie et al., 2012). Hence, commercially available HOOC-CTA and non-commercial CTAs (OEG-CTA, Azo-CTA) have been used for NAS polymerization during this project (Figure 30). Furthermore, we used trithiocarbonate function, for further end-group postmodifications.

To obtain OEG-CTA, Biotin-CTA, Azobenzene-CTA and Azo-CTA, we have opposed the corresponding primary amines to the commercial NHS-CTA (Figure 30, see Appendix 1 for protocols). Our protocol was inspired from the one reported by Bathfield *et al.* (Bathfield et al., 2006) who modified dithioesters containing a NHS function with primary amines. The difficulty of this conversion comes from the possible attack of the trithiocarbonate by amines (“thioamidation”). To avoid this side reaction, a slightly more important quantity of NHS-CTA was engaged compared to amines C$_i$-NH$_2$. This thioamidation wasn't noticed for the five investigated amines. Biotin-NH$_2$ and Azobenzene-NH$_2$ didn’t seem to react with NHS-CTA according to TLC monitoring. This method succeeded in synthesizing OEG-CTA, and Azo-CTA.

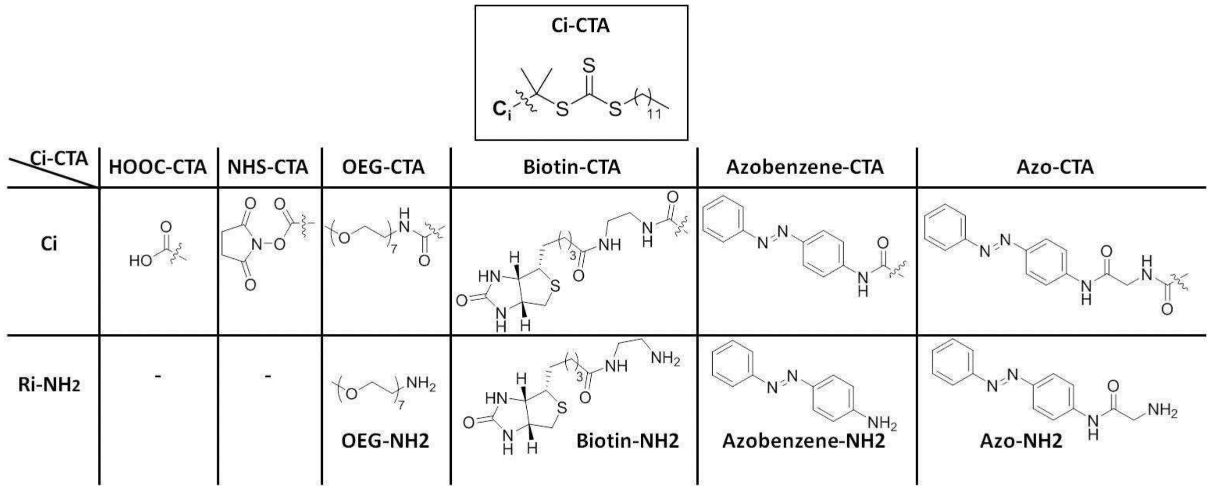

Figure 30 - C_i-CTA structure (top), HOOC-CTA and NHS-CTA are commercial. OEG-CTA and Azo-CTA were obtained by coupling NHS-CTA with the corresponding R_i-NH_2. Attempts to synthesize both Biotin-CTA and Azobenzene-CTA have failed.

The different synthesized CTA were engaged in RAFT polymerization of NAS.

2.2 RAFT polymerization of NAS

2.2.1 Kinetic monitoring of NAS polymerization in presence of HOOC-CTA

The kinetic monitoring gives some evidences of the controlled polymerization character. Hence, results on the kinetics of NAS polymerization in presence of HOOC-CTA are presented as a model for NAS polymerizations involving C_i-CTA.

During the polymerization, aliquots were regularly withdrawn from the reaction medium and analyzed by both ^{1}H-NMR (DMSO-d_6) and SEC (DMF). The comparison of the relative integral areas of the methyne backbone protons (δ 1.71−2.24 ppm, 2H) to the monomer vinyl proton (δ 6.35 ppm, 1H) was used to determine monomer conversion (α). Degree of polymerization (DP_n) and dispersity index (I) were determined by SEC.

On Figure 31A, both monomer conversion and $\ln([NAS]_0/[NAS])$ increase very slightly up to 50 minutes: the chain growth showed an induction period (~50 min) that has already been reported in RAFT polymerization of acrylamides (Qiu and Winnik, 2007; Thomas et al., 2004). It was followed by a pseudo-first order regime, characteristic of controlled polymerization.

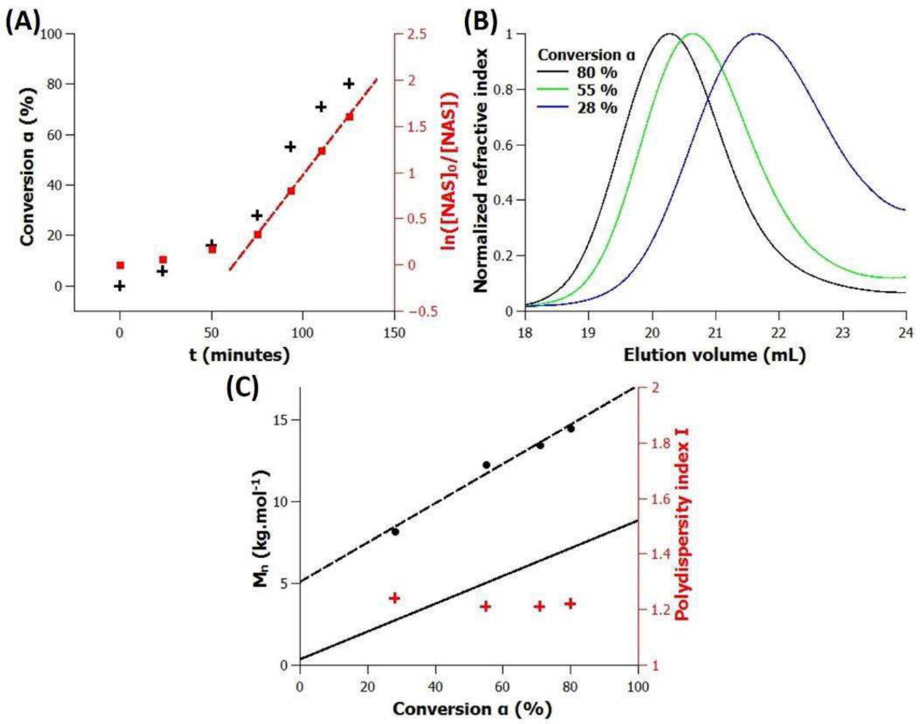

Figure 31 - Characteristic features of RAFT polymerization of NAS in DMF at 85 °C ($[NAS]_0$ = 3 mol.L^{-1}; $[NAS]_0/[CTA]_0$ = 50; $[CTA]_0/[AIBN]_0$ = 10): (A) kinetic monitoring by ^{1}H-NMR ($\ln([NAS]_0/[NAS]) = -\ln(1-\alpha)$), (B) SEC chromatograms, (C) M_n and I versus conversion. Dashed line corresponds to a linear fit of experimental M_n while solid line corresponds to the plot of the theoretical model predicting $M_n = DP_n * M_{NAS} + M_{CTA}$.

The increase in the polymer size with conversion α can be qualitatively noticed on the juxtaposition of SEC chromatograms (Figure 31B), thus giving a qualitative evidence of the controlled RAFT process. The plot of molecular weights shows a linear increase with conversion α (Figure 31C). However, the measured values are higher than the M_n predicted by the theoretical model admitted for RAFT polymerizations (Equation 1, solid line on Figure 31C) (Chiefari et al., 1998; Moad et al., 2000; Thomas et al., 2004).

$$M_{n\,theoretical} = \alpha \frac{[NAS]_0}{[CTA]_0} M_{NAS} + M_{CTA} \qquad (1)$$

Such a deviation has already been noticed in RAFT polymerizations (Convertine et al., 2006; Donovan et al., 2002a, 2002b; Favier et al., 2002; Thomas et al., 2004; Vasilieva et al., 2004) and can be explained by a model including the efficiency of the CTA (Thomas et al., 2004). Equation 2 comes from this model and differs from Equation 1 via two new parameters γ and A.

$$M_{n,\gamma} = \frac{\alpha}{\gamma} \frac{[NAS]_0}{[CTA]_0} M_{NAS} + A \qquad (2)$$

The parameter γ represents the extent of CTA utilization (efficiency) while the parameter A corresponds to an extrapolated intercept value (likely due to monomer conversion prior to the "main equilibrium"). Obviously, parameters γ and A tend respectively to 1 and M_{CTA} for ideal RAFT polymerizations. By fitting the experimental M_n with the Equation 2 (Figure 31C, dotted line), values of 0.70 and 5.1 kDa have been deduced for γ and A respectively. Here, the value γ is relatively close to 1 whereas the gap between A and M_{CTA} (364 Da) is considerable. Up to now, the origin of this phenomenon is still unclear and different explanations have been given. For example, the moderate CTA efficiency could be attributed to a high fragmentation energy of the CTA (i.e a non-efficient addition/fragmentation of the RAFT agent and low reinitiation of the preequilibrium steps).

2.2.2 Reactive parent polymers C_i-PNAS

Polymerizations were stopped once the conversion reached 80 % in order to prevent from side reactions involving the loss of the trithiocarbonate end. Polymerization conditions and characterizations of the synthesized C_i-PNAS are summarized in Table 2. Every polymer shows a dispersity index I of 1.2, which confirms the controlled NAS polymerization by C_i-CTA. Furthermore, ^{1}H-NMR analyses show that C_i-CTA were successfully incorporated into C_i-PNAS chains as end groups as illustrated on Figure 32 with HOOC-PNAS.

C_i-PNAS	$[NAS]_0$	$[NAS]_0/[CTA]_0$	$[CTA]_0/[AIBN]_0$	α [(a)]	I [(b)]	DP_n[(a)]	M_n (kDa) [(c)]
HOOC-PNAS	3 mol/L	50	10	80 %	1.2	50	8.8
OEG-PNAS	3 mol/L	50	10	81 %	1.2	46	8.7
Azo-PNAS	3 mol/L	50	10	0 %	-	-	-
Azo-PNAS40	3 mol/L	50	5	84 %	1.2	40	7.4
Azo-PNAS18	3 mol/L	25	5	40 %	1.2	18	3.6

Table 2 - Characterizations of polymers obtained after two consecutive precipitations in anhydrous diethyl ether and drying. Every polymerization was conducted at 85 °C under argon atmosphere. (a) Both final conversion α and degree of polymerization DP_n were evaluated by ^{1}H-NMR in DMSO-d_6. (b) Dispersity index I was evaluated by simple-detection SEC in DMF (polystyrene standards). (c) Molecular weight was calculated from $M_n = DP_n*M_{NAS} + M_{CTA}$.

Deduction of the DP_n could be done by different methods: spectrophotometry based on the absorption of the trithiocarbonate function, SEC and NMR analyses. In our case, the absorption of the trithiocarbonate function undergoes a marked shift from 310 nm in C_i-CTA to 325 nm in C_i-PNAS with a change in molar absorption coefficient: spectrophotometry measurements haven't been used to evaluate DP_n. Moreover, simple detection SEC doesn't give us exact molecular weights but equivalent M_n from PS calibration. Hence, DP_n have been calculated from ^{1}H-NMR (DMSO-d_6) by comparing the relative integral areas of the methylene backbone protons (δ_e 1.71−2.24 ppm, 2H) to end-group protons (δ_{a-b}) (Figure 32). For every polymerization reaching a conversion of 80 %, measured DP_n are closed to the initial $[NAS]_0/[CTA]_0$ ratio. Hence, it's possible to play on this ratio to control the polymer size. For example, two polymers of different size were obtained with this approach (Azo-PNAS40 and Azo-PNAS18, see Table 2).

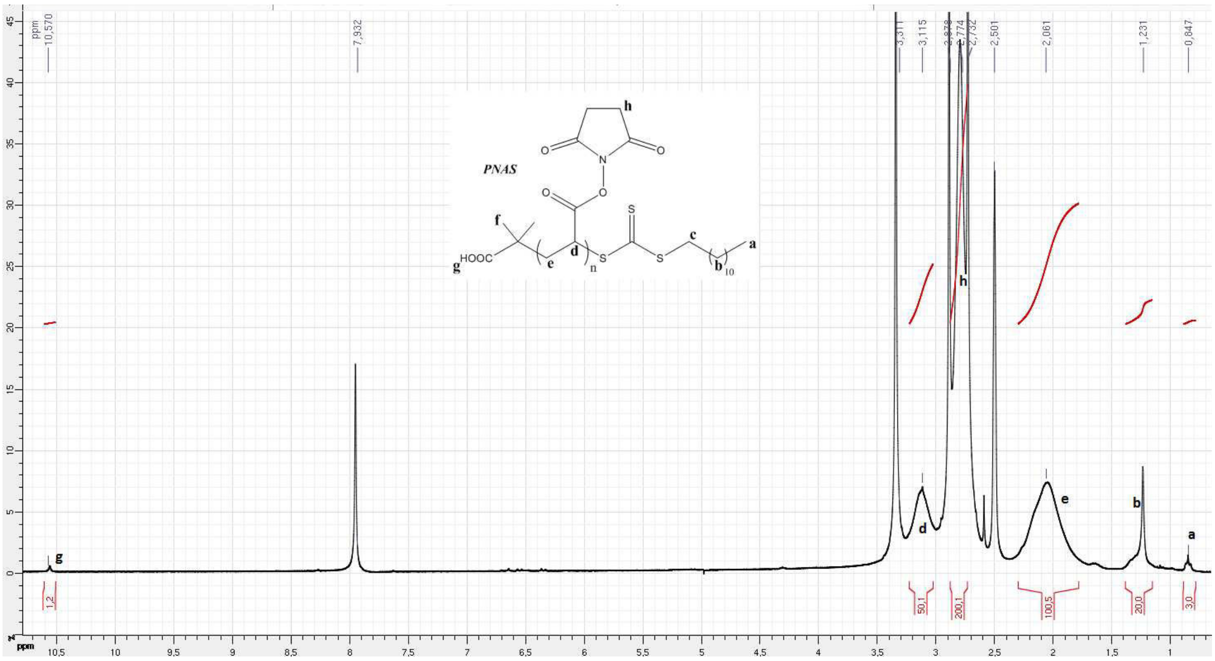

Figure 32 - ^{1}H-NMR spectrum (DMSO-d_6) of the HOOC-PNAS obtained by RAFT polymerization, after two consecutive precipitations in dried diethylether and drying under vacuum.

It is interesting to remark that polymerization in presence of Azo-CTA cannot start with small fraction of AIBN ($[CTA]_0/[AIBN]_0 = 10$, Table 2). By increasing the initial AIBN quantity ($[CTA]_0/[AIBN]_0 = 5$), the polymerization succeeded in starting. However, the conversion can't exceed 40 % with high concentration in Azo-CTA ($[NAS]_0/[CTA]_0 = 25$). This phenomenon probably comes from the N=N bond of the azobenzene. In fact, similar results while polymerizing N,N-dimethylacrylamide and 4-phenylazophenyl acrylate have been reported and attributed to the retardation effect of the azobenzene group (Kroger et al., 1994).

2.3 Post-modifications of parent polymers C_i-PNAS

2.3.1 C_i-PNAS backbone modification

Two different groups of **B**-NH_2 amines have been incorporated into the PNIPAM chains (Figure 33). First group corresponds to both Biotin-NH_2 and RGD-NH_2. These amines were used to trigger specific interactions (Biotin-Streptavidin or RGD-integrin) as discuss in Chapter 4 and 5. Azobenzene-containing amines refer to the second group and were used to develop light-responsive PNIPAM copolymers (Chapter 6).

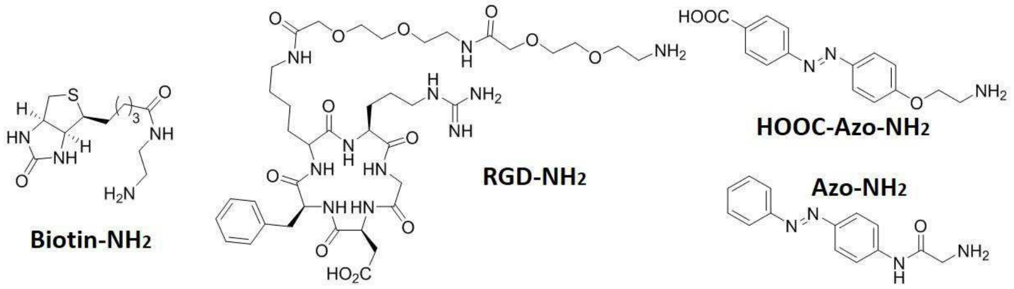

Figure 33 - B-NH_2 amines used to modify C_i-PNAS into α-C_i,ω-SH-P(NIPAM-co-B) copolymers.

Biotin-NH_2 and RGD-NH_2 reacted quantitatively with C_i-PNAS according to NMR analyses. These results were expected because Eberhardt *et al.* have shown that primary amines react quantitatively on PNAS (Eberhardt et al., 2005). Surprisingly, Azo-NH_2 and HOOC-Azo-NH_2 reacted only partially (66 % and 50 % respectively). In the case of HOOC-Azo-NH_2, the formation of zwitterion $^-$OOC-Azo-NH_3^+ can explain its weak reactivity with activated esters. Globally, by engaging different quantity in **B**-NH_2 amines, copolymers of different compositions were synthesized (see Appendix 1 - section 3.4).

The addition of an excess of Ipr-NH_2 makes it possible to convert every remaining NAS unit as it was proved by the disappearance of NHS signals (δ 2.8 ppm) on α-C_i,ω-SH-P(NIPAM-co-B) spectra. Furthermore, integrals of the different signals on these spectra suggest that hydrolysis of NAS into COOH units did not occur while working in anhydrous conditions on recently polymerized C_i-PNAS.

The conversion of PNAS into PNIPAM must be accompanied by a decrease in polymer mass. This trend was effectively noticed on SEC chromatograms (Figure 34) showing an increase in elution volume from HOOC-PNAS to α-COOH,ω-SH-PNIPAM.

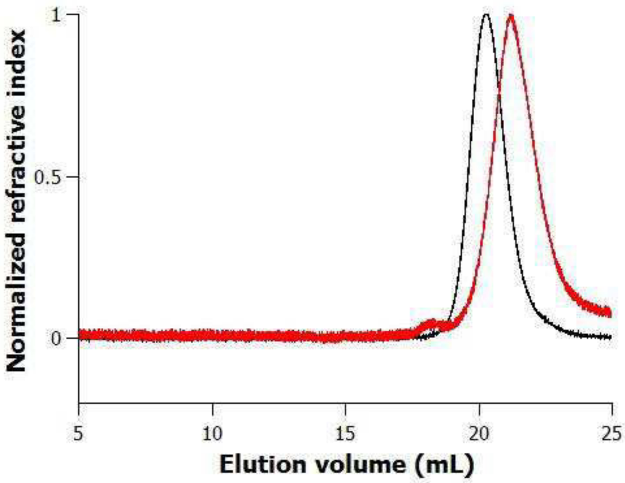

Figure 34 - SEC chromatograms of purified HOOC-PNAS in DMF (black), and the post-modified α-COOH,ω-SH-PNIPAM (red). Elution volumes > 25 mL correspond to the elution of small molecules (M_n < 1000 g.mol^{-1}). Polymer chains were eluted as a single peak in the window 18 mL-24 mL.

2.3.2 C_i-PNAS end-group modification

The excess of Ipr-NH_2 is expected to react on the trithiocarbonate function via an aminolysis, uncaging the thiol extremity. We have obtained two evidences of the aminolysis efficiency. First, by comparing UV-visible spectra of both α-C_i,ω-SH-P(NIPAM-co-B) and C_i-PNAS, the absorption of trithiocarbonate at 325 nm disappeared. Then, we tested positively the presence of thiol thanks to Ellman's reagent, a solution generating specifically a yellow product with thiols (Ellman, 1958).

We worked under reductive conditions (tributylphosphine and argon) in order to prevent the oxidative dimerization of the thiol ends in disulfide bonds. As illustrated on the post-modification of HOOC-PNAS (DP_n = 50) into α-COOH,ω-SH-PNIPAM, SEC chromatogram (Figure 34) shows one peak corresponding to a molecular weight of 6 kg.mol^{-1}, which is in agreement with the predicted molecular weight for α-COOH,ω-SH-PNIPAM (DP_n*M_{NIPAM} = 6 kg.mol^{-1}). In case of oxidative dimerization, a second peak of doubled molecular weight should appear. Under our reductive conditions, the macro-thiols α-COOH,ω-SH-P(NIPAM-co-B) seem to be preserved and were engaged with maleimides M-COOH or M-NHS (Figure 29). Hence, the thiol-ene reaction was used to introduce new end functions (COOH or NHS). The characterization of this last polymer end modification proved to be difficult. Indeed, on both α-C$_i$,ω-NHS-P(NIPAM-co-B) and α-C$_i$,ω-COOH-P(NIPAM-co-B) spectra, no ^{1}H-NMR signal was ascribed to the new end functions. This problem may come from the lack of sensitivity of ^{1}H-NMR to detect polymer end functions. Furthermore, any other routine characterization technique could give information on it. Indirect evidences of the thiol-ene modification were obtained by:

- the successful grafting of α-C$_i$,ω-NHS-P(NIPAM-co-B) derivatives on PLL. It is interesting to notice that we don't control the grafting ratio. This problem must come from the difficulty to work on polymer ends. An optimization of the chemistry involved in polymer end modifications could lead to a better control of the grafting ratio on PLL.
- a modeling of the reactivity of α-C$_i$,ω-SH-P(NIPAM-co-B) on M-COOH and M-NHS. For that purpose, the reaction between α-COOH,ω-SH-PNIPAM and a particular maleimide M* was investigated by SEC and fluorescence (Figure 35A). The singularity of this maleimide M* relies on its optical properties. Indeed, it becomes fluorescent only after reaction with thiols. The addition of α-COOH,ω-SH-PNIPAM(6) to a solution containing the maleimide M* triggered a fluorescence signal ($\lambda_{abs,\ M*}$ 385 nm, $\lambda_{em,\ M*}$ 366 nm) characteristic of activated M* (Figure 35C).On the SEC chromatogram of this reaction mixture (Figure 35B), the elution of the polymer was characterized by a signal of both UV ($\lambda_{abs,M*}$ 385 nm) and refractive index detectors (elution volume ~21 mL). These two experiments suggest that M* was covalently linked to the polymer via a thiol-ene reaction.

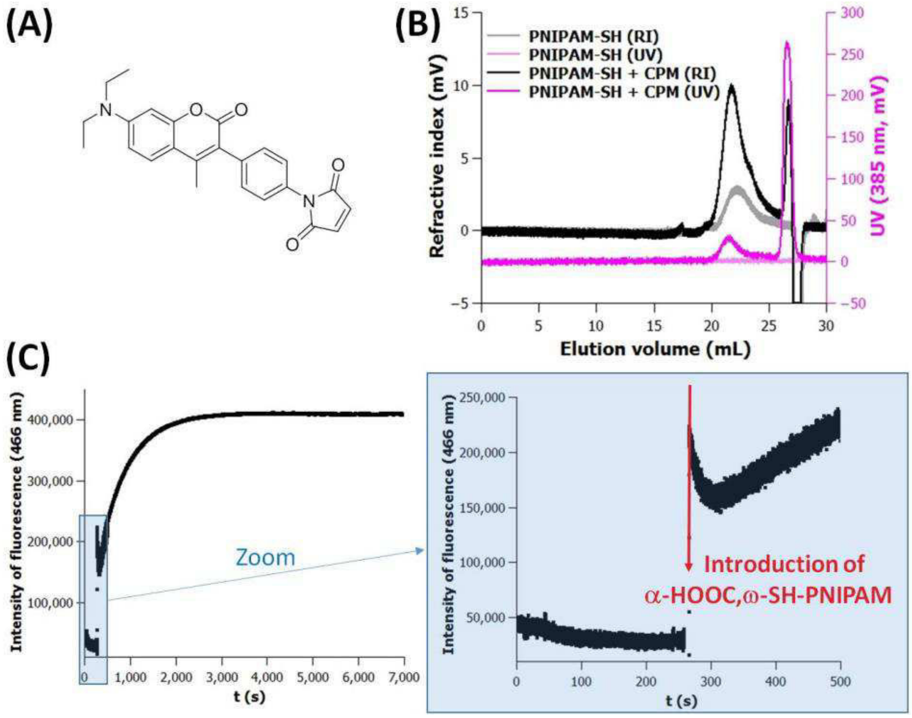

Figure 35 - (A) Chemical structure of the fluorescent-switchable maleimide M*, (B) SEC chromatograms of α-COOH,ω-SH-PNIPAM(6) in presence or in absence of M*. Elution volumes > 25 mL correspond to the elution of small molecules (M_n < 1000 g.mol^{-1}), (C) Fluorescence of a solution containing M* in DMSO upon the addition of α-COOH,ω-SH-PNIPAM(6) (λ_{exc} = 385 nm).

Maleimides were used to modify our macro-thiol because they afford stable compounds in biological conditions (Fontaine et al., 2015; Nair et al., 2014). Hydrolysis of the obtained succinimide and the reversibility of the thiol-ene reaction in presence of thiols could affect the stability of α-C_i,ω-NHS-P(NIPAM-co-B). Fortunately, these two reactions are really slow (many days) compared to the time necessary for our applications.

Conclusion

During this project, a family of PLL-g-[τ_1]A-[τ_2]α-C_i,ω-N-Butanamido-P(NIPAM-co-B)(M_n) was obtained. The versatility of the synthesis relies on the RAFT polymerization of NAS and successive post-modifications. Because the grafting ratio of α-C_i,ω-NHS-P(NIPAM-co-B) on PLL isn't completely controlled, further investigations could be done on the end modifications involved in this synthesis.

Moreover, we succeeded in synthesizing polymers corresponding to architecture 1 and 3 for the study of the ligand position (Figure 27). The synthesis of PLL-g-[0.1]α-Biotin,ω-N-Butanamido-PNIPAM(6) can't be done because we failed to obtain the corresponding Biotin-CTA (Figure 30). Indeed, it seems than Biotin-NH_2 doesn't react on NHS-CTA. As an alternative, Biotin-CTA could be obtained via a two-step synthesis (Figure 36). First, NHS-CTA should react with N_3-CH_2-CH_2-CH_2-NH_2, giving N_3-CTA. Then, Biotin-CTA could be obtained by click reaction between N_3-CTA and Biotin-BCN.

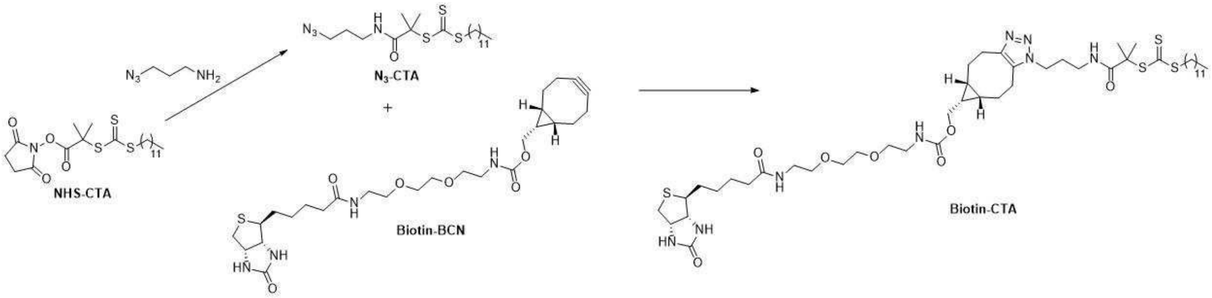

Figure 36 - An alternative synthesis of Biotin-CTA.

Bibliography

Bathfield, M., D'Agosto, F., Spitz, R., Charreyre, M.-T., and Delair, T. (2006). Versatile Precursors of Functional RAFT Agents. Application to the Synthesis of Bio-Related End-Functionalized Polymers. J. Am. Chem. Soc. *128*, 2546–2547.

Chiefari, J., Chong, Y.K. (Bill), Ercole, F., Krstina, J., Jeffery, J., Le, T.P.T., Mayadunne, R.T.A., Meijs, G.F., Moad, C.L., Moad, G., et al. (1998). Living Free-Radical Polymerization by Reversible Addition−Fragmentation Chain Transfer: The RAFT Process. Macromolecules *31*, 5559–5562.

Convertine, A.J., Lokitz, B.S., Vasileva, Y., Myrick, L.J., Scales, C.W., Lowe, A.B., and McCormick, C.L. (2006). Direct Synthesis of Thermally Responsive DMA/NIPAM Diblock and DMA/NIPAM/DMA Triblock Copolymers via Aqueous, Room Temperature RAFT Polymerization. Macromolecules *39*, 1724–1730.

Donovan, M.S., Sumerlin, B.S., Lowe, A.B., and McCormick, C.L. (2002a). Controlled/"Living" Polymerization of Sulfobetaine Monomers Directly in Aqueous Media via RAFT. Macromolecules *35*, 8663–8666.

Donovan, M.S., Sanford, T.A., Lowe, A.B., Sumerlin, B.S., Mitsukami, Y., and McCormick, C.L. (2002b). RAFT Polymerization of N,N-Dimethylacrylamide in Water. Macromolecules *35*, 4570–4572.

Eberhardt, M., Mruk, R., Zentel, R., and Théato, P. (2005). Synthesis of pentafluorophenyl(meth)acrylate polymers: New precursor polymers for the synthesis of multifunctional materials. Eur. Polym. J. *41*, 1569–1575.

Ellman, G.L. (1958). A colorimetric method for determining low concentrations of mercaptans. Arch. Biochem. Biophys. *74*, 443–450.

Favier, A., Charreyre, M.-T., Chaumont, P., and Pichot, C. (2002). Study of the RAFT Polymerization of a Water-Soluble Bisubstituted Acrylamide Derivative. 1. Influence of the Dithioester Structure. Macromolecules *35*, 8271–8280.

Feuz, L., Leermakers, F.A.M., Textor, M., and Borisov, O. (2008). Adsorption of Molecular Brushes with Polyelectrolyte Backbones onto Oppositely Charged Surfaces: A Self-Consistent Field Theory. Langmuir *24*, 7232–7244.

Fontaine, S.D., Reid, R., Robinson, L., Ashley, G.W., and Santi, D.V. (2015). Long-Term Stabilization of Maleimide–Thiol Conjugates. Bioconjug. Chem. *26*, 145–152.

Keddie, D.J., Moad, G., Rizzardo, E., and Thang, S.H. (2012). RAFT Agent Design and Synthesis. Macromolecules *45*, 5321–5342.

Kenausis, G.L., Vörös, J., Elbert, D.L., Huang, N., Hofer, R., Ruiz-Taylor, L., Textor, M., Hubbell, J.A., and Spencer, N.D. (2000). Poly(l-lysine)-g-Poly(ethylene glycol) Layers on Metal Oxide Surfaces: Attachment Mechanism and Effects of Polymer Architecture on Resistance to Protein Adsorption†. J. Phys. Chem. B *104*, 3298–3309.

Kroger, R., Menzel, H., and Hallensleben, M.L. (1994). Light controlled solubility change of polymers: copolymers of dimethylacrylamide and 4-phenylazophenyl acrylate. Macromol Chem Phys *195*, 2291–2298.

Moad, G., Chiefari, J., Chong, (Bill) YK, Krstina, J., Mayadunne, R.T.A., Postma, A., Rizzardo, E., and Thang, S.H. (2000). Living free radical polymerization with reversible addition – fragmentation chain transfer (the life of RAFT). Polym. Int. *49*, 993–1001.

Nair, D.P., Podgórski, M., Chatani, S., Gong, T., Xi, W., Fenoli, C.R., and Bowman, C.N. (2014). The Thiol-Michael Addition Click Reaction: A Powerful and Widely Used Tool in Materials Chemistry. Chem. Mater. *26*, 724–744.

Qiu, X.-P., and Winnik, F.M. (2007). Synthesis of α,ω-Dimercapto Poly(N-isopropylacrylamides) by RAFT Polymerization with a Hydrophilic Difunctional Chain Transfer Agent. Macromolecules *40*, 872–878.

Thomas, D.B., Convertine, A.J., Myrick, L.J., Scales, C.W., Smith, A.E., Lowe, A.B., Vasilieva, Y.A., Ayres, N., and McCormick, C.L. (2004). Kinetics and Molecular Weight Control of the Polymerization of Acrylamide via RAFT. Macromolecules *37*, 8941–8950.

Vasilieva, Y.A., Thomas, D.B., Scales, C.W., and McCormick, C.L. (2004). Direct Controlled Polymerization of a Cationic Methacrylamido Monomer in Aqueous Media via the RAFT Process. Macromolecules *37*, 2728–2737.

Chapter 3 - Characterizations of surfaces coated with PLL-g-PNIPAM derivatives

Contents

Introduction

In this chapter, important characteristics of PLL-g-PNIPAM adsorption are discussed (kinetics of adsorption, stability of adlayers, possibility to adsorb mixtures of PLL derivatives). Secondly, the thermal transition of PLL-g-PNIPAM coatings is described thanks to both AFM and QCM-d measurements.

1 Adsorption of PLL-g-PNIPAM on flat SiO_2 surfaces

The adsorption of PLL-g-PNIPAM derivatives on silica (SiO_2) was investigated by QCM-d and epifluorescence microscopy. These experiments were carried out with PLL-g-[0.2]PNIPAM(6). Deposition of PLL comblike chains on cleaned SiO_2 (glass coverslips and SiO_2-coated quartz crystals for respectively epifluorescence and QCM-d) spontaneously occurs from bath application of aqueous solutions of the polymer of interest (always at 1 $mg.mL^{-1}$) (see Appendix 2 for coating and patterning protocols, Appendix 3 for QCM-d).

1.1 QCM-d data on adsorption of PLL-g-PNIPAM

The kinetics of adsorption was monitored by injecting a solution of PLL-g-[0.2]PNIPAM(6) in the QCM-d cell fitted with a SiO_2-coated quartz crystal. Prior to polymer deposition (during 120 minutes), the cell was equilibrated in PBS then water was briefly flushed (Figure 37). The adsorption was triggered by the injection of the polymer solution in milliQ water (purple arrow). The polymer adsorption was revealed by a marked decrease in the resonance frequency and by an increase in dissipation. Both signals reached a plateau after less than 1 minute of incubation, suggesting that the adlayer was saturated. The cell was then rinsed successively with water and PBS (green and orange arrows). These results are similar to those obtained by Textor *et al.* on the PLL-g-PEG adsorption (Figure 23B of Chapter 1).

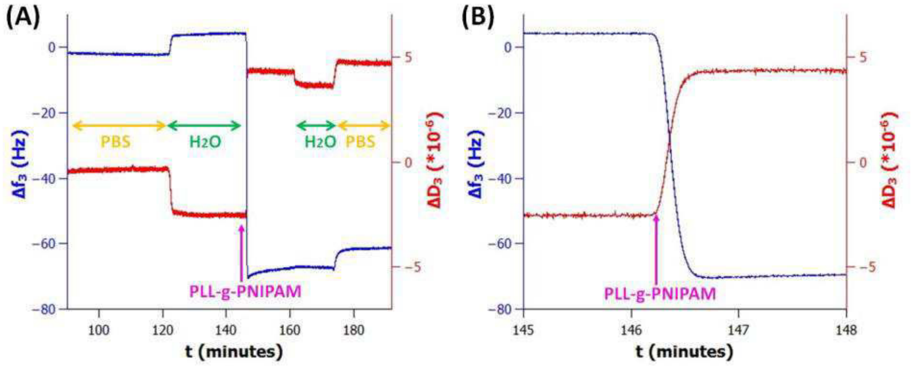

Figure 37 - QCM-d monitoring of the PLL-g-[0.2]PNIPAM(6) adsorption on SiO_2 at 25 °C. (A) Green, purple and orange arrows correspond respectively to injections of H_2O, a solution of PLL-g-[0.2]PNIPAM(6) in water (1 $mg.mL^{-1}$) and PBS. (B) Zoom between t = 145 and 148 minutes.

These data were analyzed by using a fit to a model of viscoelastic adlayers that enables to estimate some properties of the polymer layer (its thickness and viscoelastic properties, see Appendix 3). 6.1 nm, 0.0011kg/ms, and 1.1 MPa were respectively obtained for thickness, viscosity and shear modulus in PBS. It is interesting to remark that this value of thickness is close to the one measured by optical reflectometry on PLL-g-[0.2]PEG(2) coatings (DP_n ~ 50 for PEG(2) and PNIPAM(6) strands) (Table 1 of Chapter 1).

1.2 Epifluorescence data on adsorption of PLL-g-PNIPAM

To assess the control of composition in the deposited layers, coverslips were incubated with mixed solutions of PLL-g-PEG and fluorescent Alexa-labelled PLL-g-[0.2]PNIPAM(6) (name of the fluorescent polymer: PLL-g-[0.2]PNIPAM(6)*, see Appendix 1 section 4.3) in water (1 mg.mL^{-1} total concentration). Surfaces were water-rinsed, and UV-etched to form bare glass stripes used as reference for the fluorescence baseline (Figure 38A). Fluorescence intensities displayed by the pattern of stripes (Figure 38B) varied essentially in proportion to the fraction of Alexa-labeled chains present in the initial mixed coating solution. Namely, the representation of fluorescence intensity as a function of concentration in the coating solution shows values slightly below the diagonal on Figure 38C, suggesting a slightly preferential competitive adsorption of PLL-g-PEG (shift <10%, which was of the order of signal fluctuations).

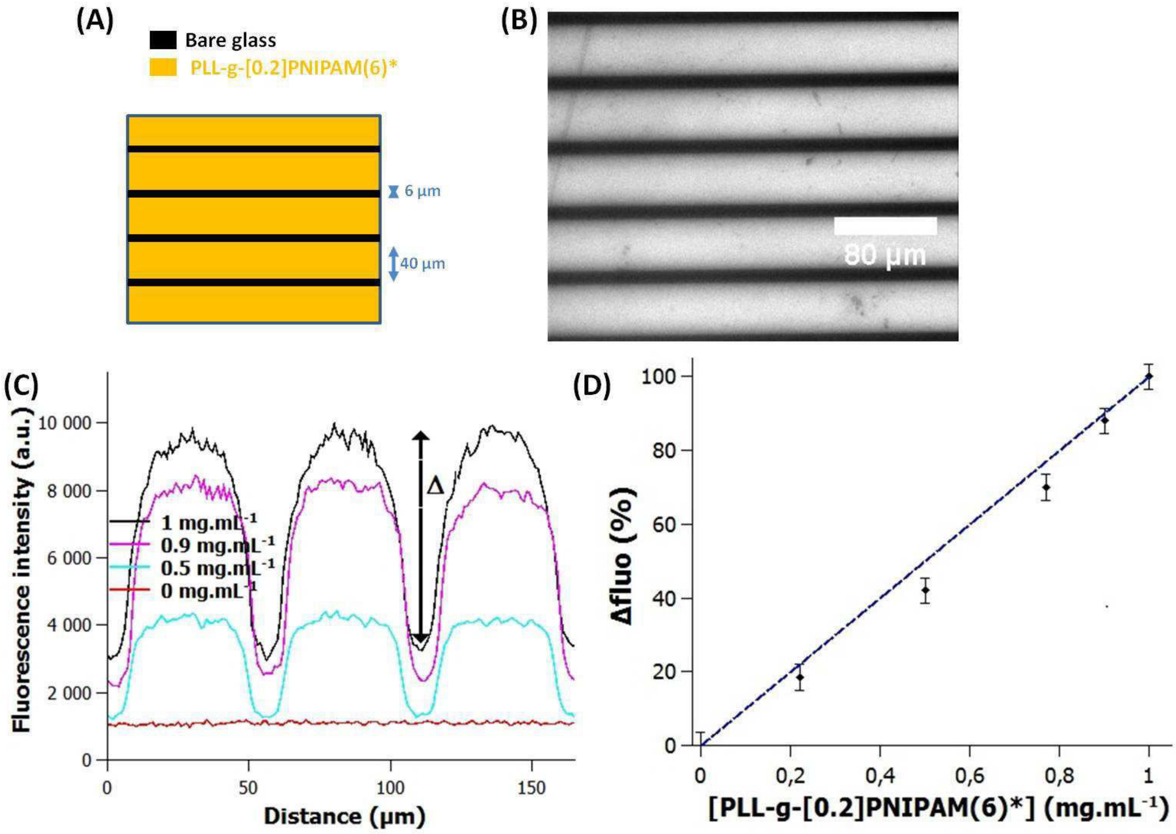

Figure 38 - Fluorescence of polymer layers deposited from mixed solutions of (PLL-g-PEG):(PLL-g-[0.2]PNIPAM(6)*) at 1 mg.mL^{-1} total concentration and varying concentration of PLL-g-[0.2]PNIPAM(6)*. (A) Representation of the glass coverslip analyzed. (B) Epifluorescence picture of such a coverslip. (C) Profiles along an axis perpendicular to UV-etched stripes (concentrations of PLL-g-[0.2]PNIPAM(6)* are indicated in the figure). (D) Difference of intensities between the etched and nonetched regions ("Δ" in (B)) normalized to 100% for pure PLL-g-[0.2]PNIPAM(6)*.

We assessed the stability of polymer layers (absence of desorption) and the absence of post-adsorption after a second exposure to PLL comb-like derivatives as follows: coverslips with large stripes of pure PLL-g-[0.2]PNIPAM(6)* and thinner of bare glass (Figure 38A) were incubated in water at different temperatures, then exposed to PLL-g-PEG or PLL-g-PNIPAM. First, the adsorbed PNIPAM layers were stable over hours-long incubation in water (no variation of fluorescence) during successive cycles of high-temperature/low-temperature incubations (Figure 39A). Second, the fluorescence of pure PLL-g-[0.2]PNIPAM(6)* stripes did not vary during incubation with a 1 mg.mL^{-1} PLL-g-PEG aqueous solution, suggesting the absence of displacement of preadsorbed PLL-g-

[0.2]PNIPAM(6)* by later addition of PLL-g-PEG (Figure 39B). Finally, incubation in PLL-g-[0.2]PNIPAM(6)* of the large stripes now coated with PLL-g-PEG showed only a weak decrease in the contrast with stripes of pure PLL-g-[0.2]PNIPAM(6)*, essentially due to an increase in fluorescence of large PLL-g-PEG stripes (Figure 39B). The weak loss of contrast after application (and rinsing out) of a solution of PLL-g-[0.2]PNIPAM(6)* indicates that the fluorescent polymer did not significantly displace preformed layers of PLL-g-PEG. Altogether, these results show that controlled composition of mixed adlayers are achieved, and that these layers are stable to rinsing and further contacts with other grafted PLL copolymers. This stability reflects the tight coulomb adsorption of PLL on glass, and high repulsion barrier against diffusion/penetration in the adlayer once they are formed.

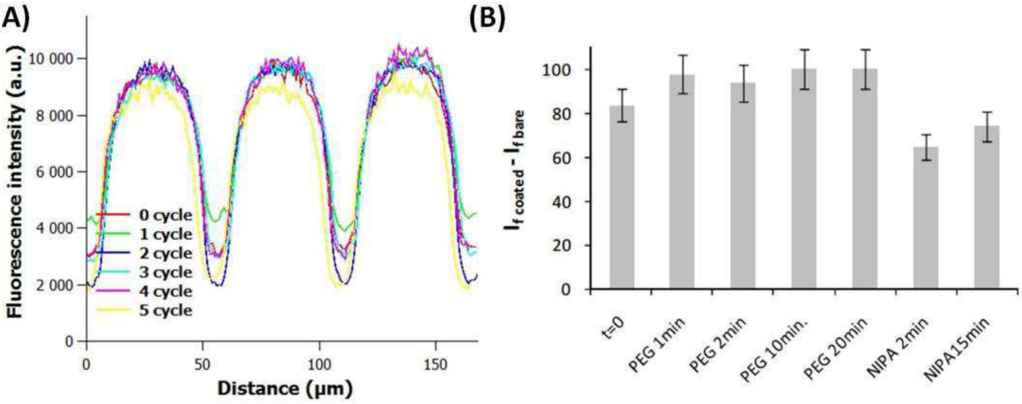

Figure 39 - Fluorescence of a glass coverslip functionalized with patterns of PLL-g-[0.2]PNIPAM(6)* as represented on Figure 38A. Profiles of fluorescence intensities were measured by epifluorescence microscopy along a line orthogonal to the stripes. (A) Coverslip subjected from 0 to 5 successive cycles of temperature switches (in one cycle, the coverslip was immersed in water at 45 °C for 2-3 min., then observed in water at 25 °C) (B) after application of a solution of PLL-g-PEG (1 mg.mL^{-1}) for increasing incubation times ($I_{f\ coated}$ - $I_{f\ bare}$ is the difference between fluorescence intensities of the large stripes and thin ones, normalized by the maximum value measured in the data set). Upon exposure to PLL-g-PEG, the bare stripes were coated with PLL-g-PEG. They were rinsed with water, and incubated in an aqueous solution of 1 mg.mL^{-1} PLL-g-[0.2]PNIPAM(6)* for 2 minutes (NIPA 2min) and 15 minutes (NIPA 15 min).

2 Thermal transition of PLL-g-PNIPAM coatings

PNIPAM is the most studied thermo-responsive polymer. Its phase transition in aqueous solution is well known and characterized (see Appendix 3). Above a threshold temperature, PNIPAM undergoes "coil-to-globule" conformational change. At low temperatures, PNIPAM chains are extended and flexible, while they become partially dehydrated and they collapse above the threshold temperature named cloud point, leading to PNIPAM precipitation via hydrophobic interchain aggregation. More details on this transition are given in Appendix 3. We studied here the transition of PNIPAM derivatives in solution by turbidimetry (see protocol in Appendix 3), or on glass surfaces by QCM-d (Appendix 3). When PLL-g-PNIPAM are adsorbed on glass, the change in conformation between hydrated coil to collapsed dehydrated globule is expected to decrease significantly the layer thickness and to affect several surface properties (wettability, rigidity, surface roughness, ...). The observation of such surface transitions are commonly characterized in the literature by contact angle measurements (Takei et al., 1994), dynamic light scattering on suspensions of PNIPAM-coated particles (Zhu and Napper, 1996), surface plasmon resonance (Balamurugan et al., 2003), neutron reflectivity (Yim et al., 2003, 2004, 2005, 2006), quartz crystal microbalance (Ishida and Biggs, 2007, 2010; Liu and Zhang, 2005), surface force apparatus (Plunkett et al., 2006), and AFM (Kidoaki et al., 2001).

The parameters modulating the temperature of transition of PNIPAM brushes on surfaces are well described, although possible impact of the attachment chemistry and/or surface chemistry are not entirely elucidated. Significant shifts of the transition temperature have been reported with variations of chain density and molecular weight (Choi et al., 2013; Xue et al., 2011; Yim et al., 2006). Choi *et al.* deduced a trend based on these two parameters as represented on Figure 40 (Choi et al., 2013). For dense and long PNIPAM chains, a homogeneous vertical phase transition occurs (Figure 40D-E). For short PNIPAM chains or highly diluted films, chains are expected to collapse under globule (Figure 40B). However, no experimental evidence of collapsed globules was acquired. At intermediate thicknesses of the PNIPAM films, inhomogeneities (called "Octopus micelle" by B.-C. Choi) appears above the critical temperature (i.e. vertical and lateral phase transition, Figure 40C).

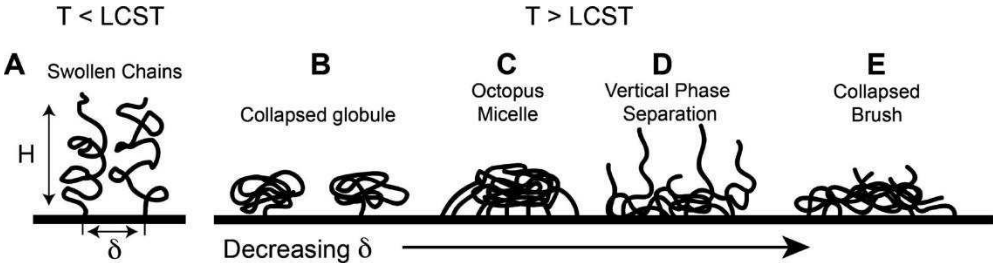

Figure 40 - Effect of the chain grafting on the PNIPAM transition (Choi et al., 2013).

In order to specify better the regime of transition corresponding to PLL-g-PNIPAM layers, we complemented measurements of transition temperatures by observations of the phase transition by AFM. These measurements were performed by F. Eghiaian (Aix-Marseille Université - Bio-AFM-Lab). Analysis of QCM-d data (with the help of G. Dubacheva (ENS Cachan - PPSM)) gave additional information on the layer properties. In the following paragraph, the transition will be discussed exclusively on PLL-g-[0.2]PNIPAM(6) coatings.

2.1 AFM data on thermal transition of PLL-g-PNIPAM coatings

Morphological changes and variation of rigidity of the deposited PNIPAM layers were investigated by *in situ* AFM in PBS buffer. A special tapping mode, PeakForce Quantitative Nanoscale Mechanical (QNM) mode®, was used to map and distinguish between nanomechanical properties (including modulus, adhesion, dissipation and deformation) while simultaneously imaging sample topography (see Appendix 3 for conditions of measurements and information about QNM mode).

First, the change in thickness of the PLL-g-[0.2]PNIPAM(6) layer was evaluated by recording topographic profiles at increasing temperature across PNIPAM-coated stripes and bare glass ones (Figure 41A-D). In tapping mode, the applied load compresses the soft polymer layer during the acquisition. Consequently, deformation was taken into account to calculate a corrected (uncompressed) thickness values for the PNIPAM layer. Referred to the average level of bare glass, the average height above PLL-g-PNIPAM layer decreased from 3.6 to ∼ 2.2 nm with increasing the temperature from 26 to 33 °C (Figure 41B). Variation of layer thickness by a factor of 1.6 corresponds to usual PNIPAM collapse transition (Yim et al., 2006).

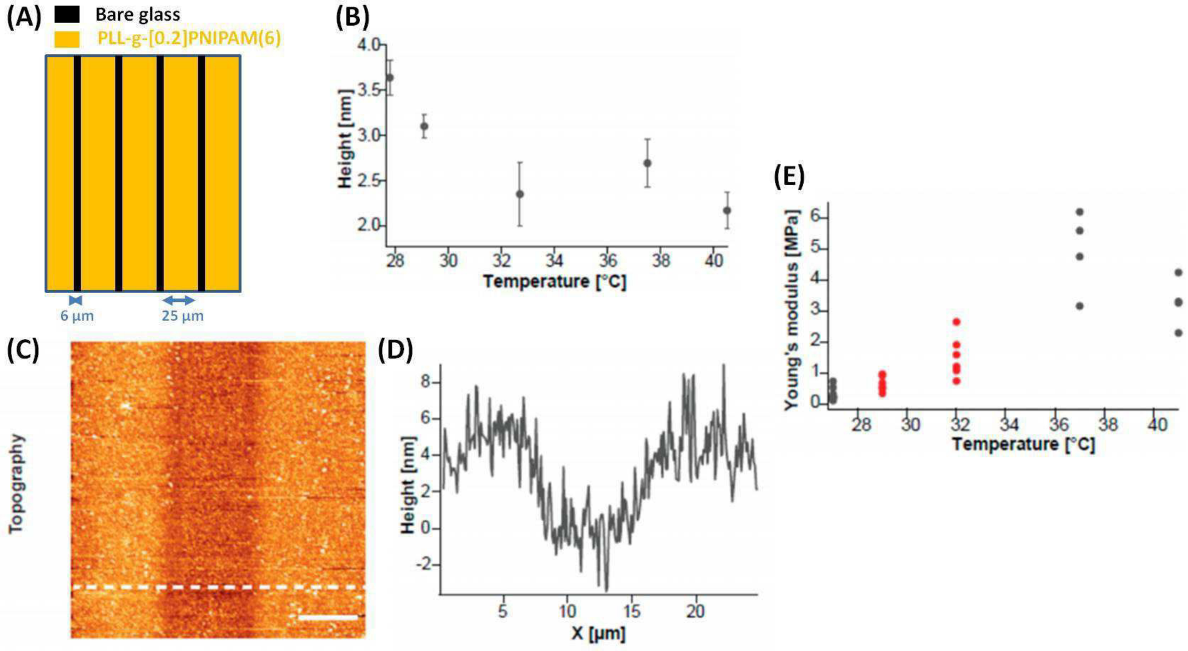

Figure 41 - *In situ* AFM measurements (Peak-Force QNM mode) of PLL-g-[0.2]PNIPAM(6) on a patterned glass surface in PBS buffer as represented in (A). (B) Height relative to bare glass, (C) topographic image (full colors scale: 20 nm, scale bar: 5 µm), (D) height profile along the dash white line. Error bars in B represent the width of the fit of data to a Gaussian distribution. (E) Rigidity modulus evaluated on ten different spots of PLL-g-[0.2]PNIPAM(6) stripes for each temperature. Each point of the graph corresponds to one measurement. Data points in grey were collected going from low to high temperatures while red points were collected going from high to low temperatures.

Topographic AFM images displayed surface roughness with protrusions having sub-micrometer lateral length scale (Figure 42). Vertically, these heterogeneities were observed at any temperature, but were weak at low temperatures (± 0.5 nm at 26 °C) and prominent at high temperatures (± 9-10 nm at 37°C). At high temperatures, vertical heterogeneities became of the same order of magnitude than the average PNIPAM thickness, suggesting that bare glass may be accessible at high temperature between these protrusions (see Figure 41B and Figure 42). The lateral size of protrusions ranged from 10 to 80 nm, which is considerably larger than dimension of an isolated PLL-g-PNIPAM chain. It is likely that these heterogeneities correspond to lateral aggregation of dehydrated PNIPAM at high temperatures. The apparition of such features on PNIPAM layers above the phase transition was previously reported as Octopus micelles (Benetti et al., 2007; Choi et al., 2013; Ishida and Biggs, 2007, 2010; Zhao et al., 1994).

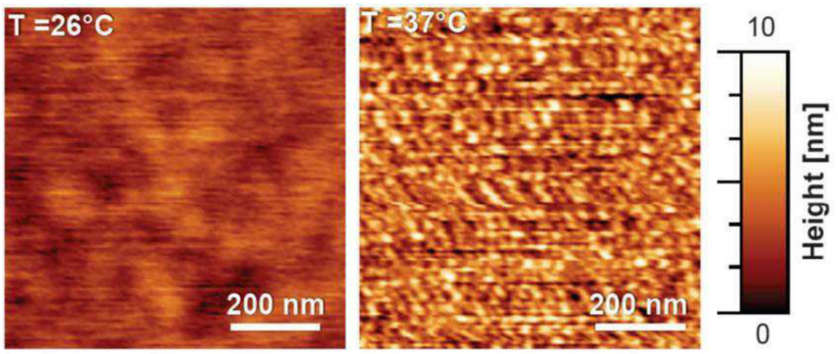

Figure 42 - PeakForce-QNM AFM topographs of a homogeneous PLL-g-[0.2]PNIPAM(6) coating in PBS Buffer at 26 °C (left) and 37 °C (right).

Morphological changes at high temperatures were accompanied by the increase in the apparent Young's modulus of the PNIPAM layer (Figure 41E) by 1 order of magnitude between 27 and 37 °C.

Finally, we scanned surfaces alternating PLL-g-PEG and PLL-g-[0.2]PNIPAM(6) stripes. Topographic scans indicate that the two layers have a similar height at low T considering AFM resolution on PLL coatings (± 0.5 nm). To investigate the influence of the temperature, adhesion maps (Figure 43, see Appendix 3 for more details on adhesion) were recorded. The two polymer layers developed similar repulsive interactions with the AFM tip at low temperature (27 °C). At 37 °C, PNIPAM patterns were revealed due to adhesive interactions with the AFM tip while the PEG layer remained repulsive in average (attractive spots appearing, but they exhibited significantly weaker attraction than above the NIPAM-coated regions). Force-distance curves were acquired on PLL-g-PNIPAM patterns (Figure 44). Namely, upon advancing the tip toward the PNIPAM-containing adlayer ("extension" in Figure 44), predominant repulsive interactions increased while decreasing distance from the surface, independently of the temperature. We assumed somewhat arbitrarily that tight compression of the layer (tip-substrate contact-like conditions) was reached at a force of repulsion of ~ 100 pN. Retraction of the tip was accordingly started at the 100 pN threshold, which was defined as the zero, contact-like distance from the glass substrate. At low temperatures, repulsions could be measured for tip-substrate distances up to ~ 5 nm (Figure 44, left), and vanished beyond 5nm. This characteristic distance corresponds to the order of the PLL-g-PNIPAM thickness, suggesting that repulsive interaction comes from steric hindrance between AFM tip and PNIPAM brushes. Interestingly, attractive interactions appeared at 37 °C in retraction curves, with adhesion strengths reaching 100 pN (Figure 44, right). We propose that attractions at high temperatures are due to hydrophobic interactions between the AFM tip and dehydrated PNIPAM chains. Measurements of extension/retraction force-distance curves on the same spot, were repeatable, suggesting that the layer was preserved (not irreversibly damaged) in the experimental conditions of compression.

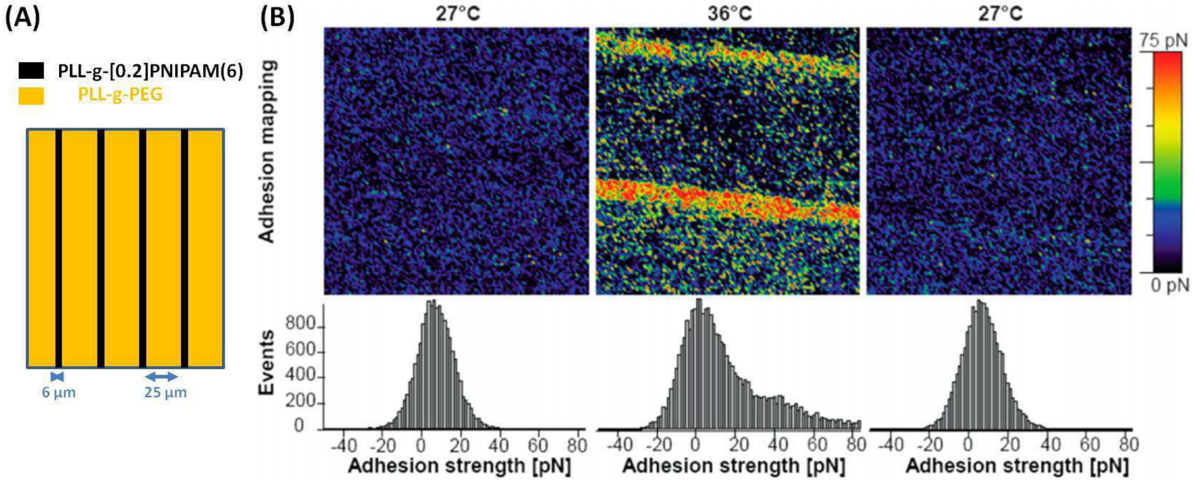

Figure 43 - PeakForce-QNM adhesive maps (B) and their corresponding distribution of forces on surface (A) in PBS Buffer. Temperature was successively set at 27 °C, 36 °C and then back at 27 °C.

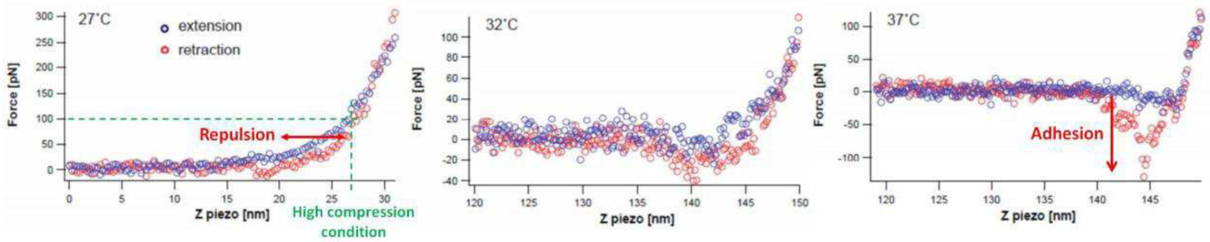

Figure 44 - AFM approaching and retraction forces above PLL-g-[0.2]PNIPAM(6) layer initially equilibrated in PBS at 27°C (left), then heated up to the temperature quoted in figures.

Changes detected by AFM (i.e. change in thickness, roughness, rigidity and adhesion) upon increasing the temperature from 26°C to 37°C were reversibly relaxed back to their initial characteristics by decreasing temperature down to 26 °C. These are evidences for reversible phase transition of PNIPAM in the PLL-g-PNIPAM adlayer.

2.2 QCM-d data on thermal transition of PLL-g-PNIPAM coatings

Further information on the transition of PLL-g-PNIPAM coatings can be obtained thanks to QCM-d measurements. *In situ* QCM-d enables to study properties of the PNIPAM layer without exerting mechanical stress contrary to AFM measurements. In addition, a kinetic monitoring of the transition can be achieved with this technique.

2.2.1 Description of the experiment

Thermal transition in PLL-g-[0.2]PNIPAM(6) adlayers was investigated by QCM-d in PBS buffer. A quartz crystal with a thin SiO_2 layer on its top was coated with PLL-g-[0.2]PNIPAM(6) using the same procedure as described in Appendix 2. The cell was rinsed with the aqueous buffer (PBS 1x). The resonance frequency and the dissipation factor were recorded continuously while imposing a temperature sweep between 19 °C and 49 °C (Figure 45). Namely, we recorded the shift of frequency (Δf) and dissipation factor (ΔD) during temperature increases “step-by-step” (with steps of 2 °C maintained for 20 minutes each), and decreases in the same stepwise manner. We focused on the third overtone (Δf_3 and ΔD_3) because every overtone gave a similar trend. The change in temperature induced variations of frequency and dissipation factor that reached a plateau after 15 minutes (Figure 45B). The qualitative analysis of values taken by these two signals at their plateaus enables us to detect the phase transition of the PNIPAM brushes.

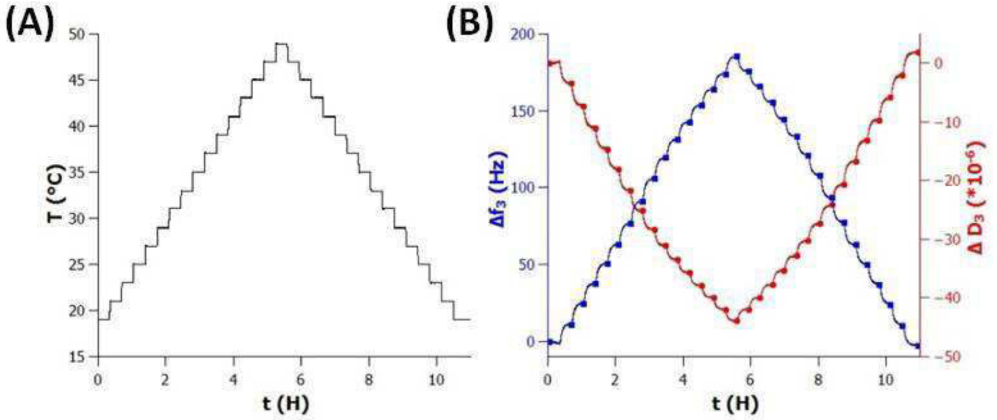

Figure 45 - QCM-d measurements on a quartz crystal coated with PLL-g-[0.2]PNIPAM(6) in PBS: (A) "step-by-step" temperature ramp, (B) (━ Δf_3) frequency and (━ ΔD_3) dissipation shifts of the third overtone where blue and red circles represent their plateau values.

2.2.2 Results

2.2.2.1 Measurements on bare crystal

To analyze the data, it is important to substrate the effects of changes in temperature of viscosity and density of the buffer. Consequently, in order to distinguish the specific contribution of the PNIPAM layer from the thermal response due to other side factors, we recorded blank data by submitting the bare crystal to the same temperature cycle. Thermal dependencies of frequency and dissipation factor are represented in Figure 46.

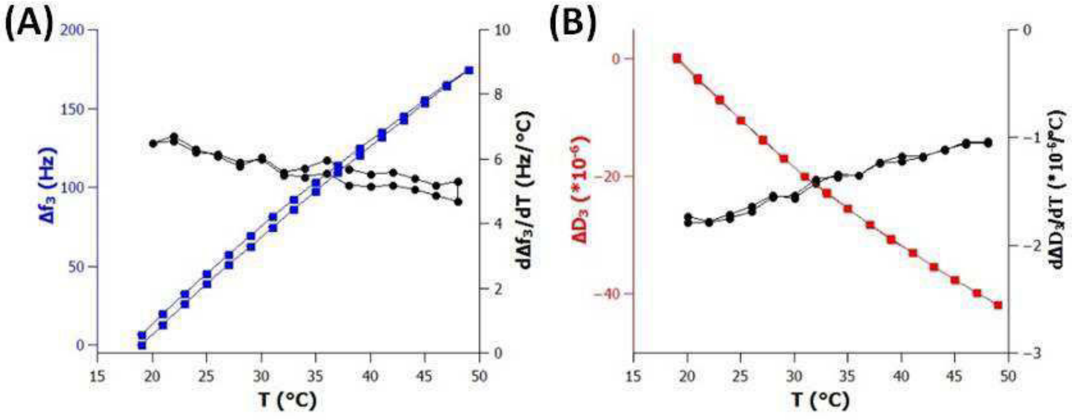

Figure 46 – Frequency (A) and dissipation factor (B) temperature dependencies of a bare quartz crystal measured from QCM-d measurements in PBS buffer over the "step-by-step" temperature cycle. The corresponding derivatives are represented in black.

According to the Figure 46B, upon heating from 19 °C to 49 °C, ΔD_3 dissipation index decreases linearly with temperature as it's underlined by its constant derivative $\frac{d\Delta D_3}{dT}$. As expected, when temperature came back to 19 °C, the dissipation index recapitulates the same value than during the increasing T-sweep. The frequency behavior is a little bit different from dissipation factor (Figure 46B). In fact, Δf_3 increased linearly with temperature ($\frac{d\Delta f_3}{dT}$ can be considered as constant on the analyzed temperature windows).

According to the Kanazawa-Gordon's model (Kanazawa and Gordon, 1985), the frequency and dissipation response of a quartz crystal immerged in a Newtonian liquid can be quantitatively described by the following equations 1 and 2:

$$\Delta f = -n^{\frac{1}{2}} f_0^{\frac{2}{3}} \left(\frac{\eta_1 \rho_1}{\pi \mu_q \rho_q}\right)^{\frac{1}{2}} \tag{1}$$

$$\Delta D = 2\left(\frac{f_0}{n}\right)^{\frac{1}{2}} \left(\frac{\eta_1 \rho_1}{\pi \mu_q \rho_q}\right)^{\frac{1}{2}} \tag{2}$$

$$\eta_1 = (1.68 - 0.024T)10^{-3} \tag{3}$$

$$\rho_1 = 1004 - 0.3T \tag{4}$$

where ρ_q and μ_q are the density and shear modulus of quartz, and ρ_1 and η_1 are the density and viscosity of the liquid medium, respectively. n is the overtone number, and f_0 is the fundamental resonance frequency (n = 1). Equation 3 and 4 represent the influence of temperature on water viscosity and density over our temperature range (with T in °C) (Laloyaux et al., 2010). Moreover, the intrinsic frequency f_0 of the quartz depends on temperature. Indeed, by acquiring the response of the bare crystal in air, we observed a linear increase in frequency with a magnitude of 40 Hz by heating from 19 to 49 °C while dissipation factor kept constant.

2.2.2.2 Measurements on crystal coated with PLL-g-PNIPAM

- ***Phase transition emphasis***

In Figure 47, we have superimposed responses of both bare and PLL-g-PNIPAM coated quartz to the heating ramp. For the two crystals, frequency increased with temperature while dissipation decreased. However, a slight deviation from the linear variation was detected for the coated crystal, providing a sign of the PNIPAM phase transition on the sensor surface. This slight deviation from the linearity can be more easily visualized on frequency and dissipation derivative plots (Figure 47B). Indeed, PLL-g-PNIPAM coated quartz shows a maximum at 32 °C ($T_{\Delta f}$) and a minimum at 30 °C ($T_{\Delta D}$) for respectively frequency/dissipation derivatives whereas these derivatives are varying weakly, and monotonously for uncoated crystal.

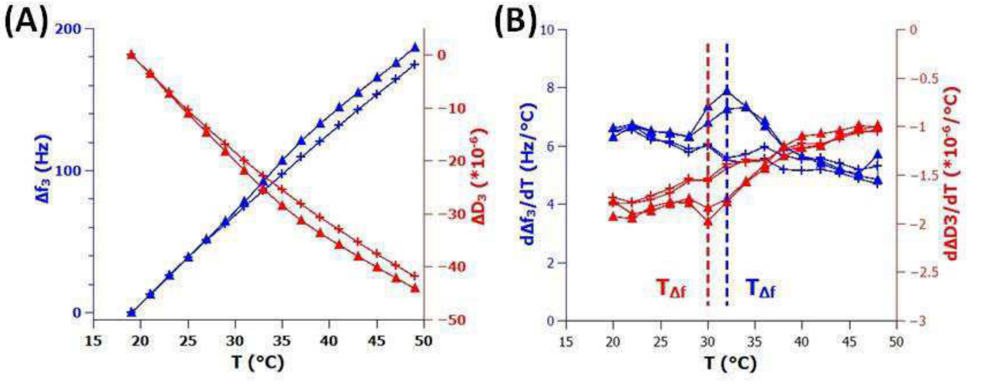

Figure 47 – Comparison of the QCM-d acquisition for bare quartz crystal (cross) and PLL-g-PNIPAM coated crystal (triangle) in PBS buffer over a "step-by-step" temperature ramp.

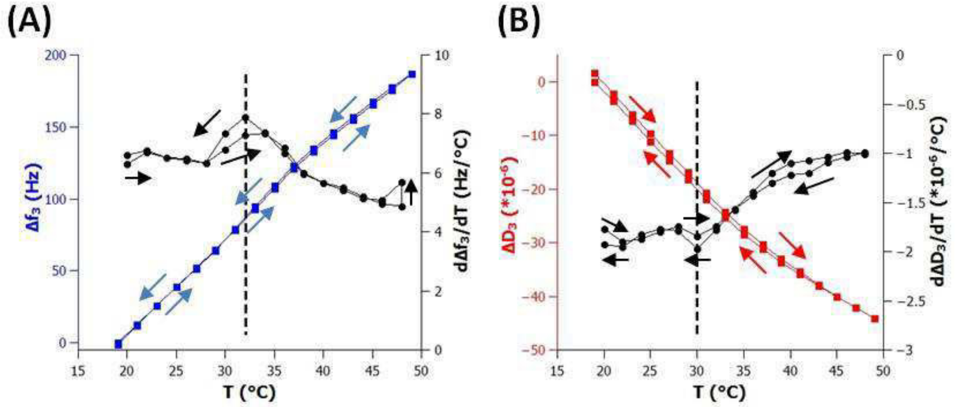

Figure 48 - Frequency (A) and dissipation (B) shifts of PLL-g-PNIPAM coated quartz crystal monitored by QCM-d in PBS buffer over the "step-by-step" temperature cycle. Their respective derivatives are represented in black and the vertical crossed line indicates their extrema. Arrows indicate the increase/decrease in temperature.

- ***Interpretation of the phase transition***

On Figure 47 (Figure 48A), we can see that an obvious increase in the slope of variation of the frequency starts above 29 °C. The derivative $\frac{d\Delta f_3}{dT}$ recovers its almost linear, slow decreasing variation above 35-36 °C which indicates that the polymer layer evolves significantly in the corresponding 6 °C temperature window. The maximum of variation being reached at 32°C is close to LCST of PNIPAM in solution. The increase in frequency during the heating process can be explained by the release of water from the polymer film when PNIPAM brushes become hydrophobic, which decreases the effective layer mass.

On the same manner, in Figure 47 (Figure 48B), the derivative of dissipation factor is initially increasing with T, and becomes abruptly decreasing above 27 °C to recover its initial trend above 35 °C. The minimum of this derivative in Figure 47B (Figure 48B) is reached at 30 °C. This means that the PNIPAM layer transition causes a decrease in dissipation factor, suggesting that collapsed PNIPAM forms a more rigid layer upon heating. This is in agreement with AFM measurements of Young's modulus. An alternative representation of the same measurements is shown in Figure 49B that displays the temperature derivatives of the difference between PNIPAM-coated and bare crystals ($\frac{d\Delta f_{3Norm}}{dT}$, $\frac{d\Delta D_{3Norm}}{dT}$).

According to frequency and dissipation results, two different temperatures corresponding to the peak/valley values ($T_{\Delta f}$ and $T_{\Delta D}$) may be defined for PNIPAM transition. In practice, the difference between $T_{\Delta f}$ and $T_{\Delta D}$ depended on the scan rate (it became lower than 1°C when equilibration steps of 40 minutes were used instead of 20 minutes). Equilibration times of longer than a few minutes are extremely long compared to conformational transition of PNIPAM chains in solution (millisecond time scale). It is likely that thermal inertia of the cell slows the kinetics of temperature homogenization, which affects the measurement of the rate of transition.

Characteristics of the phase transition

Amplitude of the phase transition

In Figure 49, plots of QCM-d signal differences between coated and uncoated crystals ($\Delta f_{3\text{-diff}}$, $\Delta D_{3\text{-diff}}$) enable us to appreciate the amplitude of the phase transition. Amplitudes of 12 Hz for frequency and 3.10^{-6} for dissipation factor were measured which is superior to the QCM-d detection limit. But, these values are actually weak compared to known surface-attached PNIPAM analyzed by QCM-d. Here, we work on thinner PNIPAM layers compared to the literature. For example, Liu *et al.* measured an amplitude of 60 Hz for frequency and 5.10^{-6} for dissipation factor while they worked on 41nm-thick PNIPAM coating (Liu and Zhang, 2005). Ishida *et al.* shown that the magnitude of the phase transition detected by QCM-d is proportional to the PNIPAM density (Ishida and Biggs, 2010). They worked on three PNIPAM brushes of same molecular weight (197 000 g/mol) but with grafting densities ranging from 0.015 to 0.337 grafts/nm². While the low density surface shows small amplitudes (30 Hz and 10.10^{-6}), a marked response was recorded on the high density substrate (2000 Hz and 180.10^{-6}).

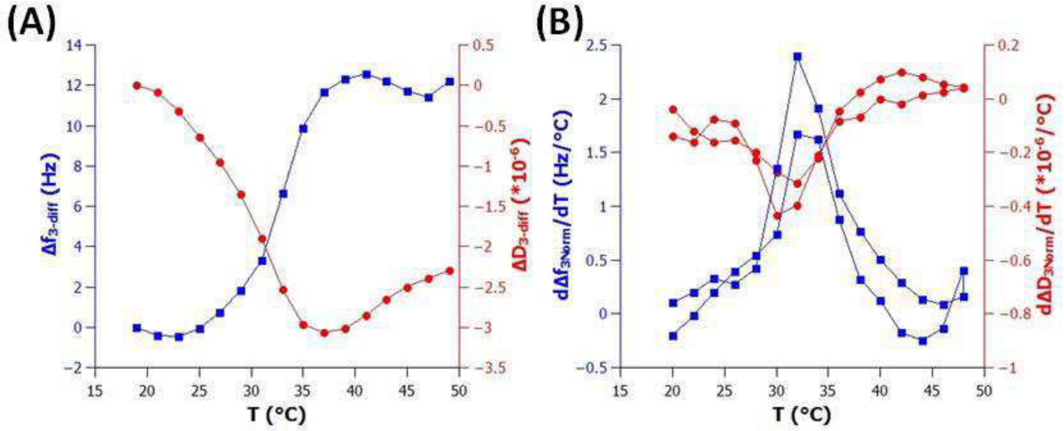

Figure 49 - (A) Temperature dependence of frequency (blue) and dissipation (red) between bare and PLL-g-[0.2]PNIPAM(6) coated quartz crystal deduced from QCM-d measurements in PBS buffer over the "step-by-step" temperature heating. (B) Derivatives of dissipation and frequency between bare and PLL-g-[0.2]PNIPAM(6) coated quartz crystal.

Reversibility of the phase transition

Dissipation and frequency curves as function of increasing and decreasing temperature sweeps in Figure 48 show no obvious hysteresis. The polymer transition of thin PLL-g-PNIPAM layer is essentially reversible. This result is surprising because hysteresis is generally reported for studies on tethered-PNIPAM transition as studied by QCM-d (Annaka et al., 2007; Liu and Zhang, 2005) and SPR (Balamurugan et al., 2003). The intra-chain and inter-chain interactions formed in the collapsed state can explain it. In our case, we propose that more uniform and more rapidly dissociated clusters of polymer are formed in the film due to 1) the relatively shorter PNIPAM strands compared to literature, 2) a degree of translational flexibility in the PLL-anchored adsorbed layer (compared to usual covalent binding).

Moreover, as frequency takes the same value at the beginning and at the end of the temperature cycle, we can consider that the mass of the layer on the top of the crystal is not modified by the transition. There is no desorption of PLL-g-PNIPAM during the reswelling of PNIPAM brushes. This is an important result for applications. Moreover, it confirms fluorescence characterizations of the robustness of non-covalently grafted PNIPAM brushes onto the quartz (see paragraph 1.2).

The reversibility over five consecutive temperature jumps above and below the transition temperature was investigated, and the corresponding acquisition is reported in Figure 50. For every temperature jump, both frequency and dissipation energy show a repeatable response: this proves the stability of this polymer film.

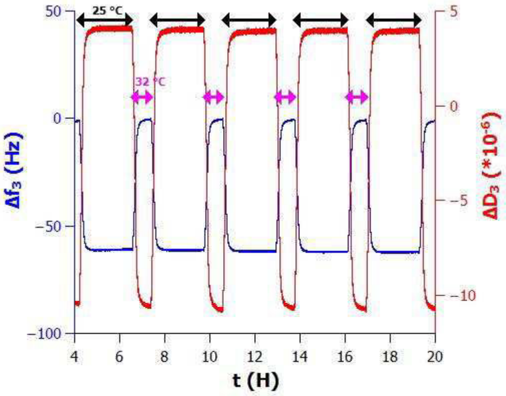

Figure 50 – Responses of a PLL-g-PNIPAM coated quartz crystal subjected to 5 consecutive temperature jumps between 25 and 32 °C in PBS as monitored by QCM-d.

Sharpness of the phase transition

Considering the change in the temperature derivative of frequency (Figure 47), PNIPAM transition occurs between 29 and 35 °C. But, this window is presumably smaller because thermal inertia of the QCM-d cell does not enable accurate determination until hours-long steps of equilibration is conducted. The transition of the same polymer in solution was investigated by turbidimetry (Appendix 3) and shows a sharper transition. Differences of behavior between the polymer in solution and tethered on a surface have been previously reported (Annaka et al., 2007; Balamurugan et al., 2003; Ishida and Biggs, 2010; Laloyaux et al., 2010; Liu and Zhang, 2005). The non-uniformity and stretching of dense PNIPAM brushes as well as the cooperativity between collapse and dehydration transitions are thought to be responsible for enlargement of the transition temperature range.

Conclusions and discussion on thermal transition of PLL-g-PNIPAM adlayers

The results presented in this chapter give a coherent insight on the collapse/swelling transition steps of the PLL-anchored polymer films. In summary, below the threshold transition temperature, dissipation factor is first affected by an increase in temperature, which can be interpreted as a rearrangement of inter-PNIPAM or PNIPAM:water interactions (increase in the effective viscosity in/or just above the layer). The onset of frequency variation occurs in a second stage (typically at temperature 1-2 °C above the dissipation one). This can be explained by the fact that conformational rearrangements occur at larger length scales than the one probed by dissipation factor at MHz frequencies. In the intermediate temperatures (window of less than 6°C), both dissipation and Young's modulus gradually evolve and haven't still reached their final value. This suggests that PNIPAM clusters are slowly rearranging with the increase in hydrophobicity of PNIPAM at increasing T. When dissipation and frequency variations become again linear (above 35 °C), we suggest that the PNIPAM layer has reached its maximum state of dehydration. As AFM pictures show nanometer-large and rigid clusters formed at high temperatures, we can attribute this conformational rearrangement to the initial stages of the PNIPAM lateral motions and inter-chain assemblies. These rearrangements are fully reversible. In PBS buffer and in water, the coulomb binding between PLL and the surface appears extremely robust to temperature cycles, and resists to competitive adsorption of other PLL-based comblike copolymers.

Finally, the temperature of transition was equal to that of PNIPAM homopolymer in solution and was not affected by adsorption of the PLL backbone. This is presumably due to the blocky nature of PNIPAM macrografts, and a relative orientation of PNIPAM strands toward the aqueous solution (absence of association with the surface). One advantage of the present design of PLL-g-PNIPAM is that possible effect of ligands or comonomers on the temperature of response can be adjusted at the stage of the PNIPAM macrograft synthesis, prior to attachment on PLL, in order to tune the temperature of response. For instance, introduction of hydrophobic (respectively hydrophilic) moieties can be used to balance ligands hydrophilicity (respectively hydrophobicity).

Bibliography

Annaka, M., Yahiro, C., Nagase, K., Kikuchi, A., and Okano, T. (2007). Real-time observation of coil-to-globule transition in thermosensitive poly(N-isopropylacrylamide) brushes by quartz crystal microbalance. Polymer *48*, 5713–5720.

Balamurugan, S., Mendez, S., Balamurugan, S.S., O'Brie, M.J., and López, G.P. (2003). Thermal Response of Poly(N-isopropylacrylamide) Brushes Probed by Surface Plasmon Resonance. Langmuir *19*, 2545–2549.

Benetti, E.M., Zapotoczny, S., and Vancso, G.J. (2007). Tunable Thermoresponsive Polymeric Platforms on Gold by "Photoiniferter"-Based Surface Grafting. Adv. Mater. *19*, 268–271.

Choi, B.-C., Choi, S., and Leckband, D.E. (2013). Poly(N-isopropyl acrylamide) Brush Topography: Dependence on Grafting Conditions and Temperature. Langmuir *29*, 5841–5850.

Ishida, N., and Biggs, S. (2007). Direct Observation of the Phase Transition for a Poly(N-isopropylacryamide) Layer Grafted onto a Solid Surface by AFM and QCM-D. Langmuir *23*, 11083–11088.

Ishida, N., and Biggs, S. (2010). Effect of Grafting Density on Phase Transition Behavior for Poly(N-isopropylacryamide) Brushes in Aqueous Solutions Studied by AFM and QCM-D. Macromolecules *43*, 7269–7276.

Kanazawa, K.K., and Gordon, J.G. (1985). Frequency of a quartz microbalance in contact with liquid. Anal. Chem. *57*, 1770–1771.

Kidoaki, S., Ohya, S., Nakayama, Y., and Matsuda, T. (2001). Thermoresponsive Structural Change of a Poly(N-isopropylacrylamide) Graft Layer Measured with an Atomic Force Microscope. Langmuir *17*, 2402–2407.

Laloyaux, X., Mathy, B., Nysten, B., and Jonas, A.M. (2010). Surface and Bulk Collapse Transitions of Thermoresponsive Polymer Brushes. Langmuir *26*, 838–847.

Liu, G., and Zhang, G. (2005). Collapse and Swelling of Thermally Sensitive Poly(N-isopropylacrylamide) Brushes Monitored with a Quartz Crystal Microbalance. J. Phys. Chem. B *109*, 743–747.

Plunkett, K.N., Zhu, X., Moore, J.S., and Leckband, D.E. (2006). PNIPAM Chain Collapse Depends on the Molecular Weight and Grafting Density. Langmuir *22*, 4259–4266.

Takei, Y.G., Aoki, T., Sanui, K., Ogata, N., Sakurai, Y., and Okano, T. (1994). Dynamic Contact Angle Measurement of Temperature-Responsive Surface Properties for Poly(N-isopropylacrylamide) Grafted Surfaces. Macromolecules *27*, 6163–6166.

Xue, C., Yonet-Tanyeri, N., Brouette, N., Sferrazza, M., Braun, P.V., and Leckband, D.E. (2011). Protein Adsorption on Poly(N-isopropylacrylamide) Brushes: Dependence on Grafting Density and Chain Collapse. Langmuir *27*, 8810–8818.

Yim, H., Kent, M.S., Huber, D.L., Satija, S., Majewski, J., and Smith, G.S. (2003). Conformation of End-Tethered PNIPAM Chains in Water and in Acetone by Neutron Reflectivity. Macromolecules *36*, 5244–5251.

Yim, H., Kent, M.S., Mendez, S., Balamurugan, S.S., Balamurugan, S., Lopez, G.P., and Satija, S. (2004). Temperature-Dependent Conformational Change of PNIPAM Grafted Chains at High Surface Density in Water. Macromolecules *37*, 1994–1997.

Yim, H., Kent, M.S., Satija, S., Mendez, S., Balamurugan, S.S., Balamurugan, S., and Lopez, G.P. (2005). Evidence for vertical phase separation in densely grafted, high-molecular-weight poly(N-isopropylacrylamide) brushes in water. Phys. Rev. E *72*, 051801.

Yim, H., Kent, M.S., Mendez, S., Lopez, G.P., Satija, S., and Seo, Y. (2006). Effects of Grafting Density and Molecular Weight on the Temperature-Dependent Conformational Change of Poly(N-isopropylacrylamide) Grafted Chains in Water. Macromolecules *39*, 3420–3426.

Zhao, W., Krausch, G., Rafailovich, M.H., and Sokolov, J. (1994). Lateral Structure of a Grafted Polymer Layer in a Poor Solvent. Macromolecules *27*, 2933–2935.

Zhu, P.W., and Napper, D.H. (1996). Interfacial coil-to-globule transitions: the effects of molecular weight. Colloids Surf. Physicochem. Eng. Asp. *113*, 145–153.

Chapter 4 - Temperature-controlled ligand accessibility in PLL-g-PNIPAM coatings

Contents

Introduction

The aim of the study developed in this chapter is to demonstrate that PLL-g-PNIPAM adlayers enable to obtain a contrast of ligand accessibility when a ligand is covalently attached to the PNIPAM chains. Many factors could be investigated, including the effect of polymer structure (length of the PNIPAM chains, density of PNIPAM macrografts in the PLL chain, position of the ligand in the chains, ...), and effect of conditions of layer preparation/manipulation (density of deposited PLL-g-PNIPAM, mixed layers of two PLL derivatives, role of bulk ionic strength, ...). Somewhat arbitrarily, we focused the study on the effect of ligand density, which can be modulated by variation of the structure of PLL-g-PNIPAM, or by mixing ligand-containing with ligand-devoid polymers.

A model system, based on the specific Biotin-Streptavidin association, was proposed to assess the accessibility of ligand in PLL-g-PNIPAM layer as a function of temperature.

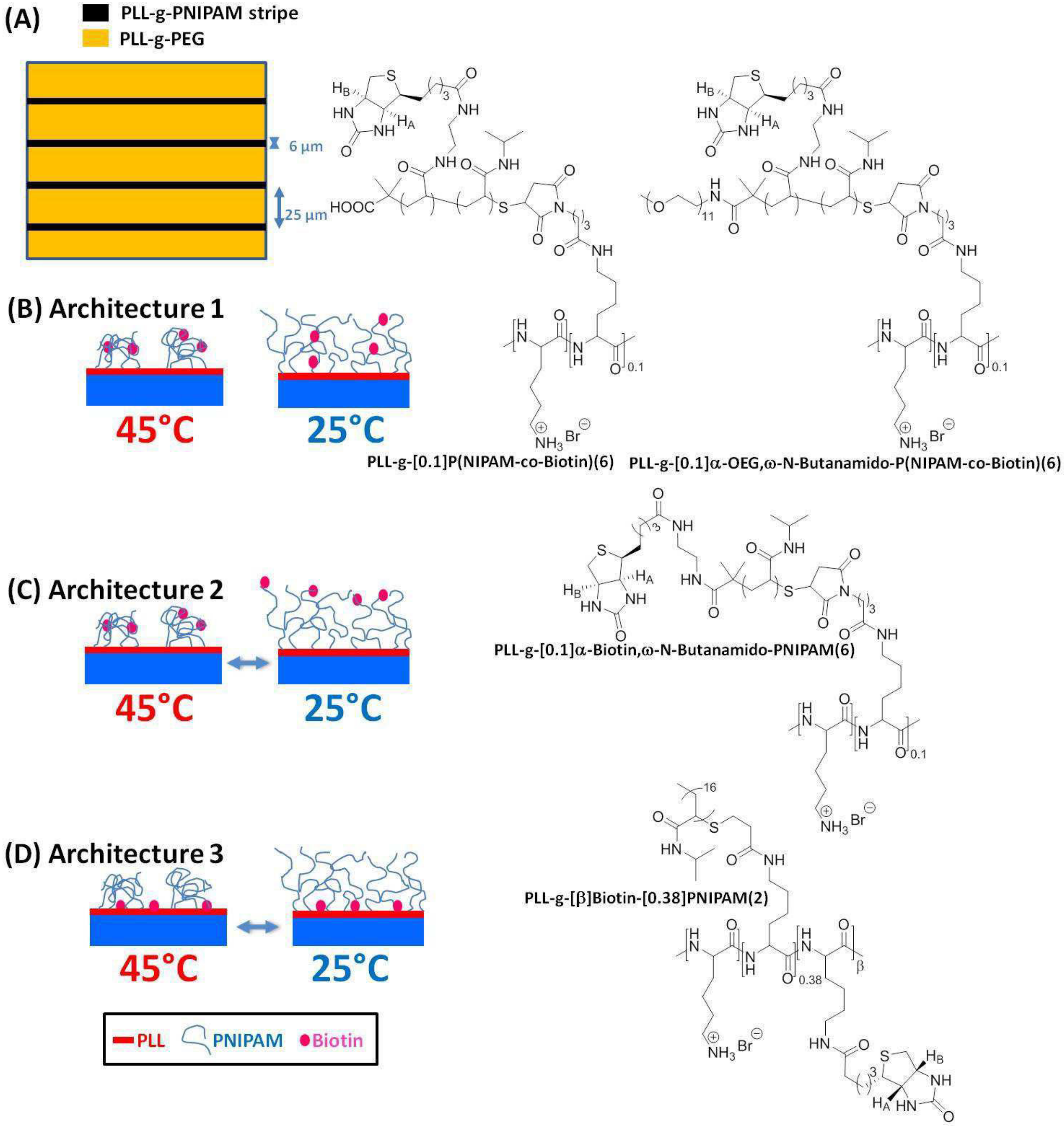

Figure 51 - (A) Coverslip used for captures of "Streptavidin particles". Representation of expected ligand accessibility on three different PLL-g-PNIPAM architectures (with the corresponding chemical structure of PLL-g-PNIPAM compounds). (B) Architecture 1: Biotin is located along PNIPAM chains - PLL-g-[0.1]P(NIPAM-co-Biotin)(6) or PLL-g-[0.1]α-OEG,ω-N-Butanamido-P(NIPAM-co-Biotin)(6), (C) Architecture 2: Biotin is located at the free extremity - PLL-g-[0.1]α-Biotin,ω-N-Butanamido-PNIPAM(6), (D) Architecture 3: Biotin is on the substrate - PLL-g-[β]Biotin-[0.38]PNIPAM(2).

In order to study the influence of the ligand position in the PNIPAM layer, three different architectures were considered (see Figure 51B-D). For architecture 1 and 2 ,Biotin is located as a side group in thermoresponsive PNIPAM chains. A priori, a better Biotin accessibility is expected at low temperatures (Figure 51B-C, swollen chains) compared to high temperatures when hard hydrophobic PNIPAM aggregates may entrap the ligand. For architecture 3, Biotin is located on the PLL backbone, which in adlayers is in contact with the glass substrate. In this case, the accessibility of Biotin may be more pronounced when PNIPAM is collapsed at high temperatures (Figure 51D). Indeed, lateral collapse of the layer creates regions that loss their polymer coverage, and consequently diminishes the distance between the upper water solution and the substrate. This predicted thermal responses assume that dense polymer layers are protein repellent, and that ligands buried in a swollen layer are not accessible, which in practice depends on the chemical nature, length and density of chains. Chemical structures of the PLL derivatives corresponding to the three architectures are represented in Figure 51. PLL-g-[0.1]P(NIPAM-co-Biotin)(6) and PLL-g-[0.1]α-OEG,ω-N-Butanamido-P(NIPAM-co-Biotin)(6) correspond to architecture 1 with 5 mol % of Biotin side groups (ca. 2-3 Biotin per macrograft). Unfortunately, the architecture 2 couldn't be studied because the synthesis of PLL-g-[0.1] α-Biotin,ω-N-Butanamido-PNIPAM(6) failed (see Chapter 2). As regards architecture 3, four PLL-g-[β]Biotin-[0.38]PNIPAM(2) polymers were synthesized differing by their proportion in Biotin (β = 0, 5, 10 and 18 %). The cloud points of these polymers in solution are close to 30 °C (see Appendix 3). To study the binding on adlayers, temperature was accordingly set to either 25 or 45 °C (respectively swollen and collapsed PNIPAM brushes).

The effect of ligand density was investigated for architecture 1 and architecture 3. On the one hand, layers of different densities were obtained by mixing biotinylated and non-biotinylated PLL derivatives of the same architecture. On the other hand, polymers bearing PNIPAM with different degrees of integration of Biotin were adsorbed to form layers containing a single type of PLL derivative. This second strategy requires more intensive work of synthesis. It has been implemented for the architecture 3 with PLL-g-[β]Biotin-[0.38]PNIPAM(2).

To determine the degree of specific binding on those biotin-containing PLL coatings, it was necessary to estimate the degree of non specific association. To this aim, coverslips with alternating 6µm-stripes of biotinylated PLL-g-PNIPAM and 25µm-stripes of repulsive PLL-g-PEG were prepared. A solution of fluorescent "Streptavidin particles" was applied on the top of the patterns, at a fixed temperatures (Figure 51A, see Appendix 4). After flushing out the unbounded particles with water, at the same temperature as incubation with the beads, the density of tightly bound particles was measured by epifluorescence, by counting the remaining particles on images of coverslips (or by measurement of the intensity of fluorescence in the case of smaller particles such as Avidin-coated Qdots) (Figure 52).

Three probes of different radii were used: large Neutravidin-coated polystyrene beads (FluoSpheres, diameter = 0.2 µm), smaller "Streptavidin-coated quantum dots" (Qdots, diameter = 15 nm) and Streptavidin-Cy3 (~ 10 nm under its monomer form).

The various patterns deposited on coverslips are summarized in Table 3 and Table 4 for architecture 1 and 3 respectively.

Short name	Thin stripes - Architecture 1			
	PLL-g-[0.1]P(NIPAM-co-Biotin)(6)	PLL-g-[0.1]α-OEG,ω-N-Butanamido-PNIPAM(6)	PLL-g-[0.1]α-OEG,ω-N-Butanamido-P(NIPAM-co-Biotin)(6)	PLL-g-PEG
$S_{NipamBiot(6)}$	1			
$S_{NipamBiot(6):PEG3:1}$	0.75			0.25
$S_{NipamBiot(6):PEG1:1}$	0.5			0.5
$S_{OEGNipamBiot(6)}$			1	
$S_{OEGNipam(6)}$		1		
$S_{OEGNipamBiot(6):PEG3:1}$			0.75	0.25

Table 3 - Short names of coverslips (Figure 51A) and composition of solutions incubated on thin stripes. Concentration of the coating polymer solutions was 1 mg.mL^{-1} in water. Columns show the concentration (mg.mL^{-1}) of each polymer in the mixed solution used to coat stripes (zero if not specified).

Short name	Thin stripes - Architecture 3	
	PLL-g-[β]Biotin-[0.38]PNIPAM(2)	PLL-g-[0.2]PNIPAM(6)
$S_{[\beta]BiotNipam(2)}$	1	
$S_{[\beta]BiotNipam(2):Nipam(6)9:1}$	0.9	0.1
$S_{[\beta]BiotNipam(2):Nipam(6)1:1}$	0.5	0.5
$S_{[\beta]BiotNipam(2):Nipam(6)1:9}$	0.1	0.9
$S_{Nipam(6)}$	0	1

Table 4 - Short names of coverslips (Figure 51A) and composition of solutions incubated on thin stripes. Concentration of the coating polymer solutions was 1 mg.mL^{-1} in water. Columns show the concentration (mg.mL^{-1}) of each polymer in the mixed solution used to coat stripes (zero if not specified).

We noticed that Biotin-Streptavidin association is stable and tight up to 70 °C. We assumed accordingly that no significant loss of association could be due to a difference of affinity between 25° and 45 °C (see Holmberg et al., 2005).

1 Effect of ligand position in PLL-g-PNIPAM

First, large particles can be conveniently distinguished as isolated spots on epifluorescence images (Figure 52), making it possible to count their degree of surface coverage. Hence, the number of bound particles on 351 µm² of thin PLL-g-PNIPAM stripes was used to quantify tight binding spots that resisted flushing with water (we noticed that the shear induced by the rinsing process was sufficient to detach the larger particles of 200nm in radius, but did not detach Qdots significantly).

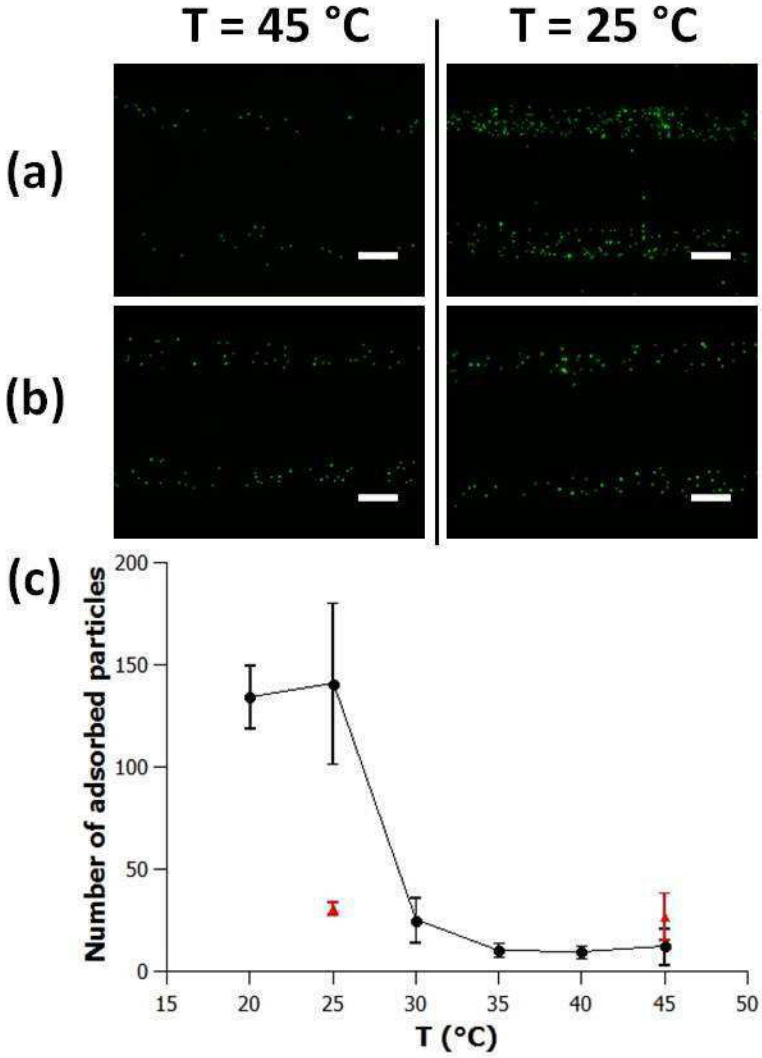

Figure 52 - Epifluorescence pictures of surfaces $S_{NipamBiot(6)}$ (a) and $S_{Nipam(6)}$ (b) after incubation with Neutravidin-coated FluoSpheres at 45 and 25 °C (scale bar = 6 µm). (c) Number of Neutravidin-coated FluoSpheres counted on PLL-g-[0.1]P(NIPAM-co-biotin)(6) stripe (circles, $S_{NipamBiot(6)}$, total surface of 351 µm²). Red triangles are controls on PLL-g-PNIPAM stripe ($S_{Nipam(6)}$).

Results of tight adhesion of large FluoSpheres on the different polymer architectures are shown in Table 5. At 25 °C, the density of bound particles is higher on the biotinylated surfaces ($S_{NipamBiot(6)}$, $S_{OEGNipamBiot(6)}$, $S_{[0.18]BiotNipam(2)}$) than on the corresponding non-biotinylated ones ($S_{Nipam(6)}$, $S_{OEGNipam(6)}$, $S_{[0.18]Nipam(2)}$) whatever the architecture. These observations suggest that specific interaction between Biotin and Streptavidin accounts for the majority of tightly adsorbed FluoSpheres at 25 °C on the top of Biotin-containing layers. At 45 °C, results are different. On layers made of architecture 1 polymers, the quantity of adsorbed particles is globally always low and of the same order of magnitude as in the case of non-specific binding. Thus non-specific binding predominates even if biotin is present. For architecture 3, specific binding is obvious at 45°C on Biotin-containing layer and low binding is observed on Biotin-devoid one. When these result are analyzed in term of the thermal switch of binding density, significant magnitude of switch between a predominantly specific binding to non-specific one is achieved on layers made of architecture 1 polymers. But no temperature effect is observed on the ligand accessibility in the "architecture 3" polymer layer, despite specific binding occurs as judged from the significantly higher binding compared to layers without Biotin. This means that PNIPAM brushes of 6 000 g.mol^{-1} can be effective to mask Biotin at high T, though the distribution of the ligand is key to achieve a good temperature-triggered contrast. This is highlighted on Figure 52C by a threshold temperature (~ 30 °C) above which the adsorption decreases drastically. This threshold temperature is close to the cloud point of the polymer in solution (36 °C). The effect of temperature on FluoSphere adsorption presumably correlates with the swelling transition of PLL-g-PNIPAM. Neutravidin-coated particles can interact with Biotin randomly distributed in swollen PNIPAM brushes, whereas adsorption of FluoSpheres is prevented above the temperature of thermal collapse (where Biotin is presumably trapped in hydrophobic aggregates of PNIPAM (the 80 nm wide, 5 nm high protrusions detected by AFM, see Chapter 3)).

Coverslip		**T**	
		45 °C	**25 °C**
Architecture 1	$S_{NipamBiot(6)}$	12 ± 9	140 ± 39
	$S_{Nipam(6)}$	27 ± 23	31 ± 6
Architecture 1	$S_{OEGNipamBiot(6)}$	28 ± 6	80 ± 11
	$S_{OEGNipam(6)}$	16 ± 2	40 ± 5
Architecture 3	$S_{[0.18]BiotNipam(2)}$	213 ± 5	208 ± 10
	$S_{[0]BiotNipam(2)}$	19 ± 2	24 ± 4

Table 5 - Number of FluoSpheres counted over 57 µm segment of PLL-g-PNIPAM-coated stripe (average over 351 µm²) after incubation with Neutravidin-coated FluoSpheres at 25 and 45 °C.

The effect of repellent OEG ends on architecture 1 can be discussed by comparing adsorption results of coverslips $S_{NipamBiot(6)}$ and $S_{OEGNipamBiot(6)}$. The number of (specifically) bound particles on $S_{OEGNipamBiot(6)}$ is lower than on $S_{NipamBiot(6)}$ at 25 °C (whereas non-specific binding is comparable on OEG-ended and COOH-ended PNIPAM). This suggests that the presence of OEG repellent extremities partially masked the Biotin, without decreasing non-specific adsorption. A detailed discussion on the effect of architecture on accessibility is premature, but this result is an indication that Biotin located near the end of the PNIPAM chains are likely more accessible.

2 Effect of ligand density

The influence of the ligand density on the temperature-controlled ligand accessibility was investigated on both architecture 1 and architecture 3 with Neutravidin-coated FluoSpheres.

2.1 Architecture 3

Because adsorption results on PLL-g-[0.18]Biotin-[0.38]PNIPAM(2) adlayers show that Biotin was always accessible irrespective of temperature, we decided to decrease the density of Biotin in these thermo-responsive PNIPAM layers. First, ligand surface density was varied by deposition of pure PLL-g-[β]Biotin-[0.38]PNIPAM(2) coatings differing by their proportion in Biotin (β = 0, 5, 10 and 18 %). In a second approach, PLL-g-[0.18]Biotin-[0.38]PNIPAM(2) was mixed with non-biotinylated PLL-g-[0.2]PNIPAM(6) (dilution of Biotin-modified PNIPAM in PNIPAM). Note that in the latter case, the non-Biotinylated polymers bear longer PNIPAM side chains of M_n 6 000 g.mol^{-1}).

2.1.1 Pure PLL-g-[β]Biotin-[0.38]PNIPAM(2) adlayers

Quantification of adsorption on pure PLL-g-[0.18]Biotin-[0.38]PNIPAM(2) coatings are shown in Figure 53. On non-biotinylated surfaces (β = 0 %), a few particles remain bound with the surface due to non-specific binding. The quantity of bound particles increases almost linearly as a function of the Biotin density (β), suggesting that the majority of tightly bound particles are attached on the polymer layer by specific interaction. However, PLL-g-[β]Biotin-[0.38]PNIPAM(2) adlayers don't show any thermal contrast of ligand accessibility (identical results of adsorption at 25 and 45 °C). This suggests that swollen PNIPAM brushes of 2 000 g.mol^{-1} are too short to mask Biotin in their collapsed state.

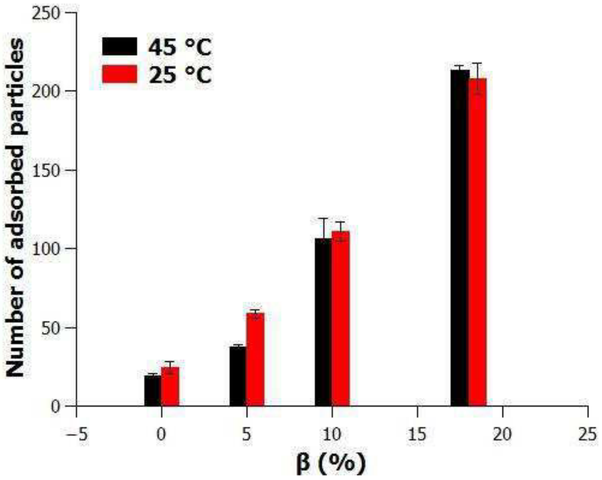

Figure 53 - Number of Neutravidin-coated FluoSpheres counted on PLL-g-[β]Biotin-[0.38]PNIPAM(2) stripe ($S_{[β]BiotNipam(2)}$, total surface of 351 µm²).

2.1.2 Mixed PLL-g-[0.18]Biotin-[0.38]PNIPAM(2)/PLL-g-[0.2]PNIPAM(6) adlayers

Quantification of adsorption on mixed PLL-g-[0.18]Biotin-[0.38]PNIPAM(2)/PLL-g-[0.2]PNIPAM(6) coatings are shown in Figure 54. Without Biotin ([PLL-g-[0.18]Biotin-[0.38]PNIPAM(2)] = 0 mg.mL^{-1}), a few particles are bound to the surface due to non-specific interactions. Similarly to results on pure PLL-g-[β]Biotin-[0.38]PNIPAM(2) adlayers, the number of bound particles increases with the Biotin density (i.e. with increasing fraction of PLL-g-[0.18]Biotin-[0.38]PNIPAM(2) used in the mixed solution with PLL-g-[0.2]PNIPAM(6)). An increasing number of specific Streptavidin-Biotin interactions accounts for this behavior. At high fraction of Biotinylated polymer ([PLL-g-[0.18]Biotin-[0.38]PNIPAM(2)] > 0.9 mg.mL^{-1} in the mixed solution containing a total concentration of 1 mg.mL^{-1}), the number of bound particles is similar at 25 and 45 °C, thus reproducing the results obtained on pure Biotinylated layers. At intermediate Biotin densities (0 mg.mL^{-1}< [PLL-g-[0.18]Biotin-[0.38]PNIPAM(2)] < 0.9 mg.mL^{-1}), the quantity of bound particles depends on the temperature. Interestingly, the effect of increasing temperature is a decrease or an increase in binding depending on layer composition. From a simplistic view (e.g. Biotin should be more accessible upon collapsing the Biotin-free brushes, Figure 51D), one may expect that the polymer composition does not affect the direction of thermal response . Our result indicates a complex mechanism of ligand accessibility, which may be due to complex interplay between PNIPAM collapse of Biotin-containing and Biotin-free PNIPAM at different temperature, that possibly form mixed or separated domains in mixed adlayers. It is difficult from the present study to interpret this inversion of the temperature-triggered accessibility. In practice, however, a full contrast between specific and fully non-specific binding (FluoSphere density < 40) was not reached.

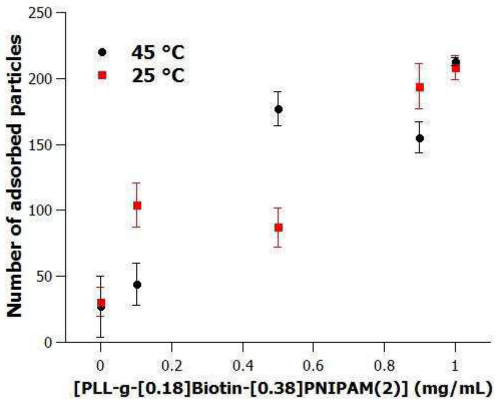

Figure 54 - Number of Neutravidin-coated FluoSpheres counted on mixed PLL-g-[0.18]Biotin-[0.38]PNIPAM(2)/PLL-g-[0.2]PNIPAM(6) stripes ($S_{[\beta]BiotNipam(2):Nipam(6)}$, total surface of 351 µm²). [PLL-g-[0.18]Biotin-[0.38]PNIPAM(2)] indicates the concentration of the PLL-g-[0.18]Biotin-[0.38]PNIPAM(2) solution used for coating (total concentration in PLL derivative: 1 mg.mL^{-1}).

2.2 Architecture 1 - Dilution of PLL-g-[0.1]P(NIPAM-co-Biotin) brushes into repellent PLL-g-PEG brushes

The effect of ligand density on architecture 1, whose pure layers can hide/display Biotin in a temperature-dependant manner (see section 1), was investigated by studying mixed PLL-g-[0.1]P(NIPAM-co-Biotin)(6)/PLL-g-PEG adlayers. Dilution of thermoresponsive PLL-g-[0.1]P(NIPAM-co-Biotin)(6) brushes were achieved in this case into non-responsive PLL-g-PEG brushes to see if it is possible to adjust the surface density of ligands, while preserving the ability to trigger thermally their accessibility.

Quantification of adsorption on mixed PLL-g-[0.1]P(NIPAM-co-Biotin)(6)/PLL-g-PEG coatings are gathered in Table 6. At 25 °C, stripes coated with mixed PLL-g-[0.1]P(NIPAM-co-Biotin)(6)/PLL-g-PEG solutions became rapidly inert upon decreasing the density of Biotin. That is, displayed low, presumably nonspecific binding, and absence of temperature-triggered binding below a fraction of 50 % PLL-g-[0.1]P(NIPAM-co-Biotin)(6) brushes ($S_{NipamBiot(6):PEG1:1}$ in Table 6). However, diluted PLL-g-[0.1]P(NIPAM-co-Biotin)(6) brushes with a fraction superior to 50 % show a temperature-triggered binding, indicating that Biotin density is a key parameter. Similar results were acquired on mixed PLL-g-[0.1]α-OEG,ω-N-ButanamidoP(NIPAM-co-Biotin)(6)/PLL-g-PEG adlayers (Table 7). Interestingly, an increasing fraction of PEG in the mixed layer is accompanied by a slight decrease in the amount of non-specific binding (from 27 to 11 in Table 6), suggesting the PNIPAM chains are also gradually masked by PEG chains.

T (°C)	$S_{NipamBiot(6)}$	$S_{NipamBiot(6):PEG3:1}$	$S_{NipamBiot(6):PEG1:1}$	$S_{Nipam(6)}$	$S_{Nipam(6):PEG3:1}$	$S_{Nipam(6):PEG1:1}$
25	140 ± 39	60 ± 38	3 ± 3	31 ± 6	15 ± 3	12 ± 9
45	12 ± 9	12 ± 12	3 ± 3	27 ± 23	20 ± 8	11 ± 2

Table 6 - Number of FluoSpheres counted over a 57µm segment of PLL-g-NIPAM-coated stripe (average over 351µm²) after incubation with Neutravidin-coated FluoSpheres at 25 and 45°C.

T (°C)	$S_{OEGNipamBiot(6)}$	$S_{OEGNipamBiot(6):PEG3:1}$	$S_{Nipam(6)}$	$S_{OEGNipam(6)}$
25	80 ± 11	52 ± 5	31 ± 6	40 ± 5
45	28 ± 6	26 ± 2	27 ± 23	16 ± 2

Table 7 - Number of FluoSpheres counted over a 57µm segment of PLL-g-NIPAM-coated stripe (average over 351µm²) after incubation with Neutravidin-coated FluoSpheres at 25 and 45°C.

3 Effect of the size of Streptavidin probes

According to adsorption of large Neutravidin-coated FluoSpheres (200 nm), a contrast of ligand accessibility with temperature has been detected only on pure or slightly diluted PLL-g-[0.1]P(NIPAM-co-Biotin)(6) adlayers. The radius of the FluoSphere probes is markedly larger than the size of PLL polymers. Penetration of these large particles in the adlayer is thus highly unlikely (Halperin and Kröger, 2012). In order to obtain more information on the switch of the accessibility of ligand, binding experiments using smaller Streptavidin-based probes were carried out.

3.1 Adsorption of Streptavidin-conjugated nanoparticles (diameter: 15 nm)

Streptavidin-conjugated Qdots have a size comparable to that of a few proteins and can probe nanometric binding sites. Epifluorescence images can't be used however to count isolated particles (as implemented with FluoSpheres), and thus, quantification of their adsorption was based on the emission intensity. In order to normalize the data (intensity may vary depending on the tuning of the microscope), the contrast between PLL-g-PNIPAM coated stripes and the 100% PLL-g-PEG stripes was used as internal reference (Table 8 and Appendix 4 for the contrast formula). The measured intensity of fluorescence on 100% PLL-g-PEG exposed to Qdots was low, but nonzero (Figure 55), and did not significantly differ at 25 and 45 °C (Table 9). Stripes coated with pure PLL-g-[0.1]P(NIPAM-co-biotin)(6), and incubated at 25 °C with Qdots, showed a significant contrast compared to PLL-g-PEG stripes present on the same glass coverslip, suggesting that specific binding occurred on the layer containing a dense amount of biotin. The specific binding of Streptavidin-conjugated Qdots on $S_{\mathrm{NipamBiot(6):PEG}}$ (i.e. stripes of pure PLL-g-[0.1]P(NIPAM-co-biotin)(6) measured with reference stripes of PLL-g-PEG) was significantly high at 25°C, and low at 45°C. Dilution of the Biotin-containing polymer in mixed layers with PLL-g-PEG (for instance, mixed PLL-g-[0.1]P(NIPAM-co-biotin)(6):PLL-g-PEG at 3:1 mol/mol) essentially decreased the binding of Qdots down to values comparable to pure PLL-g-PEG, i.e. to essentially weak non-specific associations, irrespective of temperature. In term of nonspecific adhesion of Qdots, PLL-g-[0.2]PNIPAM(6) layers without biotin compared also well with PLL-g-PEG ones (contrast <5% at 25°C, Figure 55a and Table 8). Even at 45°C when NIPAM strands are expected to collapse and become hydrophobic, weak contrast was observed compared to 100% PEG-coated regions, irrespective of the presence or absence of biotin (Figure 55a-b). Except for a possibly sharper transition between tight specific binding on 100% Biotin-containing polymer layers and weak non specific one on mixed layers with PLL-g-PEG, these results are similar to the one obtained with FluoSpheres.

T (°C)	$S_{\mathrm{NipamBiot(6)}}$	$S_{\mathrm{NipamBiot(6):PEG3:1}}$	$S_{\mathrm{Pnipam(6)}}$	$S_{\mathrm{Nipam(6):PEG3:1}}$
25	38 % ± 3.5 %	9 % ± 3 %	< 1 % ± 4 %	5 % ±5 %
45	8 % ± 3 %	5 % ± 2.5 %	5 % ± 3 %	0 % ± 5 %

Table 8 - Fluorescence contrast between NIPAM-coated stripes and PEGylated ones after adsorption of QDs.

T (°C)	$S_{\mathrm{NipamBiot(6)}}$	$S_{\mathrm{NipamBiot(6):PEG3:1}}$	$S_{\mathrm{Pnipam(6)}}$
25	50	77	60
45	70	90	85

Table 9 - Fluorescence intensity (a.u.) measured on the PEGylated stripes after adsorption of QDs (same conditions as Table 4).

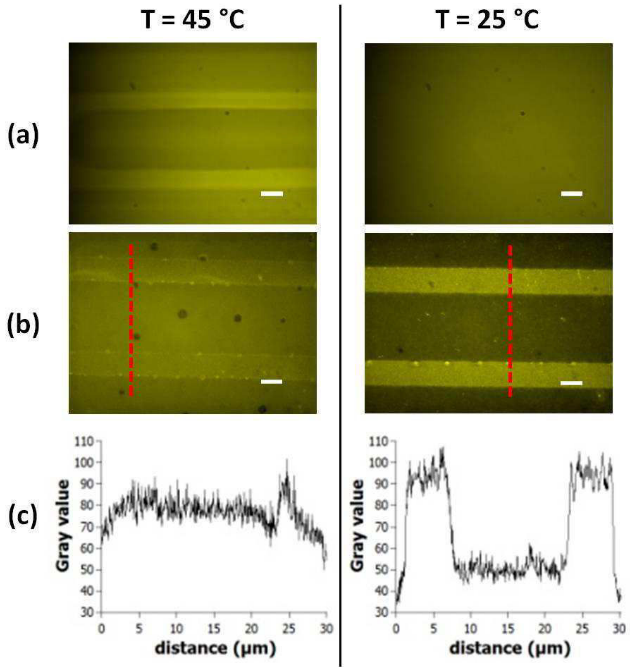

Figure 55 - Epifluorescence images of coverslips after adsorption of Qdots; $S_{Pnipam(6)}$ (a), $S_{NipamBiot(6)}$ (b), and intensity profiles along the red dashed lines (c) (scale bar = 6 µm).

3.2 Adsorption of Streptavidin-Cy3 (~ 10 nm)

Finally, we used Steptavidin-Cy3 as the smallest specific probe to assess the accessibility of Biotin. The absence of non specific binding was validated by absence of fluorescent stripe in images of non-biotinylated coverslips ($S_{Pnipam(6)}$, Figure 56a). Specific binding was reflected by fluorescent stripes recorded on $S_{PnipamBiot(6)}$, coverslips at 45 and 25 °C (Figure 56b). Similar results were obtained on mixed PLL-g-[0.1]P(NIPAM-co-biotin)(6):PLL-g-PEG layers. These results suggest that Streptavidin-Cy3 interacts specifically with Biotin without non-specific adsorption. Unfortunately, quantification of adsorption was very difficult due to the lack of reference intensity on the coverslip. Indeed, fluorescence intensity varies significantly from day to day, depending on the optical tuning of the microscope and possibly due to "parasite" external light that cannot be neglected compared to the weak fluorescence of a protein monolayer. From a qualitative point of view, it seems that Streptavidin-Cy3 are small enough to interact with Biotin in both the extended and collapsed PNIPAM brushes, but possible quantitative discussion on the degree of binding deserve further studies. Based on intensity measurements performed systematically in the same condition (the same day, single user of the microscope, ...), we determined that the amount of bound proteins is essentially constant over a large window of mixed layer compositions (mixed PLL-g-[0.1]P(NIPAM-co-biotin)(6):PLL-g-PEG layers ranging from 5 mol% to 100 mol% biotin-containing polymer, see Appendix 4). The order of magnitude of 5 mol% of Biotinylated polymer in the layer represents an average surface density of about one Biotin-containing polymer in 2000 nm^2 (coverage at about 1 to 1.5 mg/m^2 corresponds to one PLL derivative on 100 nm^2, see chapter 1) and one Biotinylated PNIPAM chain in 200 nm^2 (on average). Based on the radius of Streptavidin (~ 5 nm), a dense monolayer of proteins corresponds to the presence of one bound Biotin in about 25 nm^2. If tetramers of the proteins are considered instead of monomers, the minimal density of bonds that is formed by a monolayer decreases to about 1/100nm, suggesting that in the diluted mixed layer containing 5 mol% of Biotinylated polymers, most Biotin-containing chains are capable to bind a protein. This rough estimate essentially indicates a high accessibility of the Biotin groups.

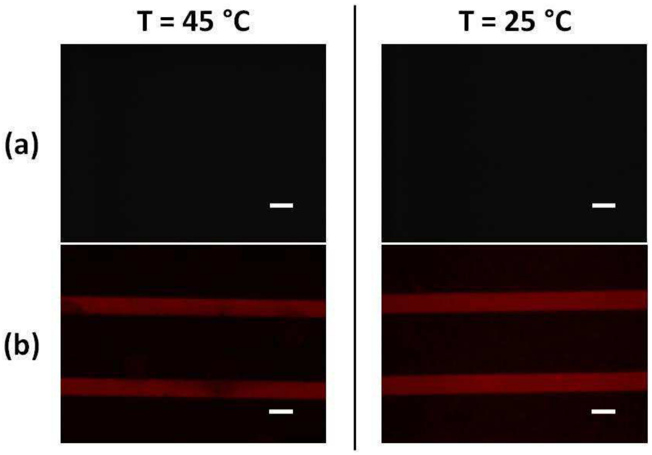

Figure 56 - Epifluorescence images of coverslips $S_{Nipam(6)}$ (a) and $S_{NipamBiot(6)}$ (b) after Streptavin-Cy3 adsorption (scale bar = 6 µm).

3.3 Discussion on the effect of probe's size on pure PLL-g-[0.1]P(NIPAM-co-Biotin)(6) adlayer

Altogether, the results from the different Streptavidin-based probes show that a size threshold probably exists on the temperature-triggered ligand accessibility as illustrated on Figure 57 with pure PLL-g-[0.1]P(NIPAM-co-Biotin)(6) adlayers. No difference of ligand accessibility is noticed for the smallest Streptavidin-Cy3 between collapsed (T = 45 °C) and swollen (T = 25 °C) layers. Bigger Streptavidin-coated particles (FluoSpheres and Qdots) show a temperature-triggered binding. As a conclusion, this adlayer is effective to expose/mask a ligand for particles that are larger than the radius of the polymer chains, and presumably cannot penetrate between adjacent PLL-g-PNIPAM whose inter-chain distance is of the order of a few nanometers. This is an interesting result in line with constraints of biological applications. Indeed, because cells sense surfaces with membrane-attached integrin receptors whose characteristic size is 8-12 nm in diameter (Xiong et al., 2002), dense coverage with repellent chains is required.

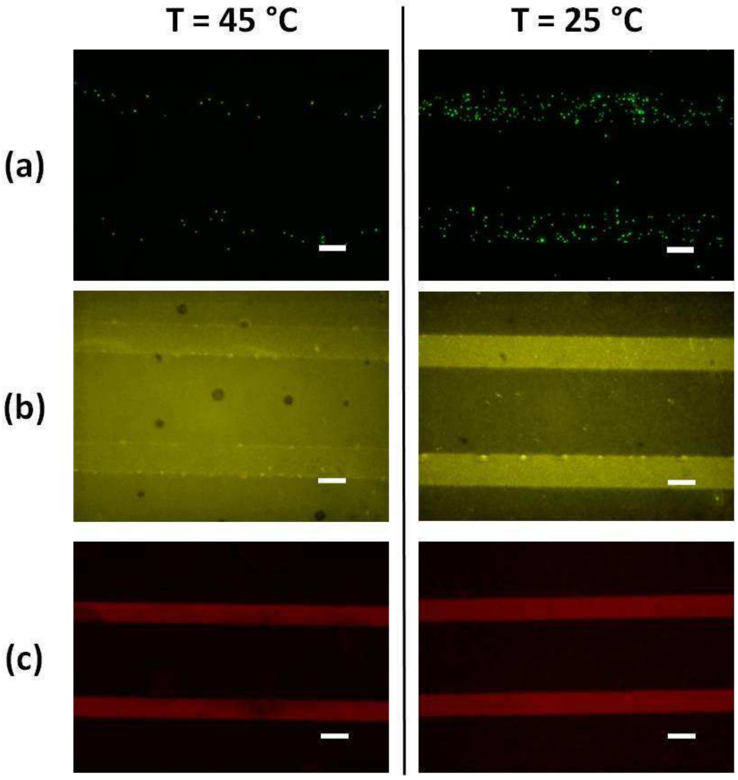

Figure 57 - Epifluorescence pictures of surfaces $S_{NipamBiot(6)}$ after incubation with Streptavidin particles of different size at 45 and 25 °C (scale bar = 6 µm): (a) FluoSpheres: 200 nm, (b) Streptavidin-conjugates nanoparticles:15 nm, (c) Streptavidin-Cy3: 10 nm.

Conclusion

In this chapter, we demonstrate that PLL-g-PNIPAM adlayers with ligands randomly positioned along thermoresponsive PNIPAM strands make it possible to control thermally ligand accessibility to particles larger than 15 nm. Consequently, such a architecture could be envisaged to control specific cell adhesion (see Chapter 5).

Binding studies with model particles give some insights into the mechanism of ligand display on PLL-g-[0.1]P(NIPAM-co-Biotin)(6) adlayers. Our results show that, above LCST, ligands were not accessible to Streptavidin-coated beads, suggesting that they are trapped in rigid aggregates of polymers (the 80 nm wide, 5 nm high protrusions detected by AFM). In these conditions, mechanisms can be proposed to interpret the lack of biotin accessibility at high T. A first possibility is that solid-like clusters of chains limit accessibility of the biotin groups (trapping inside these clusters). Lack of biotin at the surface of PNIPAM clusters above LCST is a possible consequence of hydrophobic attraction within the collapsed PNIPAM. A second possibility is that the surface roughness emerging at T > LCST diminishes accessibility due to steric effects: formation of a few nanometer thick rigid protrusions hampers the accessibility to all ligands due to the decrease in the effective area of contacts between (large) Avidin-coated beads and the upper cap of those “protrusions”. A threshold surface density of ligand is required to bind the beads (which is validated by the rapid loss of specific binding on mixed PLL-g-[0.1]P(NIPAM-co-Biotin)(6)/PLL-g-PEG layers). Roughness and/or partial burial in PNIPAM clusters are thus both capable to decrease the number of accessible biotin per unit surface below this threshold.

Conclusion on the ligand position into PLL-g-PNIPAM

Architecture 1 shows the expected thermal contrast of ligand display (a better accessibility of ligand on swollen PLL-g-P(NIPAM-co-ligand) than on collapsed chains). Up to now, we studied PLL-g-P(NIPAM-co-ligand) where ligand was randomly distributed. However, the position of the ligand along the P(NIPAM-co-ligand) can impact the efficiency of the contrast. Hence, efforts should be made to synthesize PLL-g-[0.1]α-Biotin,ω-N-Butanamido-PNIPAM(6) corresponding to architecture 2. Block α-COOH,ω-NHS-P(NIPAM-co-ligand) copolymers could be synthesized thanks to living RAFT polymerization and then grafted on PLL backbone.

Architecture 3 did not enable to design adlayers with thermal response, despite the attachment of Biotin close to the PLL backbone, i.e. presumably deeply buried in the adlayer of responsive PNIPAM chains. The shorter length of PNIPAM (2 000 g.mol^{-1} compared to 6000 in architecture 1) certainly diminishes the repulsion efficiency of the layer, possibly contributing to the lack of ligand masking. In the future, it could be interesting to synthesize PLL-g-[0.18]Biotin-[0.38]PNIPAM(M_n) with longer thermo-responsive PNIPAM grafts (M_n > 6 000 g.mol^{-1}) and see if the corresponding coating shows a thermal contrast of ligand accessibility.

Bibliography

Halperin, A., and Kröger, M. (2012). Thermoresponsive Cell Culture Substrates Based on PNIPAM Brushes Functionalized with Adhesion Peptides: Theoretical Considerations of Mechanism and Design. Langmuir *28*, 16623–16637.

Holmberg, A., Blomstergren, A., Nord, O., Lukacs, M., Lundeberg, J., and Uhlén, M. (2005). The biotin-streptavidin interaction can be reversibly broken using water at elevated temperatures. ELECTROPHORESIS *26*, 501–510.

Xiong, J.-P., Stehle, T., Zhang, R., Joachimiak, A., Frech, M., Goodman, S.L., and Arnaout, M.A. (2002). Crystal Structure of the Extracellular Segment of Integrin αVβ3 in Complex with an Arg-Gly-Asp Ligand. Science *296*, 151–155.

Chapter 5 - Cell adhesion on PLL-g-PNIPAM coatings

Contents

Introduction

This chapter reports the use of PLL-g-PNIPAM coatings to control specific cell adhesion by variations of temperature. Based on results of biotinylated PNIPAM adlayers (Chapter 4), we expect that peptide accessibility can be modulated by the collapse/swelling of peptide-containing NIPAM stands. Hence, a RGD-containing polymer was synthesized, PLL-g-[0.15]P(NIPAM-co-RGD)(6) (Figure 58, 2 RGD peptides in average per PNIPAM chain), to reversibly mask/expose RGD on glass substrates. HeLa cells were used as a model for mammalian cells because this cell line is robust (i.e. resistance to temperature changes) and express integrins. We used HeLa cells transfected with LifeAct-GFP and Vinculin-mCherry in order to covisualize respectively FAs and the actin cytoskeleton. Experiments were conducted in DMEM culture medium without serum, which diminishes the amount of protein present and in practice suppressed non-specific cell adhesion at hours-long incubation times. The objective of experiments on cell adhesion was to illustrate the possible tuning of adhesion by temperature variations. We explored the effect of the composition of polymer layers (adjustment of the density of RGD by mixing PLL-g-[0.15]P(NIPAM-co-RGD)(6) with polymers without RGD). In the appropriate range of layer compositions, we recorded adhesion/detachment of cells. Our goal differs from typical publications on stimuli-triggered cell detachment, that aim at 100% deadhesion for collecting cell sheets (tissue engineering applications). Here, we explored the possibility of fine tuning cell-substrate interaction, while keeping the cells adherent, and orienting their polarization or migration toward responsive patterns. This situation is closer to *in vivo* responses to guidance cues, and less stressful for cells. Moreover, it enables accordingly studies on triggered intracellular reorganization (e.g. FA and stress fibers growth/release) resolved in space and time.

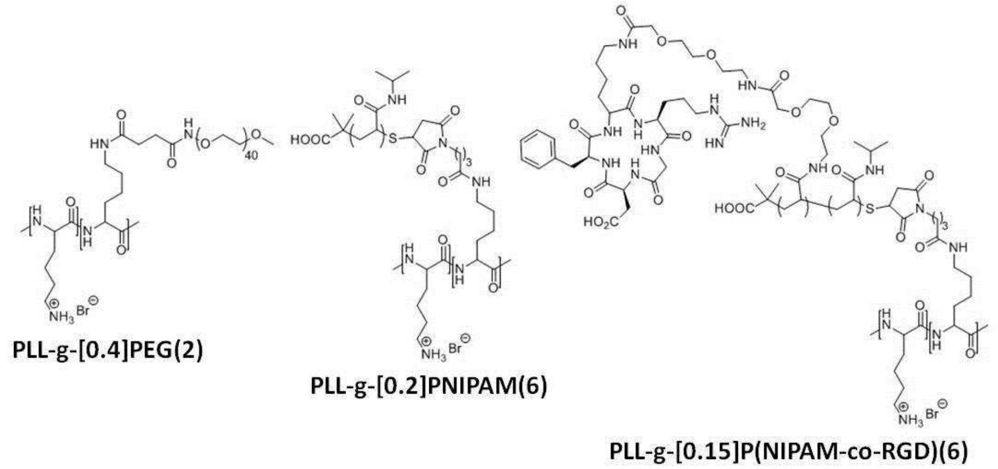

Figure 58 - Chemical structures of the three polymers used for cell adhesion experiments.

1 Pure (100 %) PLL-g-[0.15](NIPAM-co-RGD)(6) adlayers

Due to the hydrophilicity of RGD, the temperature of phase transition is expected to be shifted to a value >> 32°C for PLL-g-[0.15]P(NIPAM-co-RGD)(6). A cloud point of 40 °C was measured by turbidimetry for PLL-g-[0.15]P(NIPAM-co-RGD)(6) solution in DMEM (Appendix 3), suggesting that the zwitterionic nature of RGD markedly increases solubility. The same copolymer, once deposited on the QCM-d crystal as adlayers, was studied in DMEM (see more details in Chapter 3). The gradual drift of signal and the absence of significant variation on the derivatives of QCM-d signals (Figure

59A) suggest the absence of phase transition (in the window 19 - 51 °C) in the adlayer. This can't be attributed to a lack of sensitivity of QCM-d because the adsorbed mass of PLL-g-[0.15]P(NIPAM-co-RGD)(6) should be actually closed to the one of PLL-g-[0.2]PNIPAM(6) adlayer (grafting ratios and molecular weights of PNIPAM grafts are similar for these two polymers) (see Chapter 3 - QCM-d results of pure PLL-g-[0.2]PNIPAM(6) adlayer: $T_{\Delta f}$ = 32 °C, $T_{\Delta D}$ = 30 °C, Appendix 3). Consequently, we considered that PLL-g-[0.15]P(NIPAM-co-RGD)(6) was not collapsed in the range of experimental temperatures used for cell culture. The difference between cloud point of polymer adlayers and polymers in solution is not understood yet. It may arise from hydrophilicity and a relatively important size of the RGD+linker (compared to biotin or NIPAM monomer) which may favor extended conformers and presentation of RGD on the top of the layer to escape constraints inside the adsorbed brush. In mixed layers of PLL-g-[0.15]P(NIPAM-co-RGD)(6) and PLL-g-[0.2]PNIPAM(6), a phase transition was successfully detected by QCM-d in DMEM (9 % RGD, see Figure 59B, $T_{\Delta f}$ = 32 °C, $T_{\Delta D}$ = 30 °C) (% RGD represents here the polymer fraction (mol %) of PLL-g-[0.15]P(NIPAM-co-RGD)(6) in the solution used for deposition of the mixture). This transition is ascribed to PLL-g-[0.2]PNIPAM(6) which represents the predominant polymer fraction of the adlayer.

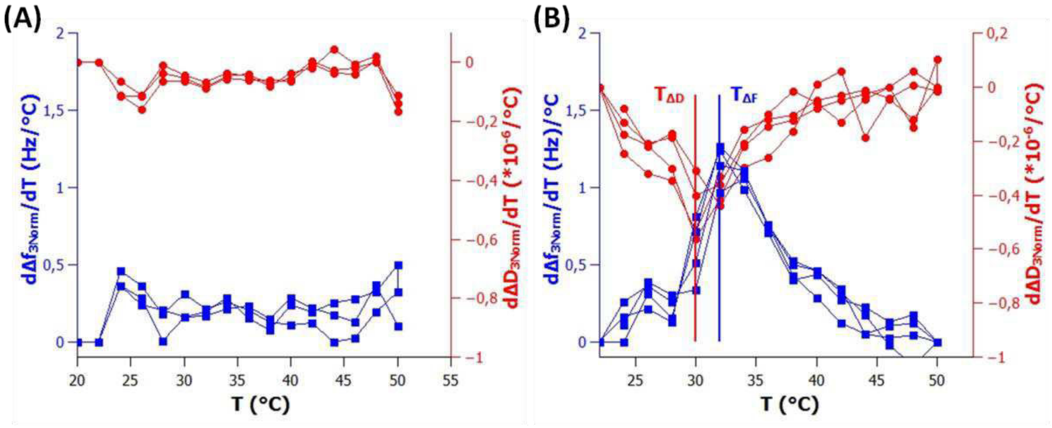

Figure 59 - Determination of the phase transition by QCM-d in DMEM of (A) pure PLL-g-[0.15]P(NIPAM-co-RGD)(6) adlayer and (B) mixed adlayer (9 % RGD) (0.1 °C.min^{-1}, 2 temperature cycles for each sample, see Chapter 3 for more details).

First, we present qualitative cell adhesion experiments conducted by seeding a high density of cells at time zero either on bare glass or on adlayers of the three polymers represented in Figure 58. After 3 H of incubation, non-adherent cells were flushed out by gentle rinsing and adherent cells were fixed for microscopy. No cell was observed on repellent PLL-g-PEG coatings (not shown), which confirms the absence of non-specific binding for this "reference" case. Similarly, no cell was attached on the top of PLL-g-[0.2]PNIPAM(6) whatever the incubation temperature (27 or 37 °C). In the literature, high surface density of PNIPAM has been reported to weaken cell adhesion. Non-specific cell adhesion on PNIPAM brushes seems to be directly linked to two main factors: density and molecular weight of PNIPAM brushes (Li et al., 2008; Nagase et al., 2011; Takahashi et al., 2010). The admitted trend is: 1) cell poorly adhere on thick hydrophobic polymer brushes at T > LCST (high density and high molecular weight) and detach at T < LCST, 2) cell cannot detach from thin polymer brushes (low density or low molecular weight), 3) in intermediate regimes, non-specific cell adhesion may occur above the critical temperature while cells detach below this temperature. This trend is illustrated on Table 10 with results of Takahashi *et al*. According to Santore's results (Chapter 1, Table 1) on PLL-g-PEG, we can consider as a first approximation a density closed to 0.1 chains/nm² of

PNIPAM strands in PLL-g-[0.2]PNIPAM(6) adlayers. This surface density is denser than the threshold density reported by Takahashi *et al* (Table 10) causing non-specific irreversible cell attachment. Consequently, cell repulsive character of PLL-g-[0.2]PNIPAM(6) coatings at 37 and 27 °C is in agreement with literature. On bare glass, cells were attached to the surface, which means here that they could not be washed out, but they didn't spread suggesting the lack of specific interaction (Figure 60A). These results highlight the antibiofouling ("passivating") properties of both PLL-g-PEG and PLL-g-[0.2]PNIPAM(6) adlayers. Moreover, it highlights the expectation that spreading will be indicative of specific binding in these conditions.

Density of PNIPAM chains	Molecular weight (g/mol)	Cell adhesive character	
		37 °C	20 °C
0.04 chains/nm²	58 000	Poor cell adhesive	Deadhesive
	49 000	Adhesive	Deadhesive
	23 000	Adhesive	Deadhesive
0.03 chains/nm²	58 000	Adhesive	Deadhesive
	49 000	Adhesive	Adhesive
	23 000	Adhesive	Adhesive
0.02 chains/nm²	58 000	Adhesive	Adhesive
	49 000	Adhesive	Adhesive
	23 000	Adhesive	Adhesive

Table 10 - Non-specific cell adhesive character of PNIPAM brushes (obtained by RAFT "grafting from" method) (Takahashi et al., 2010; Tang et al., 2014).

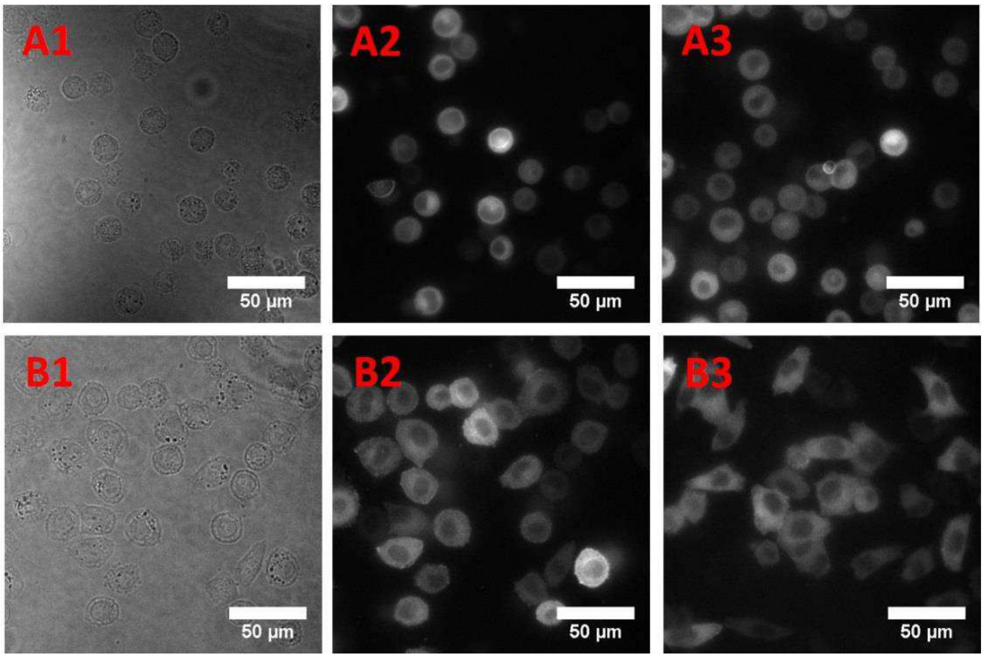

Figure 60 - Qualitative results of cell adhesion on bare glass (A1-3) and PLL-g-[0.15]P(NIPAM-co-RGD)(6) (B1-3). HeLa cells were seeded in free serum DMEM and incubated at 37 °C. After 3 H of incubation (A-B-1-2) or 24 H (A-B3), cells were fixed before observation. A-B1: transmission microscopy, A-B-2-3: epifluorescence microscopy (Actin).

Cells can interact and spread on PLL-g-[0.15]P(NIPAM-co-RGD)(6) adlayer (Figure 60B). Because the PLL-g-[0.2]PNIPAM(6) adlayer presenting no RGD is cell repellent, specific cell adhesion indicates that RGD displayed by PLL-g-[0.15]P(NIPAM-co-RGD)(6) were recognized by the cells.

Pure (100%) PLL-g-[0.15]P(NIPAM-co-RGD)(6) adlayer didn't enable measurable modulation of cell spreading or binding upon incubation at low or high temperatures due to the lack of thermoresponsive character in the adlayers: this observation is not surprising. For that reason, we turned to mixed adlayers of PLL-g-[0.15]P(NIPAM-co-RGD)(6) and PLL-g-[0.2]PNIPAM(6).

2 Cell adhesion on mixed PLL-g-[0.2]PNIPAM(6)/PLL-g-[0.15]P(NIPAM-co-RGD)(6) coatings at 27 and 37 °C

Effect of temperature on cell adhesion was investigated on mixed PLL-g-[0.15]P(NIPAM-co-RGD)(6)/PLL-g-[0.2]PNIPAM(6) adlayers of different compositions (% RGD means here the weight fraction of RGD-containing polymer in the polymer mixture). HeLa cells were seeded at a density of $5,6.10^3$ cells/cm^2 in coverslips preequilibrated in serum-free DMEM at 27 or 37 °C. Kinetic monitoring of cell adhesion was achieved by taking phase contrast images at different time of incubation (Figure 61). Quantifications consist in measuring cell area and the ratio between spread cells and highly refringent round-like cells.

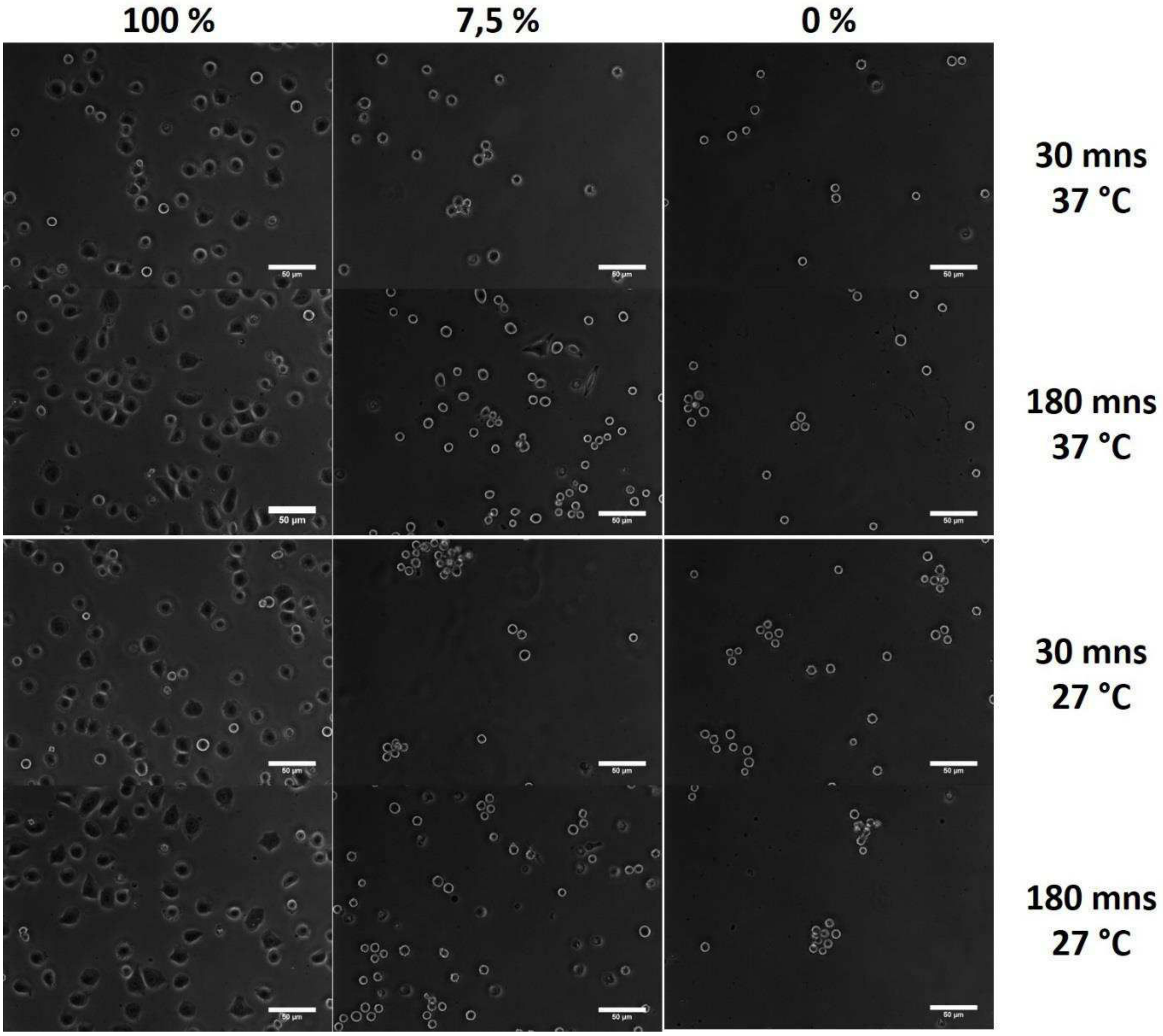

Figure 61 - Phase contrast images (20× objective, scale bar = 50 µm) of HeLa cells seeded on mixed PLL-g-[0.15]P(NIPAM-co-RGD)(6)/PLL-g-[0.2]PNIPAM(6) adlayers. Polymer composition quoted above pictures as 100, 7.5 and 0 % RGD; images taken at 30 and 180 minutes of incubation in serum-free DMEM.

The ratio between spread and round cells for different % RGD and incubation time are represented on Figure 62. After 100 minutes of incubation, the number of spread cells reached a plateau. It can be considered that incubation for 3 H was thus sufficient to enable full adhesion and spreading. For that reason, we modified slightly the quantification procedure by removing the rinsing step and focusing on the round/spread cell ratio after 3 H of incubation.

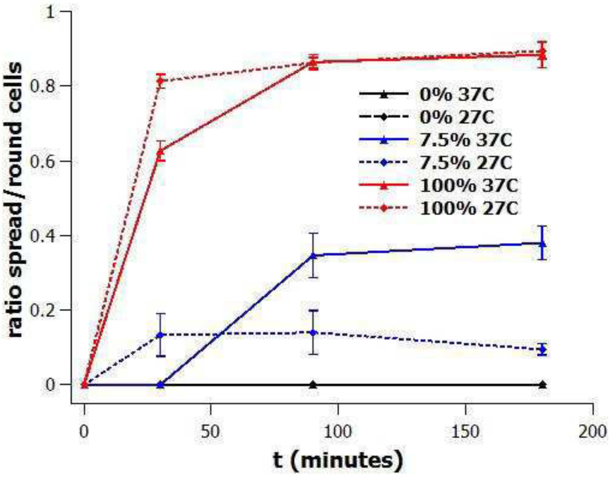

Figure 62 - Kinetic monitoring of HeLa cell adhesion on mixed PLL-g-[0.15]P(NIPAM-co-RGD)(6)/PLL-g-[0.2]PNIPAM(6) adlayers after 180 minutes of incubation at 37 or 27 °C in DMEM. Three polymer compositions were represented (black: 0 % RGD, blue: 7.5 % RGD, red: 100 % RGD).

Results of this quantification are summarized in Figure 63A-D. Without RGD (0 % RGD), cells were simply set free on the top of the substrate and didn't spread (ratio spread/round = 0, cell area ~ 100 µm²), thus confirming the cell-repulsive character of PLL-g-[0.2]PNIPAM(6) at either 27 and 37 °C. Both the ratio of spread/round cells and the mean cell area increase dramatically with increasing the RGD density. They both reach a plateau beyond a surface density of 20 % RGD. In addition, a minimal RGD density (threshold density) is required in order to trigger specific cell adhesion and spreading. It is possible to compare the experimental threshold obtained here with data in literature reporting a minimum distance between adhesive cues to induce adhesion (Arnold et al., 2004; Hudalla and Murphy, 2009; Lagunas et al., 2012). On our mixed adlayers, this threshold density is closed to 8 % RGD at 27 °C (1-2 % at 37 °C). Hudalla *et al*. reported that 1 % RGD was sufficient for cell adhesion and 5 % for spreading on mixed SAMs of ethyleneglycol thiolates and RGD-ended ethyleneglycol thiolates. The threshold adhesion-triggering distance of 70 nm reported by Spatz *et al.* (between RGD-coated dots of about 10 nm in diameter) corresponds roughly to a percentage surface coverage of 2 %.

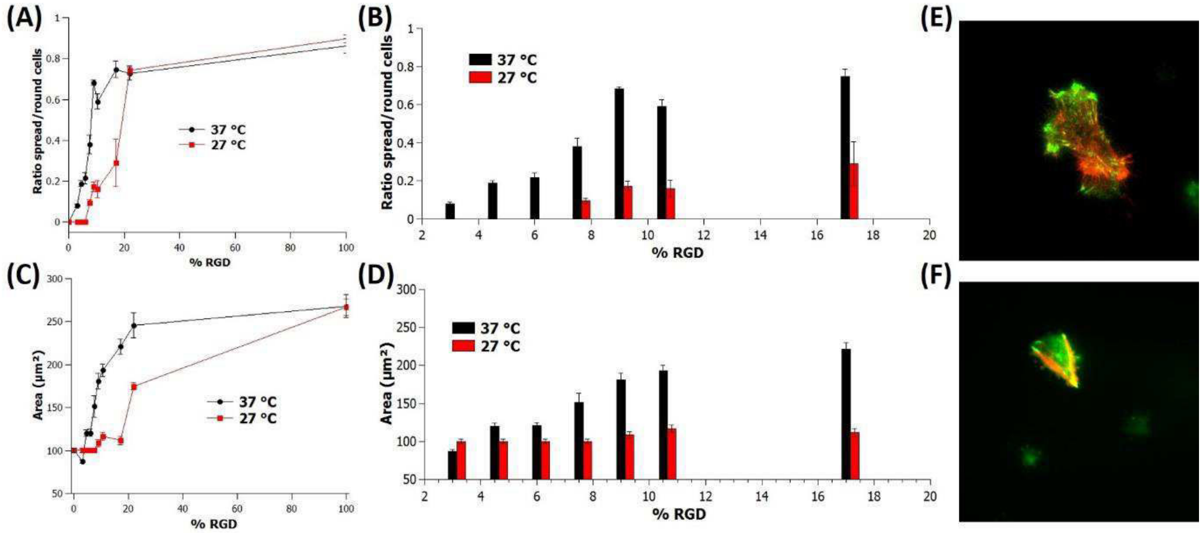

Figure 63 - Quantification of cell adhesion on mixed PLL-g-[0.15]P(NIPAM-co-RGD)(6)/PLL-g-[0.2]PNIPAM(6) adlayers after 180 minutes of incubation at 37 or 27 °C (serum-free DMEM, 3 H of incubation). (A-B) Ratio between spread and round cells. (C-D) Cell area. TIRF pictures of living cells (100× objective, green: Vinculin, red: Actin) on 7.5 % RGD at 37 °C (E) and 27 °C (F).

This threshold density is lower at 37 °C compared to 27 °C. This suggests that RGD could be more accessible when displayed by hydrophobic PNIPAM layer than in the hydrophilic PNIPAM layer. Similar increasing accessibility of RGD has been reported in mixed SAM made of short RGD-containing strands and long T-responsive ones (Mastrotto et al., 2011). However, this contrasts with biotinylated PLL-g-PNIPAM trapping biotin at T > LCST, that is shown in chapter 4. This difference of behavior can stem from the ligand hydrophilicity and volume. Indeed, Biotin may be more prone to partition into hydrophobic domains and to be trapped into collapsed and aggregated PNIPAM clusters, whereas the larger and hydrophilic (even zwitterionic) RGD-linker moieties may prefer the contact with water. Two tentative schemes can be considered to illustrate the enhanced accessibility of RGD at high temperatures. Either the PNIPAM chains of PLL-g-[0.15]P(NIPAM-co-RGD)(6) collapse in mixed clusters with those of PLL-g-PNIPAM. In this case, we propose that the hydrophilic peptides are exposed on the surface of the hydrophobic nanoaggregates formed above LCST (Figure 64 bottom). Or, PNIPAM chains from PLL-g-PNIPAM may collapse without including PLL-g-[0.15]P(NIPAM-co-RGD)(6) which doesn't undergo any transition in the temperature window of 27°C-37°C. In this case, RGD are obviously more accessible as a consequence of the decrease in steric repulsions on collapsed of the cell-repellent PNIPAM strands (Figure 64 top).

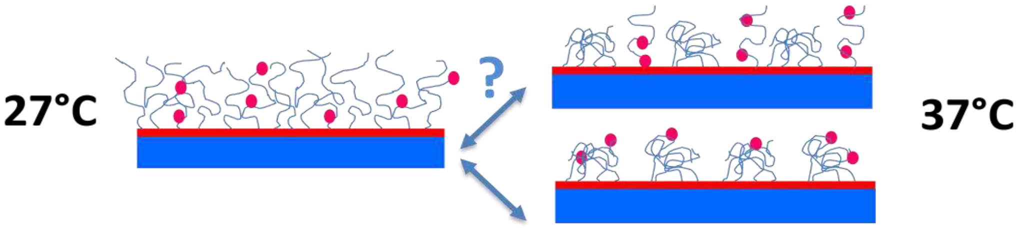

Figure 64 - Model for mixed PLL-g-[0.2]PNIPAM(6)/PLL-g-[0.15]P(NIPAM-co-RGD)(6) coatings.

The differences of cell adhesion between high/low temperatures are certainly due to a change in peptide accessibility on/in the polymer layer. However, it must be kept in mind that both elasticity and roughness are also important parameters which considerably impact the cell behavior.

Indeed, roughness was shown to vary (at nanoscale) upon thermal transition of PLL-g-PNIPAM adlayer. On the other hand, we believe that the change in rigidity from 0.5 to 5 MPa across PLL-g-PNIPAM transition (see AFM data in Chapter 3) can be ignored as regard the raw adhesion pattern. In fact, a variation of two orders of magnitude in substrate rigidity is required to impact cell adhesion (Engler et al., 2004; Huang et al., 2011). The effect of roughness on cell adhesion isn't clearly elucidated according to literature. Change of roughness, even at the nanometer scale may modify ligand accessibility for integrin whose radius is of the same order of magnitude (Chapter 4, PLL-g-[0.1]P(NIPAM-co-Biotin)(6) coatings).

It can be noticed that FAs and stress fibers are formed in the spread cells at 37°C and 27°C as seen by TIRF microscopy (Figure 63). The cells at 37°C contains fibers that are distributed in the whole cytosol, as expected for densely anchored cells. In contrast, on the rare cells that adhered at 27°C, stress fibers connect a few spots, showing the scarce number of attachment spots. A detailed analysis of the evolution of FAs as a function of the RGD density is possible thanks to PLL-g-PNIPAM tunable mixed layers. But, it was not conducted yet because we chose to find conditions of reversible adhesion/de-adhesion.

3 Cell detachment from mixed PLL-g-[0.2]PNIPAM(6)/PLL-g-[0.15]P(NIPAM-co-RGD)(6) coatings

We examined the possibility to tune surface properties in order to achieve locally triggered, reversible adhesion/de-adhesion, which is a demanding criterion about robustness and adjustability of the system. Surfaces enabling on demand de-adhesion provide in addition experimentally useful tools for studies of FAs maturation. Indeed, during migration, FAs are initiated as tiny focal complexes that assemble underneath the lamellipodium. A subpopulation of focal complexes disassembles within minutes, while the remainder grows into mature FAs that either disassemble within 10–20 min (detachment enabling migration) or carry on maturing into stable fibrillar adhesions that hamper cell motility. Thus it was interesting to consider possible application of PLL-g-[0.15]P(NIPAM-co-RGD)(6) layers to modulate this process in either directions thanks to the facile tuning of RGD density and *in situ* switch of RGD accessibility. In this context, we investigated cell detachment from PLL-g-[0.2]PNIPAM(6)/PLL-g-[0.15]P(NIPAM-co-RGD)(6) coatings.

First, the experiments were conducted on homogeneous (unpatterned) surfaces to check the detachment rate. Cells were seeded on layers of different RGD densities (9, 16, 10.5 and 100 % RGD) at 37 °C (i.e. adhesive state) to enable cell spreading (incubation at 37 °C for 3H). Detachment was triggered by decreasing temperature down to 27 °C. We measured the ratio ρ between spread and round cells as a function of time after the beginning of temperature decrease (Figure 65). The rate of cellular morphology change, from spread to round, was higher for the lowest RGD densities (but obviously kept above the threshold density enabling initial cell spreading at 37°C). Indeed, cell detachment was fast and efficient on 9 % RGD coatings ($\rho < 20$ % after 200 minutes) whereas cells didn't detach at all on 16 % RGD (as indicated by a constant ratio ρ of 100 % during the whole experiment). This suggest that extension of the PNIPAM chains without RGD induces repulsive forces on cell membrane, which triggers deadhesion (Mandal et al., 2012). On non-thermoresponsive layers (100 % RGD), no effect of temperature on cell morphology was observed, what confirms that cooling to 27°C do not affect the cell itself. Transition from spread to round morphology correlates with the variation of ligand accessibility as shown in chapter 4, though the sensitivity to RGD density appears extremely high (see difference between 10.5 and 9% RGD in Figure 65). It must be noticed that cells are still alive after detachment. In fact, we have observed re-adhesion of cells upon re-incubation at 37 °C.

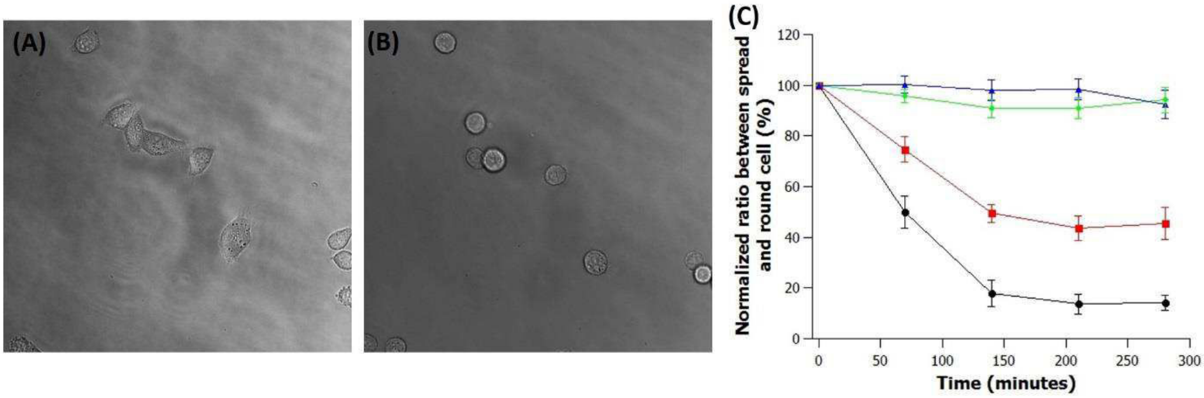

Figure 65 - Cell de-adhesion from PLL-g-[0.2]PNIPAM(6)/PLL-g-[0.15]P(NIPAM-co-RGD)(6) coatings. Cells were initially seeded in serum-free DMEM at 37 °C. After 3 H of incubation at 37 °C (image A, 9 % RGD), detachment was triggered by temperature drop (27 °C). Image B was taken after 4 H at 27 °C on the same position than image A. C: Normalized ratio between spread and round cells as a function of time (blue: 100 % RGD, green: 16 % RGD, red: 10.5 % RGD, black: 9 % RGD, average on 100 cells for each % RGD).

The characteristic time of deadhesion was here approximately 150 minutes which is only slightly longer than reported times on thermoresponsive RGD-containing layers. Similar order of magnitude of cell de-adhesion are reported in the case of layers containing covalently attached epitopes, with a trend for faster unbinding when the swollen layer is thicker. For example, 100 minutes were needed on PNIPAM hydrogels (Chapter 1 – Figure 20, (Ebara et al., 2004)) while only 15 minutes on 100nm-thick 2-(2-methoxyethoxy)ethyl methacrylate brushes (Chapter 1 – Figure 22, (Desseaux and Klok, 2014)). The accelerated detachment from layers made of PEG-containing copolymers is generally attributed to the flexibility and hydrophilicity of OEG strands that are expected to exert repulsive constraints on cells (Tang et al., 2012). This phenomenon must be all the more pronounced for thick PNIPMAM layers which are assumed to introduce permanently hydrated domains that accelerate swelling. In the literature, faster detachment were also achieved by using sacrificial layers that dissolve upon temperature shifts (Patel and Zhang, 2013), which cannot be compared to permanent layers.

As mixed PLL-g-[0.2]PNIPAM(6)/PLL-g-[0.15]P(NIPAM-co-RGD)(6) coatings can modulate specific cell adhesion between 27 and 37 °C on a broad RGD composition range (8-20 % RGD), the system enabled on the one hand to illustrate competition for adhesion on substrates containing different RGD densities, and on the other hand to check the reversibility of cell adhesion/de-adhesion.

4 An example of dynamic experiment on mixed thermo-responsive PLL-g-[0.15]P(NIPAM-co-RGD)(6)/PLL-g-[0.2]PNIPAM(6) coatings

To illustrate possible cell manipulations based on PLL-g-PNIPAM adlayers, we designed an experiment aiming to switch reversibly cell shape (Figure 66). A grid pattern was prepared with thermoresponsive vertical stripes, non-responsive adhesive horizontal stripes and a repellent PLL-g-

PEG background. Vertical stripes were coated with mixed solutions of PLL-g-[0.15]P(NIPAM-co-RGD)(6)/PLL-g-[0.2]PNIPAM(6) (7.5 - 10.5 % RGD). Consequently, these vertical stripes are adhesive at 37 °C and repellent at 27 °C. Adhesive non-responsive horizontal stripes were coated with a solution of PLL-g-[0.15]P(NIPAM-co-RGD)(6)/PLL-g-PEG (with 16 % RGD-presenting PLL compared to the total PLL amount). On this substrate, cells have to choose whether they bind on the denser RGD stripes, or on both thermo-responsive stripes and non-responsive ones. They can also change their shape between a “cross shape” (binding on the two orthogonal stripes at the "cross-road") and a “elongated shape” along one single stripe.

60 µm was chosen for the distance between stripes because cells can overlap simultaneously on two parallel stripes for smaller distances. The RGD density of non-thermoresponsive stripes was chosen in order to see the same proportion of spread cells on both thermo and non-thermoresponsive stripes. Thanks to these optimizations, we succeeded in observing “cross” cells.

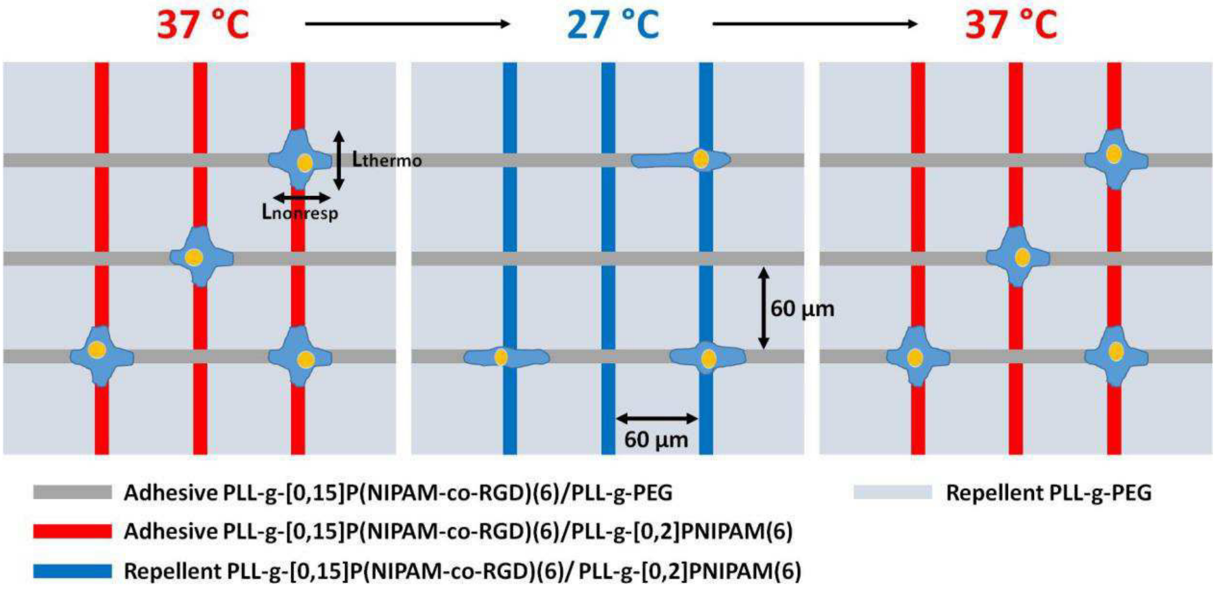

Figure 66 - Schematic representation of reversible temperature-triggered change in cell shape on grid pattern. Width of stripes is 10 µm. Vertical stripes are thermoresponsive (adhesive at 37 °C and repellent at 27 °C) while adhesive vertical stripes are non-thermoresponsive.

After 3H of incubation in serum-free DMEM at 37 °C on grid pattern, HeLa cells sitting at the cross-point between vertical and horizontal stripes adopted a cross shape. Movies of those cross-shaped cells were acquired while imposing two successive temperature jumps (first jump: 37 → 27 °C at 120 minutes, second jump: 27 → 37 °C at 320 minutes). For quantifications, we selected single cells which stayed at the intersection of vertical/horizontal stripes during the whole movie (and did not escape by migration along one stripe). One example of such a cell is highlighted on a split movie (Figure 67). During the first 120 minutes, this cell stuck on both vertical and orthogonal axes. At 27 °C, a retraction from the thermo-responsive vertical axe occurred up to cell confinement in the horizontal stripe (elongated shape) at the steady state (310 minutes). By increasing temperature back to 37 °C, this cell started again to interact on the vertical stripe.

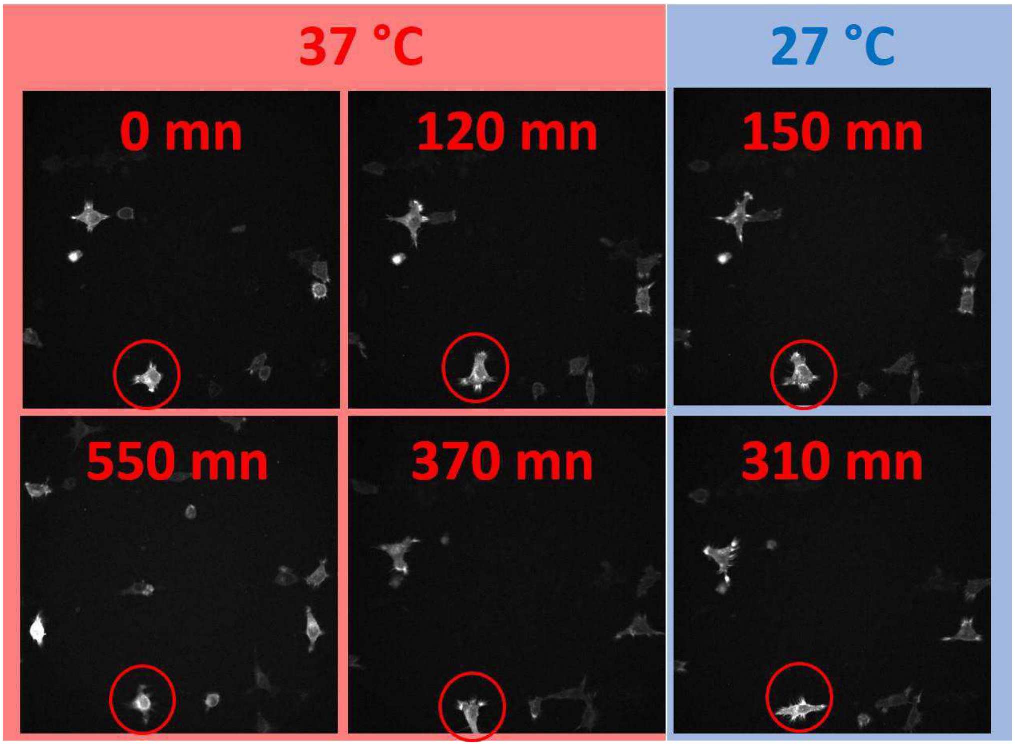

Figure 67 - Movie of HeLa cells on grid pattern (confocal, ×20 objective, Vinculin-mCherry). The cell located in the red circle was considered for quantification analyses. Thermoresponsive axe: PLL-g-[0.15]P(NIPAM-co-RGD)(6)/PLL-g-[0.2]PNIPAM(6) 9 % RGD. Non-thermoresponsive axe: PLL-g-[0.15]P(NIPAM-co-RGD)(6)/PLL-g-PEG 16 % RGD.

To quantify the change in cell shape under thermal stimulation, we evaluated the elongation of cross-shaped cells on both vertical (L_{thermo}) and horizontal ($L_{nonresp}$) axes. In order to take into account the initial cell shape dispersion, vertical and horizontal elongations were normalized by the initial length in the corresponding axes: $\frac{L-L_0}{L_0}$ (L_{thermo} and $L_{nonresp}$ are represented on Figure 66). Normalized elongations were plotted in Figure 68 (9 % RGD in thermoresponsive stripes). At the beginning, vertical elongation reached 40 % while horizontal elongation stayed constant. By decreasing T to 27 °C, repellency of vertical stripes was increased, and vertical elongation decreased back to its initial value after a retraction time τ (~ 100 minutes). This suggests that cells didn't completely retract from thermoresponsive stripes. Simultaneously, horizontal elongation increased up to 60 %. After temperature increase, horizontal elongation slightly decreased while vertical elongation sharply increased from 0 to 50 % with an evolution time τ that was similar to the retraction time. This experiment shows the reversibility of the adhesive state on PLL-g-[0.2]PNIPAM(6)/PLL-g-[0.15]P(NIPAM-co-RGD)(6) coatings. A competition between the two axes is highlighted by the opposite elongation trends on vertical and horizontal axes. The delay time τ cannot be analyzed yet in term of cell response time. In fact, the available temperature controller (change of temperature of the whole microscope) didn't achieve rapid temperature switch compared to a few minutes.

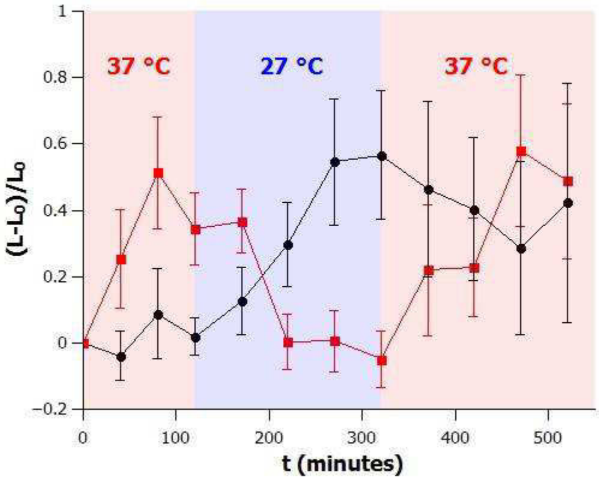

Figure 68 - Elongation of HeLa "cross-shaped" cells on thermo and non-responsive crossed stripes (average on 10 cells). Thermoresponsive stripes (red curve): PLL-g-[0.15]P(NIPAM-co-RGD)(6)/PLL-g-[0.2]PNIPAM(6) 9 % RGD. Non-thermoresponsive stripes (black curve): PLL-g-[0.15]P(NIPAM-co-RGD)(6)/PLL-g-PEG 16 % RGD.

One other way to quantify this competition consists in calculating the ratio between lengths along each direction: $({}^{Lthermo}/_{Lnonresp})_{Norm} = \frac{\left(\frac{L_{thermo}}{L_{nonresp}}\right)_t}{\left(\frac{L_{thermo}}{L_{nonresp}}\right)_0}$, normalized by its initial value at time zero. At the beginning of the experiment, at 37 °C, this ratio was constant, suggesting that an equilibrium shape was reached (Figure 69). Then, cells preferred adhesive horizontal stripes as quantified by the decrease in $({}^{Lthermo}/_{Lnonresp})_{Norm}$ at 27 °C. The ratio went back to its initial value at the end of the experiment when T was set back to 37 °C. This analysis presents more obviously the trends for competitive elongation. Similar results were finally obtained for three compositions in the thermoresponsive stripes (7.5, 9 and 10.5 % RGD) while fixing the composition of the non-responsive ones. The cell-response to the thermal stimulation is effective and reversible upon variation of RGD-containing polymer by 3%, what suggests that a correspondingly higher fraction of RGD is hidden upon temperature shift.

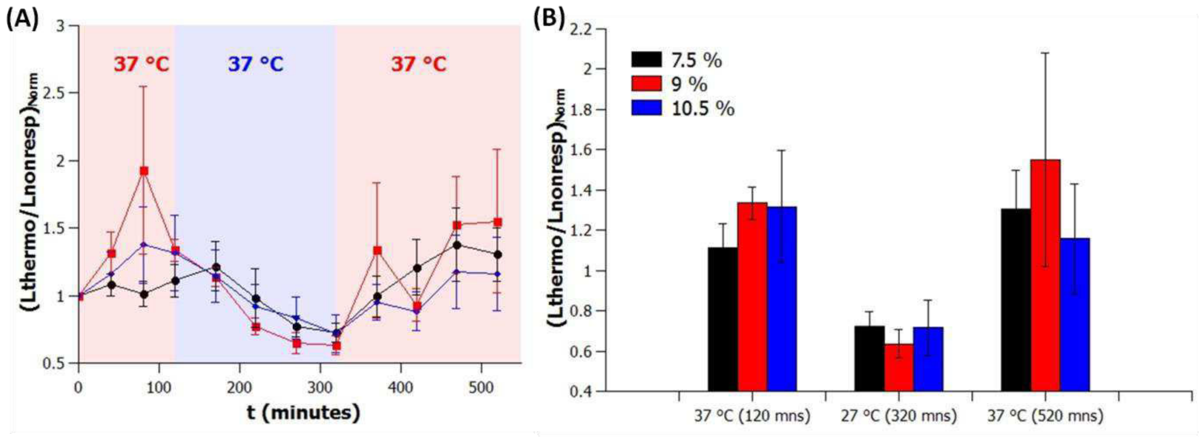

Figure 69 - Evolution of the ratio between cell length along thermo and non-responsive stripes for three compositions of the thermoresponsive axe (black: 7.5 % RGD, red: 9 % RGD, blue: 10.5 % RGD) (average on 10 cells).

Conclusion

In this chapter, we demonstrate that specific cell adhesion can be thermally modulated on mixed PLL-g-[0.2]PNIPAM(6)/PLL-g-[0.15]P(NIPAM-co-RGD)(6) adlayers of RGD densities closed to 10 % RGD. To explain the enhanced adhesion on collapsed PNIPAM brushes (37 °C) than on swollen brushes (27 °C), we assume that RGD peptides are more accessible at 37 °C although the exact mechanism isn't yet elucidated.

Moreover, we observe reversible cell adhesion thanks to cell detachment experiments. Two origins of de-adhesion on grafted thermoresponsive layers have been identified. First, weakly adsorbed matrix proteins (playing the role of epitopes on unmodified pure PNIPAM layers) are desorbed from the swollen layers; this mechanism does not apply to our system. Second, the force applied on the cell membrane by the polymer brush upon swelling breaks integrin:epitope associations in FAs (in the language of physicists, the swollen brushes exert a disjoining pressure than equal or overcome attractive surface forces). Namely, based on experimental estimates of maximal pulling strength by a cell (lower than 1 μN), and shape of membranes on the top of FAs, theoretical calculations by (Halperin and Kröger, 2012) suggest that an effective detachment is reached if the length (resp. density) of PNIPAM chains is superior to $DP_n = 200$ (resp. > 1 chain per 50 nm^2). In such calculations, a denser grafting density of PNIPAM in PLL-g-PNIPAM layers compensates somehow the shorter length of chains. However, when the target peptides is buried into the swelling PNIPAM brushes at distance shorter than the length of the fibronectin:RGD complex (about 20 nm), the repulsion due to swelling doesn't reach the cell membrane as it is hypothesized in Halperin's approach. In the case of thin PLL-g-PNIPAM layers, penetration of the complex into the swollen layer introduces nevertheless tension on the bound integrin:epitope complexes due to the osmotic repulsion exerted on the protein by the brush. This is expected to fasten unbinding by decreasing the energy barrier for integrin:epitope dissociation (Halperin and Kröger, 2012). Consequently, slow detachment may also come from the fact that repulsions emerging at low T are essentially affecting individual receptors and not the whole membrane if the layer thickness is inferior to 20 nm. Random RGD positions in the PNIPAM strands used in this study may also introduce a broad dispersity of response time. In conclusion, the present system compares with other RGD-carrying PNIPAM layers, despite the shorter length of PNIPAM strands. To improve the rate of cell responses, RGDs could be located closer to the PLL backbone or/and more repulsive ends could be added at the top of the layer. This optimization was out of the scope of this thesis.

Our dynamic experiment of temperature-triggered change in cell shape illustrates possible cell manipulations based on mixed PLL-g-[0.2]PNIPAM(6)/PLL-g-[0.15]P(NIPAM-co-RGD)(6) adlayers. In the near future, it could be interesting to study the dynamic of FA maturation on such polymer adlayers.

Bibliography

Arnold, M., Cavalcanti-Adam, E.A., Glass, R., Blümmel, J., Eck, W., Kantlehner, M., Kessler, H., and Spatz, J.P. (2004). Activation of Integrin Function by Nanopatterned Adhesive Interfaces. ChemPhysChem *5*, 383–388.

Desseaux, S., and Klok, H.-A. (2014). Temperature-Controlled Masking/Unmasking of Cell-Adhesive Cues with Poly(ethylene glycol) Methacrylate Based Brushes. Biomacromolecules *15*, 3859–3865.

Ebara, M., Yamato, M., Aoyagi, T., Kikuchi, A., Sakai, K., and Okano, T. (2004). Temperature-Responsive Cell Culture Surfaces Enable “On−Off” Affinity Control between Cell Integrins and RGDS Ligands. Biomacromolecules *5*, 505–510.

Engler, A.J., Griffin, M.A., Sen, S., Bönnemann, C.G., Sweeney, H.L., and Discher, D.E. (2004). Myotubes differentiate optimally on substrates with tissue-like stiffness pathological implications for soft or stiff microenvironments. J. Cell Biol. *166*, 877–887.

Halperin, A., and Kröger, M. (2012). Thermoresponsive Cell Culture Substrates Based on PNIPAM Brushes Functionalized with Adhesion Peptides: Theoretical Considerations of Mechanism and Design. Langmuir *28*, 16623–16637.

Huang, J., Peng, X., Xiong, C., and Fang, J. (2011). Influence of substrate stiffness on cell–substrate interfacial adhesion and spreading: A mechano-chemical coupling model. J. Colloid Interface Sci. *355*, 503–508.

Hudalla, G.A., and Murphy, W.L. (2009). Using “Click” Chemistry to Prepare SAM Substrates to Study Stem Cell Adhesion. Langmuir *25*, 5737–5746.

Lagunas, A., Comelles, J., Martínez, E., Prats-Alfonso, E., Acosta, G.A., Albericio, F., and Samitier, J. (2012). Cell adhesion and focal contact formation on linear RGD molecular gradients: study of non-linear concentration dependence effects. Nanomedicine Nanotechnol. Biol. Med. *8*, 432–439.

Li, L., Zhu, Y., Li, B., and Gao, C. (2008). Fabrication of Thermoresponsive Polymer Gradients for Study of Cell Adhesion and Detachment. Langmuir *24*, 13632–13639.

Mandal, K., Balland, M., and Bureau, L. (2012). Thermoresponsive Micropatterned Substrates for Single Cell Studies. PLoS ONE *7*.

Mastrotto, F., Caliceti, P., Amendola, V., Bersani, S., Magnusson, J.P., Meneghetti, M., Mantovani, G., Alexander, C., and Salmaso, S. (2011). Polymer control of ligand display on gold nanoparticles for multimodal switchable cell targeting. Chem. Commun. *47*, 9846–9848.

Nagase, K., Watanabe, M., Kikuchi, A., Yamato, M., and Okano, T. (2011). Thermo-Responsive Polymer Brushes as Intelligent Biointerfaces: Preparation via ATRP and Characterization. Macromol. Biosci. *11*, 400–409.

Patel, N.G., and Zhang, G. (2013). Responsive systems for cell sheet detachment. Organogenesis *9*, 93–100.

Takahashi, H., Nakayama, M., Yamato, M., and Okano, T. (2010). Controlled Chain Length and Graft Density of Thermoresponsive Polymer Brushes for Optimizing Cell Sheet Harvest. Biomacromolecules *11*, 1991–1999.

Tang, Z., Akiyama, Y., and Okano, T. (2012). Temperature-Responsive Polymer Modified Surface for Cell Sheet Engineering. Polymers *4*, 1478–1498.

Tang, Z., Akiyama, Y., and Okano, T. (2014). Recent development of temperature-responsive cell culture surface using poly(N-isopropylacrylamide). J. Polym. Sci. Part B Polym. Phys. *52*, 917–926.

Chapter 6 - Studies of poly(N-isopropylacrylamide) polymers functionalized with azobenzene to develop light-responsive brushes

Contents

Introduction

In this chapter, we describe systems undergoing *in situ* reversible responses to light. Reversibility is obviously more demanding to achieve than "one shot" photocleavage-based responses (see Chapter 1 for cleavable layers used in controlled cell de-adhesion) or *ex-situ* irreversible photopatterning. To our knowledge, reversible *in situ* optical control of hydrogels or polymer films, for controlled protein binding or cell adhesion, requires to switch interpolymer and polymer:water interactions. This is typically obtained near the solubility transition of the chains. Systems based on thermo-sensitive polymers close to cloud point T_{CP} are accordingly excellent candidates for such goal. After a short state of the art on thermo/photo-responsive polymers, our results on azobenzene-containing PNIPAM are presented.

1 State of the art on thermo- and photo-responsive polymers

1.1 How to obtain reversible photo-responsive polymers starting from thermo-responsive ones?

In general, systems based on polymers that are sensitive to a single stimulus are relatively easy to turn into polymers showing a response to multiple stimuli. In particular, isothermal switching exploiting LCST behavior has been achieved not only on PNIPAM but on a broad range of thermo-responsive polymers (poly(N-alkyl-acrylamides) (Liu and Zhu, 1999), oligo(ethylene glycol) methyl ether methacrylates (Jochum et al., 2009),...). The usual principle relies on the fact that cloud point T_{CP} depends on the hydrophilicity of comonomers. Thus a secondary trigger that is able to modulate the hydrophilicity of comonomers can induce a shift above or below the phase transition conditions at a constant temperature. Different secondary triggers are used such as a change in pH (Dai et al., 2008), added salts (Hahn et al., 1998), molecular recognition processes (Buller et al., 2011; Irie et al., 1993), and light.

During the last decades, many efforts have been made to develop light-responsive polymers based on thermo-responsive ones. Historically, it began with studies in cyclohexane solutions of azobenzene-containing polystyrenes or spirobenzopyran-modified polystyrenes by the Irie's team in 1983. They showed that the polarity change in pendant chromophores due to photo-isomerization affects the polymer-solvent and polymer-polymer interactions, resulting in light-induced polymer precipitation. Later, they similarly used azobenzene as pendant groups in PNIPAM chains to successfully photo-control the T_{CP} of poly(NIPAM-co-N-(4-phenylazophenyl)acrylamide). Bioapplications were not the aim of these pioneering studies. But, up to now, introducing chromophores into thermo-responsive polymer chains is the general strategy to design light-responsive polymers.

For bioapplications, an ideal photo-polymer must be able to reversibly collapse and to completely redissolve under light-stimulations in the visible or near IR range of wavelengths. It is essential that the light-induced shift of T_{CP} is enough large to guarantee marked responses in the conditions fixed by cell culture (temperature, ionic strength, pH, ...). Specific monomers have thus to be introduced into the light-responsive chains in order to adjust the optimal responses for each specific application. Moreover, it may be useful to come with a set of different T_{CP} (and/or photo-variation of T_{CP}). Diversity and adjustments are thus important key-words, in addition to the common requests (absence of toxicity, absence of non-specific attraction, ...).

As regards the diversity of light-sensitive groups, two main molecular transitions have been exploited to reversibly modulate T_{CP} under exposure to light: photo-dimerization and photo-isomerization.

Photo-dimerizable compounds:

Photo-dimerizable chromophores (dimethylmaleimide (Kuckling et al., 2006), coumarin (Zhao et al., 2011), and more generally compounds prone to cycloadditions (stilbene (Ivanova et al., 2000), acridizinium (Kuckling et al., 2002))) have been used as cross-linkable compounds. For example, Zhao *et al.* shown that poly(N,N-dimethylamino-ethyl methacrylate) containing coumarin moieties can tune T_{CP} by UV irradiation. They observe an increase in T_{CP} up to 30 °C for the full dimerization of polymer having 8 mol% coumarin functionalities in comparison with the initial linear polymer. Once cross-linked by irradiation at 310 nm, the loops reduce the interchain entanglement and consequently delay polymer aggregation/dehydratation. This phenomenon isn't entirely reversible: irradiation at 260 nm breaks only a part of dimers. While promising developments have been proposed for applications in material sciences (e.g. self-healing plastics), the low wavelength required up to now to activate dimerizations (<350nm) renders conventional dimerizable groups useless for manipulation of living cells. They are thus not reviewed in this manuscript.

Photochromic compounds:

Photochromic molecules are used to photomodulate reversibly the T_{CP} with wavelength in the visible range. Those photochromes undergo a reversible isomerization upon irradiation, inducing generally a polarity change and an absorption change in the chromophoric units. For polymers containing photochromes, the T_{CP} value depends on the dye polarity: an increase in T_{CP} is generally correlated with formation of more polar isomers. The number of reversible photo-reactions suited for aqueous media is however limited, reducing the choice of photochromes. Azobenzene, spiropyran (Ivanov et al., 2002), salicylideneaniline (Jochum and Theato, 2009a), and cinnamate (Laschewsky and Rekaï, 2000) are photochromes which have been used for that purpose (Figure 70).

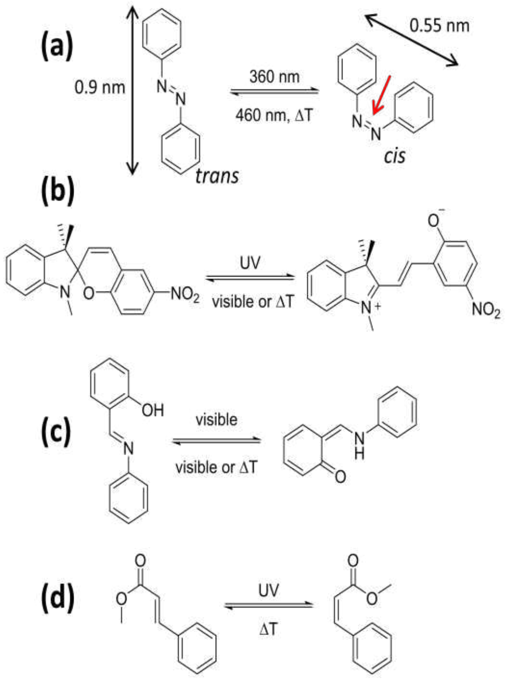

Figure 70 - Photochromes used in light- and thermo-responsive polymers: (a) azobenzene, (b) spiropyran, (c) salicylideneaniline, (d) cinnamate.

Most temperature-responsive polymers use azobenzene as light-responsive photochromes for different reasons:

- the properties of azobenzene and its grafting on diverse macromolecules are easy to adjust by introduction of various substituents; synthesis at gram scale is not an issue.
- azobenzene *cis*:*trans* conversion is highly reversible, and not very sensitive to solvent polarity.
- photoisomerization kinetics are fast (< second).

The photo-isomerization of azobenzene reaches an equilibrium between *cis* and *trans* isomers of the N=N double bond (Figure 70a). The *trans* isomer is the thermodynamically more stable form. In the dark, thermal isomerization results in recovery of the predominant *trans* isomer. The *trans* azobenzene is planar whereas the *cis* isomer isn't planar (the two aromatic cycles are twisted by about 55°). *Trans*:*cis* isomerization is also accompanied by an increase in the dipole moment (from 0 D to around 3 D for azobenzene without substituent) and a decrease in the end-to-end distance by about 3.5 Å.

1.2 Main results on thermo-responsive polymers containing azobenzene

Below, the difference of T_{CP} between UV and Blue irradiations will be referred to ΔT_{CP} $(T_{CP,UV} - T_{CP,Blue})$.

The first report on temperature- and light-responsive polymers of Kungwatchakun and Irie in 1988 (Kungwatchakun and Masahiro, 1988) describes the synthesis of poly(NIPAM-co-N-(4-phenylazophenyl)acrylamides) by direct polymerization of NIPAM with N-(4-phenylazophenyl)acrylamide. A copolymer containing 2.7 mol% azobenzene groups shows a reversible shift in T_{CP} from 21 °C to 27 °C under UV irradiation. This result is explained by the change in polarity of the azobenzene. Variation of the copolymer composition with different amount of azobenzenes shows that the photoisomerization is only effective in a narrow content range (Figure 71): ΔT_{CP} increases with azobenzene content up to 2.7 mol% then it decreases. To explain this phenomenon, Kungwatchakun and Irie suggested that the phase separation temperature depends on the balance between the hydrogen bond ability of the polymer with water and the intermolecular hydrophobic forces. While large amounts of azobenzenes increase the polarity gap between the *cis*- and *trans*-state, the global hydrophobicity also increases concomitantly. That's why Irie *et al.* proposed that the overall hydrophobicity added by the presence of azobenzene hampers solubilization in water for chromophore contents above a threshold.

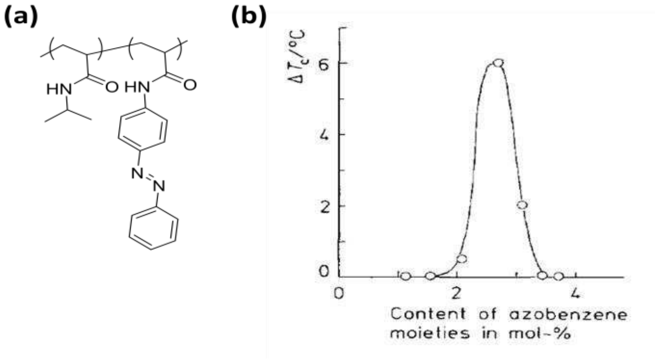

Figure 71 - First example of thermo- and light-responsive polymer: (a) chemical structure, (b) ΔT_{CP} (Kungwatchakun and Masahiro, 1988).

Several years later, Menzel *et al.* intended to increase the T_{CP} gap on a broader polymer composition in azobenzene (Kroger et al., 1994). They reported the synthesis of copolymers of N-,N-dimethylacrylamide and 4-phenylazophenyl acrylate by direct copolymerization of the corresponding monomers (Figure 72). They successfully obtained an appreciable light-induced T_{CP} gap up to 20 °C between 2 and 10 mol% in azobenzene groups. However, the transition is not sharp above 7.5 mol% azobenzene: it takes many degrees to be completely done. This broad transition is assumed to come from heterogeneities in copolymers due to non-ideal copolymerization in presence of azobenzene monomers. Indeed, N=N double bond reacts with the propagating radical, leading to retardation and reduced molar masses. To continue optimizing properties of these thermo-responsive polymers containing azobenzenes, synthetic progress had to be done.

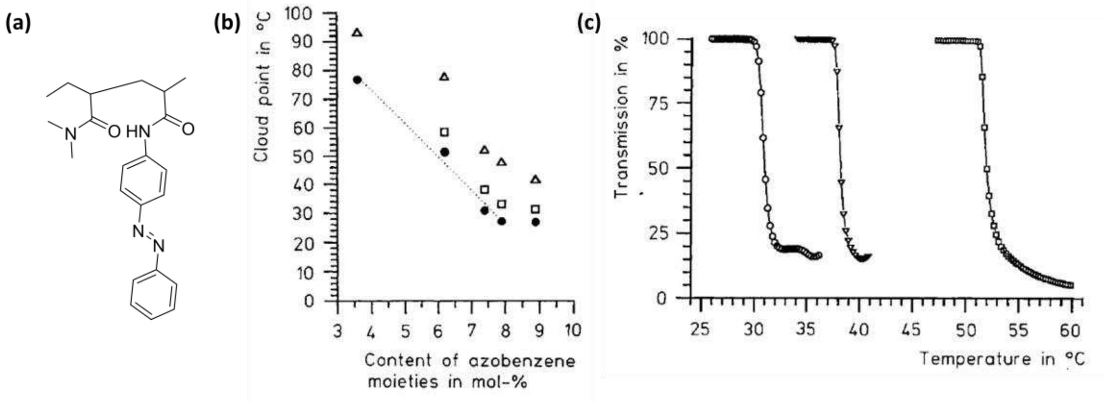

Figure 72 - Light-reponsive poly(N,N-dimethymacrylamide) developed by Kroger *et al.* (Kroger et al., 1994): (a) chemical structure, (b) T_{CP} values for different azobenzene contents (cirle: dark, triangle: UV illumination), (c) turbidity measurements of a solution containing poly(N,N-dimethymacrylamide) with 7.5 mol% azobenzene (circle: dark, triangle: blue light, square: UV light, 2.5 g.L^{-1} in water, heating rate 0,5 °C.min^{-1}).

After these promising studies, a new synthetic strategy has been developed by Menzel's team. The idea consists in firstly obtaining a well-defined parent polymer and then to functionalize it with azobenzene compounds. In 1995, Menzel *et al.* synthesized a protected poly(N-alkyl-N-hydroxyalkylacrylamide) by free radical polymerization and then functionalized it with reactive azobenzene derivatives after a deprotection step (Menzel et al., 1995). One other approach without deprotection step relies on polymerization of reactive monomers to afford a reactive precursor polymer. N-acryloxysuccinimide (Desponds and Freitag, 2003) and pentafluorophenylacrylate (Jochum and Theato, 2009b) have been used as reactive monomers, giving poly(activated esters) which can react with amines.

To optimize the magnitude of response to light (*i.e.* to reach highest variation of T_{CP} upon *cis*:*trans* isomerization) with copolymers modified by pendant azobenzene groups, diverse backbones were tested (peptides (Rodríguez-Cabello et al., 2002), modified cellulose (Zheng et al., 2004)) and additives such as cyclodextrins were successfully used. Optical shifts of cloud points by up to 20 °C could be achieved. These chains have however a higher persistence length than polyacrylic ones, which may contribute to limit the hydrophobic collapse seemingly hampering optimization of PNIPAM-based derivatives.

Recent studies benefit from the discovery of controlled radical polymerizations, which makes it possible to obtain polymers with a low dispersity and with defined extremities. Thanks to this synthetic development, studies of polymers with azobenzene located on the polymer extremities or well defined multiblock copolymers became possible, launching a revival of investigations on acrylic azobenzene-containing copolymers in order to optimize their magnitude of light-response. Zhao's team introduced copolymers alternating blocks with azobenzenes directly inserted into the polymer backbone (Boissiere et al. 2011) and PNIPAM blocks as depicted on Figure 73 (RAFT polymerization). In solution, this polymer forms flower-like micelles due to aggregation of the hydrophobic azobenzenes. These micelles stay essentially dispersed above the LCST, suggesting that dehydration of PNIPAM shell in flower-like conformation did not induce inter-micelle aggregation. PNIPAM transition occurred nevertheless close to 32°C as detected by NMR. Authors claim that with azobenzenes stacked together forming the micelle core, the multiple loops for individual PNIPAM chains could reduce the number of intermicellar bridge chains and restrict the chain entanglements upon dehydratation of PNIPAM, reducing the propensity for micellar aggregation. But, their interpretation is singular among the vast literature of PNIPAM-containing micelles. It is possible that the micelles contained a few percentage of ionized moieties, or polar groups that retarded inter-micelle aggregation. More importantly, no response to light was observed. This result confirms that azobenzene clustering "kill" the response to light. More surprisingly, this suggests that precise control of the architecture, namely loop formations, intervene in interchain aggregation.

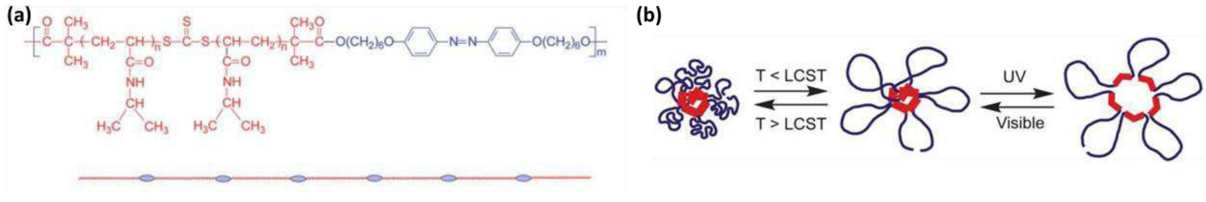

Figure 73 - PNIPAM with azobenzene regularly inserted into the polymer backbone (Boissiere et al. 2011): (a) chemical structure, (b) schematic representation of the stimuli-responsive behavior of the flower micelles obtained by dissolution of the polymer in water.

A few similar studies exist on thermo-responsive polymers with azobenzenes at the end or on the polymer chain. Some of those polymers show a direct light-response (the increase in cloud point with conversion from *trans* apolar to *cis* polar isomer), whereas others show a "reverse light-response" (characterized by negative values for ΔT_{CP}). This can be illustrated with azobenzene end-capped PNIPAM studied by Jochum *et al.* (Jochum et al. 2009) and by Akiyama *et al.* (Akiyama and Tamaoki, 2007) showing a marked and direct light-response whereas Ishii *et al.* (Ishii et al., 2011) observed a lack of photovariation in pure water and a reverse response in water:dioxane mixed solutions.

Finally, controlled radical copolymerizations enable to prepare bottle-brush architectures of macromolecules. The properties of this densest version of comb-like architectures may resemble those of grafted PLL polymers that we seek to prepare. Matyjaszewski *et al*. synthesized a macroinitiator poly(2-2-bromopropionyloxy(ethylmethacrylate)) PBPEM by ATRP, in order to prepare poly[BPEM-*graft*-(dimethylaminoethylmethacrylate-*stat*-methacryloyloxyazobenzene)] containing up to 20 mol% of azobenzene (Lee et al., 2006). These macromolecules were fully dispersed in water as small globules (with diameters inferior to 80 nm), suggesting that the controlled architecture improved solubility. Estimates of cloud points and of photo-induced variations of the hydrodynamic radius are reported, but the published data are scarce. Further studies are needed to distinguish between inter-chain aggregation (seemingly favored by the *trans* isomer form) and intrachain collapse, though this article suggests that direct responses to light can be obtained with bottle-brush architecture. Jonas *et al*. synthesized oligo(ethylene glycol)methacrylate-based brushes by ATRP (grafting from on glass substrates), that they post-modified with azobenzene up to a few mol% (Dirani et al., 2012). They found direct photo-responses, that is shrinkage of the brush upon *cis* to *trans* isomerization, but the magnitude of the response was only a few % of the expected full thermal collapse. These authors propose that steric hindrance decreases the yield of post-modification and limits the collapse, but they ignored apparently the possibility of structure-dependent reverse responses and/or vanishing responses.

1.3 "Reverse" light-response of thermo-responsive polymers containing azobenzene

Inversion of the direction of T_{CP} photoshift with increasing % azobenzene, or loss of responses to light at high % azobenzene in poly(acrylic) chains is certainly a major issue. To the best of our knowledge, the phenomenon has been reported in only six articles: the earliest being (Menzel and Kröger 1995) , (Desponds and Freitag, 2003), later by (Ishii et al., 2011; Yu et al., 2010), and only recently studied to establish convincing results on the origin of inverted responses (Miasnikova et al., 2013), (Liu et al., 2012). The mechanism proposed to interpret negative ΔT_{CP} shifts relies on hydrophobic azobenzene clustering, possibly under the form of micelles:

- Menzel *et al.* (Menzel et al., 1995) have observed for the first time this "reverse" light-response on copolymers (Figure 74). As they also observed a significant blue shift of the π-π* band with increasing azobenzene content, they assumed that chromophores formed hydrophobic clusters. In Figure 74, we can see that the T_{CP} decreases strongly with increasing azobenzene content from 1 to 4 % azobenzene and then decreases slowly above 4 % azobenzene. Authors attributed this result to aggregation hiding the hydrophobic azobenzene groups. The "reverse" photoshift of cloud point (lower T_{CP} under the *cis* UV-irradiated form in Figure 74) was similarly attributed to aggregation/clustering of *trans* azobenzene in copolymers containing the highest % azobenzene whereas polar *cis* azobenzene are well dispersed in the same conditions.

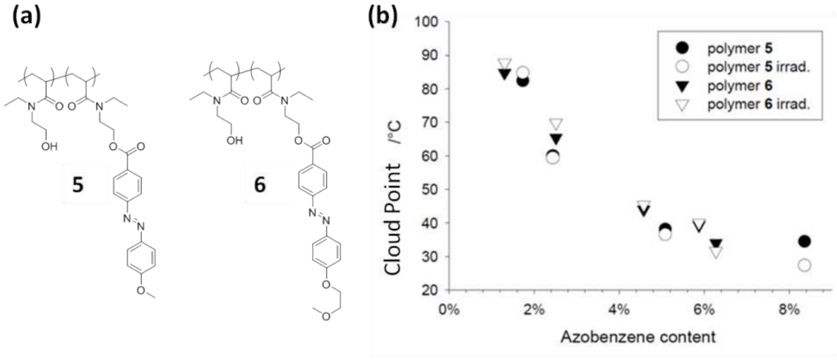

Figure 74 - Polymer structures (a) and T_{CP} behavior (b) observed by Menzel *et al.* (Menzel et al., 1995).

Similar results have been reported by Miasnikova *et al.* (Miasnikova et al., 2013) on poly(methoxydiethylene glycol acrylate) with azobenzene side groups. Contrary to Menzel's results, Figure 75 shows that the T_{CP} decreases linearly with increasing the fraction of azobenzene-containing monomers. The mechanism based on azobenzene aggregation isn't valid here. As it was firstly introduced by Desponds *et al.* (Desponds and Freitag, 2003), the packing of *trans* azobenzene can induce intrachain associations, creating loops in the polymer chain. These loops are assumed to reduce inter-chain entanglement and generate repulsions between polymer coils, increasing T_{CP} value compared to the non cross-linked polymer chain. Moreover, if azobenzene forms essentially small clusters or dimers and remain solvated by water, a linear decrease in T_{CP} with increasing azobenzene content is still expected (which differ from the case of partition of the azobenzene into micellar cores). Up to now, no proof of the formation of loops was provided experimentally. Miasnikova *et al.* concluded that a combination of both aggregation and loop effects are responsible for the reverse light-response when the azobenzene proportion increases.

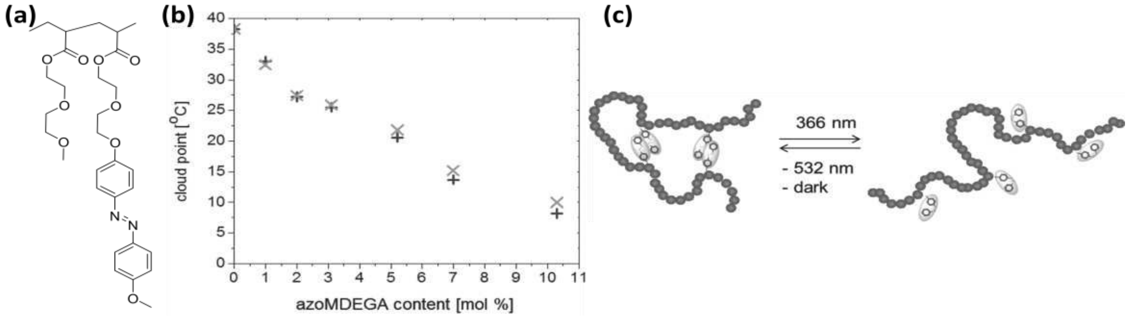

Figure 75 - Reverse behavior of light-sensitive poly(methoxydiethylene glycol acrylate) (Miasnikova et al., 2013): (a) polymer structure, (b) T_{CP} evolution with azobenzene content, (c) suggested mechanism.

- The study of amphiphilic P(NIPAM-co-oligo(ethyleneglycol)methylethermethacrylate-τazo) (PNIPAM-co-EGMA-τazo in Figure 76) by Liu *et al.* (Liu et al., 2012) shows an increase in cloud point with the azobenzene proportion when $\tau > 5$ mol%, while cloud point decreases with increasing % azobenzene at low degree of modification. This non-monotonous variation of T_{CP} is accompanied by an inverse light-response and observations by dynamic light scattering of micelles. The hydrophobic azobenzene groups become presumably hidden into the micellar core, which based on a phenomenological model is shown to quantitatively explains the increase in cloud point with increasing amount of azobenzenes per chain. The inverse light-response comes here from the partition equilibrium of the azobenzenes between the micellar core and the shell. Indeed, this partition equilibrium favors an increase in the fraction of *cis* isomer in the micelle corona, which in turn increases the effective hydrophobicity of the corona and decreases solubility of micelles upon exposure to UV light (*trans* to *cis* conversion). Under blue light, the more hydrophobic azobenzene becomes predominantly located (trapped) in the micellar core which makes the shell more hydrophilic and micelles more easy to disperse in water.

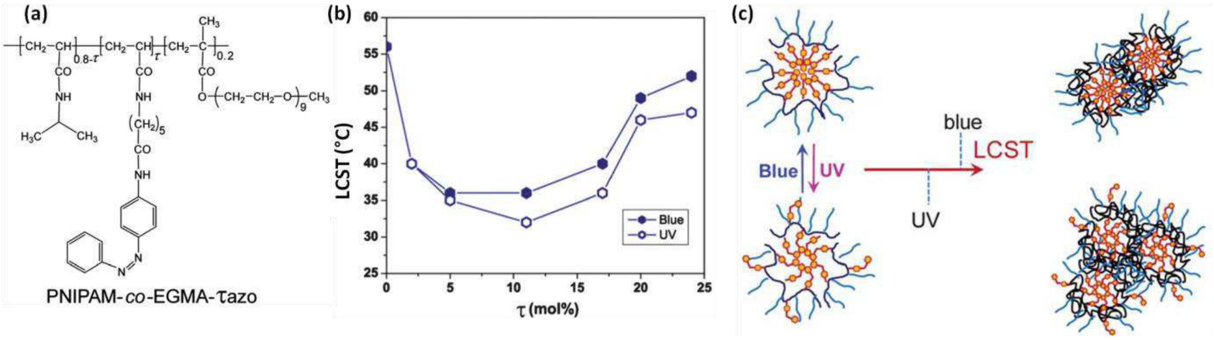

Figure 76 - Reverse behavior o*f ligh*t-sensitive PNIPAM-co-EGMA-τazo (Liu et al., 2012): (a) polymer structure, (b) T_{CP} evolution with azobenzene content, (c) suggested mechanism.

- Alternatively, Ishii et *al.* have attributed the inverse LCST behavior of α,ω-di-[4-cyanophenyl-4'-(6-hexyloxy)-azobenzene]-polyNIPAM solutions in water/1,4-dioxane (6 mol% dioxane) to the singular nature of the azobenzene used in their study (Ishii et al., 2011). The cyano substituent at 4 (para) position is singular because the *trans* isomer is in this case more polar (5 D) than the *cis* isomer (~ 3.6 D, Figure 77). Light scattering measurements show that the polymers formed micelles in water, irrespective of temperature and *cis*:*trans* isomerization. In water, the cloud point was not affected by exposure to light. In the presence of dioxanne (< 15%), the chains predominantly solubilize as isolated coils below T_{CP} for the trans-azobenzene isomer form, but formed aggregates or micelles in all other conditions (*cis* isomerization, or T > T_{CP}) (Figure 77b). The magnitude of photovariation of cloud point varies however in a non-monotonous manner with % dioxane, suggesting a subtle cross-influence between solvent-driven and isomerization-driven shifts of intra/inter-chain interactions (Figure 77c). Authors did not interpret these complex variations.

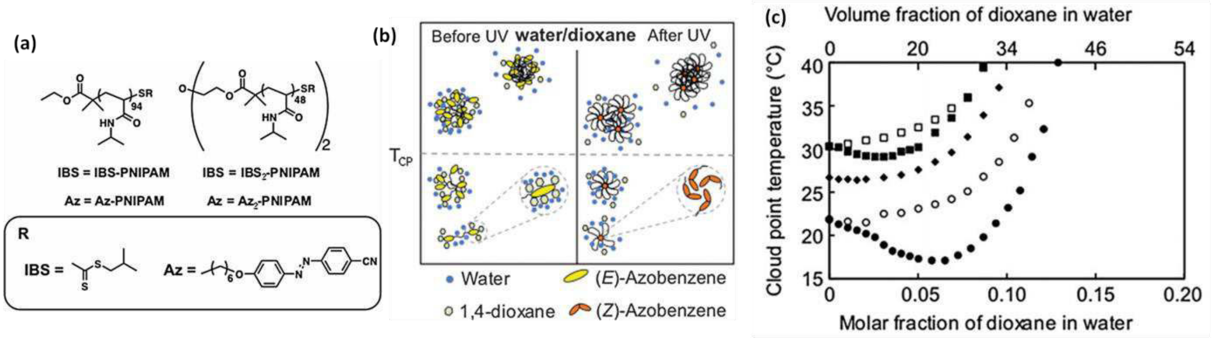

Figure 77 - "Reverse" behavior of light-sensitive IBS_2-PNIPAM and IBS-PNIPAM (Ishii et al., 2011): (a) polymer structure, (b) suggested mechanism, (c) phase diagrams of the polymer/water/1,4-dioxane ternary system established from cloud point measurements before irradiation (full symbols) and after irradiation at λ = 366 nm (open symbols) for Az_2-PNIPAM (circles), Az-PNIPAM (squares) and IBS_2-PNIPAM (diamonds).

2 Our strategy to make our PNIPAM grafts sensitive to light

2.1 The goal

Considering the diversity of observations on thermo- and light-responsive polymers, it appears difficult to predict how a thermo-responsive polymer containing azobenzene groups will behave under light stimulus in solution or deposited on a surface. Response involves multiple mechanisms including effect of architecture, polarity switch, formation of small clusters or micellar aggregates, ... At the beginning of this thesis, we considered accordingly that it was risky, but feasible to design thermo-responsive brushes on glass substrates to reach a significant optical response in conditions compatible with cell cultures. Further studies were however needed. Different factors could be considered such as the azobenzene substituents, the nature of the spacer between the polymer backbone and the azobenzene, position of the azobenzene in the chain...

During this project, optimization has been carried out as part of the development of PLL-g-PNIPAM derivatives. In particular, we wanted to keep the general synthesis of PLL-g-PNIPAM (Chapter 2). Consequently, we investigated the following possibilities:

- the architecture of the PNIPAM grafts:
  As we need one reactive end (e.g. NHS) to graft PNIPAM on the PLL, we considered **polymers bearing azobenzene as pendant groups or at a single end**. These two architectures have been studied.
- modification with azobenzene:
  The introduction of the azobenzene in the polymer chains was realized by post-modification of the reactive precursor PNAS, which uses azobenzene-containing amines.
  The introduction of the azobenzene at one extremity was made possible by using the appropriate CTA agent. We have synthesized an azobenzene-containing CTA by coupling an Azo-NH_2 with the commercial reactive CTA-NHS (see Chapter 2).

The optimization consisted in comparing the response to light, and cloud points as a function of the percentage of azobenzene introduced. To assess whether the hydrophobicity of azobenzene hampers the design of efficient systems, we also compared the effect of common phenylazophenyl moieties with that of a more polar para-carboxylate azobenzene.

2.2 The two azobenzenes used as photo-switcher

The two following azobenzene groups have been used, Azo-NH_2 and HOOC-Azo-NH_2 (Figure 78). The primary amine of these molecules is necessary to graft them on reactive parent chains whatever the final targetted polymer architecture.

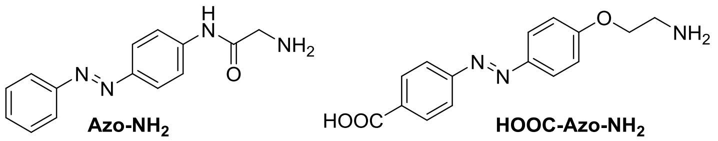

Figure 78 - Chemical structure of the two azobenzenes used for this study.

The main difference between these two compounds is the presence of a carboxylic acid in para position which enables to decrease the hydrophobicity of the azobenzene. At physiological pH, it is expected that azobenzene photochrome is under its anionic form.

These chomophores were designed with an alkyl linker between the azobenzene and the amine function. The size of the linker is an important parameter. Indeed, with linker composed of at least four carbons, hydrophobic azobenzenes are hydrophobic enough to form micelle-like aggregates (Liu et al., 2012; Ruchmann et al., 2011). This phenomenon can lead to complex auto-assemblages that we want to avoid (see Liu *et al.* (Liu et al., 2012)and comments above about PNIPAM-co-OEGMA-τazo in Figure 76). For smaller linkers, the proximity between the azobenzene and the polymer backbone may prevents this kind of association. That's why we have used linkers with only two carbons for Azo-NH$_2$ and HOOC-Azo-NH$_2$.

Spectra of Azo-NH$_2$ and HOOC-Azo-NH$_2$ in PBS buffer are given in Figure 79 for different illumination conditions. The spectrum obtained in dark is related to the *trans* azobenzene which is the thermodynamic azobenzene form. *trans* azobenzene shows a intense π-π* band near 350 nm and a weak transition near 440 nm. The irradiation of the solution at 365 nm (UV light), near from the maximun of the π-π* band, induces a decrease in intensity of the π-π* band whereas the intensity of the n-π* band slightly increases: this is characteristic of the *cis* azobenzene formation.

The isomerisation from the *cis* to the *trans* form can be achieved by light-illumination or thermically. Thermal relaxations have been studied by spectrophotometry at 20 °C. HOOC-Azo-NH$_2$ shows a longer thermal relaxation than the Azo-NH$_2$ (Table 11, Appendix 6). Contrary to the thermal relaxation, the conversion from the *cis* to the *trans* isomer by illumination near the n-π* (436 nm) doesn't lead to a full recovery of the *trans* azobenzene. This can be explained by the overlapping of the *cis*/*trans* spectra. The photo-stationary state between the two azobenzene isomers is appreciated by the π-π* absorption which is higher under dark than under blue illumination. Typically, the composition at this stationnary state is 80 % *cis* and 20 % *trans*.

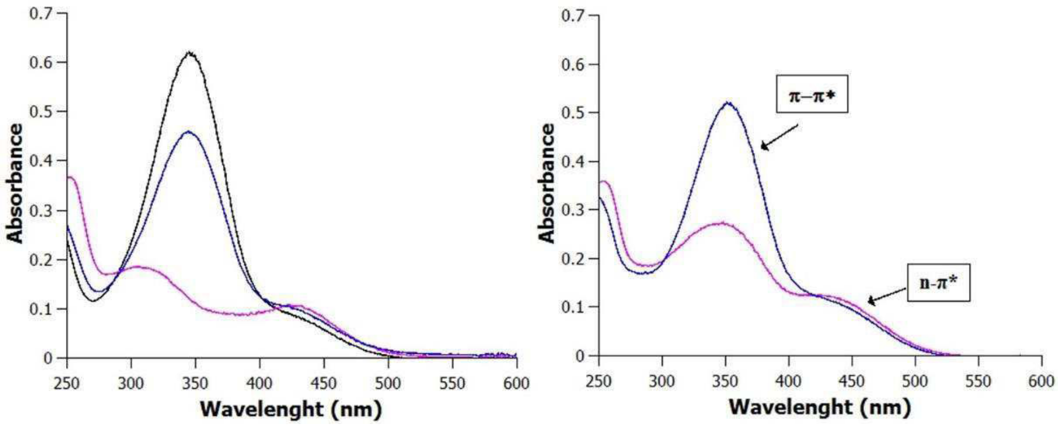

Figure 79 - UV-visible spectra of Azo-NH$_2$ and HOOC-Azo–NH$_2$ in PBS (left) [Azo-NH$_2$] = 19 µmol.L^{-1}, (right) [HOOC-Azo-NH$_2$] = 35 µmol/L, (—) after thermal relaxation in dark, (—) under blue irradiation at 436 nm and (—) UV irradiation at 365 nm.

The experiments including light-illuminations were achieved at the photo-stationary state, by irradiation on the top of solution for 15 minutes prior to measurements. Typical photo-isomerization rates were determined by monitoring the evolution of UV-visible spectra under constant light-irradiation (Figure 87). It takes less than five minutes for Azo-NH_2 and HOOC-Azo-NH_2 to reach the equilibrium (Table 11). The kinetics of photo-isomerization isn't modified in general by grafting azobenzenes on a polymer chain in diluted solution (Chen and Morawetz, 1976). The molar extinction coefficients $\varepsilon_{\pi-\pi*,\text{Blue}}$ of Azo-NH_2 and HOOC-Azo-NH_2 were evaluated under blue-illumination and we assumed that the same values can be used for polymers containing the corresponding azobenzene side groups.

Azobenzene	$\lambda_{\pi-\pi*}$	$\lambda_{n-\pi*}$	$\tau_{trans \to cis}$	$\tau_{cis \to trans}$	τ	$\varepsilon_{\pi-\pi*,\text{Blue}}$
Azo-NH_2	345 nm	430 nm	< 3 mn	< 3 mn	22 mn	2.47×10^4 L.mol^{-1}.cm^{-1}
HOOC-Azo-NH_2	352 nm	430 nm	< 5 mn	< 3 mn	*	1.48×10^4 L.mol^{-1}.cm^{-1}

Table 11 - Spectroscopic data of Azo-NH_2 and HOOC-Azo-NH_2 in PBS. Characteristic times of photo-isomerization ($\tau_{trans \to cis}$, $\tau_{cis \to trans}$) and thermal relaxation (τ) were measured at 20 °C (0.06 mg/mL, blue light: 436 nm at a power of ca. 2 mW.cm^{-2}, UV light: 365 nm at a power of ca. 10 mW.cm^{-2}). * means that the measurement hasn't been achieved.

2.3 Synthesis and characterization of HOOC-Azo-NH_2

Electrophilic reactions on diazonium salts have been reported as an effective route to azobenzene derivatives (Hamon et al., 2009). We tried two different syntheses based on diazo-coupling to obtain HOOC-Azo-NH_2.

First, one-step synthesis, described in Figure 80 will be detailed. Nitrous acid HNO_2 generated *in situ* by the acidification of sodium nitrite reacts with 4-aminobenzoic acid to give a diazonium salt. The initial transparent solution becomes green due to the diazonium formation. This diazonium compound is then used as an electrophile for the aromatic substitution on N-(2-aminoethyl)aniline. Temperature must be maintained below 5 °C to avoid the spontaneous decomposition of the diazonium. Different pH conditions for the N-(2-aminoethyl)aniline solution were attempted. Unfortunately, the desired azobenzene wasn't obtained.

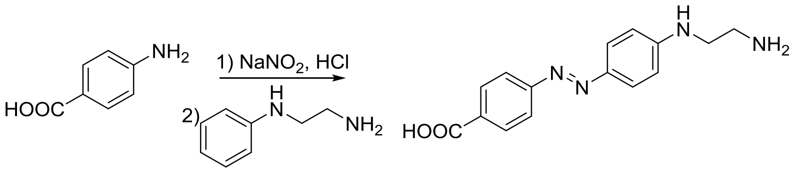

Figure 80 - one-step synthesis of an azobenzene HOOC-Azo-N-C_2H_4-NH_2.

The following four-step synthetic route inspired from the literature (Ramachandran and Urban 2011; Fang et al. 2013; Pei et al. 2011) has been used to obtain HOOC-Azo-NH_2 (**4**, Figure 81). This synthesis can be divided in two main parts: the first step is a diazoic coupling affording an azobenzene (**1**), the second step consists in introducing an ethyl linker. Protocols and characterizations are given in Appendix 1.

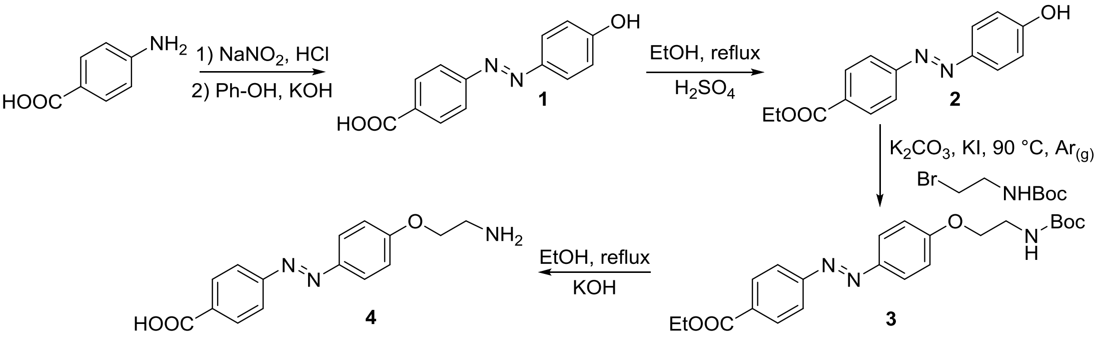

Figure 81 - four-step synthesis of HOOC-Azo-NH$_2$ (4).

Diazoic coupling

Nitrous acid HNO_2 generated *in situ* by the acidification of sodium nitrite reacts with 4-aminobenzoic acid to give a diazonium salt. This diazonium compound is then used as an electrophile to make an aromatic substitution on phenol.

4-(4-hydroxyphenylazo)benzoic acid (**1**) spontaneously precipitates during the diazoic coupling and can be easily isolated by filtration (brown solid). According to ^{1}H-NMR (Appendix 1), no purification is necessary which gives a good yield for this reaction (87 %).

Functionalization with an ethyl linker

The ethyl linker is introduced by a nucleophilic substitution of the phenol on N-Boc,2-Bromoethylamine.

Different basic conditions were attempted on compound **1** (NaOH in DMF, NaH in DMSO, K_2CO_3 in DMSO) to increase the phenol nucleophily by deprotonation. Unfortunately, once deprotonated, this product precipitates in organic solvents and consequently can't react with N-Boc,2-Bromoethanamine.

To overcome this problem of solubility, we decided to protect the carboxylic acid. 4-(4-hydroxyphenylazo)benzoic acid (**1**) in absolute ethanol with sulfuric acid conducts to the ester **2**. The yield of this esterification is low (44 %). Compound **2** is characterized by ^{1}H-NMR (Appendix 1).

Compound **2** is deprotonated by K_2CO_3 in DMSO to react on pre-activated N-Boc,2-Bromoethylamine with KI at 90 °C. After one night, thin layer chromatography shows a small fraction of **2** isn't converted. We get rid of unreacted **2** by gel chromatography on silica to afford product **3** as an orange solid (51 %). Product **3** is characterized by ^{1}H-NMR (Appendix 1).

Deprotection of both amine and carboxylic acid functions

To obtain the target azobenzene HOOC-Azo-NH$_2$ (**4**), the amine and the carboxylic functions of compound **3** must be deprotected.

Classic procedures for the deprotection of Boc-protected amine take place under acid conditions while saponification works under basic conditions. However, it has been notice in the literature that under hard basic medium primary *t*-butyl carbamate (Boc) group can provide the corresponding primary amine in excellent yield (Tom et al., 2004).

That is why potassium ethanolate in ethanol under reflux enable us to remove both the Boc and ester groups in excellent yield (88 %). Product **4** is easily characterized by 1H-NMR (Appendix 1).

The global yield of this four-steps synthesis represents 17 %. We only obtained a few milligrams of HOOC-Azo-NH_2. To improve the global yield, the protective step could have been avoided by using ethyl 4-aminobenzoate instead of 4-aminobenzoic acid as starting reactant.

3 Studies of PNIPAM copolymers with azobenzene pendant groups

3.1 Polymer synthesis and characterization

To afford the two families of polymers depicted in Figure 82, synthesis was based on one-pot post-modification of PNAS with amines (see Chapter 2). Experimental details are given in Appendix 1. Post-modifications were carried out on the same parent polymer to maintain the degree of polymerization constant. For that purpose, NAS was synthesized and polymerized by RAFT yielding the corresponding reactive precursor PNAS (DP_n = 55, index of dispersity = 1.2). The activated polyester PNAS was first dissolved in DMSO in the presence of triphenylphosphine. After complete dissolution, different amounts of Azo-NH_2:N,N-dimethylamine (α,ω-di-COOH-P(NIPAM-co-Azo[α]-NMe_2[β])(6) (left in Figure 82)), or HOOC-Azo-NH_2 (α,ω-di-COOH-P(NIPAM-co-Azo_{COOH}[α])(6) (right in Figure 82)) were added to functionalize randomly the polymer chain. After 1 hour, an excess of N-isopropylamine was allowed to react with the NAS functions. This also induced the aminolysis of the trithiocarbonate end. Finally, N-ethylmaleimide or 3-Maleimidopropionic acid were added to functionalize the thiol end, preventing polymer dimerization (via disulfide bond formation). Polymers were purified by two consecutive precipitations in diethylether and dialysis against water. ^{1}H-NMR and UV-visible spectrophotometry were used to characterized the copolymers.

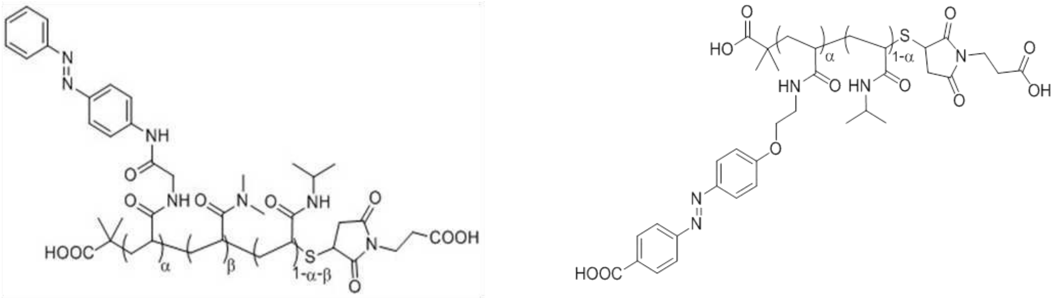

α,ω-di-HOOC-P(NIPAM-co-Azo[α]-NMe_2[β]) α,ω-di-HOOC-P(NIPAM-co-Azo_{COOH}[α])

Figure 82 - Chemical structures of the synthesized polymers α,ω-di-COOHP(NIPAM-co-Azo[α]-NMe_2[β])(6) (left) and α,ω-di-COOH-P(NIPAM-co-Azo_{COOH}[α])(6) (right).

Determination of the azobenzene proportion α by UV-vis

On Figure 83, the UV-vis spectrum of α,ω-di-COOH-P(NIPAM-co-Azo[0]-NMe_2[40]) shows no absorption between 300 and 600 nm. So, the absorption in this range for the other copolymers is specifically linked to the azobenzene pendant groups.

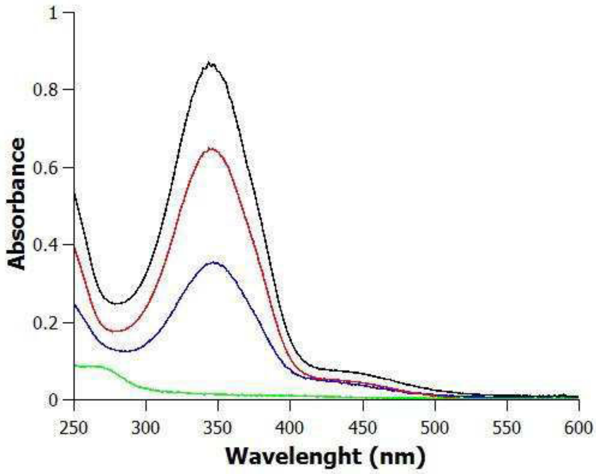

Figure 83 - UV-visible spectra of different α,ω-di-COOH-P(NIPAM-co-Azo[α]-NMe$_2$[β])(6) polymers in PBS buffer (0.06 mg/mL) under blue irradiation at 20 °C: α,ω-di-COOHP(NIPAM-co-Azo[0]-NMe$_2$[40]) (—), α,ω-di-COOH-P(NIPAM-co-Azo[4]-NMe$_2$[40]) (—), α,ω-di-COOH-P(NIPAM-co-Azo[6]-NMe$_2$[40]) (—), α,ω-di-COOH-P(NIPAM-co-Azo[9]-NMe$_2$[40]) (—).

The proportion in azobenzene α was determined by UV-vis spectrophotometry assuming that the absorption coefficient of azobenzene is the same before and after grafting. The absorption A_λ of a polymer solution can be expressed by the following equation:

$$A_\lambda = \varepsilon_\lambda \alpha c l/M$$

where ε_λ, α, c, l and M represent respectively the azobenzene absorption coefficient, the proportion in azobenzene (mol%), the mass concentration of the polymer (g.L^{-1}), the path length of light through the solution (cm) and the molecular weight of the polymer (g.mol^{-1}). The molecular weight is calculated from the NMR spectrum of the PNAS. A DP_n of 55 was measured for the parent PNAS, corresponding to M_n = 6200 g.mol^{-1} for the PNIPAM.

N.B.: In order to set the proportion between *cis* and *trans* isomers in the solution, we measured absorbances under continuous blue irradiation at 436 nm. We waited 15 minutes to be sure that the photo-stationary state was reached. We used $\varepsilon_{\pi-\pi*,\mathrm{Blue}}$ values obtained for Azo-NH$_2$ and HOOC-Azo-NH$_2$ (Table 11).

Determination of the polymer composition α and β by ^{1}H-NMR

The composition of the different copolymers was determined by ^{1}H-NMR in MeOD-d4.

Concerning α,ω-di-COOH-P(NIPAM-co-Azo[α]-NMe$_2$[β]) copolymers (Figure 84), resonance peaks (a) and (b) correspond to the polymer backbone whereas signals (c,d), (e) and (f) are respectively characteristic of the N-Isopropylamide, the N,N-dimethylamide and the azobenzene moieties. Calculations based on integrations of these signals enable us to estimate α and β. For this kind of polymers, aromatic and amide signals overlap. Consequently, aromatic protons can't be used to confirm the α value.

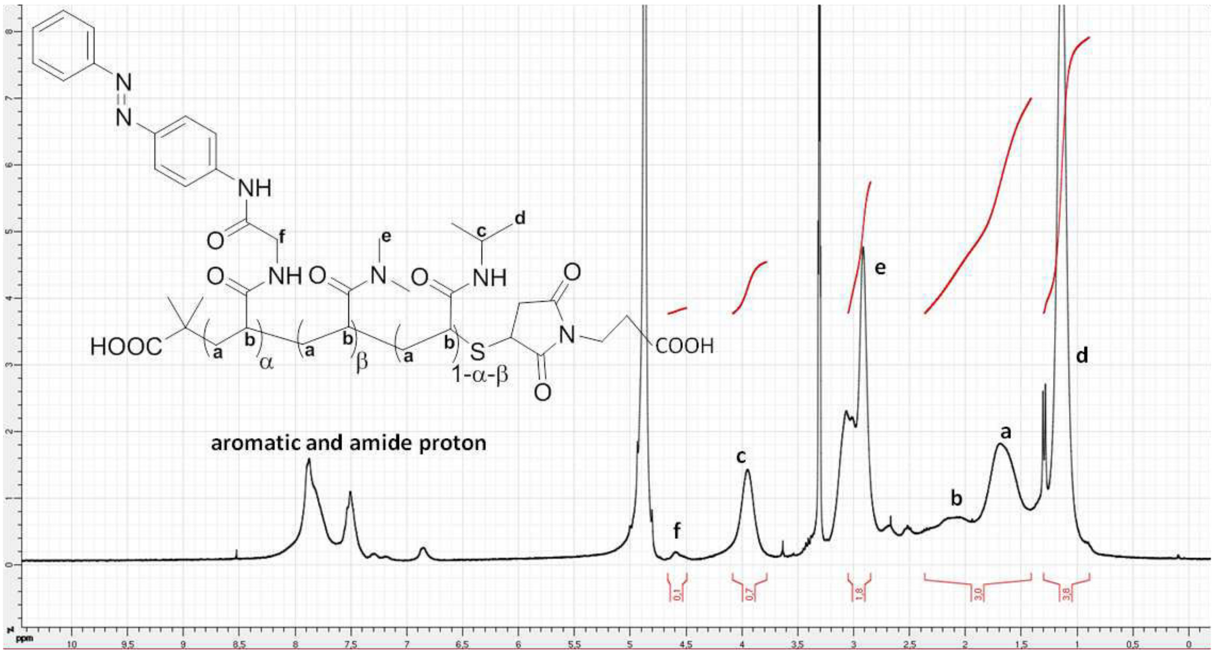

Figure 84 - ^{1}H-NMR spectrum of α,ω-di-COOH-P(NIPAM-co-Azo[9]-NMe$_2$[40]) in MeOD-d4.

Concerning α,ω-di-COOH-P(NIPAM-co-Azo$_{COOH}$[α]) copolymers (Figure 85), resonance peaks (a) and (b) correspond to the polymer backbone whereas signals (c,d) are characteristic of the N-Isopropylamide. Signals related to the azobenzene linkers can't be distinguished on this spectrum. Moreover, aromatic and amide signals overlap. Consequently, the azobenzene proportion α is deduced from the integration of (c) and (d) by assuming there is no hydrolysis of the parent polymer PNAS.

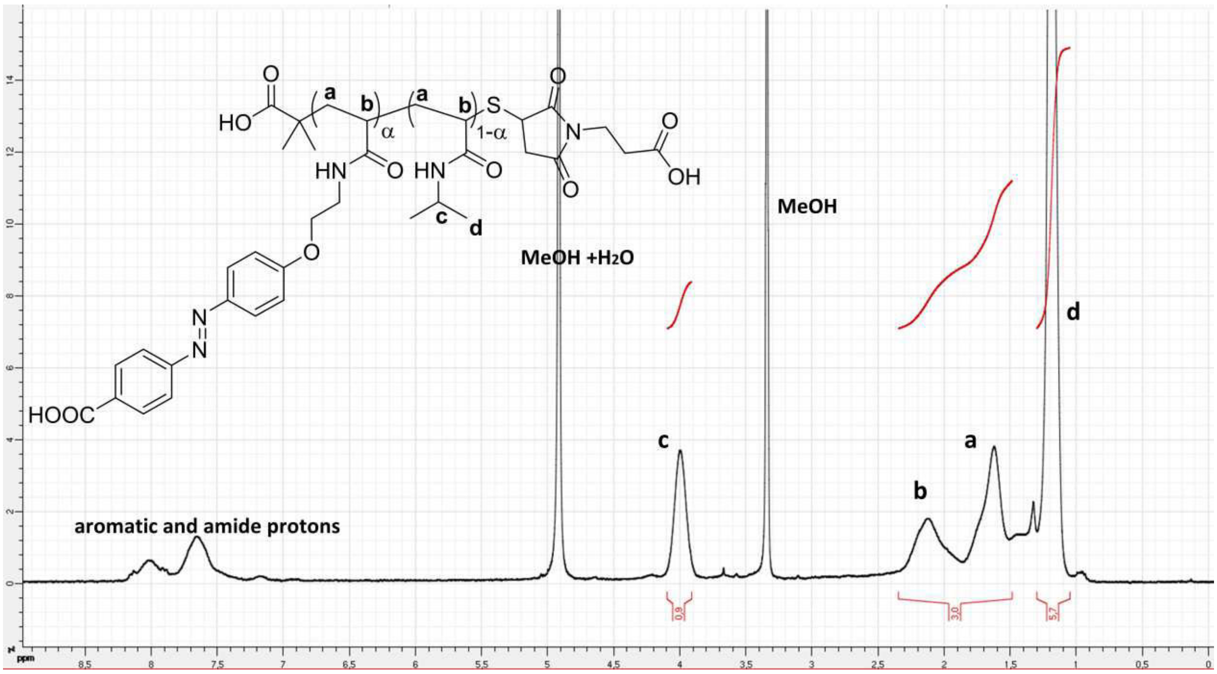

Figure 85 - ^{1}H-NMR spectrum of α,ω-di-COOH-P(NIPAM-co-Azo$_{COOH}$[21]) in MeOD-d4.

Results concerning the post-modification

Data on the synthesized copolymers are summarized on Table 12. According to β values, we can see that N,N-dimethylamine doesn't react quantitatively with PNAS polymer chain. This can be explained because secondary amines are less reactive than primary amines (Eberhardt et al., 2005). ^{1}H-NMR and UV-visible spectrophotometry give similar results concerning the azobenzene proportion α. However, the amount of Azo-NH_2 and HOOC-Azo-NH_2 grafted onto the polymer is lower than values introduced during the reaction. To explain this lack of reactivity of the primary azobenzene amines, we supposed that a fraction of these azobenzenes was obtained as ammonium salt. To improve the reactivity of these different amines on PNAS, we could neutralize the ammonium with triethylamine. In practice, this wasn't necessary because we obtained nevertheless a family of polymers with different proportions of azobenzene.

On ^{1}H-NMR spectra of α,ω-di-COOH-P(NIPAM-co-Azo$_{COOH}$[21]) (Figure 85), there is no residual peak at 2.8 ppm corresponding to the PNAS: the excess of N-isopropylamine leads to an complete PNAS conversion. Moreover, the integration of NIPAM signals shows no evidence of partial hydrolysis of the parent polymer. This is an important point because residual carboxylic acids strongly modify the LCST of polymer solutions.

Polymer	**In the feed**		**In the copolymer, α (mol%)**		**In the copolymer, β (mol%, NMR)**
	α (mol%)	**β (mol%)**	**NMR**	**UV-vis**	
α,ω-di-COOH-P(NIPAM-co-Azo[0]-NMe_2[40])	0	40	0	0	30
α,ω-di-COOH-P(NIPAM-co-Azo[4]-NMe_2[40])	4	40	2.5	2.8	30
α,ω-di-COOH-P(NIPAM-co-Azo[6]-NMe_2[40])	6	40	3	5.1	28
α,ω-di-COOH-P(NIPAM-co-Azo[9]-NMe_2[40])	9	40	5	6.9	30
α,ω-di-COOH-P(NIPAM-co-Azo[12]-NMe_2[40])	12	40	9	10	29
α,ω-di-COOH-P(NIPAM-co-Azo[18]-NMe_2[40])	18	40	10	15	28
α,ω-di-COOH-P(NIPAM-co-Azo$_{COOH}$[21])	21	0	9	*	0
α,ω-di-COOH-P(NIPAM-co-Azo$_{COOH}$[35])	35	0	17	*	0

Table 12 - List of the PNIPAM copolymers with pendant azobenzene groups obtained by one-pot post-modification of a reactive precursor PNAS (DP_n = 55). * means that the corresponding UV-visible spectrum hasn't been acquired.

3.2 Solution properties of α,ω-di-COOH-P(NIPAM-co-Azo[α]-NMe_2[β]) in PBS buffer

The LCST phase behavior of α,ω-di-COOH-P(NIPAM-co-Azo[α]-NMe_2[β]) polymers were studied by turbidity measurements (Table 13, see Appendix 3 for protocols).

Polymer	$T_{CP,Blue}$ (°C)	$T_{CP,UV}$ (°C)	ΔT_{CP} (°C)
α,ω-di-COOH-P(NIPAM-co-Azo[0]-NMe_2[40])	-	-	-
α,ω-di-COOH-P(NIPAM-co-Azo[4]-NMe_2[40])	39.6	33.3	- 6.3
α,ω-di-COOH-P(NIPAM-co-Azo[6]-NMe_2[40])	42.3	36.7	- 5.5
α,ω-di-COOH-P(NIPAM-co-Azo[9]-NMe_2[40])	36.6	30	- 6.6
α,ω-di-COOH-P(NIPAM-co-Azo[12]-NMe_2[40])	*	*	*
α,ω-di-COOH-P(NIPAM-co-Azo[18]-NMe_2[40])	*	*	*

Table 13 - Results of turbidimetry of α,ω-di-COOH-P(NIPAM-co-Azo[α]-NMe_2[β]) polymers in PBS 1x (3 mg.mL^{-1}, 0.16 °C.min^{-1}) under blue and UV irradiation. - means no phase separation occurred in the temperature range of water (i.e. between 0 and 100 °C). * means that LCST measurement cannot be done due to problems of filtration of the polymer solution at 10 °C.

Cloud points varies between 30 and 42.3 °C (Figure 86), which is in the window of interest for cell cultures. To reach this window, modification by both isopropylamine and N,N-dimethylamine was required. The LCST of PNIPAM being of 32 °C, introduction of hydrophobic azobenzene side groups markedly diminishes the temperature of solubility transition (see for instance Figure 76 and Figure 74). So, the ~ 30 mol% of N,N-dimethylacrylamides balanced the hydrophobicity of the azobenzene, which in practice enabled to reach the wished cloud points in PBS (i.e. close to the biocompatible temperature 37 °C).

The dissolution of α,ω-di-COOH-P(NIPAM-co-Azo[0]-NMe_2[β]) in PBS (3 mg.mL^{-1}) was all the more difficult that the proportion of azobenzene α increases. Every solution was filtered prior to turbidimetry. Unfortunately, solutions of polymers containing high azobenzene amounts (α,ω-di-COOH-P(NIPAM-co-Azo[12]-NMe_2[40]) and α,ω-di-COOH-P(NIPAM-co-Azo[18]-NMe_2[40])) cannot be filtered and so analyzed due to a too high proportion of aggregates.

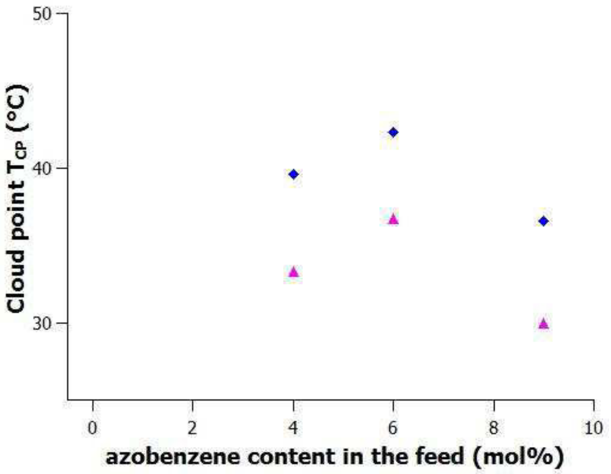

Figure 86 -Evolution of cloud points T_{CP} with the azobenzene content for α,ω-di-COOH-P(NIPAM-co-Azo[α]-NMe_2[β]) polymers: (purple triangles) TCP,UV, (blue lozenges) TCP,Blue.

Under UV light, cloud point decreases by six degrees compared to blue-irradiated samples. This corresponds to the "reverse" light-response as introduced in paragraph 1.3. Note that similar inverse variation were obtained using different amine modifications (instead of the N,N-dimethyamine): N-cyclopropylamine, methyl-OEG-amine, 2-hydroxyethylamine, which resulted in the same "reverse" behavior (though no systematic variation of the polymer composition was studied). This effect is thus general, and can't be attributed to a specific role of N,N-dimethyamine modification. For azobenzene contents comprised between 2.5 and 7 mol%, ΔT_{CP} is constant and closed to - 6 °C. These results are similar to those obtained by Menzel and Kröger (Menzel et al., 1995) (Figure 74). A mechanism involving azobenzene aggregation or loops can thus be considered to explain "reverse" light-response. UV-visible spectrophotometry have been used to obtain evidences of such a mechanism on solutions of α,ω-di-COOH-P(NIPAM-co-Azo[α]-NMe_2[β]) diluted to 0.06 mg.mL^{-1} in PBS at 20 °C. In the spectra, blue shift of the π-π* band is characteristic of the azobenzene aggregation. We can see on the Figure 83 that the maximum of absorption for the π-π* transition is at 350 nm under blue illumination irrespective of the % azobenzene. This wavelength is actually close to the one observed for the Azo-NH_2 (345 nm, see Table 11). Thus spectra don't show any significant blue shift. Furthermore, as shown in Figure 87, two isobestic points are observed in the set of spectra recorded during *cis*:*trans* conversion. This is characteristic of the presence of only two states of azobenzene: the *trans* and the *cis* isomer forms. Contribution from a third state, due to different environment of *trans* azobenzene in the free (isolated) vs clustered forms is expected to distort spectra and to introduce drifts in the isobestic points. According to these UV-visible data, no hint for clustering could be identified. It is however possible that clusters are formed irrespective of the *cis*:*trans* isomerization form, and/or that cluster formation does not affect significantly the spectra (for instance, if the first shell of hydration is not markedly affected by dimerization).

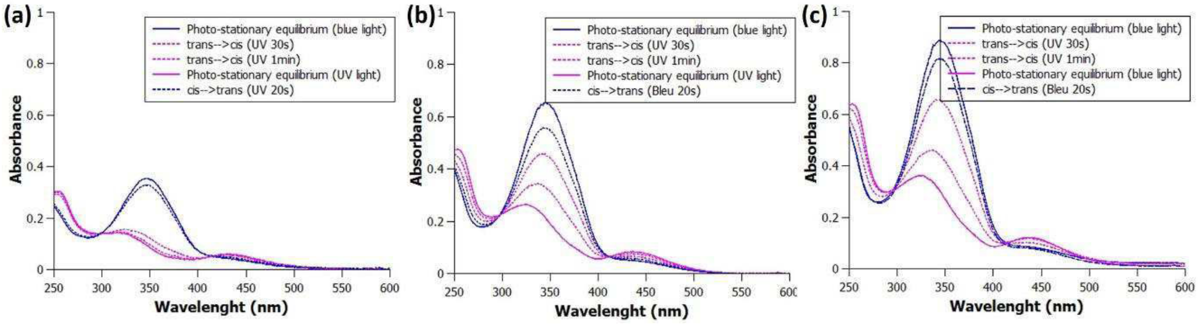

Figure 87 - UV-visible spectra of different α,ω-di-COOH-P(NIPAM-co-Azo[α]-NMe_2[β])(6) polymers in PBS buffer (0.06 mg.mL^{-1}) at 20 °C: (a) α,ω-di-COOH-P(NIPAM-co-Azo[4]-NMe_2[40]),(b) α,ω-di-COOH-P(NIPAM-co-Azo[7]-NMe_2[40]), (c) α,ω-di-COOH-P(NIPAM-co-Azo[9]-NMe_2[40]).

3.3 Solution properties of α,ω-di-COOH-P(NIPAM-co-Azo_{COOH}[α])

To assess the role of hydrophobicity of azobenzene, we compared the copolymers described in section 3.2 with PNIPAM polymers bearing anionic azobenzene groups, whose the charged nature was supposed to hinder or significantly diminish the propensity for clustering in water. Increased polarity and more importantly electrostatic repulsion between carboxylate-substituted azobenzenes should prevent π-stacking, and thus favor the "direct" light-response.

For this family of polymers modified from PNAS by reaction with HOOC-Azo-NH_2, we haven't been obliged to introduce N,N-dimethylamine to balance the (*trans*) azobenzene hydrophobicity on LCST. This presumably comes from the higher solubility of this photo-chrome.

Only two polymers have been synthesized because of the limited amount of HOOC-Azo-NH_2 available. Although we can't deduce a trend on the solubility behavior with only two polymers, a study at different pHs should give us information on the influence of azobenzene ionization on LCST values. In PBS (pH 7.4), the azobenzene compound is more hydrophilic due to its anionic nature compared to pH 3 (HCl added in PBS).

It is important to notice that the variation of polarity upon *trans-cis* isomerization of HOOC-Azo-NH_2 azobenzene may differ significantly from the typical variation of azobenzene without substituents. Indeed, the polarization of the C-COOH moieties add a contribution to the dipolar moment in HOOC-Azo-NH_2 which is similar to the case of para-cyano-azobenzene used by the Winnik's team (Ishii et al., 2011) (Figure 77 and Figure 88). If the polarization induced by this substituent dominates, the *trans* isomer may be more hydrophilic than the *cis* isomer (μ_{trans} = 5.0 D, μ_{cis} = 3.6D in the case of para-cyano-azobenzene) (Han et al., 2006), which corresponds to an apparently "reverse" response to UV exposure (decreasing solubility).

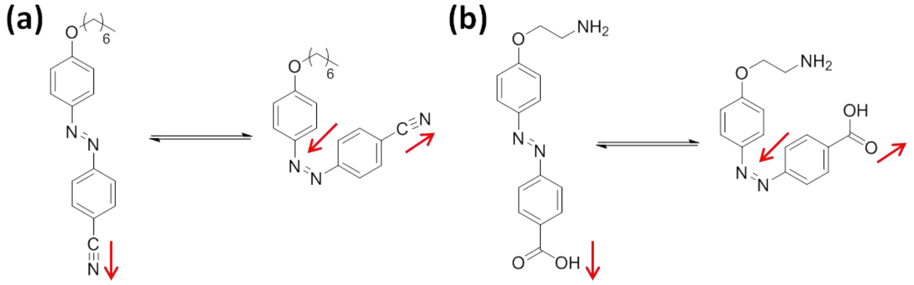

Figure 88 - schematic representation of dipolar moments (red arrows) for different azobenzenes: (a) azobenzene used by Winnik, (b) HOOC-Azo-NH_2.

The LCST phase separation of α,ω-di-COOH-P(NIPAM-co-Azo$_{COOH}$[α]) polymers were determined by turbidity measurements at two pH (7.0 and 3.0) (Table 14, Appendix 3).

Polymer	$T_{CP,Blue}$ (°C)		$T_{CP,UV}$ (°C)		ΔT_{CP} (°C)	
	PBS	HCl	PBS	HCl	PBS	HCl
α,ω-di-COOH-P(NIPAM-co-Azo$_{COOH}$[21])	37.8	18.9	39.4	23.9	+ 1.6	+ 5
α,ω-di-COOH-P(NIPAM-co-Azo$_{COOH}$[35])	45.3	30.0	46.4	34.2	+ 1.1	+ 4.2

Table 14 - Results of turbidimetry of α,ω-di-COOH-P(NIPAM-co-Azo$_{COOH}$[α]) polymers in PBS and HCl media (3 $mg.mL^{-1}$, 0.16 $°C.min^{-1}$) under blue and UV irradiations. The pH was around 3 for solutions with HCl.

First, cloud points are higher in PBS than in acidic pH conditions. This result is consistent with the increased hydrophilicity of HOOC-Azo-NH_2 with increasing pH.

Interestingly, the cloud points of the two copolymers α,ω-di-COOH-P(NIPAM-co-Azo$_{COOH}$[21]) and α,ω-di-COOH-P(NIPAM-co-Azo$_{COOH}$[35]) increase with isomerization from *trans* (blue light) toward *cis* form (UV). This increase, that is an apparent "reverse" light-response, is more pronounced at pH 3 ($\Delta T_{CP,PBS}$ = + 1°C and $\Delta T_{CP,HCl}$ = + 5 °C). Based on results of α,ω-di-COOH-P(NIPAM-co-Azo[α]-NMe_2[β]), we assume that there is still formation of azobenzene aggregates at pH 3. However, the magnitude of the “reverse” light-response decreases by increasing pH ($\Delta T_{CP,PBS}$ = + 1°C). Indeed, hydrophobic clustering of the ionized form of the Azo$_{COOH}$ at pH 7.4 may be broken.

4 Studies of PNIPAM copolymers with azobenzene at one extremity

4.1 Polymer synthesis and characterization

A set of four polymers with an azobenzene attached at one end was synthesized (Figure 89: α-Azo,ω-COOH-PNIPAM(M_n), PLL-g-[0.1]α-Azo,ω-Butanamido-PNIPAM(M_n) with M_n = 2000 and 4500 g.mol^{-1}). Data concerning the synthesis are detailed in Appendix 1 (and Chapter 2). NAS was polymerized in presence of Azo-CTA as CTA. By adjusting the relative proportions between NAS monomer and Azo-CTA, molecular weight of PNIPAM were controlled. These Azo-PNAS precursor polymers were converted in α-Azo,ω-SH-PNIPAM(M_n) with an excess of N-isopropylamine. Then, the thiol extremity was functionalized with maleimides to obtain α-Azo,ω-COOH-PNIPAM(M_n). Grafting of the end-functionalized PNIPAM strands on poly(lysine) was performed as described in Chapter 2 (1-"PLL functionalization") to yield PLL-g-[0.1]α-Azo,ω-Butanamido-PNIPAM(M_n). The degree of grafting of the PLL was evaluated at 10 % by ^{1}H-NMR.

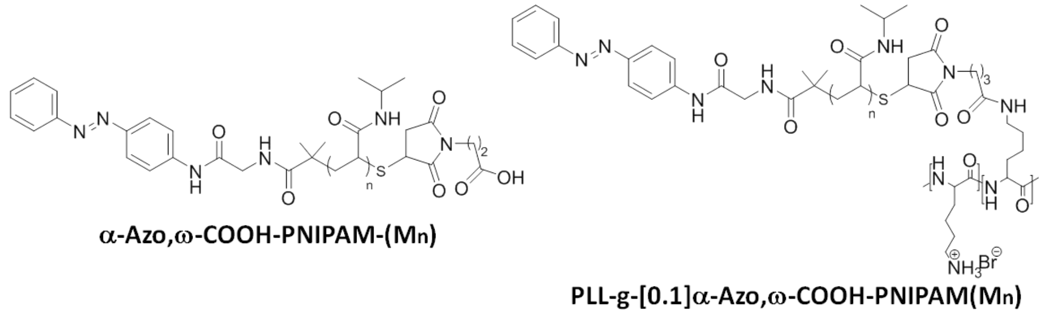
α-Azo,ω-COOH-PNIPAM-(Mn)

PLL-g-[0.1]α-Azo,ω-COOH-PNIPAM(Mn)

Figure 89 – Chemical structures of α-azobenzene,ω-COOH end-capped poly(NIPAM) (DP_n = 18 and 40, i.e. M_n = 2000 and 4500 g.mol^{-1}).

4.2 Polymer solution properties in PBS buffer

LCST of azobenzene-ended PNIPAM (turbidity measurements)

The threshold temperature of phase separation was determined in PBS, by turbidimetry measurements under light irradiation (3mg.mL^{-1}, 0.33 °C.min^{-1}). Results are summarized in Table 15 and Table 16 for α-Azo,ω-COOH-PNIPAM(M_n) and PLL-g-[0.1]α-Azo,ω-Butanamido-PNIPAM(M_n) respectively.

M_n	DP_n	α	Blue	UV	ΔT_{CP}
4500 g.mol^{-1}	40	2.5 %	27.5 °C	30.8 °C	+ 3.3 °C
2000 g.mol^{-1}	18	5.5 %	27 °C	29 °C	+ 2 °C

Table 15 - Results of turbidimetry of α-Azo,ω-COOH-PNIPAM(M_n) in PBS (3 mg.mL^{-1}, 0.33 °C.min^{-1}) under blue and UV irradiations.

In contrast to randomly modified PNIPAM, an increase in cloud point upon UV exposure is observed in solutions of end-functionalized α-Azo,ω-COOH-PNIPAM(M_n). $T_{CP,UV}$ is slightly higher than $T_{CP,Blue}$ (Table 15), suggesting the formation of more polar macromolecules under the *cis* azobenzene form (direct variation). A smaller photo-variation of cloud point for the shortest chain may however indicate the onset of inter-azobenzene clustering. Interestingly, the cloud point doesn't significantly differ between the longer and shorter chains (corresponding respectively to ratios of azobenzene/NIPAM monomers of 2.5 to 5.5 mol%). And these values of cloud points are close to the one of conventional PNIPAM (32 °C). The presence of azobenzene at one end of the chain appears to have a moderate impact on cloud point.

Concerning the PLL derivatives grafted with end-functionalized α-Azo,ω-COOH-PNIPAM(M_n), the ligh-response is also direct and increases with increasing ratio of azobenzene to NIPAM monomers (Table 16, Figure 90). The PLL backbone brings high water solubility, and may introduce steric constraints due to grafting of the end of PNIPAM chains. Both phenomena are expected to hamper clustering of the azobenzene end-groups, which is consistent with the measured direct variation of cloud points, and higher photoswitch of the polymer carrying higher percentage of azobenzene. Surprisingly, however, the cloud points are not significantly modified by the presence of PLL (Figure 91). The blocky nature of PNIPAM grafts, and distribution of PNIPAM strands on the periphery of PLL backbone are presumably the main reasons for a lack of influence of the polycationic block carrying the PNIPAM strands. Interestingly, the azobenzene placed at the external end of strands are in contrast at a position that can significantly perturb inter-PNIPAM associations (Figure 92).These results show that topologic effects play an important role on the design of light-responsive polymers.

M_n	DP_n	α	Blue	UV	ΔT_{CP}
45 g.mol^{-1}	40	2.5 %	27.2 °C	29.2 °C	+ 2 °C
2000 g.mol^{-1}	18	5.5 %	27.8 °C	34 °C	+ 6.2 °C

Table 16 - Results of turbidimetry of PLL-g-[0.1]α-Azo,ω-Butanamido-PNIPAM(M_n) in PBS (3 mg.mL^{-1}, 0.33 °C.min^{-1}) under blue and UV irradiations.

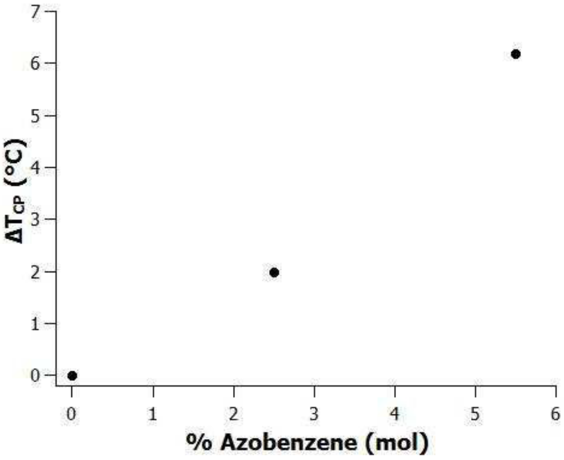

Figure 90 - Evolution of ΔT_{CP} (°C) with the azobenzene content α (mol%) for PLL-g-[0.1]α-Azo,ω-Butanamido-PNIPAM(M_n).

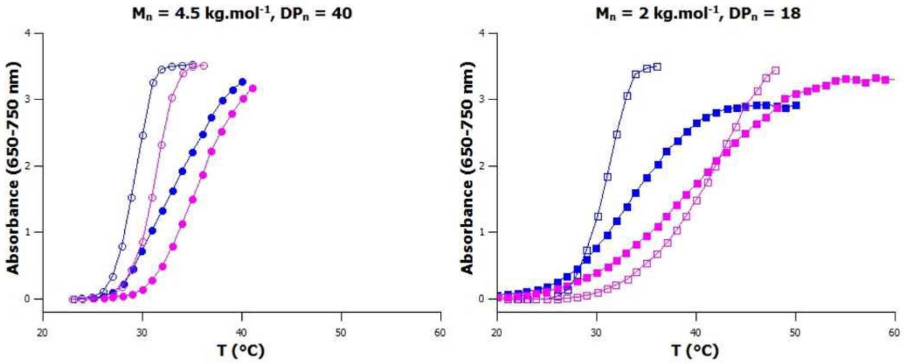

Figure 91 - Turbidity of solution of α-Azo,ω-COOH-PNIPAM(M_n) (full symbol) and PLL-g-[0.1]α-Azo,ω-Butanamido-PNIPAM(M_n) (empty symbol) in PBS (3 mg.mL^{-1}, 0.33 °C.min^{-1}). Blue/violet curve corresponds to blue/UV irradiation.

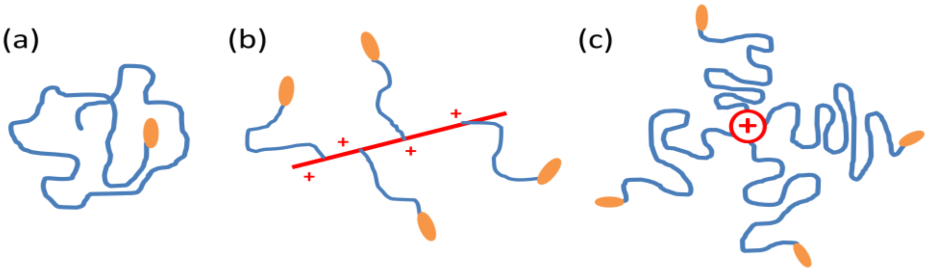

Figure 92 - Schematic conformations of α-Azo,ω-COOH-PNIPAM(M_n) (a) and PLL-g-[0.1]α-Azo,ω-Butanamido-PNIPAM(M_n) (b), (c) cross-section perpendicular to the PLL backbone of PLL-g-[0.1]α-Azo,ω-Butanamido-PNIPAM(M_n) conformation.

Photo-triggered phase transition of PLL-g-[0.1]α-Azo,ω-Butanamido-PNIPAM(2) in PBS buffer

The large gap of cloud point between the *trans* and the *cis* polymer suggest that aggregation/dissociation should be controlled at constant temperature, by exposure to light. A solution of PLL-g-[0.1]α-Azo,ω-Butanamido-PNIPAM(2) in PBS was prepared for this experiment and the aggregation was monitored by turbidimetry (Figure 93). A limpid solution at 15 °C ($T < T_{CP,Blue} < T_{CP,UV}$) was heated to 32 °C ($T_{CP,Blue} < T < T_{CP,UV}$), which triggers aggregation. Then, this sample was exposed alternatively to UV and blue light. We can see an increase in absorbance due to the PLL-g-[0.1]α-Azo,ω-Butanamido-PNIPAM(2) aggregation under blue light, and a drop in absorbance under UV light. This is indicative of the photo-controlled variation of solubility. Complete redissolution was slow, and it was incomplete during the time of experiments shown in Figure 93. Upon cycling the irradiation wavelength, the turbidity cycles suggest that phase transition was essentially reversible.

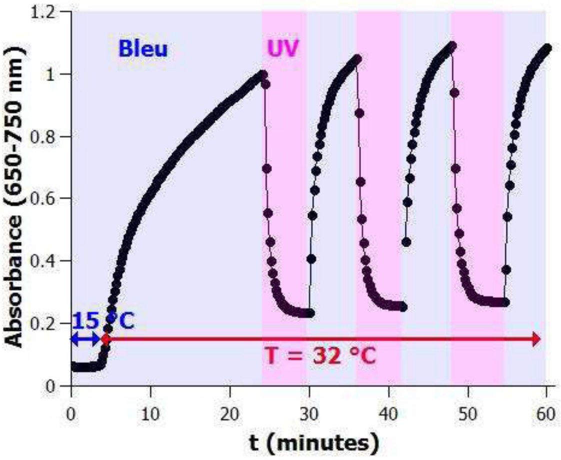

Figure 93 - Light-induced phase separation of PLL-g-[0.1]α-Azo,ω-Butanamido-PNIPAM(2) in PBS (3mg.mL^{-1}).

5 Use of azobenzene-containing PNIPAM as light-responsive polymer coatings

To assess whether azobenzene-containing PLL can help to prepare substrates with light-sensitivity, we considered two azobenzene-containing PNIPAM structures:

- the family of α,ω-di-HOOC-P(NIPAM-co-Azo-NMe$_2$)(6) copolymers, with pendant azobenzene groups along the PNIPAM chain (reverse light-response, $\Delta T_{CP} \sim -6$ °C)

- PNIPAM with one azobenzene extremity (direct light-response, $\Delta T_{CP} = +6.2$ °C for PLL-g-[0.1]α-Azo,ω-Butanamido-PNIPAM(2)).

Although the phase transition in solution of such azobenzene-containing PNIPAM was sharp, we were interested to know if this property can be preserved once the chains are deposited on a glass surface. In addition, we wanted to know if the swelling/collapse transition can contribute to expose/mask ligands on demand (that is upon irradiation). Hence, PLL-g-P(NIPAM-co-Azo-NMe$_2$-Biotin)(6) and PLL-g-[0.1]α-Azo,ω-Butanamido-P(NIPAM-co-Biotin)(2) were synthesized. Their structures are represented in Figure 94 and their cloud points in PBS solution are gathered on Table 17.

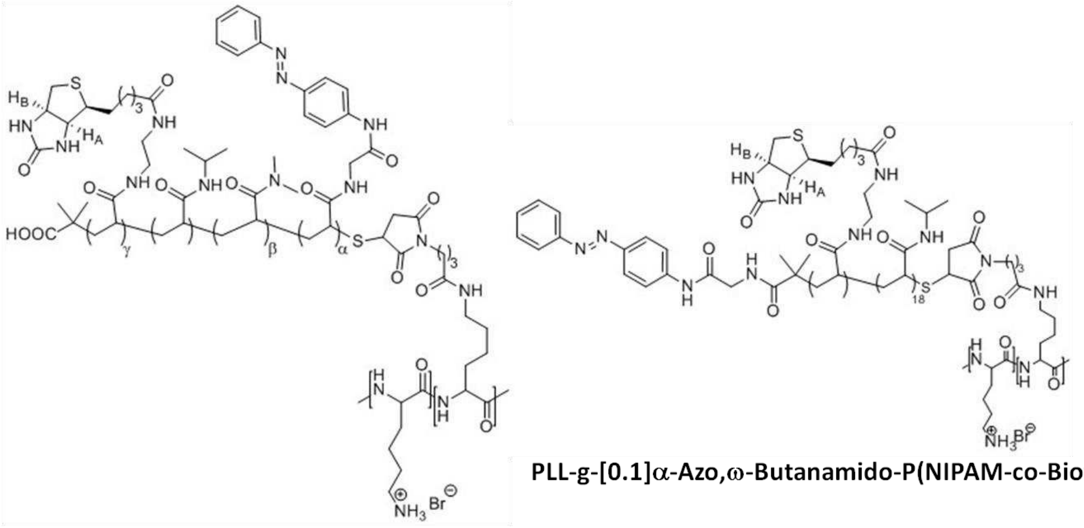

PLL-g-[0.1]α-Azo,ω-Butanamido-P(NIPAM-co-Biotin)(2)

PLL-g-P(NIPAM-co-Azo[5%]-NMe2[25%]-Biotin[5%])(6)

Figure 94 – Polymers used for investigations as light-responsive polymer coatings.

Polymer	$T_{CP,Blue}$ (°C)	$T_{CP,UV}$ (°C)	ΔT_{CP} (°C)
PLL-g-P(NIPAM-co-Azo-NMe$_2$-Biotin)(6)	26	23	- 3
PLL-g-[0.1]α-Azo,ω-Butanamido-P(NIPAM-co-Biotin)(2)	27	30.5	+ 3.5

Table 17 – Cloud point measurements by turbidimetry in PBS (3 mg.mL^{-1}, 0.33 °C.min^{-1}) under blue and UV irradiations.

The light sensitivity of PLL-g-P(NIPAM-co-Azo-NMe$_2$-Biotin)(6) and PLL-g-[0.1]α-Azo,ω-Butanamido-P(NIPAM-co-Biotin)(2) adlayers was first assessed by their ability to expose/mask Biotin under UV/Blue illuminations. Coverslips with alternating 6µm-stripes of biotinylated PLL-g-PNIPAM and 25µm-stripes of repulsive PLL-g-PEG were submitted to fluorescent Neutravidin-coated beads at accurate temperatures (Chapter 4 - Figure 51A, see Appendix 4). Figure 95 shows the number of bound particles on these adlayers.

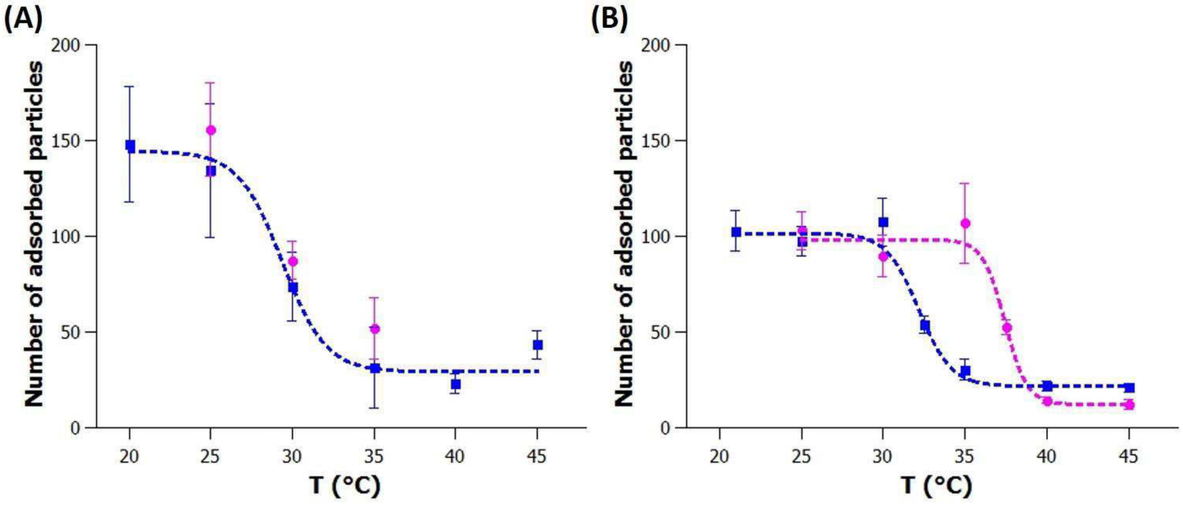

Figure 95 - Number of Neutravidin-coated FluoSpheres counted on (A) PLL-g-P(NIPAM-co-Azo$_{5\%}$-NMe$_{2,25\%}$-Biotin$_{5\%}$)(6)and (B) PLL-g-[0.1]α-Azo,ω-Butanamido-P(NIPAM-co-Biotin$_{5\%}$)(2) stripe (total surface of 351 µm²).

The two layers show a similar trend for the number of bound particles: the quantity of adsorbed beads drastically decreases above a threshold temperature (Figure 95 A-B). This result is consistent with results on PLL-g-[0.1]P(NIPAM-co-Biotin)(6) (Chapter 4 - Figure 53) suggesting that Biotin is more accessible at low temperatures than at high temperatures. Furthermore, values of adsorbed particles are of the same order of magnitude for PLL-g-P(NIPAM-co-Azo-NMe$_2$-Biotin)(6) and PLL-g-[0.1]P(NIPAM-co-Biotin)(6) layers (~ 150 particles on 351 µm² at 25 °C) while this number is inferior on PLL-g-[0.1]α-Azo,ω-Butanamido-P(NIPAM-co-Biotin)(2) layer (~ 100 particles on 351 µm² at 25 °C). Shorter PNIPAM brushes (i.e. a lower Biotin density) on PLL-g-[0.1]α-Azo,ω-Butanamido-P(NIPAM-co-Biotin)(2) layer compared to PLL-g-P(NIPAM-co-Azo-NMe$_2$-Biotin)(6) layer may explain this difference on bound particles at low temperatures. The transition temperature differs from cloud points, with a shift that is obvious in the case of the azobenzene-terminated NIPAM polymer. Because PLL-g-PNIPAM chains displayed similar cloud point and temperature of collapse once deposited on surfaces (see chapter 4), we have no clear interpretation of the present result. Further investigations are necessary to confirm the present effect.

In the case of copolymers having a reverse light response in solution, PLL-g-P(NIPAM-co-Azo-NMe$_2$-Biotin)(6) (Table 17, ΔT_{CP} = - 3 °C), the binding to Biotin wasn't modulate by light. In contrast, the threshold temperature of association of beads onto the surface was higher under UV illumination (~ 37.5 °C) than under blue illumination (~ 32.5 °C) on PLL-g-[0.1]α-Azo,ω-Butanamido-P(NIPAM-co-Biotin)(2)-covered glass (Figure 95B). PLL-g-[0.1]α-Azo,ω-Butanamido-P(NIPAM-co-Biotin)(2) keeps its direct light-response once adsorbed on surface.

To determine whether a collapse/swelling transition occurs in the azobenzene-containing PLL-g-PNIPAM adlayers, QCM-d measurements have been achieved. Preliminary data are shown in Figure 113 of Appendix 3 (section 2.3.4). Unfortunately, recorded signals on both PLL-g-P(NIPAM-co-Azo-NMe$_2$-Biotin)(6) and PLL-g-[0.1]α-Azo,ω-Butanamido-P(NIPAM-co-Biotin)(2) layers didn't show a discernible transition and were closed to the detection limit.

Conclusion

The comparison of cloud points of PNIPAM solutions, with azobenzene moieties as pendant group or as polymer end, demonstrates the importance of topological effects on the design of light-responsive polymers. Indeed, α,ω-di-COOH-P(NIPAM-co-Azo[α]-NMe$_2$[β])(6) solutions show a "reverse" light-response ($\Delta T_{CP} \sim -6$ °C) while PLL-g-[0.1]α-Azo,ω-Butanamido-PNIPAM solutions show a "direct" one ($\Delta T_{CP} \sim +6$ °C). We think that azobenzene forms loops or small aggregates to explain the "reverse" light-response of α,ω-di-COOH-P(NIPAM-co-Azo[α]-NMe$_2$[β])(6) solutions. SEC or fluorescence studies could give experimental proofs of these small aggregates (study of the effective radius of the chain with the isomerization state of azobenzene by GPC, study of the fluorescence of PNIPAM solutions in presence of pyrene which depends on the formation of hydrophobic domains (Ringsdorf et al., 1991)). Direct light-response of PLL-g-[0.1]α-Azo,ω-Butanamido-PNIPAM can be explained by both steric constraints and high solubility of PLL backbone (hampering the clustering of azobenzene).

Azobenzene-ended PLL derivatives keep their direct light-response once adsorbed on surface according to captures of Streptavidin particles on PLL-g-[0.1]α-Azo,ω-Butanamido-P(NIPAM-co-Biotin)(2) layers. These results shall however be considered as preliminary, and promising, proof of feasibility. Due to the possible complex interplay with azobenzene clustering and narrow window of cloud point shift (3 to 6°C), a systematic study of the photo-response of such copolymers has to be envisaged.

Bibliography

Akiyama, H., and Tamaoki, N. (2007). Synthesis and Photoinduced Phase Transitions of Poly(N-isopropylacrylamide) Derivative Functionalized with Terminal Azobenzene Units. Macromolecules *40*, 5129–5132.

Buller, J., Laschewsky, A., Lutz, J.-F., and Wischerhoff, E. (2011). Tuning the lower critical solution temperature of thermoresponsive polymers by biospecific recognition. Polym. Chem. *2*, 1486–1489.

Chen, D.T.-L., and Morawetz, H. (1976). Photoisomerization and Fluorescence of Chromophores Built into the Backbones of Flexible Polymer Chains. Macromolecules *9*, 463–468.

Dai, S., Ravi, P., and Tam, K.C. (2008). pH-Responsive polymers: synthesis, properties and applications. Soft Matter *4*, 435–449.

Desponds, A., and Freitag, R. (2003). Synthesis and Characterization of Photoresponsive N-Isopropylacrylamide Cotelomers. Langmuir *19*, 6261–6270.

Dirani, A., Laloyaux, X., Fernandes, A.E., Mathy, B., Schicke, O., Riant, O., Nysten, B., and Jonas, A.M. (2012). Reversible Photomodulation of the Swelling of Poly(oligo(ethylene glycol) methacrylate) Thermoresponsive Polymer Brushes. Macromolecules *45*, 9400–9408.

Eberhardt, M., Mruk, R., Zentel, R., and Théato, P. (2005). Synthesis of pentafluorophenyl(meth)acrylate polymers: New precursor polymers for the synthesis of multifunctional materials. Eur. Polym. J. *41*, 1569–1575.

Hahn, M., Görnitz, E., and Dautzenberg, H. (1998). Synthesis and Properties of Ionically Modified Polymers with LCST Behavior. Macromolecules *31*, 5616–5623.

Hamon, F., Djedaini-Pilard, F., Barbot, F., and Len, C. (2009). Azobenzenes—synthesis and carbohydrate applications. Tetrahedron *65*, 10105–10123.

Han, M.R., Hirayama, Y., and Hara, M. (2006). Fluorescence Enhancement from Self-Assembled Aggregates: Substituent Effects on Self-Assembly of Azobenzenes. Chem. Mater. *18*, 2784–2786.

Irie, M., Misumi, Y., and Tanaka, T. (1993). Stimuli-responsive polymers: chemical induced reversible phase separation of an aqueous solution of poly(N-isopropylacrylamide) with pendent crown ether groups. Polymer *34*, 4531–4535.

Ishii, N., Mamiya, J., Ikeda, T., and Winnik, F.M. (2011). Solvent induced amplification of the photoresponsive properties of α,ω-di-[4-cyanophenyl-4′-(6-hexyloxy)-azobenzene]-poly(N-isopropylacrylamide) in aqueous media. Chem. Commun. *47*, 1267–1269.

Ivanov, A.E., Eremeev, N.L., Wahlund, P.-O., Galaev, I.Y., and Mattiasson, B. (2002). Photosensitive copolymer of N-isopropylacrylamide and methacryloyl derivative of spyrobenzopyran. Polymer *43*, 3819–3823.

Ivanova, I.G., Kuckling, D., Adler, H.-J.P., Wolff, T., and Arndt, K.-F. (2000). Preparation and properties of thin films of photocrosslinkable hydrophilic polymers. Des. Monomers Polym. *3*, 447–462.

Jochum, F.D., and Theato, P. (2009a). Temperature- and Light-Responsive Polyacrylamides Prepared by a Double Polymer Analogous Reaction of Activated Ester Polymers. Macromolecules *42*, 5941–5945.

Jochum, F.D., and Theato, P. (2009b). Temperature and light sensitive copolymers containing azobenzene moieties prepared via a polymer analogous reaction. Polymer *50*, 3079–3085.

Jochum, F.D., zur Borg, L., Roth, P.J., and Theato, P. (2009). Thermo- and Light-Responsive Polymers Containing Photoswitchable Azobenzene End Groups. Macromolecules *42*, 7854–7862.

Kroger, R., Menzel, H., and Hallensleben, M.L. (1994). Light controlled solubility change of polymers: copolymers of dimethylacrylamide and 4-phenylazophenyl acrylate. Macromol Chem Phys *195*, 2291–2298.

Kuckling, D., Ivanova, I.G., Adler, H.-J.P., and Wolff, T. (2002). Photochemical switching of hydrogel film properties. Polymer *43*, 1813–1820.

Kuckling, D., Vo, C.D., Adler, H.-J.P., Völkel, A., and Cölfen, H. (2006). Preparation and Characterization of Photo-Cross-Linked Thermosensitive PNIPAAm Nanogels. Macromolecules *39*, 1585–1591.

Kungwatchakun, D., and Masahiro, I. (1988). PHOTORESPONSIVE POLYMERS - PHOTOCONTROL OF THE PHASE-SEPARATION TEMPERATURE OF AQUEOUS-SOLUTIONS OF POLY[N-ISOPROPYLACRYLAMIDE-CO-N-(4-PHENYLAZOPHENYL)ACRYLAMIDE]. Makromol Chem *9*, 243–246.

Laschewsky, A., and Rekaï, E.D. (2000). Photochemical modification of the lower critical solution temperature of cinnamoylated poly(N-2-hydroxypropylmethacrylamide) in water. Macromol. Rapid Commun. *21*, 937–940.

Lee, H., Pietrasik, J., and Matyjaszewski, K. (2006). Phototunable Temperature-Responsive Molecular Brushes Prepared by ATRP. Macromolecules *39*, 3914–3920.

Liu, H.Y., and Zhu, X.X. (1999). Lower critical solution temperatures of N-substituted acrylamide copolymers in aqueous solutions. Polymer *40*, 6985–6990.

Liu, Y.-J., Pallier, A., Sun, J., Rudiuk, S., Baigl, D., Piel, M., Marie, E., and Tribet, C. (2012). Non-monotonous variation of the LCST of light-responsive, amphiphilic poly(NIPAM) derivatives. Soft Matter *8*, 8446–8455.

Menzel, H., Kroger, R., and Hallensleben, M.L. (1995). Polymers with light controlled water solubility. *32*, 779–787.

Miasnikova, A., Benítez-Montoya, C.A., and Laschewsky, A. (2013). Counterintuitive Photomodulation of the Thermal Phase Transition of Poly(methoxy diethylene glycol acrylate) in Aqueous Solution by trans–cis Isomerization of Copolymerized Azobenzenes. Macromol. Chem. Phys. *214*, 1504–1514.

Ringsdorf, H., Venzmer, J., and Winnik, F.M. (1991). Fluorescence studies of hydrophobically modified poly(N-isopropylacrylamides). Macromolecules *24*, 1678–1686.

Rodríguez-Cabello, J. c., Alonso, M., Guiscardo, L., Reboto, V., and Girotti, A. (2002). Amplified Photoresponse of a p-Phenylazobenzene Derivative of an Elastin-like Polymer by α-Cyclodextrin: The Amplified ΔTt Mechanism. Adv. Mater. *14*, 1151–1154.

Ruchmann, J., Sebai, S.C., and Tribet, C. (2011). Photoresponse of Complexes between Surfactants and Azobenzene-Modified Polymers Accounting for the Random Distribution of Hydrophobic Side Groups. Macromolecules *44*, 604–611.

Tom, N.J., Simon, W.M., Frost, H.N., and Ewing, M. (2004). Deprotection of a primary Boc group under basic conditions. Tetrahedron Lett. *45*, 905–906.

Yu, B., Jiang, X., Wang, R., and Yin, J. (2010). Multistimuli Responsive Polymer Nanoparticles On the basis of the Amphiphilic Azobenzene-Contained Hyperbranched Poly(ether amine) (hPEA-AZO). Macromolecules *43*, 10457–10465.

Zhao, Y., Tremblay, L., and Zhao, Y. (2011). Phototunable LCST of Water-Soluble Polymers: Exploring a Topological Effect. Macromolecules *44*, 4007–4011.

Zheng, P., Hu, X., Zhao, X., Li, L., Tam, K.C., and Gan, L.H. (2004). Photoregulated Sol-Gel Transition of Novel Azobenzene-Functionalized Hydroxypropyl Methylcellulose and Its α-Cyclodextrin Complexes. Macromol. Rapid Commun. *25*, 678–682.

Conclusions & perspectives

The present work aimed to develop a simple route to prepare smart, biocompatible coatings that are capable to achieve controlled interactions with cells on demand. The need for non-invasive, reversible and local stimulation of substrates used in cell culture has been identified since decades in the context of academic biological studies (studies of migration/polarization) and in the field of tissue engineering. Diverse physico-chemical properties of the extra-cellular matrix and of cell environment play a considerable role in cell/matrix interactions (concentrations and gradients of biomolecules, rigidity, topography, ...). Hence, stimuli-responsive materials, capable to switch surface properties (in response to a non-toxic stimulus) are in demand for the dynamic control of cells. But at the same time, one shall not neglect the complexity of cell responses to perturbation of multiple surface properties. If one seeks at clear interpretations of the experimental perturbations achieved on cell behaviors, it is key to achieve systematic variation of the surface features, which at the molecular level comes down to control of surface-deposited polymer chains.

In particular, we developed PLL derivatives that spontaneously form well-controlled temperature-sensitive adlayers or light-responsive ones. The temperature- and/or light-responsive polymer moieties used to confer remote control in the layers are not new. Our specific goal was to design systems that are straightforward to implement in biology laboratories, and that reach the stage of being manipulated in cell culture conditions. On more fundamental grounds, the versatility of PLL derivatives enabled us to explore the molecular switch achieved on surfaces in a variety of well-defined mixed layers, and thus to propose design rules for an efficient coupling of the molecular properties with cell adhesion and/or ligand accessibility on surfaces. Prior to this work, various thermo-responsive polymer layers were reported in the literature to be useful for controlling reversibly cell adhesion, which was first demonstrated on layers of PNIPAM hydrogels, and more recently as 2-(2-methoxyethoxy)ethyl methacrylate brushes, able to reversibly mask/unmask biological ligands upon temperature variation. However, the formation of such polymer layers requires a complex chemistry of surface. The advantage of PLL-g-PNIPAM here relies on the electrostatic-driven adsorption on clean glass, that spontaneously forms dense surface coverage of PNIPAM strands, close to the brush regime. The resulting adlayers resist to rinsing, and to temperature cycles that switch the layer between swollen/collapsed states. Moreover, mixed adlayers can be obtained by simply immerging the anionic glass substrates in mixed solutions of two PLL-g-PNIPAM derivatives or a mixture of PLL-g-PEG with PLL-g-PNIPAM. This "grafting to" method facilitates the comparison of surface layers that only differ in term of their composition, while conveniently preserving a low degree of non-specific binding to cells or protein-coated particles. To our knowledge, very few methods enable to prepare sets of surfaces of varying composition while preserving the same chain lengths and same dispersity.

An important challenge consisted in finding the relevant parameters of PLL-g-PNIPAM adlayers to thermally modulate the accessibility of ligand in the layer. RAFT-based synthesis of macrografts used to prepare PLL-g-PNIPAM derivatives was developed, affording comb-like copolymers with well-defined architecture (control of the size, the composition and the end of PNIPAM grafts). This synthesis made it possible to study the influence of the ligand position in PLL-g-PNIPAM chains (randomly distributed in PNIPAM strands, attached at the free PNIPAM end, or attached in the surface-bound PLL). The ligand accessibility was also modulated depending on the chain length, and on length of ligand-free chains that were co-adsorbed. A comprehensive investigation of these parameters (not yet undertaken) becomes now feasible, and will deserve future studies. Our first results on the adsorption of Streptavidin-carrying particles on biotinylated PLL-g-PNIPAM adlayers show that significant contrast of Biotin accessibility can be reached as a function of temperature, when a transition between swollen and collapsed PNIPAM strands occurs in the adlayers. The modulation of particle binding was attributed to a change in effective (accessible) ligand density, in line with a rapid decrease of binding upon decreasing Biotin density (in mixed layers of Biotinylated and non-Biotinylated PLLs). The exact mechanism of accessibility modulation is however not fully deciphered (sequestration in hydrophobic clusters or indirect consequence of the formation of a rigid and rough interface). Similarly, to study dynamic control of cell adhesion, we synthesized a PLL-g-PNIPAM with adhesive peptide (RGD) along PNIPAM grafts. This RGD-PNIPAM were significantly more hydrophilic as compared with Biotinylated PNIPAM and did not undergo collapse transition at cell-culture temperature. In the configuration of mixed layer with PLL-g-PNIPAM (RGD-free PNIPAM strands), we demonstrate that the specific adhesion of HeLa cells is modulated by temperature and is lower at 27 °C above swollen layers. Control of RGD density was key to reach an effective modulation of cell spreading, showing the importance of a good control and repeatability of the surface deposition of mixed polymers. Under optimal composition conditions, cells can be quantitatively detached from layers by simply decreasing temperature showing that the presence of thick polymer films below the cells is not a required condition. These mixed PLL-g-PNIPAM layers can be directly envisaged as a new tool to study *in situ* the reorganization of focal adhesions.

Finally, we studied light-responsive PLL derivatives based on azobenzene-containing PNIPAM macrografts. A diversity of structures was considered with different azobenzene grafting densities, polarity/ionization, and comparison of polymers containing end-grafted with side-grafted chromophores. In consistency with recent reports from literature, it appears that topological effects play a significant role on the light-response. Small magnitude of responses, "inverse" responses to light (increased solubility upon formation of apolar photo-isomers) and "direct" responses (decreased solubility upon decreasing polarity by photoisomerization) were observed. The "inverse" response is presumably due to the formation in water of hydrophobic clusters of azobenzene, which is also a possible origin of the small temperature window allowing isothermal photoswitch of solubility (here, we reached a maximum shift of 6 °C between cloud points of *cis* and *trans* polymers). These results highlight the difficulty to optimize the light response of azobenzene-containing flexible chains. We conclude that robust responses of chromophore-based polymer layers will be extremely difficult to reach in water, and *a fortiori* in culture media where possible interferences may add due to non-specific interactions between proteins and hydrophobic chromophores.

As a promising extension of our work on temperature-responsive layers, we suggest at the end of this thesis that PLL-g-PNIPAM with local heating by arrays of thermoplasmonic nanoparticles should be considered as a robust route to optical control of adhesion. Indeed, a laser illumination (λ_{ecx} ~ from green to Infra-Red, power ~ 0.02 $mW.\mu m^{-2}$) is sufficient to increase locally the temperature by several degrees. Above laser-heated surfaces, PLL-g-PNIPAM shall undergo their collapse transition similar to the one demonstrated here on the whole substrate.

Appendix 1 - Protocols for synthesis

Contents

1 Materials and methods

All chemicals were purchased from Sigma-Aldrich, except diethyl ether (VWR), sodium tetraborate decahydrate (Fluka), and end-functional polyethylene glycol (PEG-NHCO-C_2H_4-CO-NHS, MW 2000 Da, RAPP Polymer). Fluorescent probes (Alexa-NHS) were purchased from LifeTechnologies. Azobis(isobutyronitrile) was recrystallized in methanol, and diethyl ether was dried on molecular sieves (4 Å) before use. Deionized water was produced via Milli-Q, Direct-Q 5 instrument (Millipore).

^{1}H-NMR spectra were recorded at 20 °C on a Bruker Topspin spectrometer (300 MHz). Chemical shifts (δ) are reported in parts per million (ppm) relative to a residual proton peak of the solvent, δ = 2.50 for DMSO-d_6 and δ = 4.79 for D_2O. Multiplicities are reported as s (singlet), d (doublet), t (triplet), q (quartet), dd (doublet of doublets), dt (doublet of triplets), or m (multiplet). The number of protons (n) for a given resonance is indicated as “nH”, and is based on spectral integration values.

Molecular weight and dispersity of polymers were determined by size exclusion chromatography in DMF at 24 °C, via elution through three Viscotek columns (CLM1014/CLM1012/CLM1011, 0.7 mL.min^{-1}) with refractive index detection (Viscotek dectector). Calibration was performed with PS standards kit (Viscotek, 1050– 64500 Da).

2 Synthesis of HOOC-Azo-NH_2

The synthesis of the azobenzene HOOC-Azo-NH_2 is discussed in Chapter 6 (section 2.3). Protocols corresponding to the four-step synthesis (Figure 96) are detailed here.

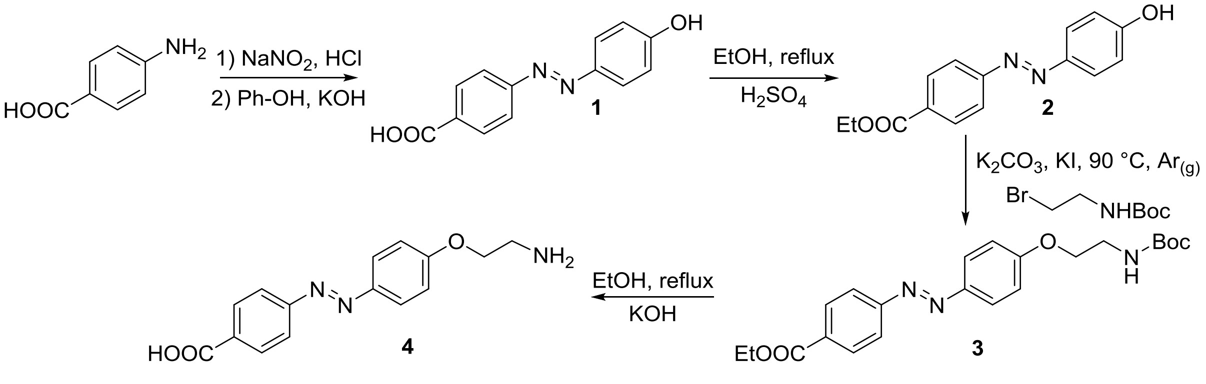

Figure 96 - Four-step synthesis of HOOC-Azo-NH_2 (4).

2.1 Step 1 - synthesis of compound 1

4-aminobenzoic acid (2 mmol, 274 mg) was added to a solution of concentrated HCl (0.9 mL) in water (0.9 mL). Sodium nitrite (138 mg, 2.0 mmol) in water (4mL) was added dropwise to the reaction mixture while the temperature was kept under 5 °C by immersion in a crushed ice bath. The solution was stirred for 15 min at 0 °C. The resulting cold solution of diazonium salt was gently added at 0 °C to a solution of phenol (188 mg, 2.0 mmol) in water (4 mL) containing KOH (0.9 g). After complete addition, the mixture was kept at 0 °C during 1 H. The resulting solid was filtered, washed with cold HCl (1M) and dried under vacuum (brown solid, 400 mg, 87 %).

δ (^{1}H-NMR, MeOD): 6.93 (2H, d, 8.9Hz), 7.88 (4H, t, 8.8 Hz), 8.16 (2H, d, 8.4Hz)

2.2 Step 2 - synthesis of compound 2

Compound **1** (400 mg, 1.65 mmol) was dissolved in absolute ethanol (55 mL) with concentrated sulfuric acid (3 drops). The reaction mixture was stirred under reflux during 4 H. After cooling to room temperature, the mixture was diluted in water and extracted with dichloromethane. The organic layer was washed with water, dried over anhydrous magnesium sulfate, filtrated and the solvents were evaporated. The product was purified by column chromatography on silica gel (dichloromethane then ethyl acetate) to afford ethyl 4-(4'-hydroxyphenylazo) benzoate **2** as an orange solid (198 mg, 44 %).

δ (^{1}H-NMR, $CDCl_3$): 1.36 (3H, t, 7.1Hz), 4.35 (2H, q, 7.1Hz), 6.90 (2H, m), 7.84 (4H, m), 8.11 (2H, m)

2.3 Step 3 - synthesis of compound 3

A mixture of ethyl 4-(4'-hydroxyphenylazo)benzoate **2** (100 mg, 0.41 mmol), 2-bromoethanamine (139 mg, 0.62 mmol), K_2CO_3 (0.24 g), and KI (4 mg) in anhydrous DMSO (5 mL) was heated at 90 °C overnight under argon. The resulting mixture was cooled to room temperature, washed with water, dried on anhydrous magnesium sulfate, filtered, and the filtrate was concentrated under reduced pressure. The product was purified by column chromatography on silica gel (dichloromethane then dichloromethane/ethyl acetate 30/1) to give the compound **3** as an orange solid (87 mg, 51 %).

δ (^{1}H-NMR, $CDCl_3$): 1.40 (3H, t, 7.0Hz), 1.44 (9H, s),1.52 (s, 1H), 3.56 (2H, m), 4.10 (2H, m), 4.35 (2H, q, 7.0Hz), 7.00 (2H, m), 7.91 (4H, m), 8.16 (2H, m)

2.4 Step 4 - synthesis of compound 4

A mixture of compound **3** (50 mg, 0.12 mmol), and KOH (50 mg) in ethanol (3 mL) was heated under reflux overnight. The resulting mixture was cooled to room temperature, washed with water, dried on anhydrous magnesium sulfate, filtered. Solvent was removed under reduced pressure to afford compound **4** as a brown solid (30 mg, 88 %).

δ (^{1}H-NMR, DMSO-d_6): 3.27 (2H, t, 4.7Hz), 4.31 (2H, t, 4.7Hz), 7.21 (2H, d, 8.9Hz), 7.95 (4H, m), 8.13 (2H, d, 8.3Hz)

3 Synthesis of α-C$_i$,ω-NHS-P(NIPAM-co-B) and α-C$_i$,ω-COOH-P(NIPAM-co-B)

The synthesis of α-C$_i$,ω-NHS-P(NIPAM-co-B) and α-C$_i$,ω-COOH-P(NIPAM-co-B) (Figure 97) is discussed in Chapter 2 (section 2).

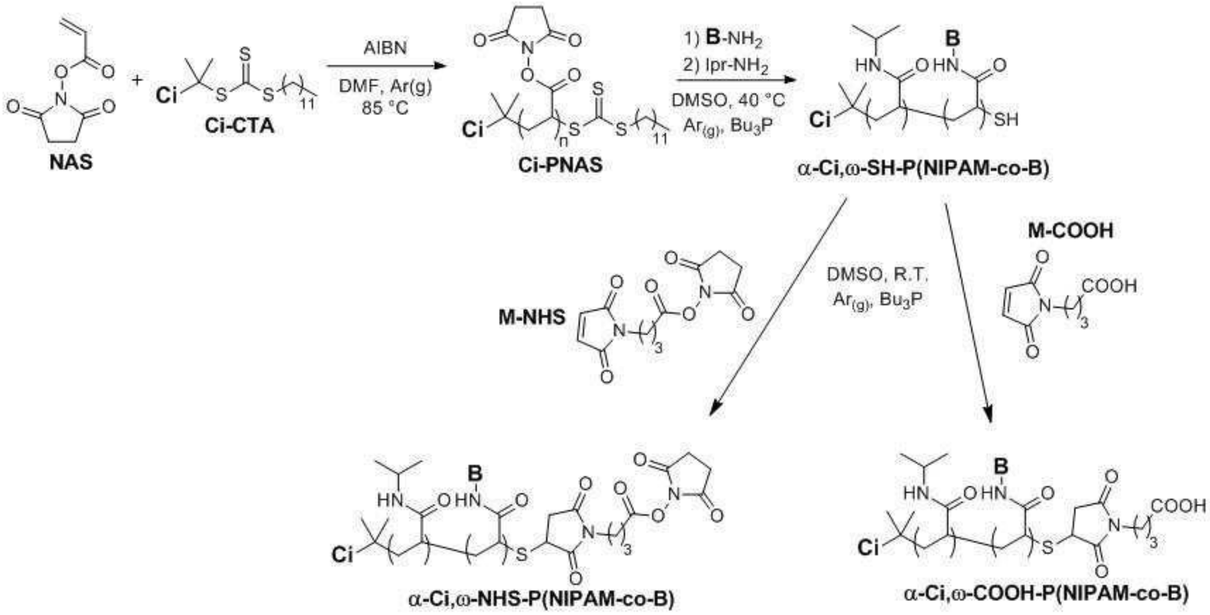

Figure 97 - Scheme of the synthetic route to α-C$_i$,ω-COOH-P(NIPAM-co-B) and α-C$_i$,ω-NHS-P(NIPAM-co-B) random copolymers.

3.1 Synthesis of C$_i$-CTAs

The synthesis of C$_i$-CTA consists in coupling NHS-CTA with the corresponding R$_i$-NH$_2$ amine (Figure 98). The synthesis is discussed in Chapter 2 (section 2.1).

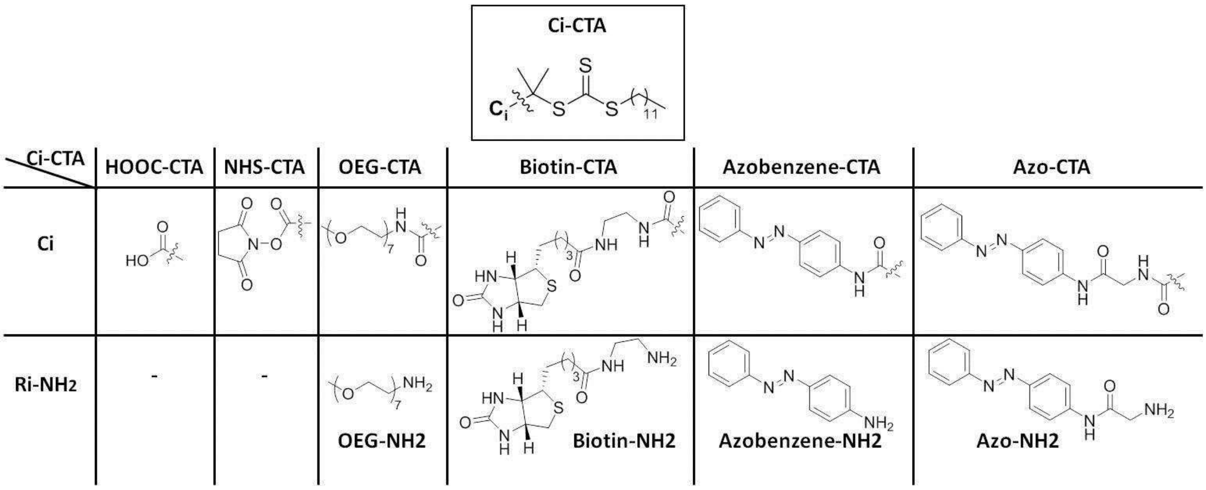

Figure 98 - C$_i$-CTA structure (top), HOOC-CTA and NHS-CTA are commercial. OEG-CTA and Azo-CTA were obtained by coupling NHS-CTA with the corresponding R$_i$-NH$_2$. Attempts to synthesize both Biotin-CTA and Azobenzene-CTA have failed.

3.1.1 Synthesis of OEG-CTA

NHS-CTA (250 mg, 0.54 mmol) was dissolved in chloroform (10 mL). A solution of OEG-NH$_2$ (254 mg, 0.50 mmol) in 1 mL of chloroform was added into the NHS-CTA solution. The reaction mixture was stirred at 25 °C for 5 H. Then, it was washed with water (2*30 mL) and dried over anhydrous magnesium sulfate. After solvent removal, the product was purified on column chromatography (dichloromethane then ethyl acetate/methanol 90/10) to afford a yellow oil (yield: 21 %, 90 mg).

δ (^{1}H-NMR, $CDCl_3$): 0.85 (3H, t, 7.0Hz), 1.16-1.40 (20H, m), 1.67 (6H, s), 3.23 (3H, t, 7.5Hz), 3.35 (3H, s), 3.36-3.70 (26H, m)

3.1.2 Synthesis of Azo-CTA

NHS-CTA (200 mg, 0.43mmol) was dissolved in chloroform (20 mL). Azo-NH_2 (102 mg, 0.41mmol) was added into the solution of NHS-CTA. Due to the low solubility of the azobenzene compound, the reaction mixture was stirred under reflux overnight. Then, it was washed with water (2*30 mL) and dried over anhydrous magnesium sulfate. After solvent removal, the product was purified on column chromatography (dichloromethane then ethyl acetate/dichloromethane1/10) to afford an orange oil (yield: 72 %, 181 mg).

δ (^{1}H-NMR, $CDCl_3$): 0.84 (3H, t, 7.0Hz), 1.13-1.38 (20H, m), 1.74 (6H, s), 3.22 (2H, t, 7.5Hz), 4.09 (2H, d, 5.8Hz), 7.17 (1H, t, 5.8Hz), 7.42-7.50 (2H, m), 7.67-7.73 (2H, m), 7.84-7.94 (4H, m), 8.54 (s, H amide)

3.2 Synthesis of N-acryloxysuccinimide (NAS, monomer)

Monomer (NAS) was synthesized as follows, a few days prior to its RAFT polymerization. N-Hydroxysuccinimide (5.0 g, 0.043 mol) and triethylamine (7.3 mL, 0.050 mol) were dissolved in chloroform (65 mL) at 0 °C. N-Acryloylchloride (3.9 mL, 0.047 mol) was added dropwise and the mix was kept under gentle stirring for 30 min at 0 °C. The reaction mixture was washed twice with 30 mL saturated NaCl solution, dried over magnesium sulfate, and concentrated by evaporation yielding viscous oil. Ethyl acetate:pentane (7 mL, 1:3 v/v) was added to the oil at 0 °C in order to induce NAS crystallization. After filtration and drying under vacuum, the product was obtained as a white solid (5.2 g, 71%).

δ (^{1}H-NMR, DMSO-d_6): 2.84 (s, 4H), 6.35 (dd, J = 10.3, 1.2 Hz, 1H), 6.52 (dd, J = 18.1, 10.4 Hz, 1H), 6.67 (dd, J = 17.2, 1.3 Hz, 1H)

3.3 Polymerization of NAS in presence of C_i-CTA (RAFT) – Synthesis of reactive parent chains C_i-PNAS

During this project, NAS was polymerized with the three different C_i-CTA represented in Figure 99.

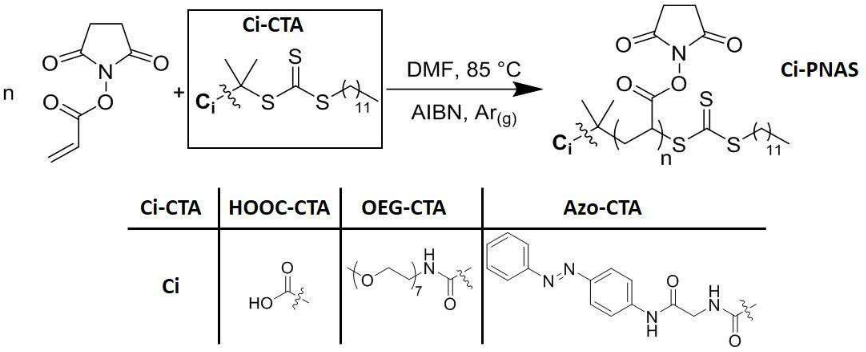

Figure 99 - RAFT polymerization of NAS with the different Ci-CTA engaged.

3.3.1 Generic protocol

NAS, AIBN, and C_i-CTA were placed into a Schlenk flask and dissolved in anhydrous DMF. The solution was degassed via four freeze-pump-thaw cycles, and heated to 85 °C under argon atmosphere. Aliquots were regularly withdrawn from the reaction medium and analyzed by ^{1}H-NMR (DMSO-d_6) to determine monomer conversion by comparing the relative integral areas of the methylene CH_2 backbone protons (1.71−2.24 ppm, 2H) to the monomer vinyl proton (6.35 ppm, 1H). Degree of polymerization (DP_n) and dispersity (I) were determined by SEC analyses in DMF. Polymerization was stopped by freezing the flask in liquid nitrogen once conversion reached 80%. The polymer was precipitated twice in dried diethyl ether, and dried under vacuum, yielding poly(NAS) as a yellow powder.

3.3.2 Specific conditions and polymer characterizations

C_i-PNAS	$[NAS]_0/[CTA]_0$	$[CTA]_0/[AIBN]_0$	NAS	CTA	AIBN	DMF	t
HOOC-PNAS	50	10	3 g 18 mmol	132 mg 0.36 mmol	6 mg 36 µmol	6 mL	2 H
OEG-PNAS	50	10	1 g 6 mmol	102 mg 0.12 mmol	2 mg 12 µmol	2 mL	3 H
Azo-PNAS	50	10	1 g 6 mmol	72 mg 0.12 mmol	2 mg 12 µmol	2 mL	3 H
Azo-PNAS40	50	5	1.5 g 9 mmol	109 mg 0.18 mmol	6 mg 36 µmol	3 mL	2.5 H
Azo-PNAS18	25	5	0.5 g 2.9 mmol	70 mg 0.12 mmol	4 mg 24 µmol	1 mL	2.25 H

Table 18 – Quantities of reactants engaged for RAFT polymerizations. t: time of polymerization.

C_i-PNAS	$[NAS]_0$	$[NAS]_0/[CTA]_0$	$[CTA]_0/[AIBN]_0$	α [(a)]	I [(b)]	DP_n[(a)]	M_n (kDa) [(c)]	$m_{\text{dried polymer}}$	yield
HOOC-PNAS	3 M	50	10	80 %	1.2	50	8.8	1.5 g	50 %
OEG-PNAS	3 M	50	10	81 %	1.2	46	8.7	0.6 g	56 %
Azo-PNAS	3 M	50	10	0 %	-	-	-	-	-
Azo-PNAS40	3 M	50	5	84 %	1.2	40	7.4	1.3 g	84 %
Azo-PNAS18	3 M	25	5	40 %	1.2	18	3.6	0.2 g	40 %

Table 19 - Characterizations of polymers obtained after two consecutive precipitations in anhydrous diethyl ether and drying. Every polymerization was conducted at 85 °C under argon atmosphere. (a) Both final conversion α and degree of polymerization DP_n were evaluated by ^{1}H-NMR in DMSO-d_6, (b) Dispersity index I was evaluated by simple-detection SEC in DMF (polystyrene standards), (c) Molecular weight was calculated from $M_n = DP_n * M_{NAS} + M_{CTA}$.

Ci-PNAS were characterized by SEC and 1H-NMR (Figure 100) as detailed in Chapter 2 (section 2.2.2).

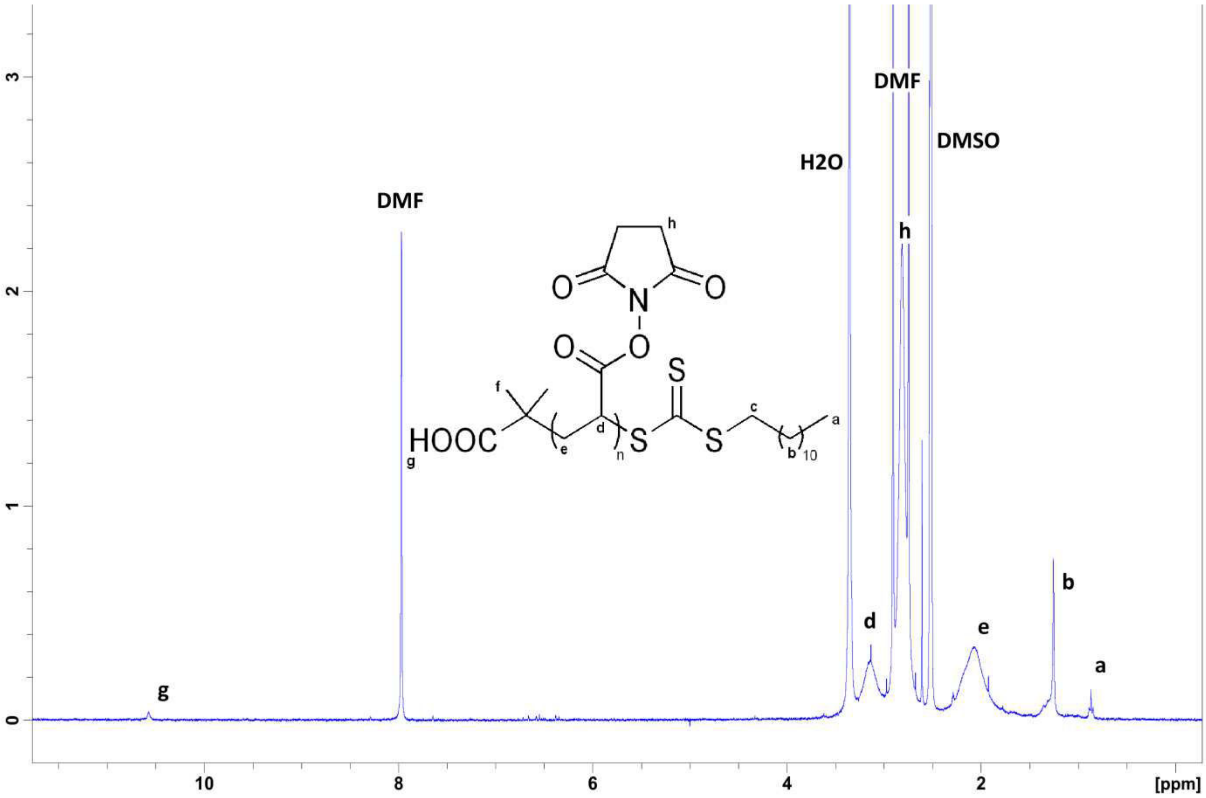

Figure 100 – ^{1}H-NMR spectrum (DMSO-d_6) of HOOC-PNAS purified after two consecutive precipitations in dried diethylether

δ (^{1}H-NMR, DMSO-d_6, **HOOC-PNAS**): 0.85 (t, J = 6.4 Hz, 3H), 1.24 (m, 20H), 1.71-2.40 (s, 100H), 2.74-2.87 (s, 186H), 2.98-3.25 (s, 55H), 10.55 (s, 1H)

δ (^{1}H-NMR, DMSO-d_6, **OEG-PNAS**): 0.85 (t, J = 6.4 Hz, 3H), 1.23 (m, 20H), 1.75-2.37 (s, 58H), 2.74-2.87 (s, 92H), 2.99-3.24 (s, 30H), 3.46-3.53 (s, 22H)

δ (^{1}H-NMR, DMSO-d_6, **Azo-PNAS40**): 0.84 (t, J = 6.8 Hz, 3H), 1.16-1.36 (m, 20H), 1.65-2.40 (s, 80H), 2.73-2.86 (s, 130H), 2.98-3.26 (s, 40H), 7.52-7.92 (m, 9H)

δ (^{1}H-NMR, DMSO-d_6, **Azo-PNAS18**): 0.84 (t, J = 6.8 Hz, 3H), 1.16-1.36 (m, 20H), 1.65-2.40 (s, 36H), 2.73-2.86 (s, 68H), 2.98-3.26 (s, 18H), 7.52-7.92 (m, 9H)

3.4 Post-modifications of C_i-PNAS into α-C_i,ω-NHS-P(NIPAM-co-B) and α-C_i,ω-COOH-P(NIPAM-co-B)

The different amines used for post-modifications are represented in Figure 101.

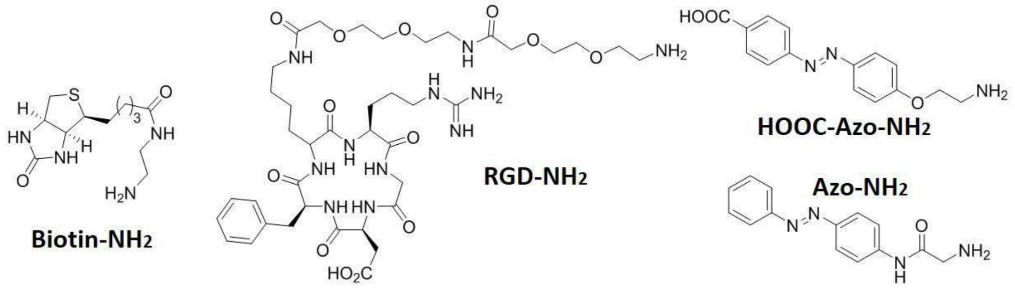

Figure 101 - B-NH$_2$ amines used to modify C_i-PNAS.

3.4.1 Synthesis of α-COOH,ω-NHS-PNIPAM(6)/α-COOH,ω-NHS-P(NIPAM-co-Biotin)(6)/α-COOH,ω-NHS-P(NIPAM-co-RGD)(6)

Freshly synthesized HOOC-PNAS (100 mg, 0.58 mmol of NAS monomers, 0.011 mmol of polymers) and tributylphosphine (0.1 mL) were dissolved in anhydrous DMSO (1.5 mL). To obtain copolymers, 5 mol % of Biotin-NH_2 or RGD-NH_2 (relative mol % to NAS) was added and the reaction bath was heated up to 40 °C for 2 h, under argon, before an excess of isopropylamine (0.12 mL, 1.5 mmol) was added. The addition of biotin/RGD was skipped to form pure PNIPAM chains. After two more hours at 40 °C, the polymer was precipitated twice into dried diethyl ether. The dried polymer contained a thiol end group. The totality of the dried polymer was dissolved in anhydrous DMSO (2 mL), with 4-maleimidobutyric acid N-hydroxysuccinimide ester (2 equivalents relative to thiols, 0.022 mmol, 6 mg) and tributylphosphine (catalytic amount) and then kept at room temperature for 6 h under argon atmosphere. The product was precipitated twice into diethyl ether and then dried under vacuum.

- **α-COOH,ω-NHS-PNIPAM(6)**

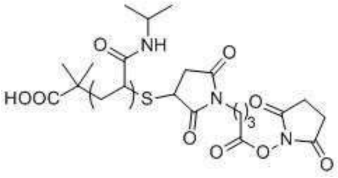

$m_{\text{dried polymer}}$ = 27 mg

δ (^{1}H-NMR, DMSO) : 0.86-1.16 (-CH_2-CH(CO-NH-CH-(C**H**$_3$)$_2$)-, 6H), 1.20-1.62 (-C**H**$_2$-CH(CO-NH-CH-(CH$_3$)$_2$)-, 2H), 1.72-2.09 (-CH_2-C**H**(CO-NH-CH-(CH$_3$)$_2$)-, 1H), 3.65-3.94 (-CH_2-CH(CO-NH-C**H**-(CH$_3$)$_2$)-, 1H), 6.86-7.80 (-CH_2-CH(CO-N**H**-CH-(CH$_3$)$_2$)-,1H)

- **α-COOH,ω-NHS-P(NIPAM-co-Biotin)(6)**

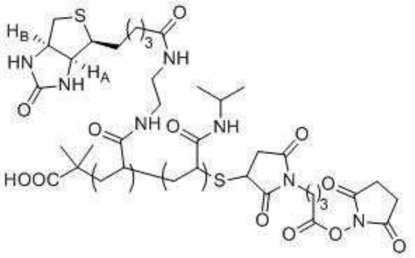

$m_{\text{dried polymer}}$ = 25 mg

δ (^{1}H-NMR, DMSO) : 0.92-1.11 (-CH_2-CH(CO-NH-CH-(C**H**$_3$)$_2$)-, 6H), 1.19-1.70 (-C**H**$_2$-CH(CO-NH-R)-, 2H), 1.78-2.12 (-CH_2-C**H**(CO-NH-R)-, 1H), 3.68-3.96 (-CH_2-CH(CO-NH-C**H**-(CH$_3$)$_2$)-, 1H), 4.09-4.15 (proton H_A related to the Biotin), 4.27-4.34 (proton H_B related to the Biotin), 6.93-7.87 (-CH_2-CH(CO-N**H**-R)-,1H)

- **α-COOH,ω-NHS-P(NIPAM-co-RGD)(6)**

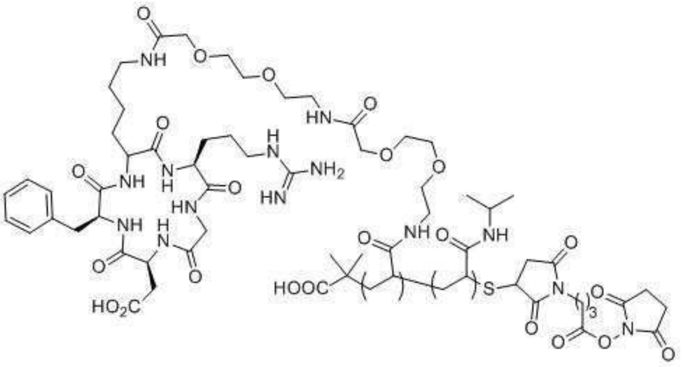

$m_{\text{dried polymer}}$ = 60 mg

δ (^{1}H-NMR, DMSO) : 0.86-1.16 (-CH$_2$-CH(CO-NH-CH-(C**H**$_3$)$_2$)-, 6H), 1.20-1.62 (-C**H**$_2$-CH(CO-NH-CH-(CH$_3$)$_2$)-, 2H), 1.72-2.09 (-CH$_2$-C**H**(CO-NH-CH-(CH$_3$)$_2$)-, 1H), 3.65-3.94 (-CH$_2$-CH(CO-NH-C**H**-(CH$_3$)$_2$)-, 1H), 6.86-7.80 (-CH$_2$-CH(CO-N**H**-CH-(CH$_3$)$_2$)-,1H), 7.16-7.40 (m, aromatic signals from phenylalanine, 1.1H)

3.4.2 Synthesis of α,ω-di-COOH-P(NIPAM-co-Azo[α]-NMe$_2$[β])(6)

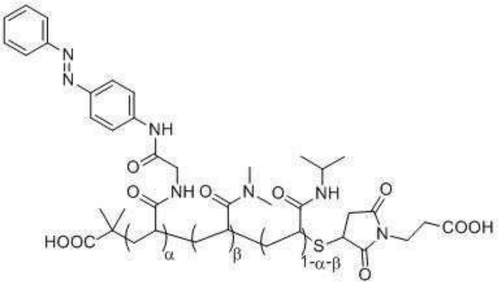

Freshly synthesized HOOC-PNAS (94 mg, 0.55 mmol of NAS monomers, 0.011 mmol of polymers) and tributylphosphine (0.1 mL) were dissolved in anhydrous DMSO (2 mL). Dimethylamine (0.22 mmol, 112 µL, 2 M, THF, β) was added and the reaction bath was heated up to 40 °C for 2 h, under argon. Azobenzene-NH$_2$ was then added (quantities are indicated in the Table 20, α) for 2 H, before an excess of isopropylamine (0.2 mL, 2.46 mmol) was added. 2 H later, N-(2-carboxyethyl)maleimide (6 mg, 0.035 mmol) was added. After two more hours at 40 °C, the polymer was precipitated twice into anhydrous diethyl ether and dried under vacuum, giving a yellow powder.

Polymer	Azo-NH$_2$ introduced	In the feed		In the copolymer, α (mol%)		In the copolymer, β (mol%, NMR)	Yield $m_{\text{dried polymer}}$
		α (mol%)	β (mol%)	NMR	UV-vis		
HOOC-P(NIPAM-co-Azo[0]-NMe$_2$[40])	0 mg, 0 mmol	0	40	0	0	30	92 % 58 mg
HOOC-P(NIPAM-co-Azo[4]-NMe$_2$[40])	5.4 mg, 0.022 mmol	4	40	2.5	2.8	30	30 % 19 mg
HOOC-P(NIPAM-co-Azo[6]-NMe$_2$[40])	8.2 mg, 0.033 mmol	6	40	3	5.1	28	65 % 41 mg
HOOC-P(NIPAM-co-Azo[9]-NMe$_2$[40])	12.2 mg, 0.049 mmol	9	40	5	6.9	30	90 % 57 mg
HOOC-P(NIPAM-co-Azo[12]-NMe$_2$[40])	16.3 mg, 0.066 mmol	12	40	9	10	29	62 % 39 mg
HOOC-P(NIPAM-co-Azo[18]-NMe$_2$[40])	24.5 mg, 0.099 mmol	18	40	10	15	28	95% 60 mg

Table 20 - Proportion of Azo-NH$_2$ α and dimethylamine β introduced in the feed. (α,β) were determined by ^{1}H-NMR in MeOD and spectrophotometry (see Chapter 6 - 3.1).

δ (^{1}H-NMR, MeOD): 0.87-1.22(-CH$_2$-CH(CO-NH-CH-(C**H**$_3$)$_2$)-), 1.35-1.79(-C**H**$_2$-CH(CO-NH-CH-(CH$_3$)$_2$)-), 1.80-2.22 (-CH$_2$-C**H**(CO-NH-CH-(CH$_3$)$_2$)-), 2.68-2.93(-CO-N-(C**H**$_3$)$_2$), 3.70-4.00(-CH$_2$-CH(CO-NH-C**H**-(CH$_3$)$_2$)-), 4.51(-NH-C**H**$_2$-CO-NH-azobenzene), 6.68-8.00(-CH$_2$-CH(CO-N**H**-CH-(CH$_3$)$_2$)- and azobenzene aromatic signals).

3.4.3 Synthesis of α-COOH,ω-NHS-P(NIPAM-co-Azo[α]-NMe$_2$[β]-Biotin[γ])(6)

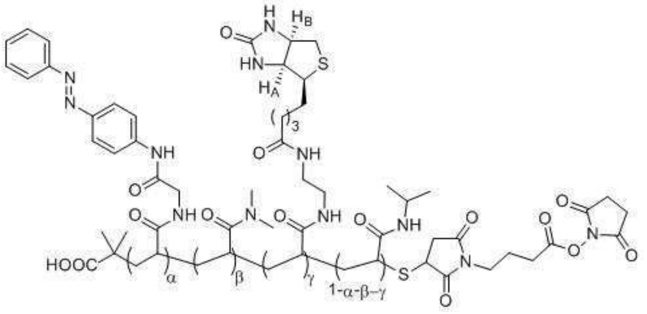

Freshly synthesized HOOC-PNAS (200 mg, 1.17 mmol of monomers, 0.023 mmol of polymers) and tributylphosphine (0.2 mL) were dissolved in anhydrous DMSO (3 mL). Dimethylamine (0.46 mmol, 237 µL, 2 M, THF) was added and the reaction bath was heated up to 40 °C for 2 h, under argon. Azo-NH$_2$ (16 mg, 0.07 mmol) and Biotin-NH$_2$ (22 mg, 0.06 mmol) was added and the reaction bath was stirred two supplementary hours, before an excess of isopropylamine (0.3 mL, 3.7 mmol) was added. After two more hours at 40 °C, the polymer was precipitated twice into anhydrous diethyl ether and dried under vacuum. The resulting dried polymer, containing a thiol end group, was firstly used for NMR and turbidimetry analyses. Then, this thiol-polymer was totally engaged in a thiol-maleimide reaction by dissolving it in anhydrous DMSO (2 mL), with 4-maleimidobutyric acid N-hydroxysuccinimide ester (17 mg, 0.06 mmol) and tributylphosphine (catalytic amount). The mixture was stirred at room temperature for 6 h under argon atmosphere. The product was precipitated twice into diethyl ether and then dried under vacuum (170 mg, yellow powder).

δ (^{1}H-NMR, MeOD): 0.99-1.23(-CH$_2$-CH(CO-NH-CH-(C**H**$_3$)$_2$)-), 1.40-1.80(-C**H**$_2$-CH(CO-NH-CH-(CH$_3$)$_2$)-), 1.90-2.25 (-CH$_2$-C**H**(CO-NH-CH-(CH$_3$)$_2$)-), 2.83-2.98(-CO-N-(C**H**$_3$)$_2$), 3.80-4.05(-CH$_2$-CH(CO-NH-C**H**-(CH$_3$)$_2$)-), 4.35-4.42 (proton HA related to the biotin), 4.53–4.61 (proton HB related to the biotin, -NH-C**H**$_2$-CO-NH-azobenzene), 6.68-8.00(-CH$_2$-CH(CO-N**H**-CH-(CH$_3$)$_2$)- and azobenzene aromatic signals). From quantitative analyses of integral areas, the polymer composition was deduced: α-COOH,ω-NHS-P(NIPAM-co-Azo[5%]-NMe_2[25%]-Biotin[5%])(6).

3.4.4 Synthesis of α-Azo,ω-COOH-PNIPAM(M_n)/α-Azo,ω-NHS-PNIPAM(M_n)/α-Azo,ω-NHS-P(NIPAM-co-Biotin)(2)

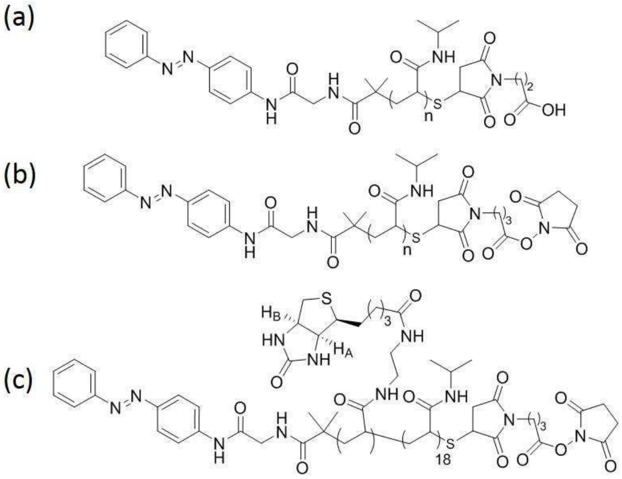

Figure 102 - Chemical structure of (a) α-Azo,ω-COOH-PNIPAM(M_n), (b) α-Azo,ω-NHS-PNIPAM(M_n), (c) α-Azo,ω-NHS-P(NIPAM-co-Biotin)(2).

Azo-PNAS (100 mg, 0.013 mmol of monomers) and tributylphosphine (0.1 mL) were dissolved in anhydrous DMSO (1.5 mL). The first amine Biotin-NH_2 was added to the solution with a proportion corresponding to the aimed grafting ratio and assuming a quantitative grafting reaction. The reaction bath was brought to 40 °C for 2 H, under argon. Then, an excess isopropylamine (0.12 mL, 1.5 mmol) was added and the temperature was maintained two more hours at 40 °C. The polymer was precipitated two times into dried diethylether. After drying under vacuum, the polymer was obtained as a yellow solid. The dried polymer contained a thiol end group (α-Azo,ω-SH-PNIPAM or α-Azo,ω-SH-P(NIPAM-co-Biotin)). The totality of the dried polymer (α-Azo,ω-SH-PNIPAM or α-Azo,ω-SH-P(NIPAM-co-Biotin)) (100 mg, 1 equiv. relative to thiol), 4-Maleimidobutyric acid N-hydroxysuccinimide ester or 3-Maleimidopropionic acid (2 equiv.) and tributylphosphine (catalytic quantity) were dissolved in anhydrous DMSO (2 mL). The solution was stirred at room temperature for 6 h under argon atmosphere. Unreacted maleimides were removed by two precipitations into dried diethylether, and the precipitated polymer was dried under vacuum. The polymer was obtained as a yellow solid.

δ (^{1}H-NMR, DMSO, **α-Azo,ω-COOH-PNIPAM**) : 0.90-1.18 (-CH_2-CH(CO-NH-CH-(C**H**$_3$)$_2$)-), 1.20-1.62 (-C**H**$_2$-CH(CO-NH-CH-(CH_3)$_2$)-), 1.72-2.11 (-CH_2-C**H**(CO-NH-CH-(CH_3)$_2$)-), 3.72-3.95 (-CH_2-CH(CO-NH-C**H**-(CH_3)$_2$)-), 6.86-7.80 (-CH_2-CH(CO-N**H**-CH-(CH_3)$_2$)-), 7.50-7.98 (aromatic signals linked to the azobenzene)

δ (^{1}H-NMR, DMSO, **α-Azo,ω-NHS-P(NIPAM-co-Biotin)**) : 0.97-1.13 (-CH_2-CH(CO-NH-CH-(C**H**$_3$)$_2$)-, 6H), 1.22-1.70 (-C**H**$_2$-CH(CO-NH-R)-, 2H), 1.78-2.15 (-CH_2-C**H**(CO-NH-R)-, 1H), 3.68-3.96 (-CH_2-CH(CO-NH-C**H**-(CH_3)$_2$)-, 1H), 4.09-4.15 (proton H_A related to the Biotin), 4.27-4.34 (proton H_B related to the Biotin), 6.93-7.87 (-CH_2-CH(CO-N**H**-R)-,1H), 7.52-7.89 (aromatic signals linked to the azobenzene)

4 Grafting of NHS-compounds on PLL

4.1 Generic protocol of grafting

Poly(lysine) (PLL-HBr, 20 mg, 95 µmol from Sigma-Aldrich) with an average molecular weight of 20 kDa was dissolved in 1 mL of 50 mM sodium tetraborate buffer pH 8.5 in water. After dissolution of the NHS-compounds, the solution was kept at room temperature overnight, dialyzed (MW cutoff 3.5 kDa) against Milli-Q water for 1 day (three renewal of the bath), and then lyophilized. To estimate the degree of grafting τ of PLL amine groups, the peak areas from unmodified lysine ($-CH-(CH_2)_3-C\mathbf{H}_2-$ NH_3) and modified ones ($-CH-(CH_2)_3-C\mathbf{H}_2-NH-CO-$) were compared on 1H-NMR spectra ($\tau = \frac{I(-(CH_2)_2-C\mathbf{H_2}-NH-CO-)}{I(-(CH_2)_2-C\mathbf{H_2}-NH_2)}$).

When NHS-terminated macrografts were engaged, aliquot was added at a final chain/lysine molar ratio of 40 mol %. In the case of the grafting with small NHS compounds (for instance, grafting with Biotin-NHS to afford PLL-g-[0.18]Biotin-[0.38]PNIPAM(2)), the engaged quantity was calculated by assuming a quantitative grafting.

4.2 PLL compounds

4.2.1 grafting of commercial NHS compounds

- **PLL-g-[0.4]PEG(2)**

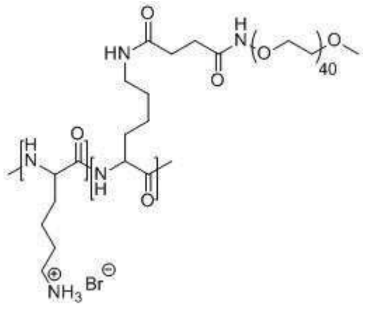

δ (^{1}H-NMR, D_2O): 1.15-1.81 (m, $-CH-(C\mathbf{H}_2)_3-CH_2-NH_3$, 6H), 2.82-2.97 (s, $-CH-(CH_2)_3-C\mathbf{H}_2-NH_3$, 1.1H), 3.03-3.17 (s, $-CH-(CH_2)_3-C\mathbf{H}_2-NH-CO-$, 0.8H), 3.23-3.35 (s, $-O-CH_2-CH_2-O-C\mathbf{H}_3$, 1.3H), 3.55-3.90 (m, $-O-C\mathbf{H}_2-C\mathbf{H}_2-O-CH_3$, 67H), 4.13-4.33 (s, $-C\mathbf{H}-(CH_2)_3-CH_2-NH_3$, 1H)

- **PLL-g-[0.27]PNIPAM(2)**

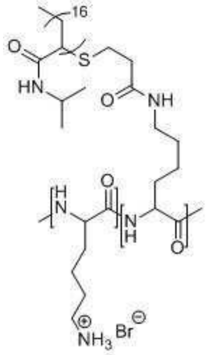

δ (RMN-^{1}H, D_2O): 0.95-1.23 (s, $-CH_2-CH(CO-NH-CH-(C\mathbf{H}_3)_2)-$, 52.6H), 1.24-2.20 (m, $-CH-(C\mathbf{H}_2)_3-CH_2-NH_3$, $-C\mathbf{H}_2-C\mathbf{H}(CO-NH-CH-(CH_3)_2)$, 34.2H), 2.87-2.98 (s, $-CH-(CH_2)_3-C\mathbf{H}_2-NH_3$, 1.5H), 3.05-3.17 (s, -CH-

(CH$_2$)$_3$-C**H**$_2$-NH-CO-, 0.5H), 3.75-3.96 (s, -CH$_2$-CH(CO-NH-C**H**-(CH$_3$)$_2$, 9.1H), 4.17-4.32 (s, -C**H**-(CH$_2$)$_3$-CH$_2$-NH$_3$, 1H)

- **PLL-g-[0.18]Biotin-[0.38]PNIPAM(2)**

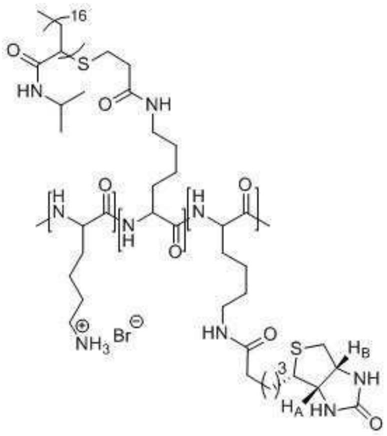

δ (^{1}H-NMR, D$_2$O): 0.89-1.18 (s, 36.6H, NH-CH(C**H$_3$**)$_2$), 1.20-2.17 (m, 24.7H, -CH-(C**H$_2$**)$_3$-CH$_2$-NH$_3$, -C**H**$_2$-C**H**(CO-NH-CH-(CH$_3$)$_2$), 2.72-2.82 (m, 1H, CH-(CH$_2$)$_3$-C**H$_2$**-NH$_3$), 2.98-3.22 (m, 1H, -CH-(CH$_2$)$_3$-C**H$_2$**-NH-CO-), 3.69-3.90 (s, 6.2H, NH-C**H**(CH$_3$)$_2$), 3.93-4.24 (m, 1H, -C**H**-(CH$_2$)$_3$-CH$_2$-NH$_3$), 4.28-4.34 (m, 0.18, **H$_A$**), 4.46-4.54 (m, 0.18, **H$_B$**)

4.2.2 grafting of synthesized α-C$_i$,ω-NHS-P(NIPAM-co-B)

- **PLL-g-[0.2]PNIPAM(6)**

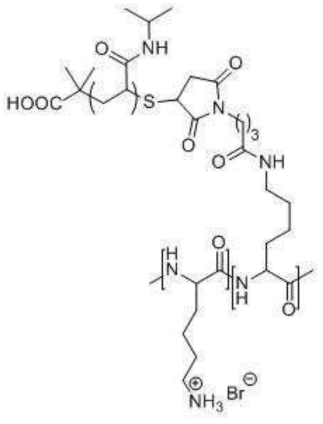

δ (^{1}H-NMR, D$_2$O): 0.95-1.23 (s, -CH$_2$-CH(CO-NH-CH-(C**H**$_3$)$_2$)-, 163H),1.24-2.20 (m, -CH-(C**H**$_2$)$_3$-CH$_2$-NH$_3$, -C**H**$_2$-C**H**(CO-NH-CH-(CH$_3$)$_2$), 93H), 2.87-2.98 (s, -CH-(CH$_2$)$_3$-C**H**$_2$-NH$_3$, 1.6H), 3.05-3.17 (s, -CH-(CH$_2$)$_3$-C**H**$_2$-NH-CO-, 0.4H), 3.75-3.96 (s, -CH$_2$-CH(CO-NH-C**H**-(CH$_3$)$_2$, 27H), 4.17-4.32 (s, -C**H**-(CH$_2$)$_3$-CH$_2$-NH$_3$, 1H)

- **PLL-g-[0.15]P(NIPAM-co-RGD)(6)**

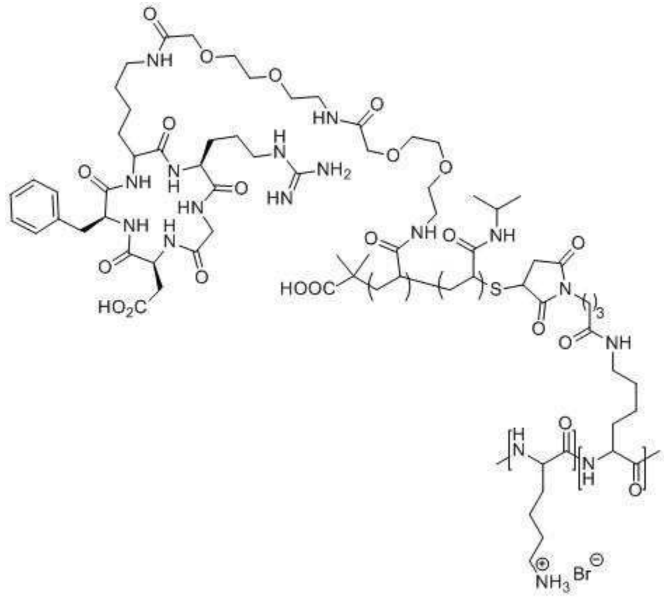

δ (^{1}H-NMR, D$_2$O): 1.00-1.27 (s, -CH$_2$-CH(CO-NH-CH-(C**H**$_3$)$_2$)-, 32.2H),1.30-2.20 (m, -CH-(C**H**$_2$)$_3$-CH$_2$-NH$_3$, -C**H**$_2$-C**H**(CO-NH-CH-(CH$_3$)$_2$), 28.3H), 2.83-3.00 (m, -CH-(CH$_2$)$_3$-C**H**$_2$-NH$_3$, 1.7), 305-3.51 (m, -CH-(CH$_2$)$_3$-C**H**$_2$-NH-CO- and RGD signals, 3.6H), 3.75-3.98 (s, -CH$_2$-CH(CO-NH-C**H**-(CH$_3$)$_2$, 6.1H), 4.22-4.35 (s, -C**H**-(CH$_2$)$_3$-CH$_2$-NH$_3$, 1H), 7.16-7.40 (m, aromatic signals from phenylalanine, 1.1H)

- **PLL-g-[0.1]P(NIPAM-co-Biotin)(6)**

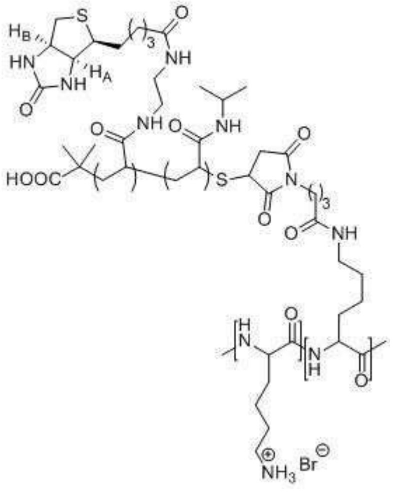

δ (^{1}H-NMR, D$_2$O): 0.92-1.22 (s, -CH$_2$-CH(CO-NH-CH-(C**H**$_3$)$_2$)-, 21H),1.26-2.29 (m, -CH-(C**H**$_2$)$_3$-CH$_2$-NH$_3$, -C**H**$_2$-C**H**(CO-NH-CH-(CH$_3$)$_2$, 20H), 2.89-3.00 (s, -CH-(CH$_2$)$_3$-C**H**$_2$-NH$_3$, 1.8H), 3.24-3.31 (s, -CH-(CH$_2$)$_3$-C**H**$_2$-NH-CO-, 0.7H), 3.73-3.96 (s, -CH$_2$-CH(CO-NH-C**H**-(CH$_3$)$_2$, 4.1H), 4.16-4.31 (s, -C**H**-(CH$_2$)$_3$-CH$_2$-NH$_3$, 1H), 4.35-4.42 (**H$_A$**, 0.2H), 4.53-4.61 (**H$_B$**, 0.2 H)

- **PLL-g-[0.1]α-OEG,ω-N-Butanamido-P(NIPAM-co-Biotin)(6)**

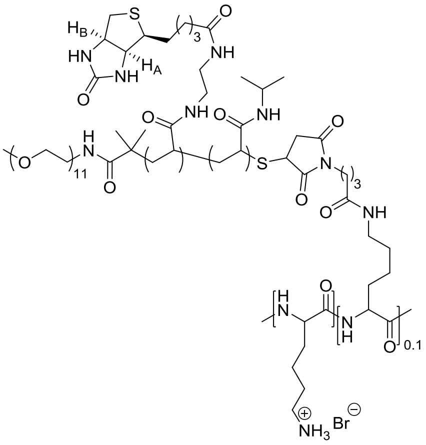

δ (^{1}H-NMR, D_2O): 0.92-1.22 (s, -CH_2-CH(CO-NH-CH-(C**H**$_3$)$_2$)-, 21H),1.26-2.29 (m, -CH-(C**H**$_2$)$_3$-CH_2-NH_3, -C**H**$_2$-C**H**(CO-NH-CH-(CH_3)$_2$, 20H), 2.89-3.00 (s, -CH-(CH_2)$_3$-C**H**$_2$-NH_3, 1.8H), 3.24-3.31 (s, -CH-(CH_2)$_3$-C**H**$_2$-NH-CO-, 0.7H), 3.55-3.90 (m, -O-C**H**$_2$-C**H**$_2$-O-CH_3), 3.73-3.96 (s, -CH_2-CH(CO-NH-C**H**-(CH_3)$_2$, 4.1H), 4.16-4.31 (s, -C**H**-(CH_2)$_3$-CH_2-NH_3, 1H), 4.35-4.42 (**H$_A$**, 0.2H), 4.53-4.61 (**H$_B$**, 0.2 H)

- **PLL-g-[0.1]α-Azo,ω-N-Butanamido-PNIPAM(4.5)**

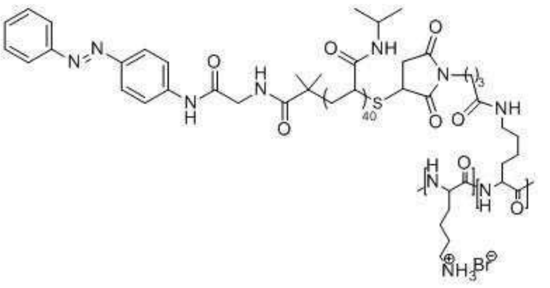

δ (^{1}H-NMR, D_2O) : 0.91-1.15 (s, -CH_2-CH(CO-NH-CH-(C**H**$_3$)$_2$)-, 62H), 1.24-2.18 (m, -CH-(C**H**$_2$)$_3$-CH_2-NH_3, -C**H**$_2$-C**H**(CO-NH-CH-(CH_3)$_2$, 45H), 2.82-2.93 (s, -CH-(CH_2)$_3$-C**H**$_2$-NH_3, 1.8H), 3.70-3.89 (s, -CH_2-CH(CO-NH-C**H**-(CH_3)$_2$, 10.9H), 4.15-4.25 (s, -C**H**-(CH_2)$_3$-CH_2-NH_3, 1H)

- **PLL-g-[0.1]α-Azo,ω-N-Butanamido-PNIPAM(2)**

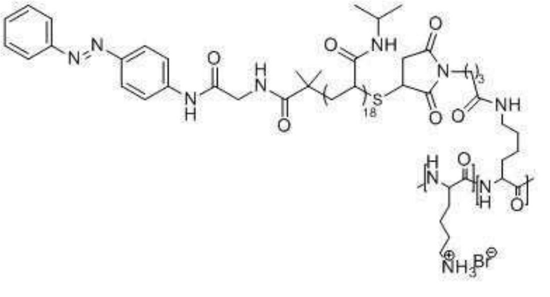

δ (^{1}H-NMR, D_2O) : 0.87-1.16 (s, -CH_2-CH(CO-NH-CH-(C**H**$_3$)$_2$)-, 74H), 1.19-2.19 (m, -CH-(C**H**$_2$)$_3$-CH_2-NH_3, -C**H**$_2$-C**H**(CO-NH-CH-(CH_3)$_2$, 53H), 2.83-2.92 (s, -CH-(CH_2)$_3$-C**H**$_2$-NH_3, 1.8H), 3.67-3.90 (s, -CH_2-CH(CO-NH-C**H**-(CH_3)$_2$, 12.9H), 4.15-4.25 (s, -C**H**-(CH_2)$_3$-CH_2-NH_3, 1H)

- **PLL-g-[0.1]α-Azo,ω-N-Butanamido-P(NIPAM-co-Biotin)(2)**

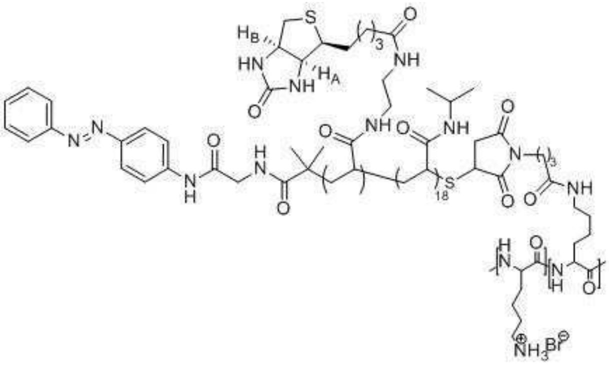

δ (^{1}H-NMR, D$_2$O) : 0.90-1.16 (s, -CH$_2$-CH(CO-NH-CH-(C**H**$_3$)$_2$)-, 22.5H), 1.18-2.23 (m, -CH-(C**H**$_2$)$_3$-CH$_2$-NH$_3$, -C**H**$_2$-C**H**(CO-NH-CH-(CH$_3$)$_2$, 23H), 2.83-2.91 (s, -CH-(CH$_2$)$_3$-C**H**$_2$-NH$_3$, 1.7H), 3.16-3.21 (s, -CH-(CH$_2$)$_3$-C**H**$_2$-NH-CO-, 0.3H), 3.67-3.87 (s, -CH$_2$-CH(CO-NH-C**H**-(CH$_3$)$_2$, 4H), 4.16-4.22 (s, -C**H**-(CH$_2$)$_3$-CH$_2$-NH$_3$, 1H),4.28-4.32 (proton HA related to the Biotin, 0.2H), 4.45-4.50 (proton HB related to the Biotin, 0.2H)

- **PLL-g-P(NIPAM-co-Azo[5%]-NMe2[25%]-Biotin[5%])(6) (or PLL-g-P(NIPAM-co-Azo-NMe$_2$-Biotin)(6))**

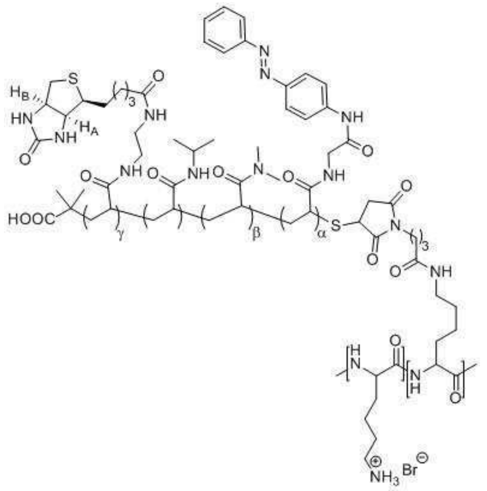

δ (^{1}H-NMR, D$_2$O): 0.92-1.22 (s, -CH$_2$-CH(CO-NH-CH-(C**H**$_3$)$_2$)-),1.26-2.29 (m, -CH-(C**H**$_2$)$_3$-CH$_2$-NH$_3$, -C**H**$_2$-C**H**(CO-NH-CH-(CH$_3$)$_2$), 2.68-3.00 (m, -CH-(CH$_2$)$_3$-C**H**$_2$-NH$_3$, -CO-N-(C**H**$_3$)$_2$), 3.24-3.31 (s, -CH-(CH$_2$)$_3$-C**H**$_2$-NH-CO-), 3.73-3.96 (s, -CH$_2$-CH(CO-NH-C**H**-(CH$_3$)$_2$), 4.16-4.31 (s, -C**H**-(CH$_2$)$_3$-CH$_2$-NH$_3$), 4.35-4.42 (**H$_A$**), 4.53-4.61 (**H$_B$**), 4.6 (s, azobenzne-NH-CO-C**H**$_2$-NH), 7-8.5 (m, aromatic signals of azobenzene + N**H** amide)

4.3 Fluorescent labelling with Alexa-NHS

Alexa Fluor 532 NHS ester was dissolved in DMSO (1 mg/mL). PLL-g-[0.2]PNIPAM(6) or PLL-g-[0.4]PEG(2) (20 mg) was dissolved in 0.4 mL of 50 mM sodium tetraborate buffer pH 8.5. An aliquot of the DMSO solution of Alexa NHS ester was added into aqueous solution (1.2 equivalent of Alexa-NHS relative to PLL molecule). The mixture was stirred for 4 h at room temperature in the dark, prior to dialysis (SpectraPore membrane, MWCO 3.5 kDa) against Milli-Q water for 1 day, and lyophilized yielding a fluorescent powder.

- **Alexa-labelled PLL-g-[0.4]PEG(2)**

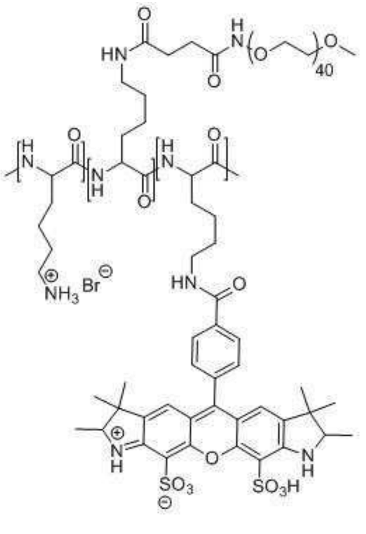

- **Alexa-labelled PLL-g-[0.2]PNIPAM(6) (or PLL-g-[0.2]PNIPAM(6)*)**

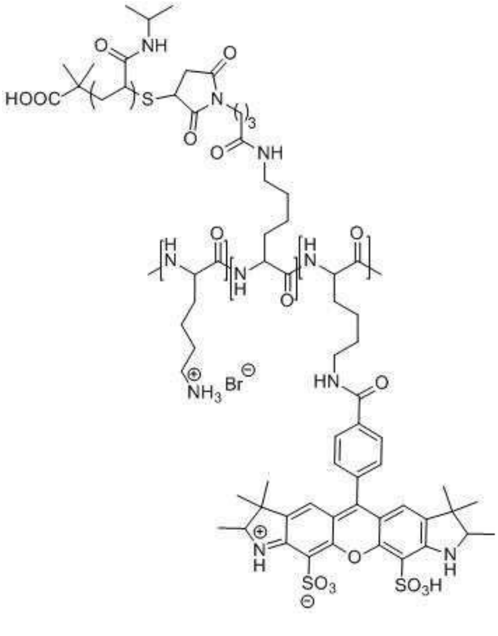

Appendix 2 – Coating and patterning with PLL derivatives

Contents

1 Coating of coverslips with PLL derivatives

The following substrates were coated with PLL derivatives:

- Glass coverslips for microscopy and AFM:

  Coverslips (diameter: 40 mm) for chamber FCS2 from Bioptechs, catalog number: 130119-5.

  WillCo-dish®KIT - Glass Bottom Dish (diameter: 35 mm), catalog number: KIT-3522

- Quartz crystal for QCM-d: QSX 303, Biolin Scientific

Substrates were washed with technical ethanol, sonicated for 45 min in a solution of sodium hydroxide (1 mol.L^{-1}), and rinsed with Milli-Q water. A solution of PLL derivatives in Milli-Q water at a total polymer concentration of 1 mg.mL^{-1} was deposited on the top of surfaces at room temperature for 1 h. The coated surfaces were rinsed with Milli-Q water, and stored at 4 °C (in water for storage time <2 days, or after drying under flushing nitrogen for longer storage times).

2 Photolithography to obtain micrometric patterns of PLL derivatives

UV photolithography was used to prepare surfaces displaying micrometric patterns of PLL derivatives (Figure 103). First, a chromium synthetic quartz photomask (Toppan, product type: 5'' QZ M1X) was cleaned with technical ethanol and deep UV light for 5 min. A precoated coverslip was placed under the photomask, and exposed for 15 min to deep UV (UV ozone cleaner from BioForce Nanosciences) in order to etch thin stripes separated by UV protected gaps. The coverslip was immobilized on the mask using a small drop of water (typically 7 µL) as the « glue » (this volume has to be adapted to the size of surfaces). After etching, the coverslip was rinsed with Milli-Q water, and a 1 mg/mL solution of PLL derivatives in Milli-Q water was deposited on the surface and incubated for 1 h. Finally, the glass was rinsed with water and stored at 4 °C.

The characteristic sizes of patterns were adjusted for the intended application (width of the stripes, distance between the stripes).

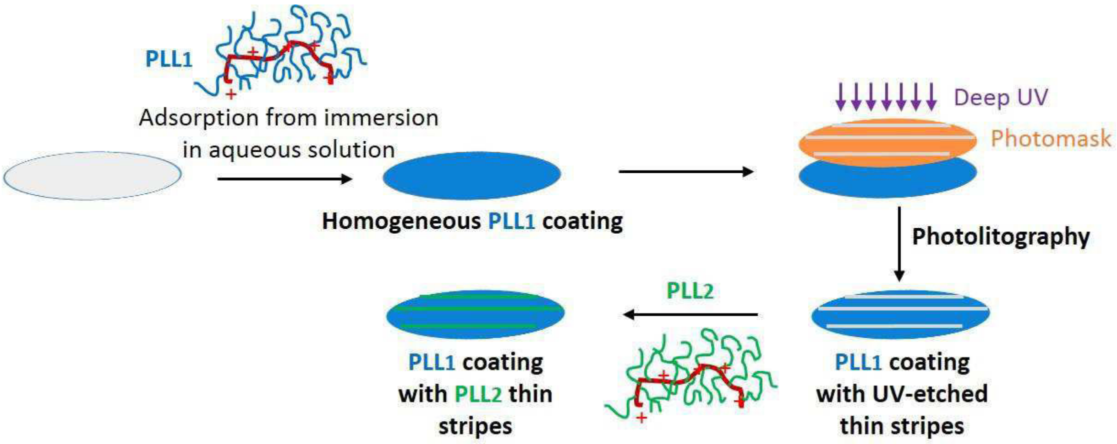

Figure 103 - UV-photolithography technique used to form micrometric patterns of PLL derivatives.

Appendix 3 - PNIPAM phase transition

Contents

1 PNIPAM phase transition in aqueous solution

1.1 Generalities

PNIPAM is known for more than seventy years and the number of related papers in the literature is still increasing (Schild, 1992). This enthusiasm comes from its unusual thermal behavior in aqueous solution. Indeed, PNIPAM is a thermoresponsive polymer, with a lower critical solution temperature (LCST) of 32 °C in water. When an aqueous solution of PNIPAM is heated beyond this critical temperature, PNIPAM collapses and a phase segregation takes place. As this behavior is sharp (~ 5 °C) and reversible, it has been used for different applications with PNIPAM in solution, in hydrogel or in films.

1.1.1 Characteristics of the phase transition

Phase diagram of PNIPAM

PNIPAM is an uncharged thermo-responsive polymer which shows a phase segregation during heating process. The typical phase diagram for polymers with a LCST behavior is represented on Figure 104. On the diagram, LCST corresponds to the minimum of the demixing curve *i.e.* to an accurate polymer fraction, ϕ_{LCST}. The critical temperature for any polymer fraction, ϕ, is called the cloud point. In the literature, LCST is improperly used for cloud point.

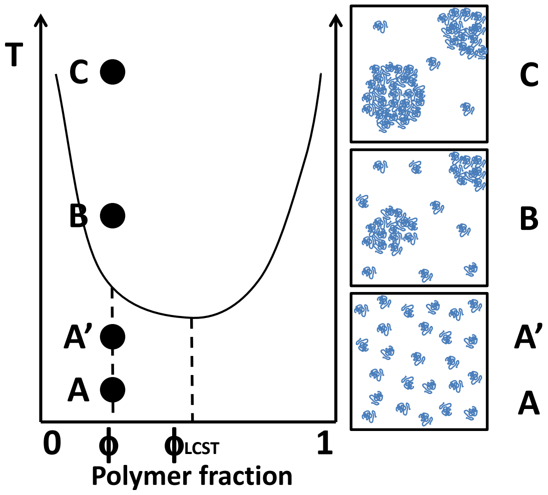

Figure 104 - Typical phase diagram of a LCST polymer solution.

For temperatures under cloud point, PNIPAM is entirely miscible in solution with a hydrophilic coil conformation. Once the temperature is increased above the demixing curve, PNIPAM coils collapse to a hydrophobic globule conformation prior to their aggregation via interchain hydrophobic interactions, giving a biphasic system (Wu and Zhou, 1995). A polymer-rich phase of lower polarity is formed and is suspended in the water-rich phase (Figure 104B-C). Consequently, different methods can be used to determine the critical temperature of PNIPAM solutions such as differential scanning calorimetry (Howard G. Schild and Tirrell 1990), light scattering (Wang et al., 1998), Compton scattering (Juurinen et al., 2014), viscometry (Badiger and Wolf, 2003), fluorescence (Ringsdorf et al., 1991), IR (Maeda et al., 2001), and NMR (Durand et al., 2000). UV-visible spectrophotometry is the most widespread technique to measure cloud points (turbidimetry). Although these techniques don't follow the same physico-chemical properties during the phase transition, every technique gives similar cloud point values. During this project, cloud points have been determined by UV-visible spectrophotometry.

Heskins and Guillet were the first to draw the PNIPAM phase diagram in water on a broad concentration range by light scattering and viscometry (Figure 105) (Heskins and Guillet, 1968). The cloud point temperature is constant between 0.01 and 0.4 % (massic fraction in PNIPAM) which represents a wide concentration range. According to this diagram, LCST corresponds to 31 °C and 15 % polymer fraction.

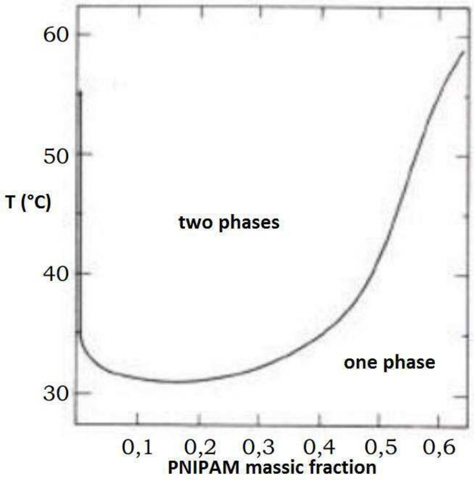

Figure 105 - Phase diagram of PNIPAM in water (Heskins and Guillet, 1968).

More recently, different teams have intensively studied this transition and some differences with the Heskins' diagram were noticed. Rika *et al.* (Rika et al., 1990) found a critical temperature between 34 and 35 °C by dynamic light scattering (weight fraction: 10^{-6}-0.1 %) while Schild and Tirell reported a phase diagram without minimum between 0.04 and 0.4 % (microcalorimetry) (Schild and Tirrell, 1990). Van Durme *et al.* obtained a monotonous decrease in critical temperature up to 0.4 % by differential scanning calorimetry (Van Durme et al., 2004). To sum up, for polymers with high molecular weight (>20 000 g.mol^{-1}), the phase diagram is flat on a wide concentration range. The differences observed can be explained by two main reasons:

- Polymer samples used in every study are different and the transition depends on many structural factors (molecular weight, salt, polymer concentrations, …)
- Experimental techniques and protocols are different in the literature. For example, the heating rate is a key parameter (Badiger and Wolf, 2003; Schild and Tirrell, 1990). Indeed, Schild *et al.* have reported that heating rates above 0.5 °C.min^{-1} imply a considerable effect on the measured critical temperature.

"Coil-to-Globule" transition

The observation of the PNIPAM "Coil-to-Globule" transition is a challenge due to the favorable interchain aggregation. In 1998, the Wu's team succeeded for the first time in visualizing this transition by using light scattering on a narrowly distributed ($M_w/M_n < 1.1$), high molar mass (10^7 g.mol^{-1}), and highly diluted (0.67 µg.mL^{-1}) polymer sample (Wang et al., 1998). The collapse manifests by a decrease in the gyration radius of one order of magnitude (Figure 106). In the entirely collapsed globule, there is still 66 % of initial water. The hysteresis can be attributed to the formation of intrachain hydrogen bonding in the globule state.

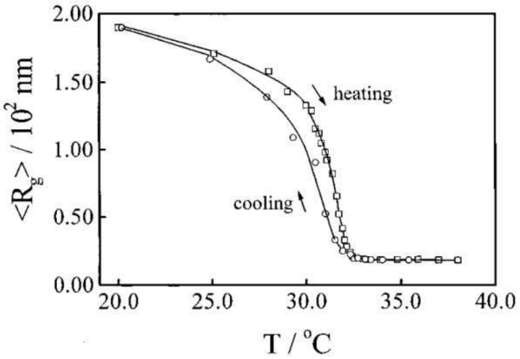

Figure 106 - Evolution of the gyration radius during the coil-to-globule transition (Wang et al., 1998).

Origin of the phase transition

The behavior of a polymer in solution reflects monomer-monomer, monomer-solvent, and solvent-solvent interactions. The water-water interactions are particularly high and are characterized by a partially ordered structure. Both enthalpy and entropy play a role in thermo-sensitivity of PNIPAM (Schild, 1992).

At temperatures lower than cloud point, PNIPAM dissolution in water comes from the formation of hydrogen bonds between the amide function and water molecules. These interactions give an exothermic mixing enthalpy. As water molecules can't interact with isopropyl groups by hydrogen bonding, water must be reoriented around these apolar groups. There is formation of clathrate-like structures (Figure 107). This latter phenomenon, known as the hydrophobic effect, results in a decreased entropy upon mixing. The exothermic enthalpy of the hydrogen bonds formed between the polymer polar groups and water molecules is considered as the initial driving force for PNIPAM dissolution.

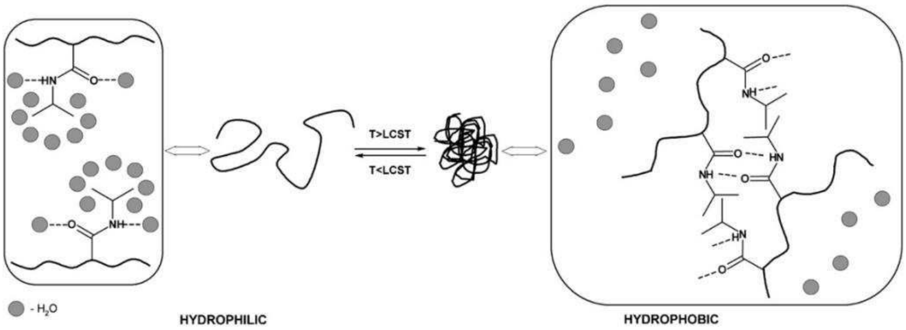

Figure 107 - Illustration of the PNIPAM phase transition (Dimitrov et al., 2007).

At higher temperatures, the phase segregation comes from two effects:

- the increase in entropy due to the water liberation from the ordered clathrate-like structures around the isopropyl groups

- the weakening of hydrogen bonds between water and amides.

However, these remarks have to be taken with caution. Indeed, origins of this phenomenon are still debated.

1.1.2 Influence of some factors on the phase transition

Molecular weight effect

Cloud point is sensitive to molecular weight for small PNIPAM. Indeed, Schild *et al.* shown that cloud point increases as molecular weight decreases from 16.10^4 to $0,5.10^4$ g/mol while Fujishige *et al.* reported constant cloud point values for polymer ranging from 5.10^4 to 840.10^4 g/mol (Howard G. Schild and Tirrell 1990; Fujishige, Kubota, and Ando 1989).

Comonomer effect

Synthesis of PNIPAM copolymers represents an effective solution to modulate the LCST from 0 to 100 °C in water. Indeed, the introduction of monomers more hydrophilic than NIPAM enables to increase its LCST whereas more hydrophobic monomers cause a decrease in LCST values. This effect is well illustrated by the P(NIPAM-*co*-2-hydroxyisopropylacrylamide) copolymer family made by Maeda *et al.* (Maeda et al., 2006) (Table 21).

% HIPAM	0	10	30	50	80	100
LCST (°C)	31.6	36.7	41.8	55.0	80.0	-

Table 21 - LCST of a P(NIPAM-*co*-2-hydroxyisopropylacrylamide) copolymer family (Maeda et al., 2006).

Topological effect

The architecture of PNIPAM plays a role on the cloud points. Indeed, Qiu *et al.* shown that LCST is higher for cyclic PNIPAM than for linear PNIPAM of the same molecular weight (Qiu et al., 2007). Zhao *et al.* reported a considerable increase in LCST due to the presence of loops into PNIPAM (Zhao et al., 2011).

Wan *et al.* (Wan et al., 2010) compared LCST values of linear, star and dendrimer PNIPAMs. Linear PNIPAM shows the higher LCST value while the lower value is attributed to the dendrimer structure. This phenomenon can be explained in terms of the n-cluster effects (Plummer et al., 2006). Due to the high chain density inside the dendrimer-like topology, PNIPAM segments were densely packed and the interactions between the polymer chains and water molecules was highly weakened, which may led to the sharp decrease of LCST.

Cosolute effect

Salts lower cloud points of PNIPAM solutions as it has been shown by Freitag *et al.* with the Hofmeister series (Freitag and Garret-Flaudy, 2002). Similarly, uncharged solutes can have an effect on critical temperature as illustrated by the LCST decrease caused by saccharides (Kim et al., 1995).

1.2 Cloud point measurements by turbidimetry

- **Generic protocol**

To determine cloud point (T_{CD}) of thermo-responsive polymers in solution, the absorbance between 650 and 750 nm was measured as a function of temperature, T. The absorption spectra were acquired using a diode array UV-visible spectrophotometer (Evolution Array, Thermo Scientific) equipped with a Peltier temperature controller ($\pm 1\ °C$). Samples for thermal analysis were prepared by dissolution of polymers in buffers (MilliQ water, PBS or DMEM) at a concentration of 3 mg.mL^{-1}. Typically, 0.5 mL of the polymer solution was filtered through a 0.2 µm syringe filter (Millex, Millipore) into a quartz cell of 1 cm path length and subjected to a heating sweep between 15 °C and 70 °C at a sweep rate of + 0.33 °C.min^{-1}. Measurements were done in duplicate, by repeating the T-sweep on the same sample that was cooled to 10–15 °C for 15 minutes under stirring prior to the second sweep of heating steps.

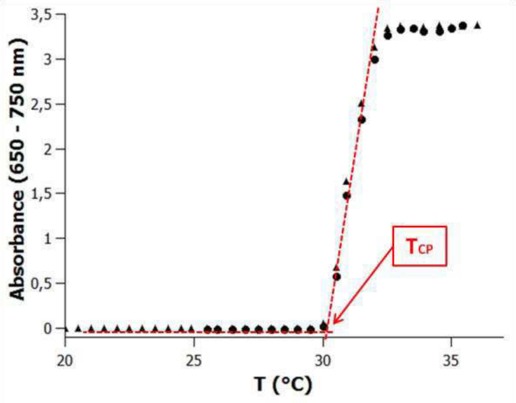

Figure 108 - Determination of cloud point by UV-visible spectrophotometry. Turbidimetry measurements for a PLL-g-[0.2]PNIPAM(2) solution (3 mg.mL^{-1}, 0.33 °C.min^{-1}, PBS) (circles correspond to the first temperature sweep while triangles to the second).

The onset of turbidity above a threshold temperature indicates polymer aggregation. The cloud point value was defined as the crossover temperature between the two asymptotes represented on Figure 108. The first asymptote represents the absorbance baseline corresponding to a clear solution of hydrated polymer at low temperatures. The second asymptote represents the increase in absorbance due to the polymer aggregation.

- **Determination of cloud points under light illumination**

To investigate the light response of azobenzene containing polymers, cloud points were determined under blue and UV state by using the generic protocol (Figure 109). The polymer solution was continuously irradiated during the turbidimetry measurement to maintain a blue/UV photostationary equilibrium. Photoirradiation were carried out using a photodiode system CoolLED PE-2 (Roper Scientific, France) which emits blue light (436 nm at a power of *ca.* 2 mW cm²) or UV light (365 nm at a power of *ca.* 10 mW.cm^{-2}). The CoolLED illuminated the solution via the top of quartz cuvette, in a direction orthogonal to the light path of the spectrophotometer.

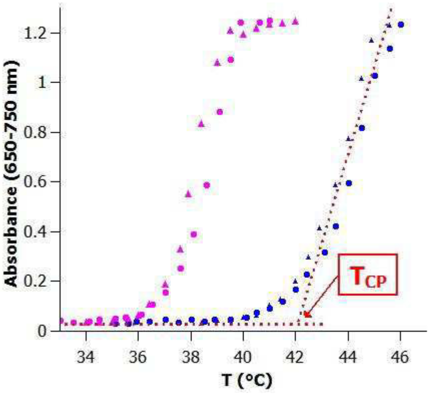

Figure 109 - Determination of cloud point by UV-visible spectrophotometry. Turbidimetry measurements for a α,ω-di-COOH-P(NIPAM-co-Azo[6]-NMe_2[40]) solution (3 mg.mL^{-1}, 0.33 °C.min^{-1}, PBS) under blue and UV illumination (circles correspond to the first temperature sweep while triangles to the second, blue and purple symbols correspond respectively to blue and UV irradiation).

- **Results**

In the Table 22, results of turbidimetry analyses are given for polymers used during this project. Formula of the corresponding polymers are reported in Appendix 1.

Polymer	Buffer	T_{CP} (°C)	$T_{CP,Blue}$ (°C)	$T_{CP,UV}$ (°C)
PLL-g-[0.38]PNIPAM(2)	H_2O	33.1	-	-
PLL-g-[0.18]Biotin-[0.38]PNIPAM(2)	H_2O	33.5	-	-
PLL-g-[0.1]P(NIPAM-co-Biotin)(6)	H_2O	36.1	-	-
PLL-g-[0.2]PNIPAM(6)	H_2O	32	-	-
PLL-g-[0.2]PNIPAM(6)	PBS	30	-	-
PLL-g-[0.2]PNIPAM(6)	DMEM	29.9	-	-
PLL-g-[0.1]P(NIPAM-co-RGD)(6)	H_2O	40.5	-	-
PLL-g-[0.1]P(NIPAM-co-RGD)(6)	DMEM	40	-	-
PLL-g-P(NIPAM-co-Azo-NMe_2-Biotin)(6)	PBS	-	26	23
α-Azo,ω-COOH-PNIPAM(4.5)	PBS	-	27.5	30.8
α-Azo,ω-COOH-PNIPAM(2)	PBS	-	27	29
PLL-g-[0.1]α-Azo,ω-Butanamido-PNIPAM(4.5)	PBS	-	27.2	29.2
PLL-g-[0.1]α-Azo,ω-Butanamido-PNIPAM(2)	PBS	-	27.8	34
PLL-g-[0.1]α-Azo,ω-Butanamido-P(NIPAM-co-Biotin)(2)	PBS	-	27	30.5

Table 22 – Cloud points of the different polymers used during this project (determined by turbidimetry).

2 Phase transition of PLL-g-PNIPAM adlayers

2.1 Atomic Force Microscopy (AFM)

2.1.1 Principle of AFM measurements in PeakForce Quantitative Nanoscale Mechanical (QNM) mode®

PeakForce Quantitative Nanoscale Mechanical (QNM) mode® is a special tapping mode, used to map and distinguish between nanomechanical properties (including modulus, adhesion, dissipation and deformation) while simultaneously imaging sample topography.

Figure 110(i) demonstrates what happens when the periodically modulated probe interacts with the surface (frequency ~ 2 kHz). The top (dashed) line represents the Z-position of the modulation as it goes through one period plotted as a function of time. The lower line (solid) represents the measured force on the probe during the approach (blue) of the tip to the sample, while the red part represents the force while the tip moves away from the sample. When the tip is far from the surface (point A), there is little or no force on the tip. As the tip approaches the surface, the cantilever is pulled down toward the surface by attractive forces as represented by the negative force (below the horizontal axis). At point B, the attractive forces overcome the cantilever stiffness and the tip is pulled to the surface. The tip then stays on the surface and the force increases until the Z position of the modulation reaches its bottom-most position at point C. This is where the peak force occurs. The peak force (force at point C) during the interaction period is kept constant by the system feedback. The probe then starts to withdraw and the force decreases until it reaches a minimum at point D. **The adhesion is given by the force at this point D.** The point where the tip comes off the surface is called the pull-off point. This often coincides with the minimum force. Once the tip has come off the surface, only long range forces affect the tip, so the force is very small or zero when the tip-sample separation is at its maximum (point E).

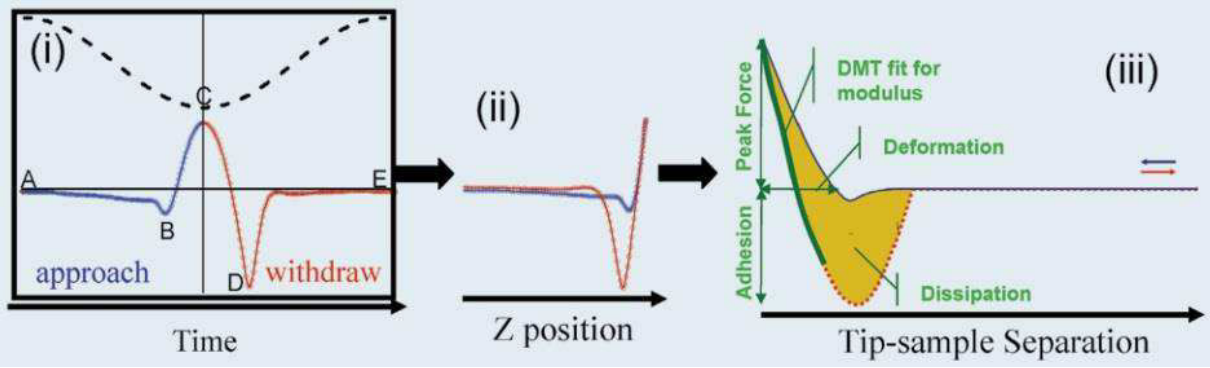

Figure 110 - Schematic representation of PeakForce QNM data and consequent analyses (Figure extracted from Application Note #128, Bruker). (i) Plot of force and piezo Z position as a function of time, including (B) jump-to-contact, (C) peak force, (D) adhesion. (ii) A traditional force curve eliminates the time variable, plotting Force vs Z piezo position. (iii) For fitting purposes it is more useful to plot force vs separation where the separation is calculated from the Z piezo position and the cantilever deflection.

Figure 110(ii) shows the same data as Figure 110(i) but with the force plotted as a function of the distance. Since we control the Z position of the modulation as a function of time and we measure the deflection of the cantilever as a function of time, it is possible to eliminate the time variable and plot the force against the Z-position. Once a force curve is obtained, it is must be converted to a force versus separation plot for fitting and further analysis. The tip-sample separation is different from the Z position of the modulation since the cantilever bends. Figure 110(iii) is a sample of a force-separation plot illustrating the types of information that can be obtained. The most commonly used quantities are elastic modulus, tip-sample adhesion, energy dissipation, and maximum deformation.

2.1.2 Protocol used for AFM measurements

Atomic force microscopy (AFM) was performed on a Bruker Catalyst instrument, using OLYMPUS AC40-TS cantilevers (nominal spring constant 0.09 N/m). Polymer-coated glass coverslips were immersed in PBS buffer (137 mM NaCl, 2.7 mM KCl,10 mM sodium phosphate buffer pH 7.4) that was previously filtered on membranes with a 0.2 µm pore size. A heated plaque coupled to the AFM X-Y scanner enabled us to modify the sample temperature, which was monitored by immersing a thermocouple under the AFM head. Prior to each AFM measurement, we allowed the sample to equilibrate for 15 min. AFM imaging was performed in PeakForce mode, using a 150-200 pN set point. In this mode, a piezoelectric actuator oscillates the cantilever with a sine wave in vertical direction and at a 1 kHz frequency, different to the cantilever resonance, thus enabling the acquisition of fast force vs distance curves (FZ curves) during X-Y scan. Information collected from PeakForce maps was: sample height, deformation, tip-sample adhesion force, and Young's modulus (as determined by a real-time fitting of force versus distance curves considering the following assumptions).

(1) Maps of the tip-sample adhesion, calculated by fitting a baseline to FZ curves and determining the lowest force point in the retraction curves (i.e., when the cantilever is pulled away from the sample). Single FZ curves were also performed on the sample at points that were chosen in the PeakForce topography and adhesion map. The indentation velocity was 2 µm.s^{-1}, and the force set point was 200 pN.

(2) Topographic scan. Due to the application of force onto the surface during topographic scan, the raw data contain the contribution of the local compression of the soft polymer layer. To remove the effect of layer deformation, heights were recalculated at each pixel by extrapolation of the effective tip position corresponding to zero applied force. To this aim, measurement of the polymer height as obtained by the PeakForce topography map was added to the deformation maps of the polymer at the force set point. The average polymer height was obtained by fitting a gauss function to the height histograms and calculating the difference between polymer-covered and bare glass regions.

(3) Estimation of Young's modulus. An effective Young's modulus was determined by fitting the Dejarguin−Müller−Toporov model of adhesive contact to the extension curve (nominal tip radius = 10 nm, Poisson's ratio ν = 0.3), following the equation:

$$F - F_{adh} = \frac{4}{3}\frac{E}{1 - \nu^2} R^{1/2}\delta^{3/2}$$

with $F - F_{adh}$ being the total force from the adhesion peak to the maximum force used for fitting, E the Young's modulus, R the tip radius, δ the indentation, and ν the Poisson ratio. The DMT model was also applied to real-time fitting of force vs distance curves in PeakForce tapping. Prior to fitting curves, it was established that, excluding tip−sample adhesion events, no hysteresis was observed between the extension and retraction force versus indentation curves.

2.2 Quartz Crystal Microbalance with dissipation (QCM-d)

2.2.1 Principle of the QCM-d technique

QCM is based on the inverse piezoelectric effect: alternating applied voltage leads to a cyclical deformation, resulting in an oscillatory motion. If the frequency of the applied voltage matches the crystal's resonance frequency (or multiples thereof called overtones), a standing wave is generated inside the crystal.

Depending on the cut of the crystal relative to its crystallographic axes, different kinds of oscillations may arise. AT-cut crystals, used in QCM (Figure 111A), vibrate in the so-called thickness-shear mode, where the two surfaces move in an antiparallel fashion (Figure 111B). In resonance, crystal surfaces are located at the antinodes of a standing wave with the wavelength 2d/n, where d is the crystal thickness and n is the overtone order (odd), leading to the resonance frequency f_n=nc/2d, where c is the speed of sound in quartz. In liquids and gases, shear-waves decay rapidly, making QCM interface-specific.

There are several ways to perform QCM measurements. One can examine the polarization at the crystal surface as a function of the frequency of the applied voltage, the so-called "impedance analysis". This yields two parameters per overtone, the resonance frequency f_n and the bandwidth Γ_n (Figure 111C). The alternative is the "ring-down" scheme developed by Rodal *et al.* (Rodahl et al., 1995), referred to as QCM-d, where the external driving voltage is turned off intermittently and the oscillations are left to decay freely. Given that quartz is piezoelectric, a voltage is generated during these decaying mechanical oscillations. This signal is recorded, also yielding two parameters per overtone, the resonance frequency f_n and the dissipation D_n (Figure 111D). The dissipation parameter is given by $D = \frac{1}{\pi f \tau}$ and is dimensionless, defined as $D = \frac{1}{Q} = \frac{E_{dissipated}}{2\pi E_{stored}}$,with Q being the quality factor, $E_{dissipated}$ being the energy dissipated during one oscillatory cycle and E_{stored} being the energy stored in the oscillating system. Bandwidth and dissipation are equivalent, with $D_n = 2\Gamma_n/f_n$ (Figure 111C-D). All of these approaches require that the quartz crystal is coated with electrodes (typically gold, Figure 111A). During this thesis, QCM-d measurements were performed thanks to the "ring-down" method.

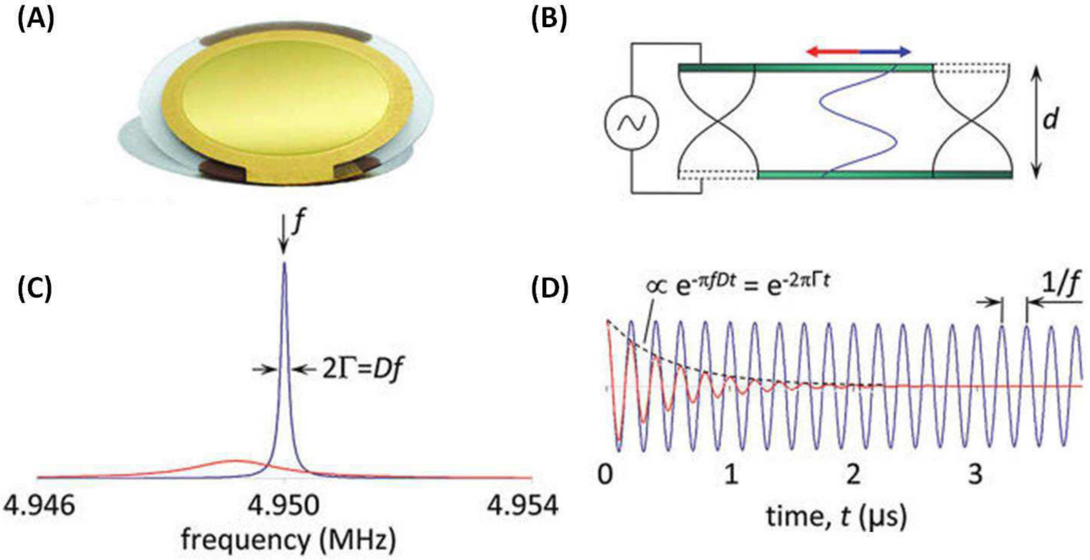

Figure 111 - Schematics of QCM-d operation (Reviakine et al., 2011). (A) A photograph of a 4.95 MHz AT-cut quartz crystal where the yellow color is due to the gold electrode. (B) Side view of the crystal. Application of oscillatory voltage results in a cyclical deformation, where top and bottom surfaces move tangentially in an antiparallel fashion. The fundamental frequency (black waves at the edges of the crystal) and the third overtone (blue wave in the middle) are illustrated. The motion of the crystal is greatly exaggerated for clarity. In reality, the thickness of the crystal is ~ 300 µm, while the amplitude of motion is of the order of at most a couple of nanometers in aqueous solution (it depends on the driving voltage and overtone order). (C) Resonances observed when a crystal is in air (blue) or in liquid (red). These are the typical spectra obtained with impedance analysis. The excitation frequency (here exemplified by the fundamental frequency) is plotted on the x-axis. The y-axis represents the amplitude of the current passing through the crystal, or equivalently, the amplitude of the crystal's shear motion. Two parameters are used to characterize the resonance: its frequency f and its bandwidth Γ. (D) QCM-d uses a so-called ring-down method, where the driving voltage is intermittently switched off and the decay in time of the oscillation is monitored. From the decay curve, the resonance frequency f and the energy dissipation D=2Γ/f are extracted. The blue decay curve in this figure corresponds to a crystal oscillating in air. The red curve corresponds to the dissipation of $1,6.10^{-1}$, a great exaggeration for illustrative purposes. For comparison, the dissipation of a bare crystal in water is ~ $3,5.10^{-4}$ at the fundamental. The two types of measurements, impedance analysis and ring-down, are strictly equivalent; the two types of curves shown in parts C and D are related to each other by a Fourier transform.

QCM-d measures the changes in the resonance frequency, Δf, and dissipation, ΔD, of a sensor crystal upon interaction of soft matter with its surface. The QCM-d response is sensitive to the mass (including any hydrodynamically coupled water) and mechanical properties of the surface-bound layer. QCM-d measurements were performed in flow mode on silica-coated QCM-d sensors (QSX 303, Biolin Scientific), using a Q-Sense E1 system equipped with Flow Module (Biolin Scientific) in aqueous solution (PBS or DMEM buffers). The module temperature was maintained with a precision of 0.02 °C. Overtones j = 3, 5, 7, 9, 11, and 13 were recorded, corresponding to resonance frequencies of approximately 15, 25, 35, 45, 55 and 65 MHz. Changes in dissipation, ΔD, and normalized frequency, $\Delta f = \Delta f_j/j$, for $j = 3$ are presented; any other overtone would have shown similar trends.

2.2.2 Qualitative and quantitative analyses of QCM-d data

The qualitative analysis of QCM-d measurements relies on the following approximations:

- Frequency is inversely proportional to the mass of the layer in contact with the sensor surface. In our case, this layer consists in PNIPAM brushes and water molecules.
- Dissipation is mainly linked to the viscoelastic properties of the top layer. A decrease in dissipation corresponds to a stiffening of the layer.

The qualitative analysis of QCM-d measurements depends on films deposited on the quartz sensor. PLL-g-PNIPAM coatings can be considered as laterally homogeneous films according to Reviakine *et al.* (Reviakine et al., 2011). Moreover, PLL-g-PNIPAM coatings may dissipate energy. Hence, the thickness and viscoelastic properties were determined by fitting the QCM-d data to a viscoelastic model (Reviakine et al., 2011) implemented in the software QTools (Biolin Scientific). The film density was assumed to be 1.0 g.cm^{-3}.

Viscoelastic model for laterally homogeneous films

The QCM response for laterally homogeneous viscoelastic films is successfully treated by a continuum model based on the analysis of shear wave propagation in viscoelastic media. For thin films (film thickness much thinner than the wavelength of the shear-acoustic wave in the film), frequency and bandwidth shifts are related to the areal mass density of the film and its viscoelastic properties as follows (Johannsmann, 1999, 2008):

$$\Delta f_n \approx -\frac{n}{C} m_f \left(1 - n\omega_f \rho_l \eta_l \frac{G_f^{"}}{\rho_f\left(G_f^{*2} + G_f^{"2}\right)}\right)$$

$$\Delta \Gamma_n \approx \frac{n}{C} m_f n\omega_f \rho_l \eta_l \frac{G_f^{*}}{\rho_f\left(G_f^{*2} + G_f^{"2}\right)}$$

Here, subscripts l and f refer to the liquid and the film, respectively. η_l, ρ_l are the viscosity, the density of the liquid. η_f, ρ_f and h_f are the viscosity, the density and the thickness of the adsorbed film. The mass sensitivity constant C depends solely on the fundamental resonance frequency f_F and the material properties of the quartz crystal (the angular fundamental resonance frequency: $\omega_F = 2\pi f_F$). For crystals with $f_F = 5$ MHz, it is 18 ng.cm^{-2}Hz^{-1}. $m_f = \rho_f h_f$ is as usual the areal mass density of the film (mass per unit area). The storage modulus G* describes material elasticity, i.e., the relationship between applied force and the extent of deformation. It can be thought of as a spring constant. The loss modulus G" = ωη describes viscous energy dissipation in the material subjected to deformation, where the viscosity η can be thought of as a friction coefficient that relates the applied force to the rate of deformation. This yields a well-defined equivalent thickness and viscoelastic properties. The application of the viscoelastic model requires a certain amount of care. It has five independent fitting parameters: the areal mass density $\rho_f h_f$, the shear moduli G* and G", which enter as products with density, ρ_fG* and ρ_fG", and the exponents α* and α" describing the frequency dependence of the moduli. An assumption about film density ρ_f is required to obtain film thickness and the actual values of the shear moduli. In soft matter, $\rho_f \approx 1$ g.cm^{-3} is often a reasonable assumption.

2.2.3 Protocol for detecting transition of PLL-g-PNIPAM coatings

Transition of PLL-g-PNIPAM adlayers was investigated by QCM-d in buffers (PBS or DMEM). A quartz crystal with a thin SiO_2 layer on its top was coated with PLL-g-PNIPAM. Both resonance frequency and dissipation were recorded continuously while imposing a temperature cycle to the QCM-d cell between 19 °C and 49 °C. More exactly, we recorded the shift of frequency (Δf) and dissipation (ΔD). Temperature first increases step-by-step (with steps of 2 °C maintained for 20 minutes), then decreases in the same manner.

2.2.4 Summary of analyzed polymer coatings

Detection of the transition was achieved on different PLL-g-PNIPAM coatings on PBS and/or DMEM (Table 23).

Adsorbed Polymer	Buffer	$T_{\Delta f}$ (°C)	$T_{\Delta D}$ (°C)	T_{CP} (°C)
PLL-g-PEG	PBS	×	×	×
PLL-g-[0.2]PNIPAM(6)	PBS	32	30	30
PLL-g-P(NIPAM-co-Azo-NMe$_2$-Biotin)(6)	PBS	26*	×	26
PLL-g-[0.1]α-Azo,ω-Butanamido-P(NIPAM-co-Biotin)(2)	PBS	26*	×	27.8
PLL-g-[0.15]P(NIPAM-co-RGD)(6)	DMEM	×	×	40
PLL-g-[0.2]PNIPAM(6)/PLL-g-[0.15]P(NIPAM-co-RGD)(6) 1/10	DMEM	32	30	-

Table 23 – PNIPAM collapse temperatures on PLL-g-PNIPAM coatings determined by QCM-d based on frequency ($T_{\Delta f}$) and dissipation ($T_{\Delta D}$) signals. Cloud points T_{CP} were measured by turbidimetry. × means that any transition was detected. * means that acquired signal for PNIPAM transition was closed to the detection limit.

For PLL-g-P(NIPAM-co-Azo-NMe2-Biotin)(6), PLL-g-[0.1]α-Azo,ω-Butanamido-PNIPAM(2) and PLL-g-[0.15]P(NIPAM-co-RGD)(6) (raw data in Figure 112), it was difficult to detect signature of the phase transition by QCM-d while it was evident by turbidimetry. For PLL-g-[0.15]P(NIPAM-co-RGD)(6), the grafting ratio of PNIPAM side chains is lower than for PLL-g-[0.2]PNIPAM(6). We can assume that the quantity of adsorbed PNIPAM was too low to induce an important magnitude on frequency and dissipation energy during the transition. Similarly, for PLL-g-[0.1]α-Azo,ω-Butanamido-PNIPAM(2), the lack of response may come from PNIPAM grafts which are three folds smaller than grafts of PLL-g-[0.2]PNIPAM(6).

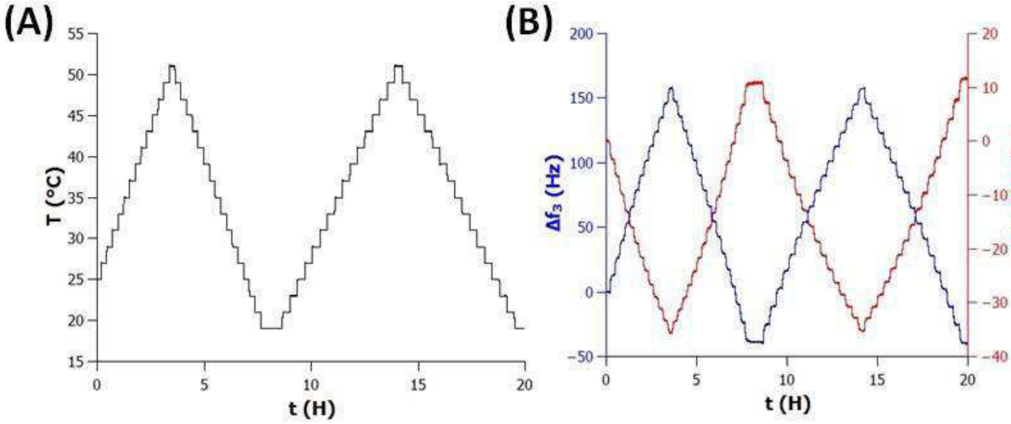

Figure 112 - QCM-d measurements on a quartz crystal coated with PLL-g-[0.1]P(NIPAM-co-RGD)(6) in DMEM: (A) "step-by-step" temperature ramp, (B) (–, Δf_3) frequency and (–, ΔD_3) dissipation shifts of the third overtone.

Phase transition of PLL-g-P(NIPAM-co-Azo-NMe$_2$-Biotin)(6) and PLL-g-[0.1]Azo-P(NIPAM-co-Biotin)(2) layers was investigated by QCM-d in PBS without illumination (See Chapter 3 for more details). Recorded signals didn't show a discernible transition and were closed to the detection limit (Figure 113). For the two polymers, frequency derivatives seem to reveal a maximum at ∼ 26 °C (close to their cloud points under blue light).

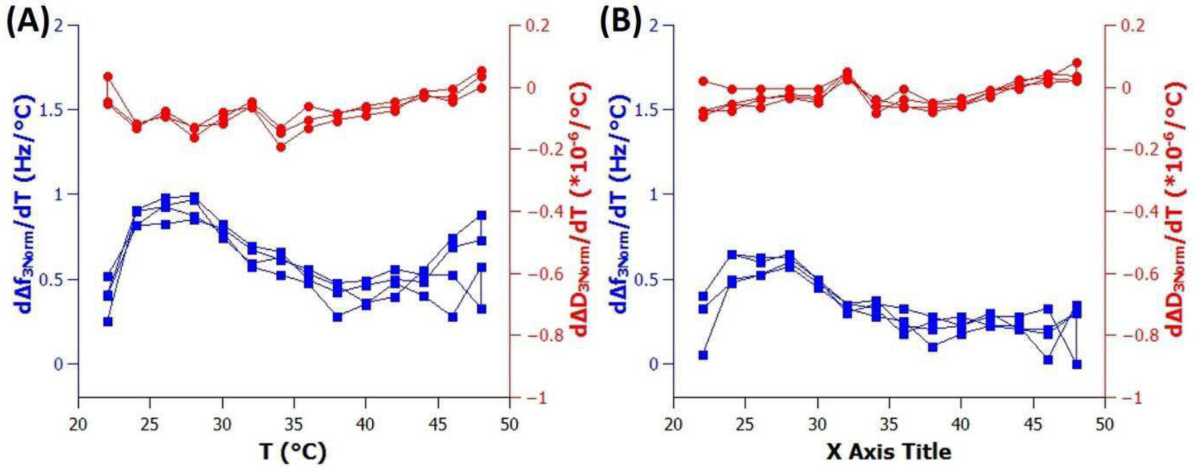

Figure 113 - Determination of the phase transition by QCM-d of (A) PLL-g-P(NIPAM-co-Azo-NMe$_2$-Biotin)(6) and (B) PLL-g-[0.1]α-Azo,ω-Butanamido-P(NIPAM-co-Biotin)(2) in PBS without illumination (See Chapter 3 for more details).

Bibliography

Badiger, M.V., and Wolf, B.A. (2003). Shear induced demixing and rheological behavior of aqueous solutions of poly(N-isopropylacrylamide). Macromol. Chem. Phys. *204*, 600–606.

Dimitrov, I., Trzebicka, B., Müller, A.H.E., Dworak, A., and Tsvetanov, C.B. (2007). Thermosensitive water-soluble copolymers with doubly responsive reversibly interacting entities. Prog. Polym. Sci. *32*, 1275–1343.

Durand, A., Hourdet, D., and Lafuma, F. (2000). Thermoassociative Graft Copolymers: NMR Investigation and Comparison with Rheological Behaviour. J. Phys. Chem. B *104*, 9371–9377.

Freitag, R., and Garret-Flaudy, F. (2002). Salt Effects on the Thermoprecipitation of Poly-(N-isopropylacrylamide) Oligomers from Aqueous Solution. Langmuir *18*, 3434–3440.

Heskins, M., and Guillet, J.E. (1968). Solution Properties of Poly(N-isopropylacrylamide). J. Macromol. Sci. Part - Chem. *2*, 1441–1455.

Johannsmann, D. (1999). Viscoelastic analysis of organic thin films on quartz resonators. Macromol. Chem. Phys. *200*, 501–516.

Johannsmann, D. (2008). Viscoelastic, mechanical, and dielectric measurements on complex samples with the quartz crystal microbalance. Phys. Chem. Chem. Phys. *10*, 4516–4534.

Juurinen, I., Galambosi, S., Anghelescu-Hakala, A.G., Koskelo, J., Honkimäki, V., Hämäläinen, K., Huotari, S., and Hakala, M. (2014). Molecular-Level Changes of Aqueous Poly(N-isopropylacrylamide) in Phase Transition. J. Phys. Chem. B *118*, 5518–5523.

Kim, Y.-H., Kwon, I.C., Bae, Y.H., and Kim, S.W. (1995). Saccharide Effect on the Lower Critical Solution Temperature of Thermosensitive Polymers. Macromolecules *28*, 939–944.

Maeda, T., Yamamoto, K., and Aoyagi, T. (2006). Importance of bound water in hydration–dehydration behavior of hydroxylated poly(N-isopropylacrylamide). J. Colloid Interface Sci. *302*, 467–474.

Maeda, Y., Nakamura, T., and Ikeda, I. (2001). Changes in the Hydration States of Poly(N-alkylacrylamide)s during Their Phase Transitions in Water Observed by FTIR Spectroscopy†. Macromolecules *34*, 1391–1399.

Plummer, R., Hill, D.J.T., and Whittaker, A.K. (2006). Solution Properties of Star and Linear Poly(N-isopropylacrylamide). Macromolecules *39*, 8379–8388.

Qiu, X.-P., Tanaka, F., and Winnik, F.M. (2007). Temperature-Induced Phase Transition of Well-Defined Cyclic Poly(N-isopropylacrylamide)s in Aqueous Solution. Macromolecules *40*, 7069–7071.

Reviakine, I., Johannsmann, D., and Richter, R.P. (2011). Hearing What You Cannot See and Visualizing What You Hear: Interpreting Quartz Crystal Microbalance Data from Solvated Interfaces. Anal. Chem. *83*, 8838–8848.

Rika, J., Meewes, M., Nyffenegger, R., and Binkert, T. (1990). Intermolecular and intramolecular solubilization: Collapse and expansion of a polymer chain in surfactant solutions. Phys. Rev. Lett. *65*, 657–660.

Ringsdorf, H., Venzmer, J., and Winnik, F.M. (1991). Fluorescence studies of hydrophobically modified poly(N-isopropylacrylamides). Macromolecules *24*, 1678–1686.

Rodahl, M., Höök, F., Krozer, A., Brzezinski, P., and Kasemo, B. (1995). Quartz crystal microbalance setup for frequency and Q-factor measurements in gaseous and liquid environments. Rev. Sci. Instrum. *66*, 3924–3930.

Schild, H.G. (1992). Poly(N-isopropylacrylamide): experiment, theory and application. Prog. Polym. Sci. *17*, 163–249.

Schild, H.G., and Tirrell, D.A. (1990). Microcalorimetric detection of lower critical solution temperatures in aqueous polymer solutions. J. Phys. Chem. *94*, 4352–4356.

Van Durme, K., Van Assche, G., and Van Mele, B. (2004). Kinetics of Demixing and Remixing in Poly(N-isopropylacrylamide)/Water Studied by Modulated Temperature DSC. Macromolecules *37*, 9596–9605.

Wan, X., Xu, J., and Liu, S. (2010). Facile synthesis of dendrimer-like star-branched poly(isopropylacrylamide) via combination of click chemistry and atom transfer radical polymerization. Sci. China Chem. *53*, 2520–2527.

Wang, X., Qiu, X., and Wu, C. (1998). Comparison of the Coil-to-Globule and the Globule-to-Coil Transitions of a Single Poly(N-isopropylacrylamide) Homopolymer Chain in Water. Macromolecules *31*, 2972–2976.

Wu, C., and Zhou, S. (1995). Thermodynamically Stable Globule State of a Single Poly(N-isopropylacrylamide) Chain in Water. Macromolecules *28*, 5388–5390.

Zhao, Y., Tremblay, L., and Zhao, Y. (2011). Phototunable LCST of Water-Soluble Polymers: Exploring a Topological Effect. Macromolecules *44*, 4007–4011.

Appendix 4 – Captures of fluorescent probes on PLL-g-PNIPAM patterns

Contents

1 Generic protocol used for captures of fluorescent probes

Adsorption of 4 fluorescent probes on PLL-g-PNIPAM coatings was investigated by using the following samples:

- Neutravidin-coated FluoSpheres (Polystyrene beads from LifeTechnologies, 0.2 µm diameter at 1% solids diluted 50 fold in Milli-Q water)
- Streptavidin-conjugated quantum dots (QDot565 Strepavidin-conjugate from LifeTechnologies, 0.1 µM in Milli-Q water)
- Streptavidin labeled with cyanine dye (Cy3) (solution of Streptavidin-Cy3 in 0.01 M phosphate buffered from Sigma-Aldrich, diluted 10 fold in Milli-Q water)
- BSA (Albumin from Bovine Serum, Texas Red® conjugate, from ThermoFisher, A23017.

Patterned coverslips were mounted in a flow cell (Figure 114), which enabled accurate control of the temperature and fluorescence imaging (Focht Chamber System 2, FCS2 from Bioptechs, pictures taken under a LEICA DMIRE-2 microscope, equipped with a long-focal×60 dry objective, a ScopeLED Roper Scientific illuminator, and Retina 6000 Q-imaging camera). The chamber was filled with Milli-Q water and heated at the desired temperature Te for 15 min. Water present in the chamber was then rapidly ejected by flushing air, and replaced by 100µL of fluorescent sample preheated at Te. After incubation for 15 min, the chamber was rapidly emptied by flushing air and then rinsed with 2 mL of Milli-244 Q water at Te. Epifluorescence pictures were recorded.

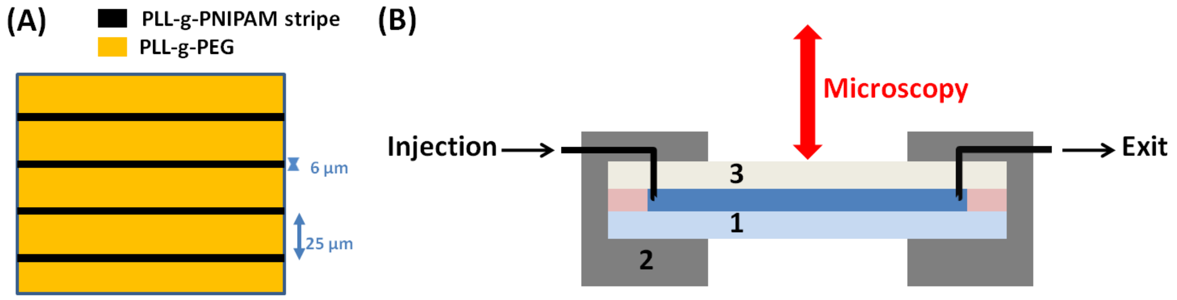

Figure 114 - (A) Coverslips used for adsorption of fluorescent probes on PLL-g-PNIPAM stripes.(B) Representation of the FCS2 chamber, 1 : PLL-coated glass coverslip, 2 : metallic self locking base, 3 : optical surface coated with an electrically conductive transparent thin film of Indium-Tin Oxide (ITO). 2 and 3 make it possible to control accurately temperature.

Adsorption of 0.2 µm beads (FluoSpheres) was quantified by directly counting beads on stripes (average on six 351µm²-stripes). For smaller particles, quantification was based on the contrast defined as $(I_{stripe} - I_{PEG})/(I_{stripe} + I_{PEG})$, with $I_{stripe}/_{PEG}$ being the average intensities measured on six stripes.

2 Adsorption of Streptavidin-Cy3 on mixed PLL-g-[0.1]P(NIPAM-co-biotin)(6):PLL-g-PEG adlayers

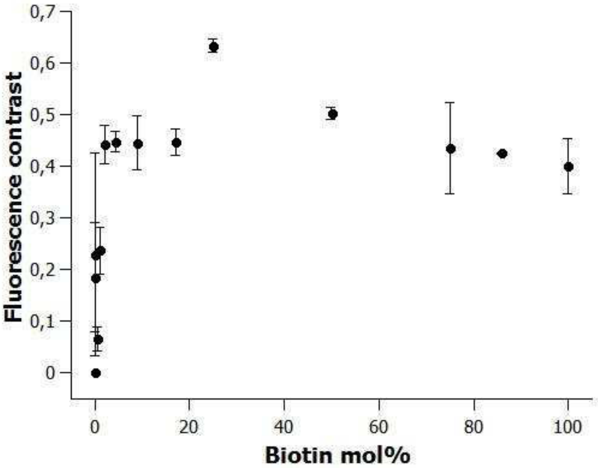

Figure 115 - Fluorescence contrast between mixed PLL-g-[0.1]P(NIPAM-co-biotin)(6):PLL-g-PEG stripes and PEGylated ones after adsorption of Streptavidin-Cy3 (coverslip Figure 1(A)). (% Biotin represents here the polymer fraction (mol %) of PLL-g-[0.1]P(NIPAM-co-Biotin)(6) in the solution used for deposition of the mixture.) (Contrast: $(I_{stripe} - I_{PEG})/(I_{stripe} + I_{PEG})$.)

3 Non-specific protein adsorption on PLL-g-[0.2]PNIPAM(6)

The evaluation of non-specific protein adsorption was investigated using fluorescent BSA (Albumin from Bovine Serum, Texas Red® conjugate, from ThermoFisher, A23017). Independently of the set temperature, fluorescent stripes revealed non-specific adsorption on PLL-g-[0.2]PNIPAM(6) stripes (coverslip Figure 114(A), $S_{Nipam(6)}$ in Table 4 - Chapter 4). This result must be kept in mind for cell adhesion experiments. In particular, serum-free media should be used to avoid non-specific cell adhesion

Appendix 5 - Cell experiments

Contents

Cell experiments were achieved on HeLa cells previously transfected with LifeAct-GFP and Vinculin-mCherry. HeLa cells were cultured in polystyrene flasks in Dulbecco's modified Eagle's medium (DMEM) (Lifetech) supplemented with 10 % fetal bovine serum (FBS) (Gibco) and 1 % penicillin/streptomycin (Lifetech). Cells were detached from the flasks by trypsinization in serum-free DMEM.

1 Cell seeding

WillCo-dish®KIT were assembled with a polymer-coated glass bottom dish (diameter: 35 mm). Before seeding, dishes were rinsed with serum-free DMEM and placed into an incubator with 2 mL of serum-free DMEM for 30 minutes to equilibrate the polymer adlayer at the good temperature (27 °C or 37 °C). Hela cells were seeded on the coverslip in DMEM without serum. Dishes were placed in an incubator at 27 or 37 °C in 5 % CO_2 atmosphere.

2 Qualitative experiments of cell adhesion

Approximatively 261.10^3 cells were seeded on preincubated WillCo-dish and the slides were incubated at 37 °C. After 3 H of incubation, cells were rinsed with PBS, fixed for 15 minutes with 4 % paraformaldehyde in PBS, and finally rinsed with PBS. For each slide, transmission pictures were taken using a dry 40× objective.

Analyzed slides: PLL-g-PEG, PLL-g-[0.2]PNIPAM(6), PLL-g-[0.15]P(NIPAM-co-RGD)(6), bare glass

3 Quantification of cell adhesion

260.10^3 cells were seeded on preincubated WillCo-dish at T_{exp} (37 or 27 °C) (density: $5,6.10^3$ cells/cm²). Then, slides were placed in incubator at T_{exp} for 3 H. To kinetically monitor cell adhesion, slides were regularly taken for microscopy observations (phase contrast, dry 20× objective). From each slide, 5 pictures were recorded and analyzed with ImageJ to determine both the mean cell area and the ratio between spread and round cells.

Analyzed slides: mixed adlayers of PLL-g-[0.15]P(NIPAM-co-RGD)(6) and PLL-g-PEG (% RGD represents the polymer composition (mol %) in PLL-g-[0.15]P(NIPAM-co-RGD)(6) of the solution used for coating); mixed adlayers of PLL-g-[0.15]P(NIPAM-co-RGD)(6) and PLL-g-[0.2]-PNIPAM(6).

On mixed adlayers of of PLL-g-[0.15]P(NIPAM-co-RGD)(6) and PLL-g-[0.2]-PNIPAM(6), TIRF pictures were taken (100× objective) to covisualize LifeAct-GFP and Vinculin-mCherry.

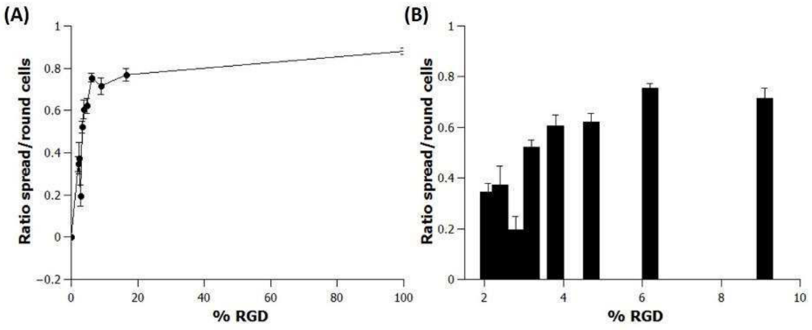

Figure 116 – (A) Comparison of the ratio between spread and round HeLa cells at 37 °C 3 H postseeding on mixed adlayers of PLL-g-[0.15]P(NIPAM-co-RGD)(6) and PLL-g-PEG. (B) Zoom closed to the RGD threshold density.

4 Cell detachment

260.10^3 cells were seeded on preincubated WillCo-dish at 37 °C (density: $5,6.10^3$ cells/cm²). Then, slides were placed in incubator at 37 °C for 3 H. Cell detachment was triggered by placing slides in microscope at 27 °C. To kinetically monitor cell deadhesion, movies were recorded (phase contrast, dry 40× objective, 0.1 image/min). From each slide, 10 positions were recorded and analyzed with ImageJ to determine both cell area and the ratio between spread and round cells.

5 Reversible temperature-triggered change in cell shape

Study of cell shape change was achieved on grid pattern (Figure 117). A PLL-g-PEG coverslip was first patterned with mixed solutions of PLL-g-[0.15]P(NIPAM-co-RGD)(6)/PLL-g-[0.2]PNIPAM(6) (7.5 - 10.5 % RGD) (vertical stripes). Then, a second patterning step with a solution of PLL-g-[0.15]P(NIPAM-co-RGD)(6)/PLL-g-PEG (16 % RGD) (horizontal stripes) afforded the “grid pattern”. (With of stripes: 10 µm, distance between stripes: 60 µm).

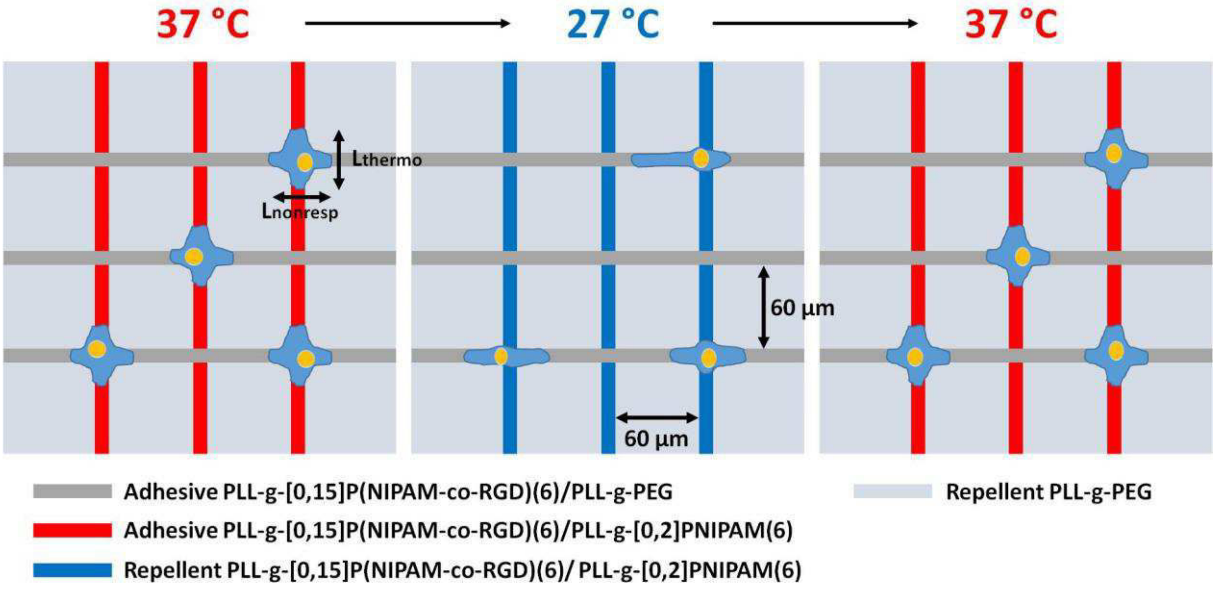

Figure 117 - Schematic representation of reversible temperature-triggered change in cell shape on grid pattern. With of each stripe is 10 µm. Vertical stripes are thermoresponsive (adhesive at 37 °C and repellent at 27 °C) while adhesive vertical stripes are non-thermoresponsive.

85.10^3 cells were seeded on preincubated WillCo-dish at 37 °C. Then, slides were placed in incubator at 37 °C for 4 H. Movies (520 minutes, 1picture/10minutes) were recorded while imposing to two consecutive temperature jumps (first jump: 37 → 27 °C at 120 minutes, second jump: 27 → 37 °C at 320 minutes).

Quantification were achieved on phase contrast movies (dry 20× objective, 10 positions were recorded on each sample) considering only single cells located at an intersection during the whole movie. Elongation $\frac{L-L_0}{L_0}$ was evaluated on both vertical and horizontal directions. The ratio between lengths on each axe: $({}^{Lthermo}/{}_{Lnonthermo})_{Norm} = \frac{\left(\frac{L_{thermo}}{L_{nonthermo}}\right)_t}{\left(\frac{L_{thermo}}{L_{nonthermo}}\right)_0}$ was evaluated. Average on 10 cells was finally calculated for these two parameters.

Appendix 6 - Thermal relaxation

The absorption spectra were acquired using a diode array UV-visible spectrophotometer (Evolution Array, Thermo Scientific) equipped with a Peltier temperature controller.

Photoirradiation were carried out using a photodiode system CoolLED PE-2 (Roper Scientific, France) which emits blue light (436 nm at a power of ca. 2 mW cm²) or UV light (365 nm at a power of ca. 10 mWcm²).

To estimate the kinetics of thermal relaxation, solutions containing azobenzene were obtained in PBS. The concentration in azobenzene was adjusted in order to have an important change of adsorption under UV light at the wavelength attributed to the π- π^* transition of the trans isomer ($\lambda_{\pi-\pi^*}$). Moreover, the absorption at $\lambda_{\pi-\pi^*}$ was inferior at 1. The solution was irradiated under UV up to reach the photo-stationary *trans*:*cis* equilibrium between the isomers of azobenzene. After UV irradiation, the absorbance at $\lambda_{\pi-\pi^*}$ was monitored while the temperature was maintained at an accurate temperature.

Absorption at $\lambda_{\pi-\pi^*}$ at given time (A_t) under constant temperature is described by the following relationship: $\ln(A_t - A_\infty/A_0 - A_\infty) = -t/\tau$ where A_0 and A_∞ represent the initial absorption at $\lambda_{\pi-\pi^*}$ and the absorption at the thermodynamic equilibrium respectively. First order rate constant of cis-trans isomerization, $1/\tau$, is determined by fitting experimental data with this equation.

- **<u>Azobenzene-NH$_2$</u>:** T = 20 °C, τ = 22 minutes, $\lambda_{\pi-\pi^*}$ = 345 nm

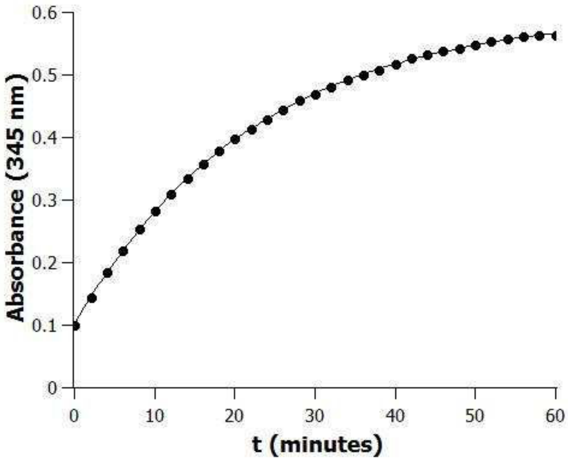

- **PLL-g-[0.1]α-Azo,ω-Butanamido-P(NIPAM-co-Biotin)(2):** T = 20 °C, τ = 80 minutes, $\lambda_{\pi-\pi^*}$ = 345 nm

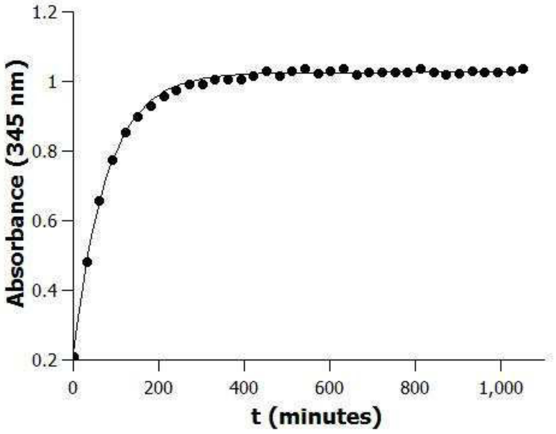

- **α,ω-di-COOH-P(NIPAM-co-Azo[9]-NMe$_2$[40])(6):** T = 20 °C, τ = 8.5 H, $\lambda_{\pi-\pi^*}$ = 345 nm